



**HAL**  
open science

# Vers la simulation de perfusion du myocarde à partir d'image tomographique scanner

Clara Jaquet

► **To cite this version:**

Clara Jaquet. Vers la simulation de perfusion du myocarde à partir d'image tomographique scanner. Traitement des images [eess.IV]. Université Paris-Est, 2018. Français. NNT : 2018PESC1117 . tel-02085886

**HAL Id: tel-02085886**

**<https://pastel.hal.science/tel-02085886>**

Submitted on 31 Mar 2019

**HAL** is a multi-disciplinary open access archive for the deposit and dissemination of scientific research documents, whether they are published or not. The documents may come from teaching and research institutions in France or abroad, or from public or private research centers.

L'archive ouverte pluridisciplinaire **HAL**, est destinée au dépôt et à la diffusion de documents scientifiques de niveau recherche, publiés ou non, émanant des établissements d'enseignement et de recherche français ou étrangers, des laboratoires publics ou privés.



TOWARD MYOCARDIUM PERFUSION FROM X-RAY  
COMPUTED TOMOGRAPHY

Clara Jaquet

Thesis co-directors

Hugues Talbot, Laurent Najman

Thesis co-supervisors

Charles Taylor, Leo Grady, Michiel Schaap, Irène Vignon-Clementel

PhD in Computing science

Defense on December 18th 2018

Université Paris Est

École Doctorale MSTIC

Jury

Irène VIGNON-CLEMENTEL	INRIA	President
Hervé DELINGETTE	INRIA	Reviewer
Frans VAN DE VOSSE	TU Eindhoven	Reviewer
Patrick CLARYSSE	CREATIS, CNRS	Examiner



Clara Jaquet: *Toward myocardium perfusion from X-ray computed tomography*, © December 2018



## ABSTRACT

---

Recent advances in medical image computing have allowed automated systems to closely assist physicians in patient therapy. Computational and personalized patient models benefit diagnosis, prognosis and treatment planning, with a decreased risk for the patient, as well as potentially lower cost. HeartFlow Inc. is a successful example of a company providing such a service in the cardiovascular context. Based on patient-specific vascular model extracted from X-ray CT images, they identify functionally significant disease in large coronary arteries. Their combined anatomical and functional analysis is nonetheless limited by the image resolution. At the downstream scale, a functional exam called Myocardium Perfusion Imaging (MPI) highlights myocardium regions with blood flow deficit. However, MPI does not functionally relate perfusion to the upstream coronary disease.

The goal of our project is to build the functional bridge between coronary and myocardium, by extrapolating the functional analysis from large coronary toward the capillary bed. This objective requires extension from the coronary model down to the microvasculature combined with a functional analysis leading to the myocardium compartment.

We expand a tree generation method subjected to functional principles, named Constrained Constructive Optimization, to generate multiple competing vascular trees. The algorithm simulates angiogenesis under vascular volume minimization with flow-related and geometrical constraints, adapting the simultaneous tree growths to patient priors. This method provides a hybrid image-based and synthetic geometric model, starting from segmented epicardium coronary down to synthetic arterioles, filling the left ventricle myocardium.

We then build a multiscale functional analysis pipeline to allow blood flow simulation from the coronaries to the myocardium. This is achieved with a 1D coronary model compatible with the hybrid vasculature, and a spatial blood flow distribution analysis of the terminal segments. The latter is performed using a similar nomenclature to MPI, to enable patient-specific comparison with functional ground-truth data.

We connected the vascular anatomy to blood flow distribution in the myocardium on several patient datasets. This multiscale framework points out several leads to refine the vascular network generation and fluid simulation methods. This patient-specific anatomical and functional extrapolation is a first gateway toward myocardium perfusion from X-ray CT data. Building such personalized compu-

tational model of patient could potentially help investigating cardiovascular complex physio-pathology, and, finally, improve the patient care.

Keywords:

patient specific modeling - cardiac vascular network generation - functional analysis - coronary arteries - myocardium perfusion

## RÉSUMÉ

---

De nos jours, les progrès de l'informatisation de l'imagerie médicale assistent au plus près les médecins dans leur soin au patient. Des modèles personnalisés computationnels sont utilisés pour le diagnostic, pronostique et planification du traitement, en diminuant les risques pour le patient, et potentiellement les frais médicaux.

Heartflow est l'exemple même d'une compagnie qui réussit ce service dans le domaine cardiovasculaire. À partir d'un modèle extrait d'images tomographiques rayons X, les lésions avec impact fonctionnel sont identifiées dans les artères coronaires. Cette analyse qui combine l'anatomie à la fonction est néanmoins limitée par la résolution de l'image. En aval de ces larges vaisseaux, un examen fonctionnel dénommé Imagerie de Perfusion du Myocarde (IPM) met en évidence les régions du myocarde affectées par un déficit de flux sanguin. Cependant, l'IPM n'établit pas de relation fonctionnelle avec les larges vaisseaux coronaires lésés en amont.

L'objectif de ce projet est de construire la connection fonctionnelle entre les coronaires et le myocarde, en extrapolant l'analyse fonctionnelle depuis les larges vaisseaux vers le lit capillaire. À cette fin, il faut étendre le modèle vasculaire jusqu'aux microvaisseaux, et mener une analyse fonctionnelle en direction du compartiment myocardique.

Nous étendons une méthode de génération d'arbre vasculaire basée sur la satisfaction de principes fonctionnels, nommée *Constrained Constructive Optimization* (*Optimization Constructive sous Contraintes*), pour qu'elle s'applique à de multiples arbres vasculaires en compétition. L'algorithme simule l'angiogénèse avec minimisation du volume vasculaire sous contraintes de flux et de géométrie adaptant la croissance simultanée des arbres aux caractéristiques du patient. Cette méthode fournit un modèle hybride composé de coronaires épiscopales extraites d'images et de vaisseaux synthétiques jusqu'aux artérioles, emplissant le ventricule gauche du myocarde.

Puis, nous construisons un pipeline d'analyse fonctionnelle multi-échelle pour étendre la simulation de flux depuis les coronaires vers le myocarde. Cela consiste en un modèle de flux coronaire 1D compatible avec la vasculature hybride, et l'analyse de la distribution spatiale des flux provenant des segments terminaux. Cette dernière est réalisée dans une nomenclature similaire à celle de l'IPM pour permettre la comparaison avec des données de vérité terrain fonctionnelles.

Nous avons relié l'anatomie du réseau vasculaire à la distribution de flux dans le myocarde pour plusieurs patients. Cette analyse multi-échelle permet d'identifier des pistes pour affiner les méthodes de gé-

nération vasculaire et de simulation de flux. Cette extrapolation anatomique et fonctionnelle personnalisée est une première passerelle pour la simulation de perfusion du myocarde à partir d'imagerie tomographique scanner. La construction d'un tel modèle computationnel personnalisé pourrait aider à la compréhension de la physio-pathologie cardiovasculaire complexe et, enfin, à la santé du patient.

Mots clefs :

modèle personnalisé du patient - génération de réseau vasculaire cardiaque - analyse fonctionnelle - artères coronaires - perfusion du myocarde

## RÉSUMÉ LONG

---

De nos jours, les progrès de l'informatisation de l'imagerie médicale assistent au plus près les médecins dans leur soin au patient. Les avancées de l'imagerie médicale permettent d'acquérir divers signaux avec une large gamme de résolution spatiale et temporelle. Par ailleurs, des phénomènes physiologiques tel que l'hémodynamique par exemple, sont à présent simulés à l'aide de modèles numériques génériques. En personnalisant ces simulations à l'aide d'images anatomiques ou fonctionnelles du patient, on peut ainsi construire des modèles personnalisés computationnels. Ceux-ci sont utilisés pour le diagnostic, le pronostic et la planification du traitement. Ils améliorent ainsi l'accompagnement thérapeutique du patient en diminuant les risques, et potentiellement les frais médicaux.

Heartflow est l'exemple même d'une compagnie qui réussit ce service dans le domaine cardiovasculaire. L'entreprise propose une solution non invasive pour le diagnostic des lésions dans les vaisseaux coronaires : FFRct, illustrée en figure 1a. La géométrie des artères coronaires du patient est extraite à partir d'une image tomographique du cœur par rayons X. Dans ce modèle anatomique personnalisé, le flux sanguin est simulé. Ainsi, ce processus identifie les lésions qui impactent la fonction de transport du sang dans les artères coronaires. Cette analyse, qui combine l'anatomie à la fonction, est néanmoins limitée par la résolution de l'image.

En aval de ces larges vaisseaux, un examen fonctionnel dénommé Imagerie de Perfusion du Myocarde (IPM) permet de quantifier le sang transporté dans le tissu musculaire du cœur. Le résultat est produit sous forme d'une cartographie polaire du myocarde, illustré en figure 1b. Cet examen consiste à détecter la distribution d'un agent de contraste dans le tissu, en soumettant le patient à des conditions de repos et de stress. La comparaison de ces deux situations met en évidence les régions du myocarde affectées par un déficit de flux sanguin. Cependant, l'IPM n'établit pas de relation fonctionnelle avec les larges vaisseaux coronaires lésés en amont.

L'objectif de ce projet est de construire la connection fonctionnelle entre les coronaires et le myocarde, en extrapolant l'analyse hémodynamique depuis les larges vaisseaux vers le lit capillaire. À cette fin, il faut étendre le réseau vasculaire du patient jusqu'aux microvaisseaux, et mener une analyse fonctionnelle en direction du compartiment myocardique. Sachant que l'examen IPM ne fournit une vérité terrain que pour le ventricule gauche du myocarde, nous concentrons

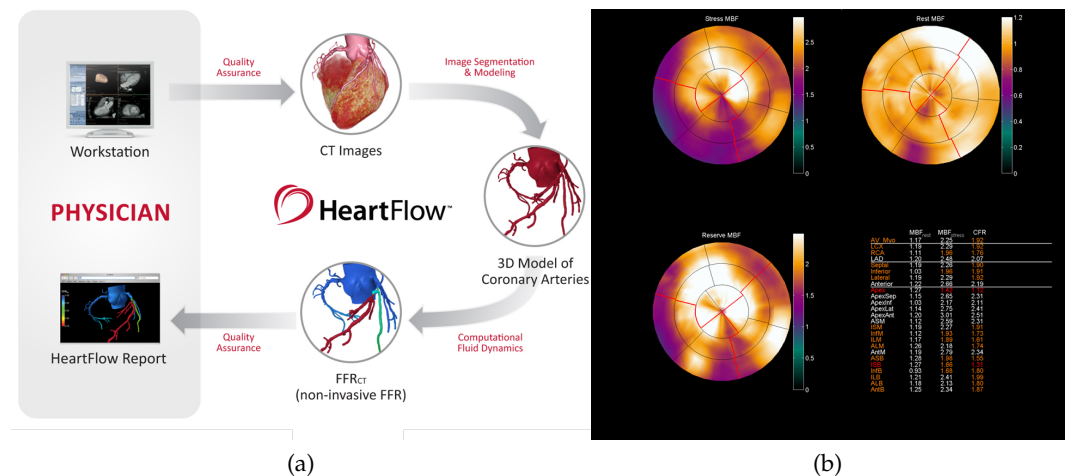


FIGURE 1 – Illustration de deux examens pour le diagnostic de pathologies coronariennes. (a) FFRct, processus de l’outil diagnostique. (b) : IMP par examen water-PET, exemple de résultat de patient malade. Haut : stress (gauche) et repos (droite). Bas : ratio des résultats stress et repos, dit réserve. Dans cet exemple, on observe une section sur la gauche particulièrement déficitaire.

notre travail sur cette seule chambre cardiaque.

Plusieurs méthodes pour générer des réseaux vasculaires en territoire contraint existent, mais aucune n’a été appliquée pour l’extension de coronaires spécifiques d’un patient. Dans cet objectif, nous nous sommes intéressés à une méthode nommée Constrained Constructive Optimization (Optimisation Constructive sous Contraintes). Celle-ci consiste à simuler l’angiogénèse, la croissance du réseau vasculaire concomitante du tissu perfusé. Cette méthode repose sur la satisfaction de plusieurs principes fonctionnels. Notamment, elle considère une distribution homogène des flux dans le territoire perfusé, et elle minimise l’énergie du réseau vasculaire, symbolisée par son volume total. De plus, elle garantit la satisfaction de lois hémodynamiques à l’échelle d’une bifurcation et de l’arbre entier. Cet algorithme de génération d’un arbre vasculaire a évolué : initialement en 2D, puis en 3D, ensuite impliquant une croissance par étape, et enfin adapté à la forme concave du ventricule, cf figure 2. Cependant, cette méthode ne génère qu’un seul arbre vasculaire dans un territoire simulé.

Inspirée de la CCO, nous proposons donc une méthode innovante afin de générer plusieurs arbres vasculaires, et respecter les caractéristiques du patient : CCO Forest. Dans cette méthode, la croissance simultanée, et donc compétitive, des arbres vasculaires est guidée par le flux associé à chaque arbre. Nous avons établi une preuve de concept en territoire simulé 2D, présentée en figure 3. Elle démontre que le ter-

ritoire perfusé obtenu est proportionnel au flux de l'arbre vasculaire, ce qui est cohérent avec la littérature.

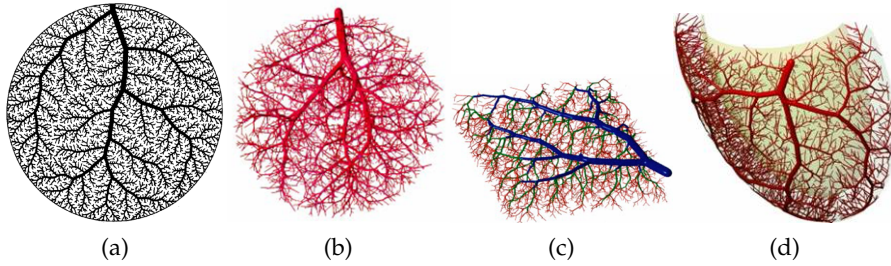


FIGURE 2 – Evolution de l'algorithme CCO : visuel des résultats de (a) CCO en 2D [85], (b) CCO en 3D [54], (c) CCO avec croissance par étape [55], (d) CCO non convexe pour le ventricule [86]

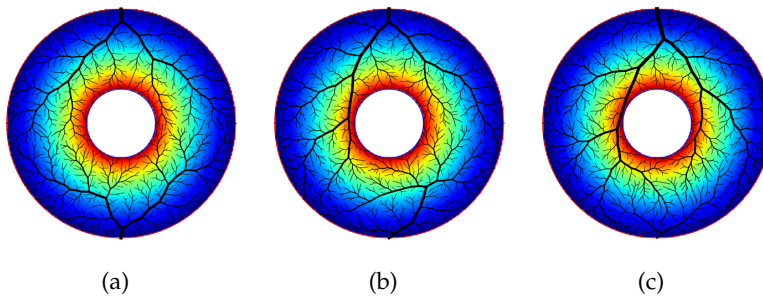


FIGURE 3 – Illustration de la preuve de concept de CCO Forest en territoires simulés non convexes, avec divers flux  $q$ , pour deux arbres (celui du haut : "h", celui du bas : "b"). (a) :  $q_h = q_b$ . (b) :  $q_h = 2q_b$ . (c) :  $q_h = 9q_b$ . Le dégradé de couleurs représente la distance à la concavité centrale.

Afin de personnaliser cette méthode pour les données de patients, nous utilisons la segmentation des gros vaisseaux et du ventricule, extraits de la tomographie rayons X. Nous distribuons des arbres vasculaires synthétiques à chaque extrémité et le long du réseau segmenté, selon un modèle statistique issu de la littérature. Nous associons à chacun des arbres un flux proportionnel à son diamètre. Nous initialisons chaque arbre avec un premier segment qui le relie à la surface du ventricule. Puis, nous effectuons une croissance de la forêt d'arbres vasculaires en deux étapes : d'abord sur la surface du ventricule, et ensuite dans son volume entier. Afin d'obtenir une cohérence avec le réseau segmenté, lors de la croissance des arbres nous appliquons des contraintes géométriques angulaires, et rejetons tout segment intersectant les vaisseaux pré-existants. La méthode est illustrée dans la figure 4. Elle produit un modèle hybride composé des coronaires extraites d'images et de segments synthétiques jusqu'aux artérioles, emplantant le ventricule gauche du myocarde. Nous avons appliqué CCO Forest sur 6 patients, produisant un réseau vasculaire de

6000 segments terminaux chacun. L'algorithme démontre robustesse et répétabilité. Les caractéristiques morphométriques des réseaux hybrides obtenus montrent une bonne corrélation avec les statistiques de la littérature.

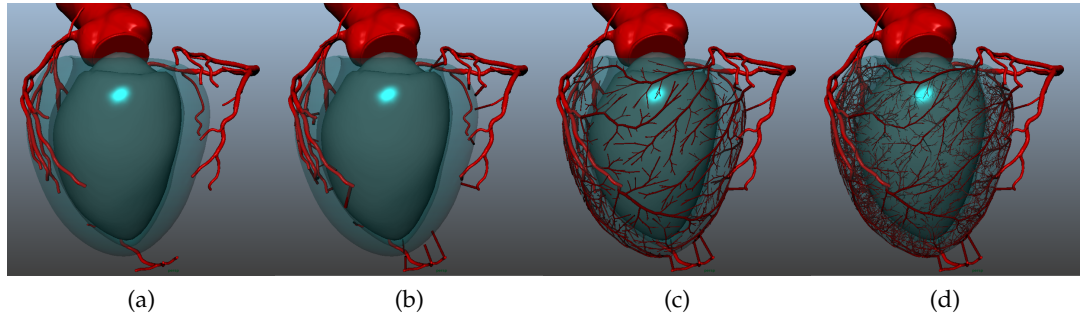


FIGURE 4 – Illustration de CCO Forest sur un patient. (a) : éléments initiaux fournis à l'algorithme. (b) : distribution du premier segment de chaque arbre connectant à la surface du ventricule. (c) : croissance en surface, jusqu'à obtenir 1000 segments terminaux. (d) : croissance dans le volume, atteignant 6000 segments terminaux.

Afin d'analyser les propriétés fonctionnelles des réseaux générés, et de permettre la comparaison avec la vérité terrain, nous construisons un pipeline d'analyse fonctionnelle multi-échelle qui étend la simulation de flux depuis les coronaires vers le myocarde. Celui-ci se compose de trois outils.

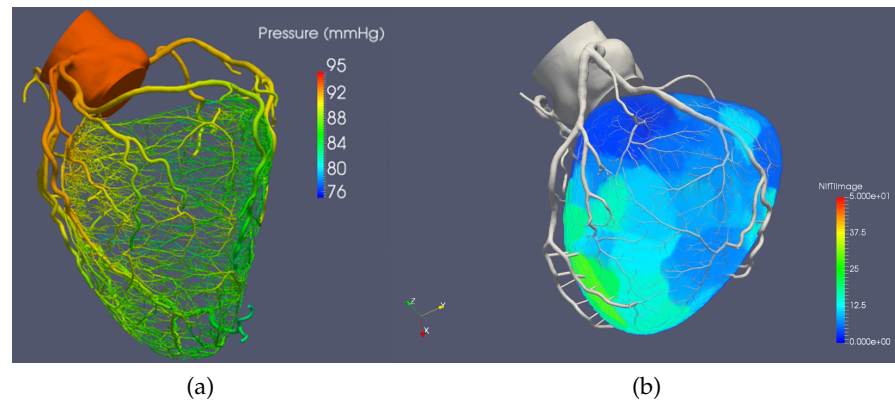


FIGURE 5 – Visualisation des résultats des deux premières étapes du pipeline d'analyse fonctionnelle. (a) Simulation des pressions dans le réseau hybride avec notre modèle 1D Navier-Stokes. (b) Distribution des flux des segments terminaux dans le myocarde.

Tout d'abord, nous simulons le flux sanguin dans le réseau hybride à l'aide d'un modèle de flux artériel 1D résolvant le système d'équations de Navier-Stokes. Ce modèle est construit pour simuler

des conditions de repos ou de stress similaire à celui impliqué pour l'examen d'IPM. Il est construit avec l'hypothèse d'un fluide idéalisé, au flux non turbulent, en régime constant. Les conditions aux limites imposent une pression aortique de référence à l'entrée des coronaires, et des flux déterminés aux segments terminaux, qui sont actualisés au fur et à mesure des itérations. La résolution du système fournit les champs de pression et de flux dans l'ensemble du réseau vasculaire. La figure 5a illustre les pressions obtenues sur l'exemple d'un patient en condition de repos.

Puis, nous analysons la distribution spatiale des flux aux segments terminaux. Pour cela nous divisons le myocarde en une multitude de sous-volumes, et comptabilisons les flux des segments terminaux dans chacun d'entre eux. Cette estimation des flux à l'échelle du myocarde est illustrée en figure 5b. Elle permet d'étudier les intervalles de distribution de flux à l'échelle globale et locale, pour les comparer à ceux de la littérature.

Enfin, nous transposons cette distribution de flux dans le format de cartographie polaire similaire à l'IPM, visible en figure 6. À cette fin, nous décomposons le ventricule en 17 régions, selon un système de coordonnées polaires correspondant à la nomenclature de la littérature. Les flux associés à ces régions sont ensuite projetés sur la cartographie 2D représentant le ventricule. Cette représentation permet une comparaison qualitative et quantitative avec les données de vérité terrain IMP.

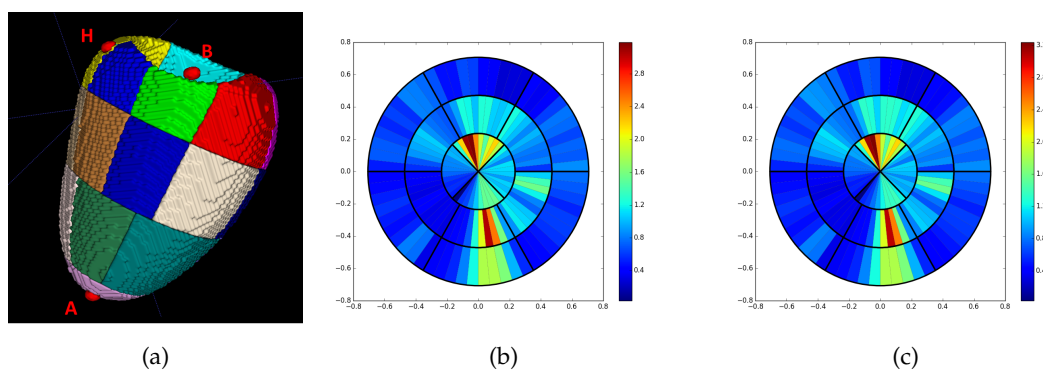


FIGURE 6 – Conversion vers le format de cartographie polaire IPM. (a) Décomposition du myocarde en 17 régions selon la nomenclature de référence. Les ellipsoïdes rouges définissent les axes du système de coordonnées polaires. (b) et (c) Projection de la distribution des flux aux segments terminaux de chaque région dans la cartographie 2D. Résultat en condition de repos (b), et de stress (c).

Nous avons appliqué ce pipeline sur 4 réseaux hybrides de patients peu symptomatiques. Les valeurs de flux, pressions et résistances dans les vaisseaux sont cohérentes avec la littérature. Cependant la distribution des flux à l'échelle du myocarde présente une hétéro-

généité non physiologique, responsable d'un manque de corrélation avec les données de vérité terrain. Le pipeline met donc en évidence les caractéristiques à améliorer.

Nous avons relié l'anatomie du réseau vasculaire à la distribution de flux dans le myocarde pour plusieurs patients. Cette analyse multi-échelle permet d'identifier des pistes pour affiner les méthodes de génération vasculaire et de simulation de flux.

Des améliorations indépendantes, à chaque étape du processus, peuvent désormais être mises en place et leur impact analysé sur l'ensemble de la chaîne. Notamment, pour la génération du réseau vasculaire, le nombre de segments terminaux et leur distribution en surface ou dans le volume peuvent être étudiés pour identifier un paramétrage spécifique du patient. De plus, l'extrapolation des flux vers le myocarde pourrait être simulée avec un modèle plus représentatif de la physiologie : un modèle poreux correspondant au lit capillaire du myocarde, couplé au modèle de flux dans les vaisseaux. Également, la résolution et palette de couleurs de la cartographie polaire seront améliorées pour affiner la comparaison qualitative avec les données de vérité terrain. Par ailleurs, la validation de ce processus devra être effectuée sur un plus grand panel de patients. Ce panel inclura des données avec une unique lésion aiguë du coronaire dont les conséquences sur la perfusion du myocarde seront clairement identifiées dans les données IPM.

Cette extrapolation anatomique et fonctionnelle personnalisée est une première passerelle pour la simulation de perfusion du myocarde à partir d'imagerie tomographique scanner. La construction d'un tel modèle computationnel personnalisé fournirait de nombreuses perspectives. En particulier, ce modèle permettrait d'affiner les simulations de flux menées dans les larges coronaires pour FFRct, en fournissant des conditions aux limites plus proches des caractéristiques du patient. De plus, la résolution de problèmes inverses via ce modèle améliorerait la planification du traitement. Ce modèle pourrait être élargi au ventricule droit et à l'ensemble des chambres cardiaques, pour produire une analyse plus complète du système. Dans une même approche, cette extrapolation anatomique et fonctionnelle pourrait être appliquée à d'autres organes. De tels modèles computationnels personnalisés bénéficieraient à la compréhension de physio-pathologies complexes et, enfin, à la santé du patient.

## PUBLICATIONS

---

Parts of this project have appeared in the following publications.

### ABSTRACT PRESENTED IN INTERNATIONAL CONFERENCE

Clara Jaquet, Laurent Najman, Hugues Talbot, Leo Grady, Hyung Jin Kim, Irene Vignon-Clementel, and Charles J Taylor. « Hybrid image-based and synthetic geometric models for patient-specific simulation of coronary blood flow from the large arteries to the myocardium. » In: *World Conference of Biomechanics* (2018)

### INTERNATIONAL JOURNAL

To appear: Clara Jaquet, Laurent Najman, Hugues Talbot, Leo J Grady, Michiel Schaap, Buzzy Spain, Hyun Jin Kim, Irene Vignon-Clementel, and Charles A Taylor. « Generation of patient-specific cardiac vascular networks: a hybrid image-based and synthetic geometric model. » In: *IEEE Transactions on Biomedical Engineering* (2018)

### PATENTS

Leo Grady, Michiel Schaap, Charles A Taylor, and Clara Jaquet. *Systems and methods for predicting perfusion deficits from physiological, anatomical, and patient characteristics*. US Patent App. 15/088,733. 2016

Clara Jaquet, Michiel Schaap, Ying Bai, Leo Grady, and Charles A Taylor. *Systems and methods for determining and visualizing a functional relationship between a vascular network and perfused tissue*. US Patent App. 15/088,512. 2016



## ACKNOWLEDGEMENTS

---

As my thesis directors, I would like to thank Laurent Najman and Hugues Talbot. I benefited tremendously from your wealth of expertise as I have learned a vast amount through every good or bad working days. Through our collaboration I also acquired skills in patience and conflict resolution, which I am certain, will pave the grounds for my future endeavors. Thank you for your patience and your involvement all throughout these years.

With regard to sponsoring this research project I would like to thank HeartFlow. In particular I would like to express my deep gratitude to the representatives who lay their trust in me for this topic, and advised me during this PhD: Charles Taylor, Leo Grady and Michiel Schaap. This work also involved many people within the company, I would like to thank specially Jin, Buzzy, Matthew, Karl, who closely contributed to the project. Also, a special mention for Kelly, Leslie, Laurence, Jean-Luc and Arnaud for providing smiling support with data, tools and engineering processes. Thank you all for welcoming me during my visits and making me feel part of the company.

Irene Vignon-Clementel joined the project bringing in her skills and also a great support helping me to understand a field I was unfamiliar with. A warm thanks for your rigorous pedagogy and your continuous guidance. It was an honor to have you at the Presidency of the jury. Also, for his enthusiasm and passionate work a great thanks to Lazaros Papamanolis. I hope you learned at least as much as I did during our collaboration.

Thank you to Paul Knaapen and Roel Driessen for providing perfusion data, and welcoming me at VU Medical Center. A special gratitude to Roel for the in-depth introduction to the clinical aspects of perfusion imaging.

I would like to thank Hervé Delingette and Frans Van De Vosse for their constructive and detailed review of my manuscript. Thank you to Patrick Clarysse for examining and sharing his skills while analyzing this research. Thank you to all three for your positive interest into this project.

This PhD would not have been successful without a warm personal support.

To my brothers in arms of the LIGM & ESIEE, we've been through so much all together! Thank you for bearing my moods, and comforting me with tea-times, sweets, cheese or just spirit. It was indeed a pleasure to share the extra-work time with you all.

Also I would like to thank my friends who endured my PhD student feelings all along those years. My fencing dream team: Mathilde, Celia, Tutu, and my Fée Clochette, nothing can defeat your positive energy. Geographically distant but supporting in spirit, thank you to Lisa, Yasemin, Fred and Quynh-Anh.

Finally I would like to thank my whole family for their care and support. Thank you to my grand-parents for their curiosity and advice. Thank you Dad for encouraging me in superior studies, and your help to find the adequate words when it becomes important. Thank you Mum for pushing me further, with your joyful energy, and dealing with my americano-german accent. Thank you Victoire for your daily challenging scientific question, you did indeed prepare me for the defense! Thank you Pierre for watching over all of us.

I was lucky to have you all accompany me through all these years, and I look forward to the future steps...

# CONTENTS

---

<b>Introduction</b>	<b>1</b>
Personalized computational patient . . . . .	3
Coronary artery disease . . . . .	4
Perfusion . . . . .	5
Objective . . . . .	8
<b>I VASCULAR MODEL GENERATION</b>	<b>11</b>
<b>1 CONTEXT</b>	<b>13</b>
1.1 Cardiovascular anatomy . . . . .	13
1.1.1 Heart anatomy . . . . .	13
1.1.2 Coronary tree . . . . .	14
1.2 State of the art . . . . .	16
1.2.1 Model derived from anatomical data . . . . .	17
1.2.2 Model constructed from functional principles . . . . .	19
1.2.3 Objective . . . . .	20
<b>2 METHODS</b>	<b>21</b>
2.1 Assumptions . . . . .	21
2.2 CCO algorithm . . . . .	22
2.2.1 Tree growth . . . . .	22
2.2.2 Territory specificity . . . . .	23
2.3 CCO Forest: Extension of CCO to multiple trees . . . . .	24
2.3.1 Forest initialization . . . . .	24
2.3.2 Forest growth . . . . .	25
2.4 CCO forest adapted to patient data . . . . .	26
2.4.1 Patient priors . . . . .	28
2.4.2 Patient-specific constraints . . . . .	30
<b>3 RESULTS ON PATIENTS</b>	<b>35</b>
3.1 Data . . . . .	35
3.2 Testing algorithm repeatability . . . . .	36
3.3 Testing algorithm robustness . . . . .	38
3.4 Summary of the results . . . . .	47
<b>4 ALTERNATIVE METHOD OF VASCULAR MODEL GENERATION</b>	<b>49</b>
4.1 Algorithm alternative . . . . .	49
4.2 Comparing RB algorithm results with PB results . . . . .	49
<b>5 DISCUSSION</b>	<b>53</b>
5.1 Perspective of improvements . . . . .	53
5.2 Limits of validation . . . . .	55
<b>II FUNCTIONAL ANALYSIS</b>	<b>57</b>
<b>6 CONTEXT</b>	<b>59</b>
6.1 Cardiovascular function . . . . .	59

6.1.1	Cardiac cycle . . . . .	59
6.1.2	Coronary function . . . . .	60
6.1.3	Cardiovascular complexity . . . . .	60
6.2	Heart modeling: state of the art . . . . .	63
6.2.1	Existing models . . . . .	63
6.2.2	Coupled perfusion and coronary models . . . . .	66
6.3	Objective . . . . .	67
6.3.1	Myocardium perfusion imaging data . . . . .	67
7	CFD IN CORONARIES . . . . .	71
7.1	Assumptions . . . . .	71
7.2	Model . . . . .	72
7.2.1	Boundary conditions . . . . .	73
7.2.2	Algorithm for the 1D model . . . . .	73
8	FUNCTIONAL ANALYSIS PIPELINE . . . . .	77
8.1	Vessel flow . . . . .	77
8.2	Vessel pressure . . . . .	77
8.2.1	Study per element . . . . .	77
8.2.2	Study along segment order . . . . .	78
8.2.3	Study along vessel path . . . . .	79
8.3	Resistance . . . . .	83
8.4	Shear rate . . . . .	84
8.5	Terminal segment flows . . . . .	84
8.5.1	Relative distribution . . . . .	85
8.5.2	Distribution in myocardium . . . . .	85
8.5.3	Comparison with perfusion exams . . . . .	89
9	DISCUSSION . . . . .	95
9.1	Improvement and validation of the pipeline tools . . . . .	95
9.2	Validation of the personalized computational model extrapolation . . . . .	96
	<b>Conclusion</b> . . . . .	99
	Achievements . . . . .	101
	Framework : independent refinements . . . . .	101
	Validation using the framework . . . . .	103
	Perspectives . . . . .	104
	<b>III APPENDIX</b> . . . . .	109
10	CCO IMPLEMENTATION REPORT . . . . .	111
11	CONVERGENCE PROCESS . . . . .	129
12	MORPHOMETRY STUDY ON EPICARDIAL NETWORKS . . . . .	131
13	MORPHOMETRY STUDY OF EPICARDIAL CORONARIES . . . . .	133
14	VASCULAR MODEL RESULTS ON ADDITIONAL DATASET . . . . .	169
15	POROUS MODEL, COUPLED WITH VASCULAR CFD . . . . .	177
15.1	Porous model equations . . . . .	177
15.2	Coupling . . . . .	179
15.2.1	Initialization . . . . .	179

15.2.2	Iterations . . . . .	181
15.2.3	Test results on simplified geometry . . . . .	181
15.2.4	Preliminary result on patient data . . . . .	187
15.2.5	Future work . . . . .	188
16	CONTRIBUTIONS	191
16.1	Personal contributions . . . . .	191
16.2	Contributions of collaborators . . . . .	191
	BIBLIOGRAPHY	195



## INTRODUCTION



## INTRODUCTION

---

### PERSONALIZED COMPUTATIONAL PATIENT

Nowadays, computer science assists physicians in many aspects of patient care.

Medical informations have become mostly digitized: anatomical and physiological parameters are stored in medical record, tracked by sensors via monitoring, or imaging techniques. Technology progress has enabled the acquisition of various signals from genetics to phenotype expression, and digitize them. Such acquired signals can be very rich in content, from scalar value to multiple dimension matrices, thus computer science also provides tools to organize and classify them. These tools can sometimes help physicians to confront the patient information with generic statistical models, in order to detect discrepancies.

In parallel, development has also occurred in the modeling field, to describe and simulate function of living organism at all scales: from the atomic to the whole body scale via molecular interaction, cellular metabolism, and organ systems. These models are derived from biology, physics, chemistry and mathematical laws describing a functional process, that have been theoretically and experimentally validated on many occurrences.

These two fields, digitized patient and functional modeling, have naturally converged to patient-specific modeling.

Medical imaging has shown spectacular progress in the last decades. It provides now a huge panel of spatial and time resolution, from cellular to macroscopique scale. Combined with extensive models of physiology, medical imaging provides powerful instruments: personalized computational patient models, as termed in particular by Nicolas Ayache [5]. These instruments are defined by a generic computational model adapted to patient characteristics acquired from anatomical or functional imaging. These models provide quantification useful for diagnostic, predict pathological evolution or therapy effect, conduct treatment planning and even intervention assistance (with robotization, virtual or augmented reality). They allow to simulate, learn and predict via less invasive exams, to improve patient care.

The personalized computational patient model has taken the research world by storm, connecting clinical, industrial and academia with many collaborations. Current organ related projects mostly fo-

cus on brain and cardiovascular diseases. National and international organization like the Brain initiative (USA, starting in 2013), human brain Project (Europe, starting in 2013) bring researchers together from public and private fields to cooperate. Similarly in cardiovascular, the euHeart project set up by the European Commission from 2008 to 2012, with 16 partners, involving in particular Philips, has contributed to better healthcare, device innovation, and the Virtual Physiological Human environment. Now the Living Heart project led by Dassault, with close to 100 partners, is currently investigating several possibilities for patient specific modeling, pushing forward its use in all medical aspects.

HeartFlow Inc is a successful pioneer in medical service provided from personalized computational patient modeling. They propose a non-invasive solution for coronary artery disease diagnostic, which is detailed in the next section. With more than 10 000 patients having so far benefited from HeartFlow's analysis, the company is revolutionizing cardiovascular clinical care. Accounting for more than 150 patents and publications, the company looks forward to improving patient care with innovative techniques. HeartFlow sponsored this academical research project, and invited the VU Medical Center cardiology team to join it as a clinical partner. On the academic side, this project assembled researchers from Laboratoire d'Informatique Gaspard Monge (LIGM) at Université Paris Est and REO team of INRIA. The LIGM A3SI team contributed with skills in image analysis, image processing and optimization while the REO project-team of INRIA provided expertise in numerical simulation of biological flows and cardiac electrophysiology.

#### CORONARY ARTERY DISEASE

Coronary heart disease (CHD) is the leading cause of death worldwide, affecting millions of people in both developed and developing countries. It is caused by atherosclerosis: build up of fats, cholesterol and other substances in the coronary artery walls, resulting in waxy plaques. If these lesions restrict blood flow, this can lead to ischemia, which damages the heart muscle.

Biomedical research has brought up several kinds of therapy to prevent or cure CHD. According to a severity triage, the patient can be treated with drug medical therapy, implanted stent, or bypass surgery, as shown in [Figure 7](#).

Risk to the patient and costs increase at each of these steps. Hence assessment of disease severity is a crucial parameter to provide the best care to the patient. This triage can be established from different exams, which can be divided into two groups. One group of exams focuses exclusively on the anatomy (e.g. are there significant steno-

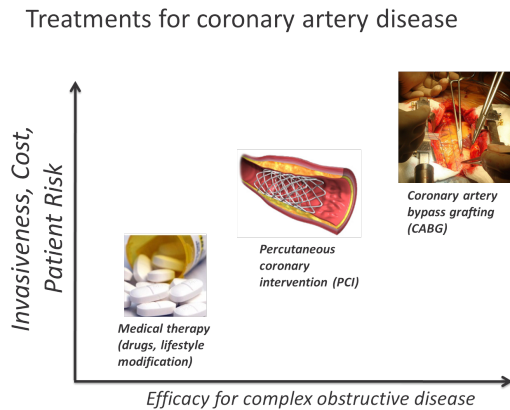


Figure 7 – Treatments for coronary artery disease according to severity.

sis that may benefit from stenting?), while other modalities focus on physiology and function (i.e. are there regions of myocardial muscle tissue under-perfused as a result of these stenoses? is flow obstructed inside coronaries?). In the functional group, Fractional Flow Reserve (FFR) is a gold standard exam to measure pressure in the vessel before and after the lesion using a pressure sensor catheter during an invasive coronary exam [78], [29].

HeartFlow has developed the first non invasive cardiac exam bridging anatomy and physiology fields: FFRct, standing for "FFR estimated from Computed Tomography". The process is presented in figure 8. It relies on X-Ray CT, an exam to acquire a 3D anatomical image. The acquisition is achieved following standard protocol defined by the Society of Cardiovascular CT [2]. In the produced cardiac image, vessels are detected and segmented with a proprietary process to build a 3D model of the arteries. The model accuracy is highly relevant thus it is verified by experts after automatic computation. The personalized 3D model is then used to simulate blood flow and calculate blood pressure, in order to assess global disease severity and detect hemodynamically significant lesions on the coronary tree [97]. Hence FFRct links both anatomical and functional analysis of the coronaries. However this exam does not provide the relationship between vessel disease and the affected myocardium territory.

#### CARDIAC PERFUSION

Myocardium Perfusion Imaging (MPI) provides local information about the amount of oxygenated blood transported to the myocardium. The comparison between rest and stress conditions highlights the regions with a perfusion deficit. Contrast attenuation maps are created which are overlaid on the left ventricle representation, and possibly correlated with coronary images. Physicians use this type of exam to estimate blood transport from the coronary compartment to the my-

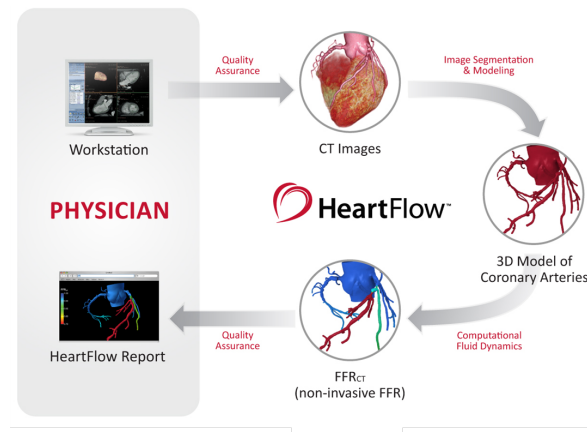


Figure 8 – FFR<sub>ct</sub>: process of the diagnosis tool

ocardium. Depending on the MPI modality, the myocardial blood flow (MBF) measure can be qualitative: with only a visual analysis; semi-quantitative: using the relative difference between rest and stress; or quantitative: by providing the absolute MBF value. The two latter measures have the advantage of minimizing the subjective influence of the analyst. However, the absolute MBF can only be obtained from dynamic acquisition.

#### *Cardiac perfusion modalities*

Four major modalities currently exist in MPI, relying on different physical principles.

Single Photon Emission Computed Tomography (SPECT) measures a radioisotope contrast agent concentration via the detection of single photon emission resulting from the radioisotope desintegration. It is the most commonly used in clinic. It provides qualitative and semi-quantitative measures [73]. For research purpose images are acquired dynamically in order to obtain quantitative measures. Because of its lowest resolution, SPECT demonstrates lower sensitivity and specificity than other MPI modalities.

Positron Emission Tomographie (PET) measures radiotracer concentration by detecting an indirectly produced correlated pair of photon. This modality is routinely used to provide qualitative and semi-quantitative measures [104], but can additionally provides absolute MBF when acquired dynamically. This modality necessitates a high equipment cost for the radiotracer production.

Cardiac Magnetic Resonance Imaging (CMR) measures molecular relaxation time shortening under nuclear magnetization, which is proportional to the concentration of contrast agent. This modality is mainly interpreted with visual analysis for clinical purpose [73]. The

measure of absolute MBF is currently only performed in research [104] due to relatively complex post processing steps.

CT Perfusion (PCT) measures the X-Ray attenuation of an injected contrast agent. Because of radiation exposure, it is mostly applied as a static imaging process on patients, consequently providing only qualitative and semi-quantitative measures [104].

The typical output of MPI is a 2D representation of the myocardium perfusion decomposed into 13 or 17 regions, called a polar map. Based on statistical distributions, these regions correspond to coronary vessel territory, that help identify the main diseased vessels.

Several work have associated MPI to coronary anatomical imaging in order to relate vessel disease to perfusion defect [13], [27]. However they only provide a spatial relationship and requires to double the number of exam for the patient. Thus all MPI modalities share the similar limitations:

- In clinical practice no quantitative measure is provided, only the relative perfusion between territories is assessed, which makes analysis dependent on the identification of normal perfusion regions. Without an absolute MBF measure, there is no blood transport quantification available in this exam: only quantification in the myocardium compartment.
- The correspondence established between obstructive coronary artery lesions and myocardial regions with a perfusion defect is only a spatial one derived from group statistics and is not patient-specific.
- There is a gap between the visible vascular anatomy and myocardium flow distribution. In this gap physicians are making assumptions about the vessels that are too small to image, the microvasculature distribution and how blood is transported through the vascular system.
- The most common perfusion tests are expensive and require injection of a radioactive contrast agent that increases a patient's radiation exposure.

Consequently, MPI is not able to functionally relate myocardium perfusion to obstructive disease in the large coronary arteries. This prevents accurate identification of the vessels that may benefit from revascularization therapies such as coronary stenting or coronary artery bypass grafting.

However, Lo et al. have shared some evidence [26] demonstrating MPI information can be beneficial to blood flow modeling in diseased coronaries. This work-in-progress illustrates the value of the functional relationship between coronary and myocardium compartments. Extending the functional coronary information from FFRct with information on patient specific myocardium perfusion would enable practitioners to accurately assess the perfusion system and quantify

it. Such a tool would relate lesions directly with the impacted myocardial tissue and thereby overcome the above-mentioned downsides of MPI. Moreover, in contrast with other perfusion techniques, no additional perfusion exam would be needed.

#### OBJECTIVE

The goal of this project is to extend the functional analysis of FFRct from the coronaries to the myocardium compartment. This requires the extension of the coronary model to microvasculature scale combined with a functional analysis leading to the myocardium. As in MPI, this blood flow simulation will focus on the left ventricle myocardium.

##### *Extend the coronary model to microvasculature scale*

HeartFlow's coronary tree model provides the main vessels and sub-branches. This coronary tree should be extended to arteriole vessels in order to populate the left myocardium compartment. The space filling coronary model has to respect anatomical and physiological constraints of the patient. It can potentially be modeled as an optimization problem with topological requirements and an energy formulation.

##### *Functional analysis pipeline*

A set of instruments to analyze the blood transport function of the generated vascular model needs to be produced. This pipeline relies on hemodynamics law applied to the patient-specific vasculature, for two physiological conditions: rest and stress. It should provide a blood flow distribution analysis within the left myocardium, and should enable comparison with MPI ground-truth data.

This manuscript is divided in two parts.

The first one focuses on the vascular network generation. The first chapter introduces the cardiovascular anatomy and provides a review of vascular generation model that can be found in the literature. We propose a method for patient-specific vascular network generation in chapter 2. The third chapter analyzes morphometry of the results obtained when applying this method to a set of patients. In the fourth chapter we compare our proposal with an algorithmic alternative, then we discuss perspectives and validation in the chapter 5.

The second part of this work provides a functional analysis of the generated vasculature. We introduce the cardiovascular function and blood flow modeling state of the art in the chapter 6. In the next

chapter, we propose a method for vessel blood flow modeling compatible with our vascular model. Chapter 8 provides the combination of functional analysis tools to assess blood flow distribution in the vessels and the myocardium. We discuss this pipeline in chapter 9.

Finally we summarize our contributions, discuss limitation, validation and perspectives in the conclusion.



## Part I

### VASCULAR MODEL GENERATION

In this part we present the vascular model generation work. In the first chapter we introduce the context of this topic, cardiovascular anatomy, and current state of the art. Then in a second chapter we describe our method to generate patient-specific vascular network. In the third chapter we present the results obtained for several patients. The fourth chapter compares results of the current method with an alternative form of the algorithm. And finally in the fifth chapter we discuss perspectives and validation.



## CONTEXT

---

### 1.1 CARDIOVASCULAR ANATOMY

#### 1.1.1 *Heart anatomy*

The human heart is a muscular organ that pumps blood via the circulatory system throughout the body. It is composed of 4 chambers, presented in [Figure 9](#).

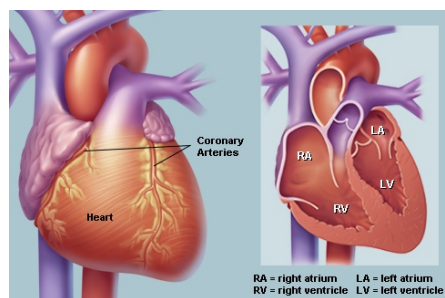


Figure 9 – Heart anatomy, figure from WebMD [106]

- The atria, two superior chambers, receive the blood from veins:
  - The right atrium receives blood returning from the body via the superior and inferior vena cavae.
  - The left atrium receives the oxygenated blood via the pulmonary veins.
- The ventricles, two inferior chambers, which receive blood from each respective atrium via valves, and propel it out of the heart.
  - The right ventricle pumps blood through the pulmonary artery to the lungs for oxygenation.
  - The left ventricle pumps oxygenated blood via the aorta throughout the body.

The walls of the heart chambers are primarily composed of cardiac muscle. The myocardium is a single unit functional cardiac muscle, whose cells all contract simultaneously. The two ventricles form a myocardium, and the two atria form a second one. In this project, we will focus on the ventricle myocardium (referred in this paper as myocardium).

The heart wall is defined by 3 layers, see [figure 10](#).

- The epicardium covers the surface of the heart, it functions as a protective layer.
- The myocardium (or mid-layer) is the muscular wall of the heart consisting of cardiac muscle cells wrapping around the myocardium in a spiral.

— The endocardium covers the inner surface of the heart, it delineates the blood pools of each ventricle.

The whole heart is enclosed in a pericardial sac containing serous fluid, that minimizes friction during heart contractions. The largest coronaries lay within this pericardial cavity along the epicardium.

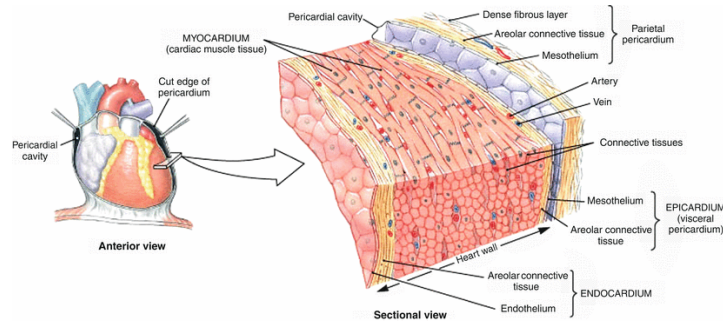


Figure 10 – Heart wall (figure from Weinhaus [8])

### 1.1.2 Coronary tree

As with all organs, the heart requires a blood supply. The aorta gives rise to arteries, which bring blood to the myocardium.

Epicardial arteries, referring to arteries on the heart surface, are called coronaries because of their (upside down) crown shape. Small arteries arise from these epicardium vessels to perforate the myocardium wall, bringing blood to muscle cells toward the endocardium, cf [Figure 11](#) (a). The arteries subdivide into arterioles (100–300  $\mu\text{m}$  diameter), that keep subdividing themselves, becoming thinner and thinner to end as millions of capillaries (5–10  $\mu\text{m}$  diameter).

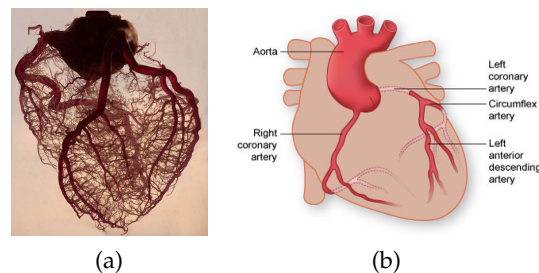


Figure 11 – Coronary anatomy. (a) The whole coronary artery tree: from epicardial vessels to arterioles. (b) Main coronary arteries arising from aorta: RCA, LAD and LCX. Figure from Texas Heart Institute [1].

Coronary arteries are presented in figure [Figure 11](#) (b), they arise on aorta from two origin points called ostia.

— One ostium is located on the right side of the aorta, above the right ventricle. It corresponds to the origin of the Right Coro-

nary Artery (RCA). This main vessel runs on the right side of the myocardium, and often reaches the posterior side of the left myocardium.

- One ostium is located superior to the left ventricle on the aorta, corresponding to the Left Main root (LM). This coronary is divided into two main segments : Left Anterior Descending (LAD) and Left Circumflex (LCX). Both these main vessels run on the left side of the myocardium.

Biologically, coronary tree dominance is defined according to the main artery innervated by the atrioventricular node. This establishes the major difference in anatomic structures [30] :

- A right dominant coronary tree presents a major RCA vessel to supply the posterior side of the myocardium. Approximately 70% of people have a right dominant coronary tree.
- A left dominant coronary tree has a major LCX vessel to supply the posterior side, it is presented in approximately 20% of people.
- A co-dominant coronary tree, existing in 10% of people, is equivalently blood supplied by both RCA and LCX.

#### 1.1.2.1 Detailed coronary organization

Originally, detailed coronary anatomy studies were conducted ex vivo through vascular casting and histology on sectioned myocardium tissues. Because of ethical constraints relating to such protocol, coronary anatomy has first been mainly studied on pigs [59], [105], [60], [101]. Kassab's work [59] is a major reference providing the first, still most complete statistical data of the entire porcine coronary vasculature. However the information for vessels below 0.4 mm in diameter are independent from their parents: the histological study does not enable to connect micro-vasculature to the larger diameter arteries. A few studies on human coronaries were conducted on small amount of post mortem data [113], but only focused on epicardial vessels [65].

In addition of statistical analysis, these studies enabled to observe a physiological principle of minimum work previously defined by Murray [74]. This principle applies on bifurcation level to relate parent and children radii with a power law. Zhou et al. have generalized this principle to tree scale, and validated it on Kassab's statistical data [114]. From this study they provide a stem-crown scaling relationship connecting stem diameter and subtree volume with a power law. Later on, Kassab et al. [57] show that this principle applies in other vascular and pulmonary trees, to minimize both cost of the tree structure construction, and fluid conduction. At the micro-vascular scale, the histology studies highlighted capillary organization follows myocytes (muscular cells) orientation.

In the last decades, progress in imaging technologies have enabled to provide whole heart visualization, with semi or fully automatic

measurements of the extracted coronary model. X-ray angiography (on human [25], or dogs [95]), and CT ([111]) allow the analysis of large to small coronaries. With a higher irradiation level, micro-CT enables the visualization of smaller vessels down to a few micrometer in diameter, to visualize whole rats coronary network [37]. And recently, an ex-vivo protocol, cryomicrotome fluorescence imaging provides complete arterial coronary vasculature. It is applied on dog and pig hearts [40], [81], and on a single human dataset, by Rivolo et al. [81].

These imaging studies have confirmed the previously evoked stem-crown relationship. Van Horssen et al. [39] even described a functional stem-crown relationship, relating stem flow to the crown volume, and demonstrated how the scaling laws vary depending on depth of the coronary tree. In addition, with the continuity of the extracted structures (from macro to micro vessels) and their location within the myocardium, Van Horssen et al. [100] highlighted a coronary structure depending on myocardium layer destination. They demonstrate that the endocardium is perfused by a small subset of penetrating arteries.

#### 1.1.2.2 *Vascular classification*

To analyze the whole coronary vasculature, several classification methods have been established, which assign a generation between ostium and capillary vessels to each segment.

The major classification system was defined by Strahler [94]. It originally comes from geographical studies ([41]): it has been used then for bronchial tree, pulmonary arteries and veins by Horsfield [38]. Several Strahler classification methods have been proposed with evolution:

- The first method assigns order starting from the leaves (0), and increase order at each bifurcation.
- In the second Strahler method, a constraint is added. If generation 3 meets generation 2, parent vessel remains generation 3 (instead of 4), so method handles asymmetry.
- The third method is called Diameter Defined Strahler Order (DD Strahler), and was created by Kassab [59]. It reproduces Strahler's system, but uses radii intervals to determine the generation. It defines 11 radius ranges, from generation 1, corresponding to pre-capillaries (about 10  $\mu\text{m}$  in diameter) to generation 11, corresponding to largest epicardial coronaries (around 3 mm in diameter).

## 1.2 STATE OF THE ART

In the last two decades, advances in the medical imaging field have enabled detailed in vivo studies of the human coronary arteries in

health and disease [3]. However the resolution limitations of available noninvasive medical imaging devices (CT, MRI, etc) have prevented the detection of vessels below the epicardial level. At present only ex-vivo acquisition protocols such as using cryomicrotomes have made it possible to segment the microvasculature [32], a procedure that cannot be applied on a living human heart. Consequently computer generated vascular models have been proposed to simulate and study the flow distribution down to the microvasculature level.

Vascular model generation methods can be classified in two categories: either derived from anatomical data or built from functional principles.

### 1.2.1 *Model derived from anatomical data*

Many generated models are derived from anatomical data. They use the Strahler ordering and connectivity matrix defined by Kassab et al. from porcine hearts [59].

Single vascular trees were first generated in 2D, by Mittal et al. [70], involving only length and diameter. This model subjected to blood flow analysis [71] showed a power law relationship between stem diameter and crown flow.

Kaimovitz et al [50] adapted vascular networks to the 3D ventricle geometry. They partition the network into 3 sub-networks corresponding to myocardium layers: epicardium, transmural myocardium and endocardium. For each of these they assign topology and geometry according to Kassab's morphometry (depending on main vessel name). The reconstruction of the subnetwork is constrained to lay in a specific space: 3D for transmural, 2D for epicardial and endocardial. It ensures anatomy constraints depending on the myocardium regions: left or right ventricle. In the end they concatenate the sub-networks, and improve the connections with annealing algorithm. The generated left and right coronaries are shown in figure 12. The authors compared many morphometry characteristics of their model with references but did not provide a functional assessment of the generated vasculature.

Smith et al. proposed an extension of a segmented epicardial network, from a canine epicardial dataset [91]. The geometry and topology of the tree follows Kassab's morphometry data. The spatial localization of each new edge is determined by optimizing a cost function depending on self avoidance, boundary avoidance, and hemodynamic bifurcation. The result is presented in figure 13. Based on this multiple tree generation method and Kassab's morphometry data, Bassingthwaihte et al. [7] have produced a coronary model for an hemodynamic study. The model of the Left Anterior Descending vessel (LAD) is constrained in either a slab or a cylinder space, and

composed of ten million segments. The filling space network is not fully satisfying as it presents small unrealistic knot-like structures. The estimated pressure upstream and downstream for each segment diameter does not agree with the literature for the endocardium, but was correct for the epicardium. Despite some unrealistic features, this anatomically derived model performs well as a starting point for blood flow simulation demonstrating spatial flow pattern similar to observations in normal hearts.

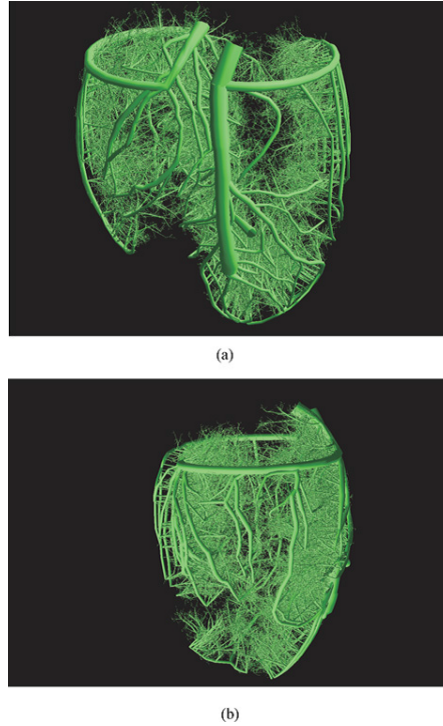


Figure 12 – Figures from Kaimovitz [50] : A rendering of the entire arterial tree consisting of the epicardial, transmural and perfusion sub-networks

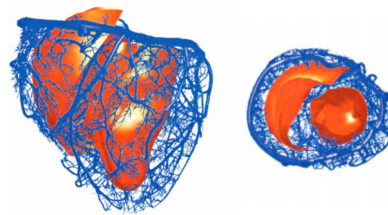


Figure 13 – Figures from Smith [91] : Antero(left) and superior view (right) of the inner ventricular surface, the extended epicardial mesh until the generation order 6

### 1.2.2 *Model constructed from functional principles*

Other vessel tree generation methods aim to satisfy functional principles. They all share two main assumptions. First, flow is evenly distributed into the perfused volume. Second, Nature attempts to achieve its goal with minimal work. Such idea leads to the resolution of optimization problems, where the function to be minimized can be diversely defined.

The global optimization method introduced by Georg et al. in 2010 [31] defines random points in the perfused volume and generate the intermediate vasculature that minimizes the total vascular volume. The optimization produces suboptimal global structures, and goes on until all random points are connected into a single tree. This method has been used to generate liver vasculature which showed anatomical correspondence with statistics from experimental data, but was not functionally assessed. Another tree generation approach was presented, by Tawhai et al. [96] and validated for bronchial airway models against statistical data. This approach uses a Monte Carlo recursive algorithm, which constrains bifurcation angles and segment lengths. The single tree generation methods [31] and [96] have been validated only for convex shape territories and do not rely on fluid dynamic law.

In contrast, the Constraint Constructive Optimization (CCO) method proposed by Schreiner et al. [85] relies on hemodynamic principles, and was adapted to the concave shape of the left ventricle [86]. The CCO method consists of a single tree angiogenesis simulation governed by minimizing a target function: the total tree volume. It satisfies two haemodynamic laws at bifurcation scale: Murray's law and Poiseuille's law (physical law defining the pressure drop in a tube). This single tree generation algorithm has evolved from Schreiner's work in 2D [85], to 3D [54], then staged growth [55], and has finally been adapted to the left ventricle concave shape [86], see figure 14. Karch et al. demonstrate that flow properties of 3D simulated models approximate experimental data well [56]. This algorithm has also been adapted to generate connecting artery and veinous tree in liver by Kretowski [63] to simulate CT images showing contrast agent propagation. An extension of the algorithm was also proposed by Blanco et al. [11], performing subdomain partitionning based on flow distribution, before growing a single tree in each subdomain. However, if the result looks plausible, the domain partitioning has neither been validated against ground-truth data, nor adapted to cardiac concave territory.

Another recent method has been proposed by Keelan et al. [61], that also handles non convex territory for vascular networks. It minimizes pumping power and blood volume with a simulated annealing

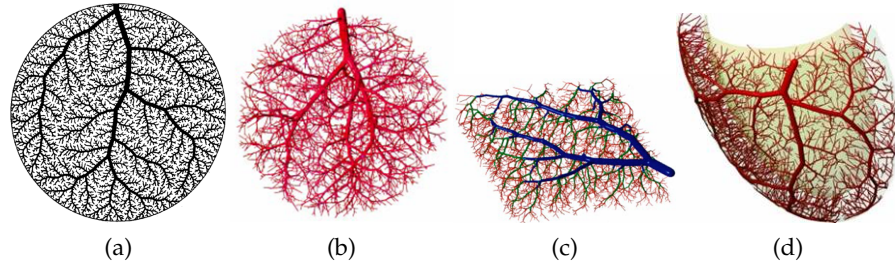


Figure 14 – CCO algorithm evolution: result visualization of (a) 2D CCO [85], (b) 3D CCO [54], (c) Staged growth CCO [55], (d) Non convex CCO for LAD [86]

approach to generate left and right coronary models. The generated vasculature matches the pig morphometry as analysed by Kassab but has not been functionally assessed. In addition this method is convenient for generating a complete vasculature, but uses no prior information on the epicardial network that can be extracted from cardiac CT.

### 1.2.3 Objective

Methods derived from anatomical data are based on animal studies and not human data, thus we cannot ensure they are representative of patient morphometry. In addition, with the aim of deriving a functional analysis from the generated vascular network, it seems more coherent to rely on functional principles for its construction. To generate a patient-specific model we must use all available priors, in particular the segmented epicardial arteries. Extension of this image based model requires a multi-tree network generation method. We describe this method in the following chapter.

## METHODS

---

### 2.1 ASSUMPTIONS

Here we describe the assumptions and parameters we used to build our vascular trees. The tree is constituted of cylindrical segments. It begins with a root segment, and all downstream end segments are called terminal segments. The produced tree is binary and its total number of segments is calculated from the number of terminal segments  $n_{\text{term}}$ :

$$n_{\text{tot}} = 2n_{\text{term}} - 1 \quad (1)$$

The terminal segments correspond to arteriole level, feeding a non-modeled micro-vasculature. The whole tree and non-modeled micro-vasculature are embedded into a determined volume referred to as the perfusion territory.

The blood is modeled as an incompressible, homogeneous Newtonian fluid, under a steady state. It is approximated as fully developed, unidirectional, axisymmetric flow in cylindrical geometry under laminar flow conditions. The resistance  $R$  and the pressure drop  $\Delta p$  of a segment  $j$  are defined according to Poiseuille's solution by:

$$R_j = \frac{8\mu l_j}{\pi r_j^4} \quad (2)$$

$$\Delta p_j = R_j q_j \quad (3)$$

with  $\mu$  the viscosity, and  $l$ ,  $r$ ,  $q$  respectively the segment length, radius and flow. The total resistance of the tree is calculated recursively by tree decomposition into segments, considering parallel and serial arrangements. The flows at all terminal segments  $q_{\text{term}}$  are equal, and delivered into the micro-circulation. Because of flow conservation, the sum of the  $q_{\text{term}}$  corresponds to the perfusion flow at the root  $q_{\text{perf}}$ .

The tree is subjected to Murray's law [74], with a power law coefficient  $\gamma$  set to 3.

$$r_0^\gamma = r_1^\gamma + r_2^\gamma \quad (4)$$

The law is derived from ideal conditions, and in reality the  $\gamma$  observed in coronaries varies between 2 for large vessels and 3 for small ones [101],[114],[57],[66], [109]. Since we generate vessels below the CT resolution of the segmented network, we use a value of 3, corresponding to a range from small arteries down to arterioles.

## 2.2 CCO ALGORITHM

The CCO algorithm combines computational fluid dynamics laws, network geometry and topology optimization to simulate vascular network growth. Below we summarize the algorithm proposed by Schreiner [86] which is the basis of our method. The fully detailed implementation of the CCO method is described in appendix 10.

### 2.2.1 Tree growth

In Schreiner's method the tree is constrained into a growing perfusion territory, and the target function minimizes the total tree volume, which is calculated considering the segments cylindrical shape:

$$t_v = \pi \sum_{j=1}^{n_{\text{tot}}} l_j r_j^2 \quad (5)$$

Knowing the final volume of perfusion territory  $v_{\text{perf}}$  the *micro-circulatory black box* volume  $\mu_{\text{box}}$  [85], i.e. average perfusion territory of each terminal segment, is defined:

$$\mu_{\text{box}} = v_{\text{perf}} / n_{\text{term}} \quad (6)$$

The number of terminal segments in the tree, at the current step of the algorithm is called  $k_{\text{term}}$ . Before each new added segment, the current perfusion territory volume  $v_{k_{\text{term}}}$  is incremented by one  $\mu_{\text{box}}$  to simulate tissue growth concomitant with vascular growth. All segments and their radii are stretched correspondingly to this volume inflation. The territory at step  $k_{\text{term}}$ , before adding a new segment, has a corresponding volume :

$$v_{k_{\text{term}}} = (k_{\text{term}} + 1) \times \mu_{\text{box}} \quad (7)$$

Note that we do not recalculate positions after tree stretching but compute a conversion of any distance  $d$  (length, radius or others) measured from the final world  $f_{\text{world}}$  to the  $k_{\text{world}}$  via a scaling factor (explained in appendix 10):

$$d_{k_{\text{world}}} = d_{f_{\text{world}}} \times \sqrt[3]{\frac{k_{\text{term}} + 1}{n_{\text{term}}}} \quad (8)$$

Segments are added one by one and subject to both local-scale optimization (at the single bifurcation scale) and global-scale optimization (at the tree scale), as detailed below. A random location,  $\text{new\_loc}$ , is picked under geometrical and physiological constraints to be used as a candidate for segment extremity. Its connection is tested with neighboring segments: the two points defining the neighboring segment and  $\text{new\_loc}$  are joined at a bifurcation point. Each

connection is subject to a local optimization: the bifurcation point location minimizes the bifurcation volume under the constraints of determinant flow, following Kamiya's work [53]. Since the segment joining the bifurcation point to `new_loc` is a terminal segment, by definition it carries a flow  $q_{\text{term}}$ . After adding the new bifurcation, the tree flow is incremented by one  $q_{\text{term}}$  and the hydrodynamic resistance of the tree must be adjusted by recursively traversing all subtrees, and propagating a radius rescale up the tree. The optimal connection is then selected among all connections as the one minimizing the target function (total tree volume  $t_v$ ), to achieve the global optimization process.

### 2.2.2 Territory specificity

In the original CCO method [85] the perfused volume is assumed convex and homogeneously filled. In a subsequent article [86], Schreiner et al. adapt the growth specifically to the left ventricle wall shape, which is a non-convex territory, and induce a perfusion gradient.

To achieve adaptation to a non-convex territory, they define a function similar to an electrical potential to represent a non convex domain between two isosurfaces [86]. Ranging from 0, the outer surface, to 1, the inner surface of the ventricle wall, the function  $w(x)$ , provides a continuous and differentiable interpolation of the domain. Schreiner uses this spatial information during tree growth to confine the generated bifurcations inside the perfusion domain. We compute the domain function with a discrete Poisson solver called the random walker algorithm [33].

In addition, the domain function is used to define different stages of the growth. To reproduce the vessel distribution wrapping the ventricle surface before penetrating the myocardium layers, Schreiner uses the principle of staged growth defined by Karch [55]. The first segments generated are constrained to a thick hypersurface corresponding to the epicardial layer. Then, in a second stage, the vascular growth is extended inside the myocardial volume of the whole left ventricle, called hereafter the ventricular volume. During this second stage, the target function is weighted with the domain function  $w$ :

$$t_{v,s} = \pi \sum_{s=1}^{n_{\text{tot}}} l_s r_s^2 w(m_s) \quad (9)$$

with  $m_s$  the segment midpoint.

Finally, the domain function is also used for a last purpose. As observed by Buss et al. [12], the perfusion density is actually inhomogeneous: the density of arterioles and capillaries in the endocardial layers is higher than in the epicardium. This gradient of perfusion density can be modeled according to the domain function: the new terminal segment locations are subject to a distribution test. This

test ensures that the density of accepted points increases closer to the endocardium layer. As in [86], we use a factor of 3 between epicardium and endocardium terminal segment density.

### 2.3 CCO FOREST: EXTENSION OF CCO TO MULTIPLE TREES

To produce a patient specific vascular network, we aim at extending the downstream vasculature of a segmented model holding multiple epicardial coronaries. Hence the method is required to generate several vascular trees inside the same territory. In order to generalize the angiogenesis to multiple trees, such as in a physiological process, these trees should grow in a simultaneous manner. This contemporaneous growth intrinsically induces competition between trees.

Here we propose an innovative method enabling growth of several competing trees within the same perfusion territory. We call the association of  $F$  trees inside a single perfusion territory a *forest*. We seek to minimize its total volume defined by:

$$T_v = \sum_{i=1}^F t_v^i \quad (10)$$

The forest growth is built following principles similar to CCO: territory growth concomitant to tree growth. These trees grow in a competitive process depending on their relative inlet flow. From here on, variables relative to a forest start with a capital letter, and those relative to single trees start with a lowercase letter.

#### 2.3.1 Forest initialization

First, we define the forest parameters.  $V_{\text{perf}}$  and  $N_{\text{term}}$  are respectively the perfusion territory volume and the total number of terminal segments that the forest needs to reach. During forest growth we calculate  $K_{\text{term}}$ , the total number of terminal segments belonging to all the trees, and we end growth when it is equal to  $N_{\text{term}}$ . Each tree is initialized with a root radius  $r_{\text{root}}$ , and a target inlet flow  $q_{\text{targ}}$  that the tree has to reach at the end of the forest growth.

We can calculate the total forest flow  $Q_{\text{perf}}$  that has to be reached at the end of the forest growth, and considering an homogeneous distribution, the flow at each terminal segment of the forest  $Q_{\text{term}}$  is estimated:

$$Q_{\text{perf}} = \sum_{i=1}^F q_{\text{targ}}^i \quad (11)$$

$$Q_{\text{term}} = Q_{\text{perf}}/N_{\text{term}} \quad (12)$$

In a similar fashion as CCO algorithm, the *micro-circulatory black box* volume is calculated with:

$$V_{Mbox} = V_{perf}/N_{term} \quad (13)$$

As in the CCO algorithm, each tree is initialized with a random first segment, the root segment. The positioning of the root segment can be critical to promote tree growth, particularly so for close neighbors (a segment could block path of its neighbor). We constrain the maximum root segment length to be proportional to the flow ratio between the tree and its closest neighbor. The maximum length criterion  $l_{max}^i$  for each root segment is:

$$l_{max}^i = \frac{d_{cn}^i q_{targ}^i}{q_{targ}^{cn} + q_{targ}^i} \quad (14)$$

In this formula,  $d_{cn}^i$  is the distance to the closest neighbor tree,  $q_{targ}^i$  is the target flow of the considered tree, and  $q_{targ}^{cn}$  is the target flow of its closest neighbor. With this constraint, tree roots cannot block the future territory of their neighbors.

### 2.3.2 Forest growth

When growing several trees in the same territory, a competition takes place. In order to obtain a coherent distribution, we influence this competitive process with relative tree flow.

For each tree we know the target flow  $q_{targ}$  that the tree has to reach at the end of forest growth, and the flow at each step of the forest growth  $q_{K_{term}}$ . We identify the largest flow  $q_{targ}^b$  carried by the tree of index  $b$ .

During growth, each tree growth speed depends on its relative flow, meaning its flow relative to the largest tree flow. trees are not allowed to grow when their current flow does not correspond to the final forest flow distribution. After each added segment, for all trees  $i$  we calculate the relative flow at step  $K_{term}$ :

$$\chi_{K_{term}}^i = q_{K_{term}}^i / q_{K_{term}}^b \quad (15)$$

and compare it with the target relative flow:

$$\chi_{targ}^i = q_{targ}^i / q_{targ}^b \quad (16)$$

If  $\chi_{targ}^i \geq \chi_{K_{term}}^i$ , the tree is "activated", meaning it can get new connections. Otherwise, its growth is temporarily suspended. An exception is made for the largest flow tree, which is only constrained by its target flow  $q_{targ}^b$ .

The method is described in the flow chart Fig. 16. As a proof of concept we computed this multiple speed growth for 2 trees within

a 2D, non-convex simple geometry territory, see Fig. 15. Physiological parameters used were in a similar range as Schreiner 's et al [85]. These simulations correspond to 3 different flow distributions, which are tested with 3 different random seeds. The average attained flows over the 3 different random seeds are presented in table 1. Also, in this table we present an estimation of tree perfusion territory calculated from a discrete Voronoi tessellation, also known as *skeleton by influence zone* [89], using terminal segment locations as markers. With this method we observe an average relative error of  $2 \times 10^{-3}$  between target and attained flow for all trees. The area of the perfused territory is proportional to attained tree flow with a correlation coefficient of 0.991.

This simultaneous tree growth method works for two or more competing trees, which is an important improvement with respect to the original CCO technique. In particular it can be used to extend the segmented coronary model, as we discuss in the next section.

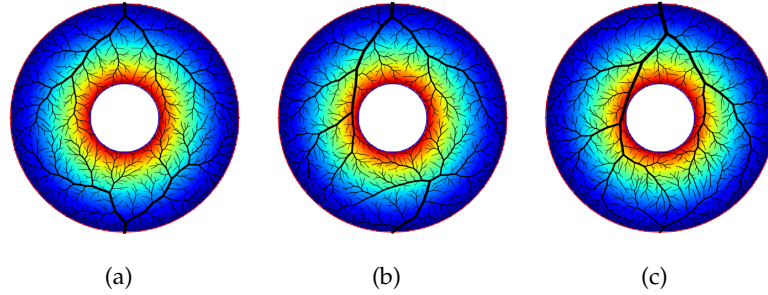


Figure 15 – Example of forest growth proof of concept in simulated 2-D non convex territories, with varying flows. (a) : equal target flow. (b): upper tree flow twice the bottom tree flow. (c): upper tree flow 9 times the bottom tree flow. The colormap represents the potential function from 0 (blue) to 1 (red).

Table 1 – Measures on CCO Forest results

	Simulation 1		Simulation 2		Simulation 3	
	tree 1	tree 2	tree 1	tree 2	tree 1	tree 2
Target flow (%)	50	50	66.7	33.3	90	10
Attained flow (%)	50.1	49.9	66.7	33.3	$90.03 \pm 0.05$	$9.97 \pm 0.05$
Territory (%)	$55.6 \pm 0.8$	$44.4 \pm 0.8$	$67.5 \pm 0.8$	$32.5 \pm 0.8$	$89.0 \pm 0.4$	$10.9 \pm 0.4$

#### 2.4 CCO FOREST ADAPTED TO PATIENT DATA

The primary goal of the proposed methods to create hybrid image-based and synthetic geometric trees is to extend the segmented epi-

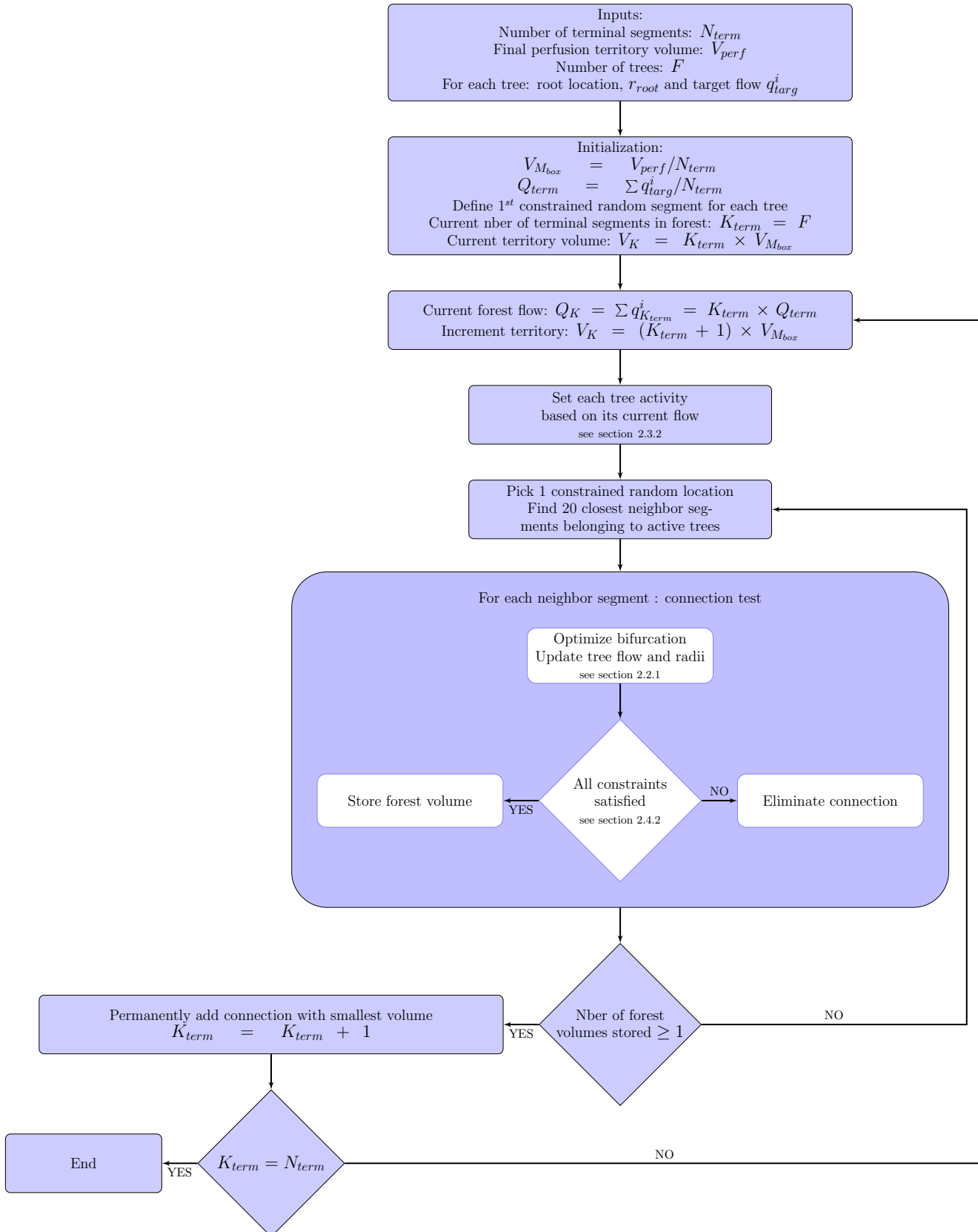


Figure 16 – Flow chart of forest algorithm

cardial model originating from human cardiac CT image data. To generate this patient-specific hybrid model, for each patient we start with a segmentation of the heart, its chambers and coronary arteries visible in the image data. Of these we use the left ventricle, left atrium, epicardial coronary arteries, and the volume containing all these elements: the whole heart segmentation. In addition, to initialize the forest we need to estimate flow and radius at each segmented vessel outlet and at some sections along the segmented vessels.

To generate the downstream vasculature, we apply a patient-specific CCO forest. From here on, segmented epicardial coronaries are referred as vessels while the generated vasculature from forest growth is referred to as segments.

#### 2.4.1 Patient priors

We select  $F$  points on the coronary vessels that correspond to the root location for the forest trees. These root points are distributed at each vessel tip, as well as along the vessels according to Kassab's connectivity matrix [59] and patient-specific branch patterns. We measure the length of all in-between bifurcations vessel sections. The average value is calculated and used as a threshold. If a vessel section has a length above this threshold, root points are added until the average length is reached. Because we focus on trees growing inside the left ventricular volume, we only use the root points located within 10 mm from the left ventricle.

Each root point is associated with a root radius  $r_{\text{root}}$  and a target flow value  $q_{\text{targ}}$  to initialize the forest. For a root point located at vessel tip, the root radius corresponds to the vessel radius, ensuring continuity. For a root point located along a vessel, the root radius is derived from the Strahler order of the connectivity matrix and parent diameter. Since the segmented coronary model includes vessels down to a diameter of 1.2 mm, no root point above Strahler order 9 is distributed along the vessels to ensure that only vessels below the image resolution are added to the lateral surfaces of the patient-specific model. The total baseline flow  $Q_{\text{perf}}$  is estimated from the left ventricle mass. Target flow for each tree is determined based on the root radius:

$$q_{\text{targ}}^i = \frac{(r_{\text{root}}^i)^{2.7}}{\sum_{i=1}^F (r_{\text{root}}^i)^{2.7}} Q_{\text{perf}} \quad (17)$$

The left ventricle segmentation corresponds to the final perfusion territory, with a perfusion volume  $V_{\text{perf}}$ , perfused by the forest trees. Most coronary vessels of interest lie on the left ventricle, but some are not directly on its surface because of fat and connective tissue. Therefore we consider an enclosing perimeter to work in: the whole

heart segmentation. The random walk functions are calculated in both the heart and left ventricle segmentations. Because we grow trees within these two compartments, our potential function ranges from 0 to 2. The heart function ranges between 0, on surface, and 1, at left ventricle border. The left ventricle function ranges between 1, for the epicardium, and 2, for the endocardium. The sum of these functions is used as the potential for the forest growth. In addition, the concavity of the left ventricle is set to 3, to be distinguished as a forbidden territory. The potential function is illustrated in the figure 17.

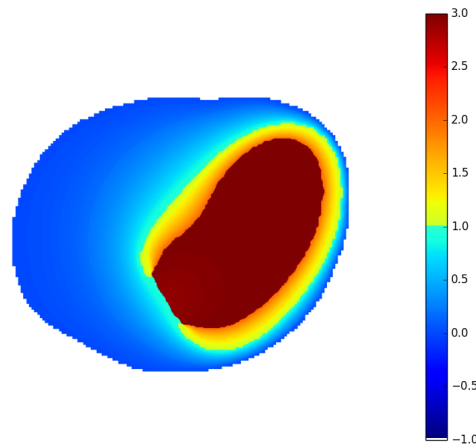


Figure 17 – Domain function on an axial slice of the heart. The random walk potential ranges from 0, the heart surface, to 2, the endocardium surface, being set at 1 on epicardium surface. The left ventricle blood pool is a forbidden territory set to the value 3.

Segment growth is constrained to the heart volume, but not initially to the ventricle volume. In order to prevent segments crossing over the ventricle blood pool, we connect the blood pools of the left ventricle and left atrium with a geodesic dilation [89] inside the heart. This reconstruction process is computed with the ventricle blood pool as a marker and the inverted ventricle myocardium image as a mask, so that the dilation of the ventricle blood pool does not extend on the ventricle myocardium. It is iterated until the dilated blood pool covers 2% of the left atrium blood pool territory. This threshold was empirically determined, so that the dilated part of the blood pool, that we name the cap, corresponds approximately to the combined mitral and aortic valve regions. The sum of the left atrium blood pool and the cap constitute a forbidden territory, see example figure 18.

During growth, each new segment crossing this forbidden territory is eliminated from the candidate list.

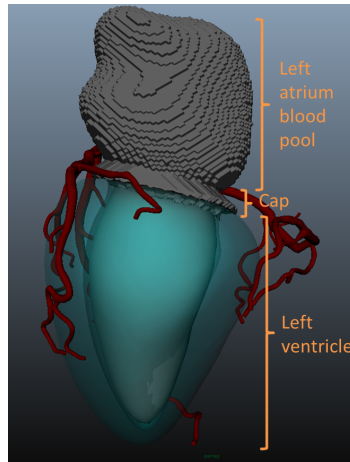


Figure 18 – Example of left ventricle cap: connection between left ventricle blood pool and left atrium blood pool

#### 2.4.2 Patient-specific constraints

As in Schreiner’s method, the growth is divided into 2 stages: in the first one, the territory is limited to a thin region near the left ventricle surface, whereas the second stage takes place in the whole ventricle volume. We expect more segments in the volume than over the surface. In our experiments, we empirically switch from stage 1 to stage 2 when  $K_{\text{term}} = \frac{1}{6} N_{\text{term}}$ .

Since overlapping segments are not physiologically plausible, during both stages, segments may not intersect with any tree segment or vessel or cross under vessels, i.e. between the vessel path and endocardium.

##### 2.4.2.1 Stage 1 constraints

During the modeled growth on the ventricle surface, the tree growth speed is flow dependent, as described in section 2.3.2. The candidate location  $\text{new\_loc}$  is randomly picked on the ventricle surface. The bifurcation point resulting from the local optimization process is projected on the surface of the epicardium. The segments are constrained within the epicardial layer, defined as a domain derived from the potential values:  $w(x) < 1.3$ .

To achieve coherence and continuity between the vessel and synthetic networks, an angle constraint is applied between the vessel direction and the vector stemming from the tree root to the new tested location, called vessel-to-tree angle. Since an angle equal to or greater than  $90^\circ$  is not optimal in a volume-minimizing network, we empirically set the maximal angle to  $80^\circ$ . Any connection with a vessel to tree angle above this threshold value is eliminated from the candidate list. Because the first stage is subjected to many constraints (surface territory, angle and flow constraints), the angle and flow constraints

are progressively relaxed (in 5% increments) if no new connection has been found after 100 iterations.

#### 2.4.2.2 Stage 2 constraints

During this second stage, to ensure filling the whole ventricle, the angular constraint is eliminated, and segments can now cross below vessels as long as bifurcations are entirely located inside the inner half of the left ventricle.

However, since three-dimensional space offers much more freedom with the location of new segments, the growth speed cannot be constrained anymore with the hypersurface method described in 2.3.2: the resulting growth would interpenetrate competing trees too much, yielding unlikely configurations. Thus we combine a flow convergence process with a candidate location selection process to control tree growth during this stage.

**FLOW CONVERGENCE PROCESS.** We seek to control the current tree flow so that it does not exceed its target flow. One way to achieve this is to deactivate trees once they reach their target flow. However due to geometrical configurations and constraints some trees experience limited growth and never reach their target flow. To ensure distribution of the whole forest flow we estimate an adaptive deactivation threshold every  $\frac{1}{12}N_{\text{term}}$  connections:

$$\text{thresh}^i = q_{\text{targ}}^i + p^i \quad (18)$$

This threshold is tree-specific to maintain relative flow distribution. To calculate  $p^i$ , we identify all blocked trees, i.e. trees that have not grown since the last checkpoint. We estimate  $Q_{\text{lost}}$ , the sum of the flow gaps between target  $q_{\text{targ}}$  and current flow  $q_K$ . The  $p^i$  values correspond to the proportion of  $Q_{\text{lost}}$  relative to the tree target flow. Once a tree has reached its threshold value, it is permanently deactivated. This flow convergence process is fully described in appendix 11.

**CANDIDATE LOCATION SELECTION PROCESS.** As a consequence of the flow convergence process, regions containing deactivated trees can become connected to far away trees, which induce physiologically unlikely networks. To avoid this, while still allowing some interpenetration between trees, we apply a selection on the new location before testing for connection. The closest tree neighbor has to be activated to accept `new_loc` for connection test.

In addition, the accepted candidate locations are subject to the epicardial to endocardial gradient following Schreiner [86]. The new terminal segment locations `new_loc` are subject to a distribution test. Reminding that all points  $x$  on the epicardium surface have a domain function value  $w(x) = w_{\text{epi}} = 1$ , and on endocardium surface

$w(x) = w_{\text{endo}} = 2$ , the probability density is defined from the epicardium surface  $d(w_{\text{epi}}) = 0.5$  to  $d(w_{\text{endo}}) = 1.5$ . This ensures a density ratio of 3 between these two surfaces (see section 2.2.2). For each `new_loc` we calculate the probability density based on its domain function value:

$$d(\text{new\_loc}) = 0.5 + w(\text{new\_loc}) - w_{\text{epi}} \quad (19)$$

We compare this value with a uniform random number  $\epsilon \in [0.5, 1.5]$ . If  $d(\text{new\_loc}) < \epsilon$ , the new location is accepted to be submitted to connection test. Otherwise this `new_loc` is rejected and a new one is randomly picked inside the ventricle.

The whole algorithm progress is illustrated in Fig. 19, showing the crucial intermediate steps of the algorithm.

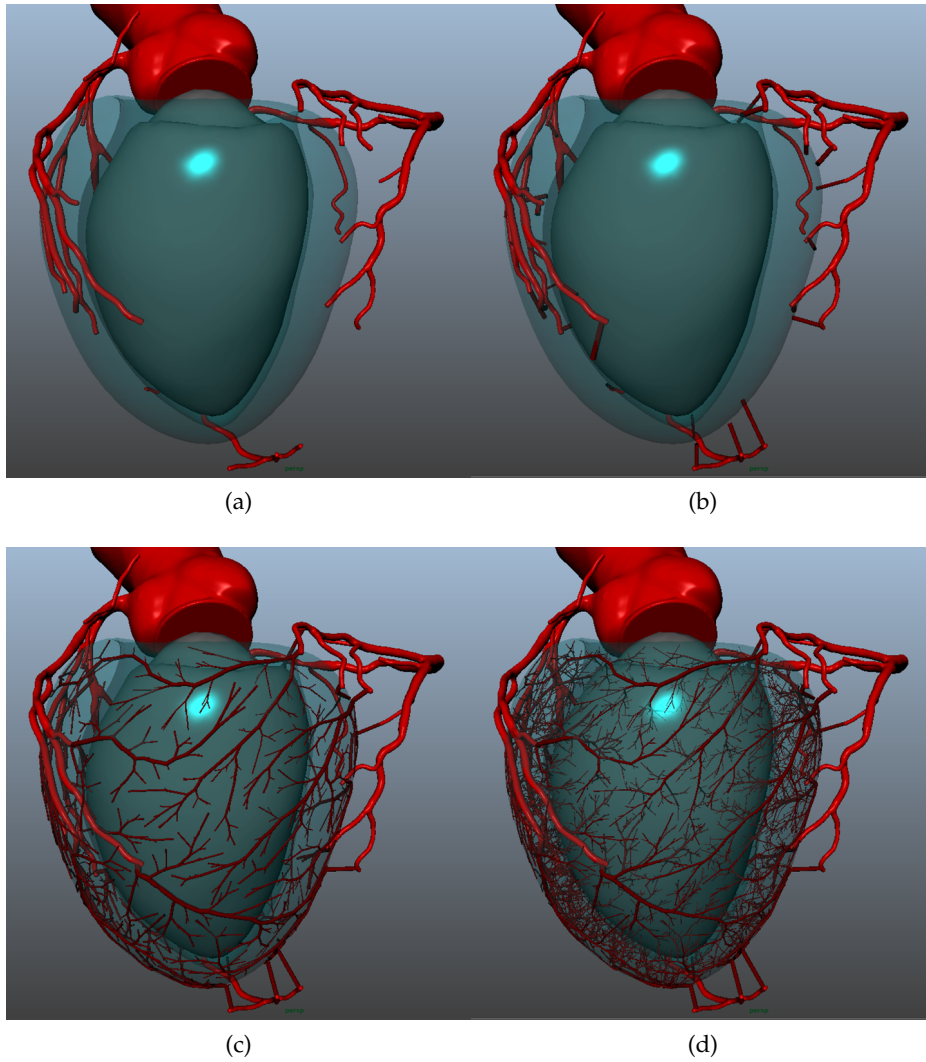


Figure 19 – Illustration of forest growth on patient. (a): inputs provided. (b): distributing first segment on left ventricle surface for each tree. (c): surface growth (stage 1) reaching 1000 terminal segments. (d): inner growth (stage 2) reaching 6000 terminal segments.



## RESULTS ON PATIENTS

---

We generate synthetic networks for 6 different patient datasets. During stage 1, the forest is grown on the ventricle surface only, until 1000 terminal segments are generated. During stage 2, the forest is extended inside the whole ventricle volume, until 6000 terminal segments are finally reached. The total number of segment was empirically estimated: considering Murray’s law, 6000 terminal segments should be enough to reach terminal segments with diameter corresponding to arterioles (below 0.1 mm radius). In addition, in Schreiner et al. [86], they generate a 2000 terminal segment tree for the LAD only, so tripling this number to generate downstream vasculature for LAD, LCX and RCA, would seem adequate to a whole left ventricle network.

To study the algorithm behavior dependency on the initialization, we used varying random seeds to generate 5 synthetic networks with 6000 terminal segments on one randomly picked patient. We also grew the tree forest on 5 other cases, to analyze the adaptability of our algorithms to varying patient anatomy.

The algorithm is implemented in python 3.5 with numpy 1.4 and scipy 0.17.0, parallelized over 20 cores. We use AMD Opteron(TM) Processor 6274 processors to run the calculations.

### 3.1 DATA

The CT scans are acquired on 6 patients using different CT scanners, representing the major manufacturers. Two datasets were acquired on a Siemens Somatum Definition CT scanner, two others on General Electric Healthcare DL and Light Speed VCT scanners, and two on a Philips iCT 256 scanner. Coronary segmentation is achieved using custom methods (HeartFlow, Inc., Redwood City, California, USA) to extract coronary arteries from the aorta down to a diameter estimated to be approximately 1.2 mm. Patients with low disease burden and a variety of network profiles were selected. The patient segmented networks range from 13 to 27 vessel outlets, with thin to large vessels, tortuous and straight vessels. One patient is left-dominant, and the other 5 were right-dominant. Three patients had myocardial bridges, i.e. where the epicardial vessels had an intramyocardial course for a portion of the vessel length. Heart chambers and whole heart segmentation was achieved with an automatic tool based on a random forest voxel classifier followed by active shape modeling fitting [17].

### 3.2 TESTING ALGORITHM REPEATABILITY

One randomly picked patient dataset was used to generate 5 networks with different random seeds.

The generated networks all fill the entire left ventricle, spreading over the entire surface and penetrating into the left ventricle tissue. In all cases, segmented vessels were correctly avoided by segments, yielding a plausible-looking outcome. It is interesting to point out that the algorithm intrinsically induces a partial segregation of the perfusion territories: trees interpenetrate but not much. This is due to the minimization of the total vascular volume. With the same number of outlets, trees that would be deeply sharing perfusion territory would have longer segments than trees which would not interpenetrate. These trees would therefore not be minimizing their volume and therefore the networks' efficiency. When varying the random seed, the geometrical and optimization constraints enforced by our algorithms lead to different but similar-looking networks, see Fig. 20.

Over all 5 generations, the average total volume of the generated synthetic networks is  $1261 \pm 43 \text{ mm}^3$ . Since the algorithm's objective is to minimize this value, such a low standard deviation indicates that our algorithm yields repeatable results that are likely near the global optimal.

**TREE FLOWS** The algorithm succeeds in distributing flows close to the target values for most trees: the correlation coefficient between target and attained flow is  $0.92$  over the 5 seed simulations.

**TERMINAL SEGMENT DIAMETERS** The terminal segment diameter distribution is very similar for all seeds, with a mean value of  $171 \pm 61 \mu\text{m}$ , see Fig. 21. When performing a pair-wise distribution comparison we obtain an average  $R^2$  of  $0.97 \pm 0.02$ , and a mean slope of  $1.02 \pm 0.02$ .

**PERFUSION TERRITORIES** To analyze the distribution of the vascular network within the left ventricle, we estimate the perfusion territory from a discrete Voronoi tessellation. To compute this Voronoi we use the terminal segment end locations as markers, and attribute speed relative to their diameter. This calculation is equivalent to a Laguerre Tessellation, and approximates the dependency between vessel diameter and perfused tissue, see Seiler [87]. From this calculation we can observe the distribution of  $\Omega_i$ , the perfusion territory associated to each terminal segment end. As can be seen on figure 22, the results calculated over varying random seeds for the same patient show a low variability. When comparing distributions pair by pair,

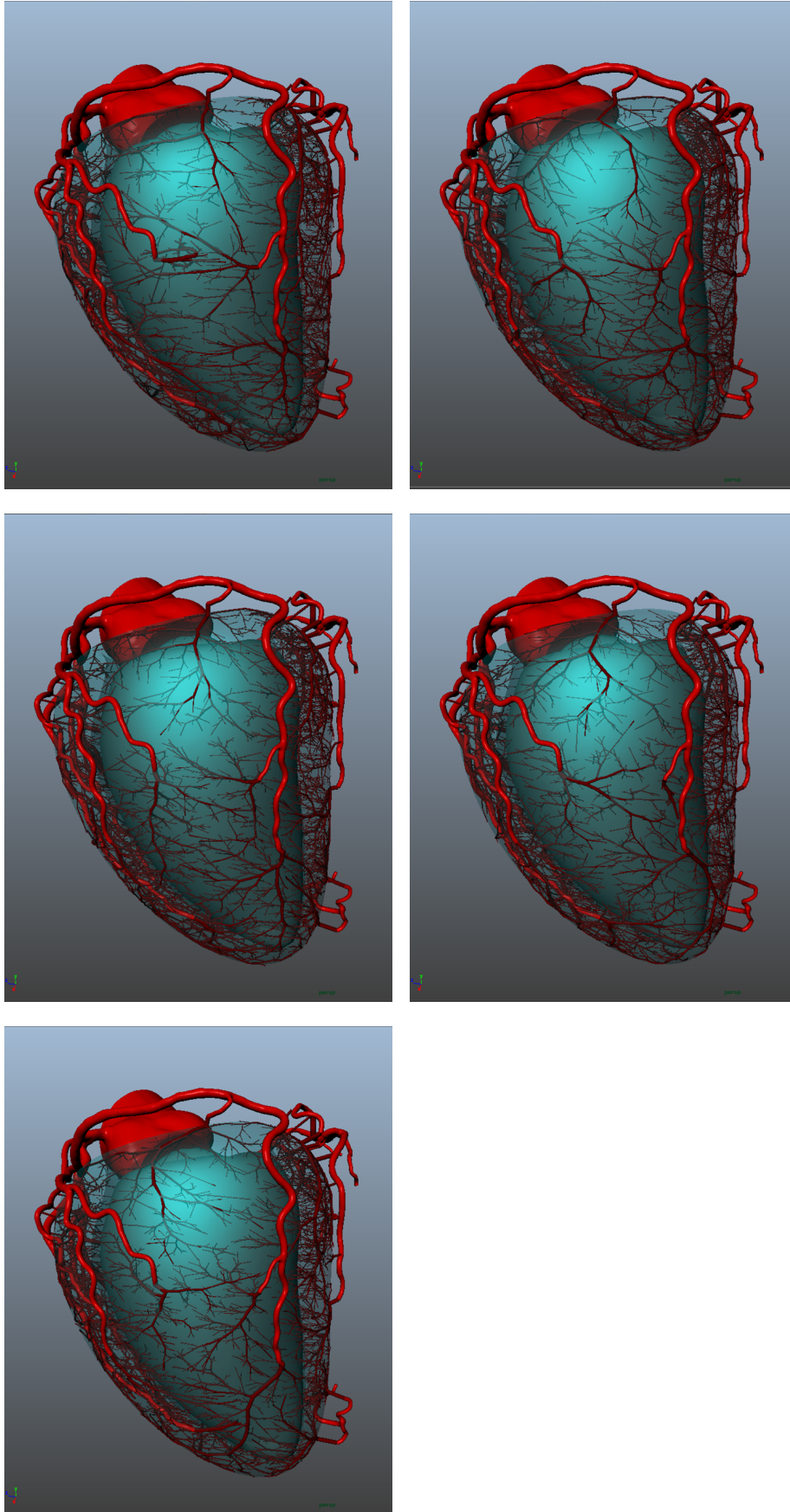


Figure 20 – Results with 5 varying random seeds on the same patient (case 6): 6000 terminal segment networks. Rendering achieved with *Renderman* in *Maya Autodesk*.

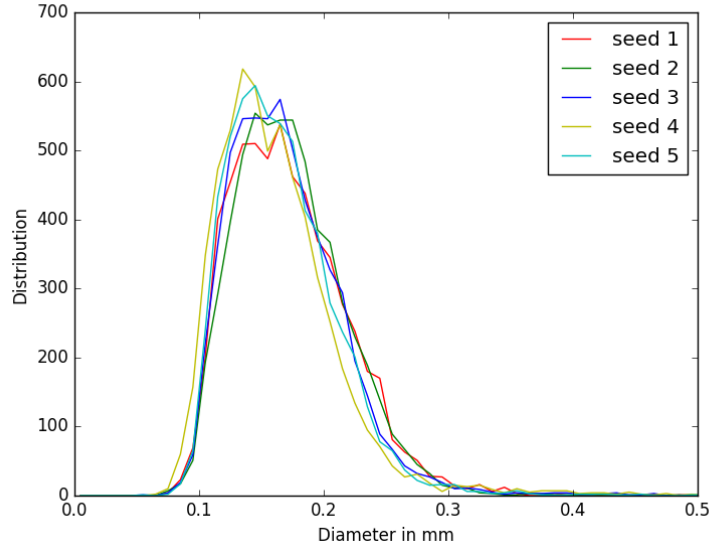


Figure 21 – Terminal segment diameters distributions for 5 different random seeds on the same patient.

we obtain an average  $R^2$  of  $0.991 \pm 0.002$ , and a slope of  $1.01 \pm 0.02$ . This demonstrates the algorithm produces perfusion territories with strong correlation for varying vascular networks on the same patient.

Overall we conclude that our algorithm produces reproducible, plausible vascular networks.

### 3.3 TESTING ALGORITHM ROBUSTNESS

The forest growth methodology was applied on 6 distinct patient datasets. As the number of outlet and branching pattern varies across patients, the number of grown trees is patient-specific. The number of generated trees was respectively 33, 51, 38, 61, 52 and 50.

All 6 generated networks adapt to patient priors, and correlate with the segmented vessels in a plausible way, see Fig. 23.

To assess generated network coherence and continuity with the segmented vessels, we compare the morphometry of the combined network, joining segmented and synthetic models, with morphometry of pigs according to Kassab [59].

**DIAMETER DEFINED STRAHLER ORDERING** In order to compare with the Kassab morphometry, we classify vessels and segments according to the *Diameter Defined Strahler ordering* [59]. All segments range between order 4 and 9, while vessels range between order 9 and 11. The segment average diameter along order correlates with the Kassab measures, as shown in Fig. 24. For all labels (RCA,

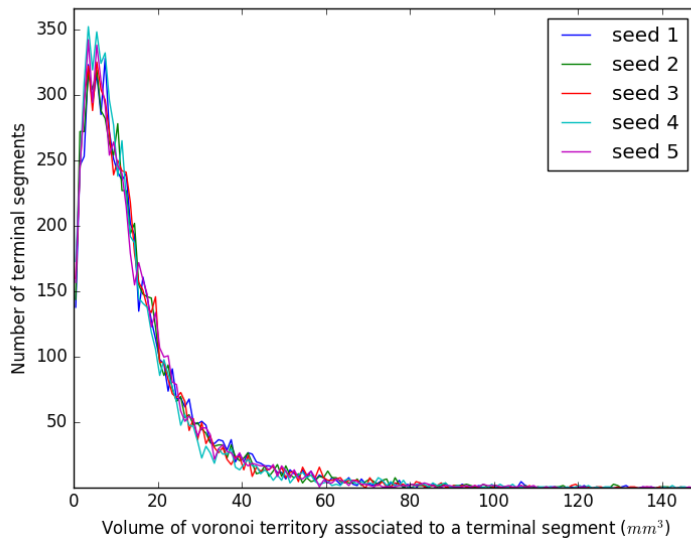


Figure 22 – Distribution of  $\Omega_i$ , volume associated to terminal segments, obtained from a Laguerre Tessellation, for 5 different vascular networks generated on the same patient.

LAD, LCX), the coefficient determination  $R^2$  values of Kassab are above 0.99, and so are the 6 patient ones relative to Kassab's fits. We conclude that our Strahler ordering classification is correctly implemented and can be used to study other morphometric parameters.

**ELEMENT LENGTH** Together with the Strahler ordering, we define an element as a series of segments belonging to the same Strahler order [59]. The element lengths are plotted against the Kassab fitted models in Fig. 25.

Apart from the order 11, elements are equal or significantly longer in our model. It is likely due to the heart shape [18], which is more elongated in humans compared to pigs due to gravity acting on the bipedal upright stance. Consequently the coronaries need to spread around a larger surface, with longer vessels. We conducted a study on 1287 human segmented coronary models which confirms this hypothesis, see figure 60 in appendix 12.

**BIFURCATION ASYMMETRY** Bifurcation asymmetry observed in our model has a similar trend compared to the data reproduced from tables in the online supplement of Kaimovitz [51]. The observed ratio is everywhere higher for small child over parent (SCoP) segment diameters, and everywhere lower for large child over parent (LCoP) segment diameters, see Fig. 26 and 27. This suggests a globally more symmetrical network. An important point is that our simulation ensures continuity between the segmented and simulated net-

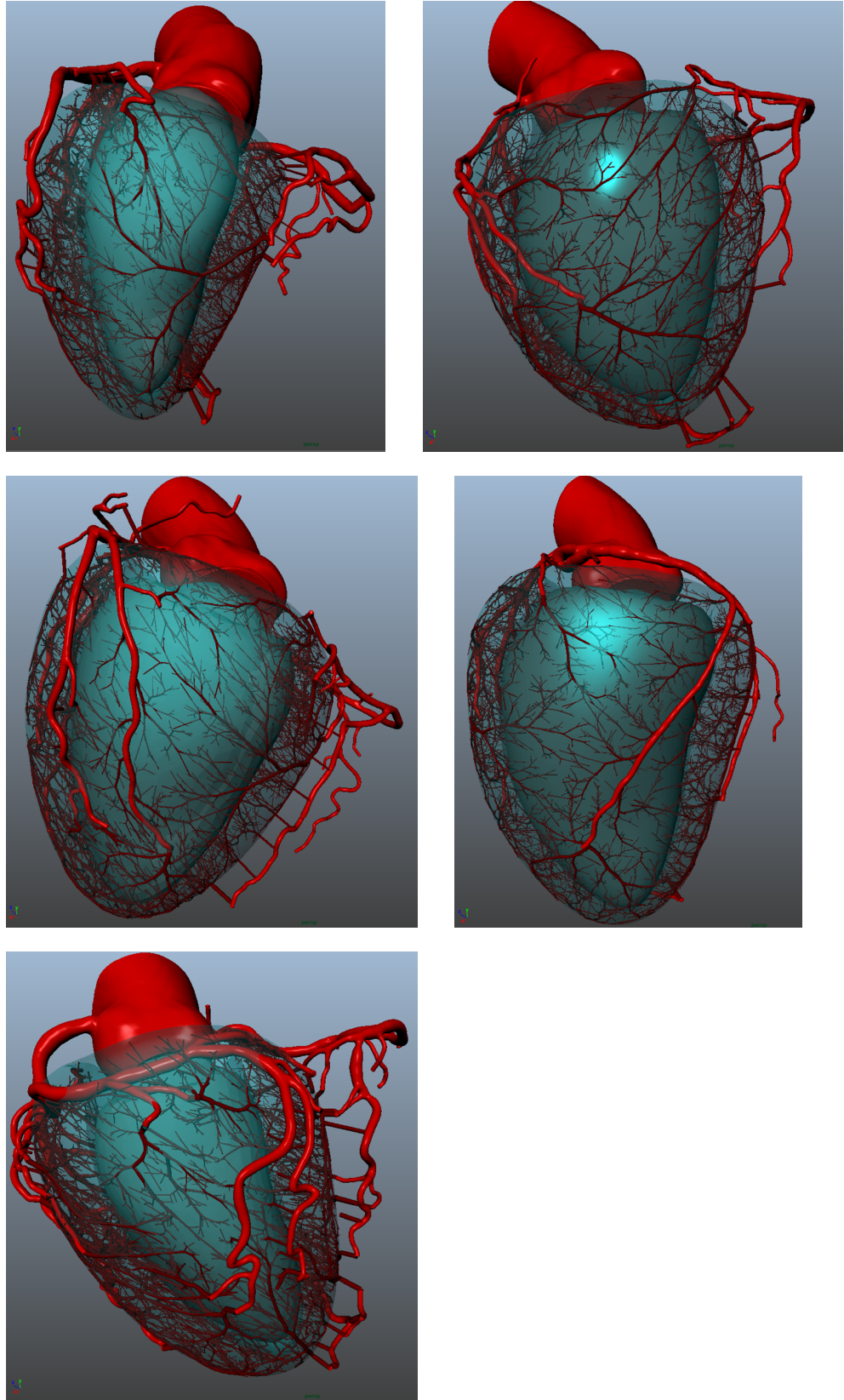


Figure 23 – Results on 5 patients (case 1 to 5): 6000 terminal segment networks. Rendering achieved with *Renderman* in *Maya Autodesk*.

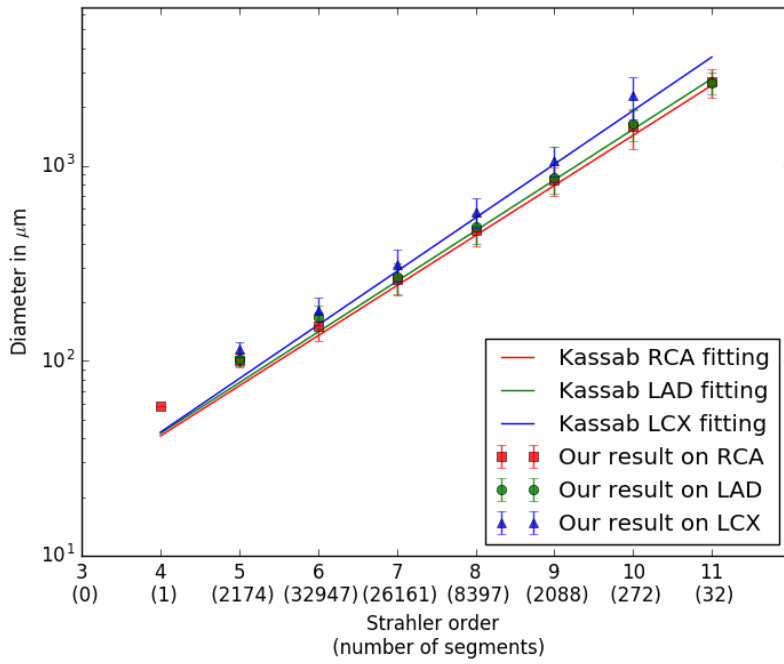


Figure 24 – Measures along Strahler order for each label on 6 patients: Average segment diameter compared with Kassab’s fit.

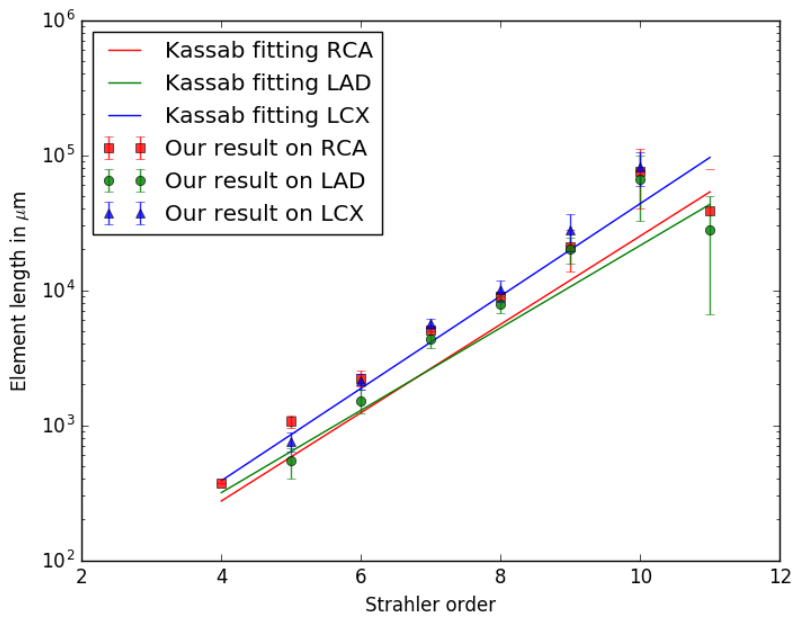


Figure 25 – Measures along Strahler order for each label on 6 patients: Average element length compared with Kassab’s fit.

works. Since the SCoP diameter ratios are observed to be already higher for the segmented network, this is carried over to the simulated one. The converse is true for the LCoP diameter ratios.

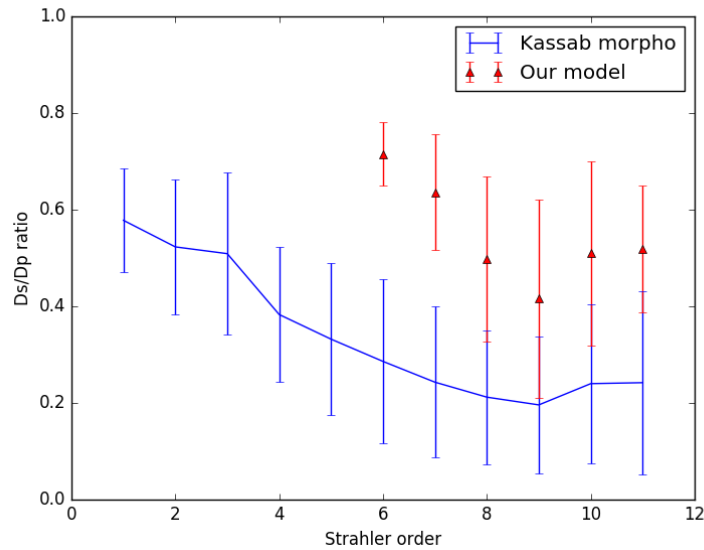


Figure 26 – Asymmetry study of results compared with Kassab morphometry: SCoP segment radius ratio.

**TREE FLOWS** Most of the 285 trees reach their target flow, with a correlation coefficient of 0.86, see figure 28.

Out of the 285 trees, 62 trees had difficulty growing, and never reach their target flow (they stay below 80% of their target flow). Among these, 18 trees did not succeed in growing at all because of initialization issues. This was due to their first segment, which did not reach the left ventricle surface. Other non-growing trees got stuck during growth due to a constraint that prevents bifurcations to degenerate, i.e. bifurcation for which one of the segments is larger than its own length. Most of the connections tested with these trees are rejected because of this constraint (83% observed on 372 randomly picked connection tests). However the geometric configuration at the tree roots (left ventricle surface, vessel orientation, tree neighbors) does not enable bifurcation with longer segments. When we remove these outlier trees, the correlation coefficient between the target and attained flow improves to 0.96.

**TERMINAL SEGMENT DIAMETERS** Over the 6 cases, we observe unimodal terminal segment diameter distributions. The average value is  $174 \pm 53 \mu\text{m}$ , see Fig. 29

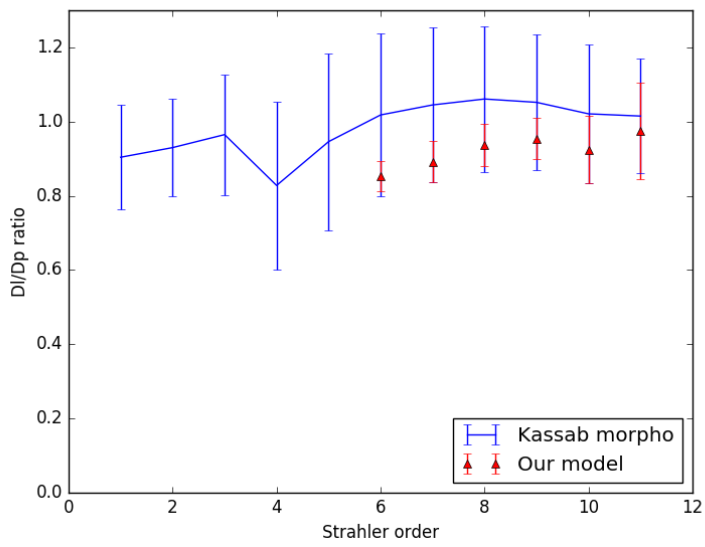


Figure 27 – Asymmetry study of results compared with Kassab morphometry: LCoP segment radius ratio.

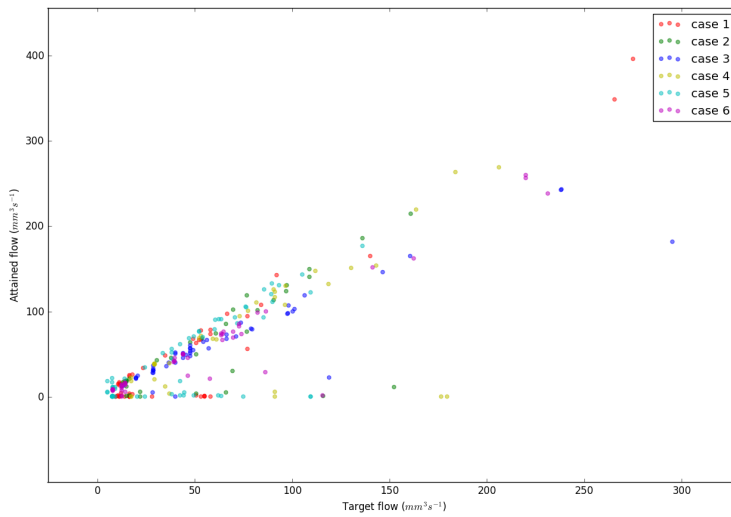


Figure 28 – Correlation between target and attained flow on 6 cases.

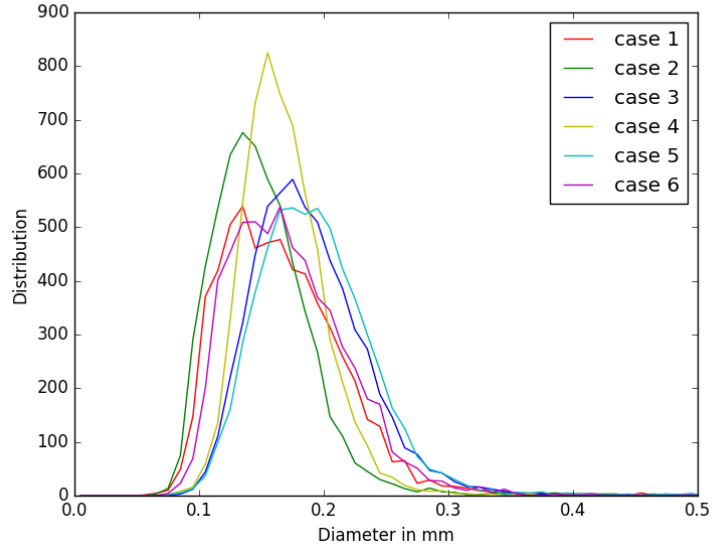


Figure 29 – Terminal segment diameters distributions for 6 different patients.

**PERFUSION TERRITORIES** For each patient the mean volume associated to a terminal segment ( $\Omega_i$ ) is very close to the  $M_{\text{box}}$  volume calculated as an assumption to initiate the CCO Forest algorithm, see table 2. Knowing that the perfusion territory is divided by a high number ( $N_{\text{term}} = 6000$ ), it would actually be surprising to obtain an average value far from  $M_{\text{box}}$ .

The Voronoi results count some territories with a null value, which are due to the speed influence for close terminal segment neighbors. Also, the mode  $\Omega^{\text{MF}}$ , average volume appearing with a maximal frequency, is lower than  $M_{\text{box}}$  by a factor of 2 to 15, and the standard deviation can reach 300 %, which both corroborate with the distribution heterogeneity. The distribution zoomed on its mode is presented in figure 30.

Table 2 – Voronoi distribution

Volumes in $\text{mm}^3$	$M_{\text{box}}$	Mean $\Omega_i$	Std $\Omega_i$	$\Omega^{\text{MF}}$
Case 1	14.3	13.6	21.9	1.
Case 2	11.8	11.6	22.0	3.
Case 3	24.4	24.8	30.0	1.
Case 4	25.4	24.7	83.2	11.
Case 5	16.9	16.6	42.1	3.
Case 6	15.8	16.0	17.7	7.

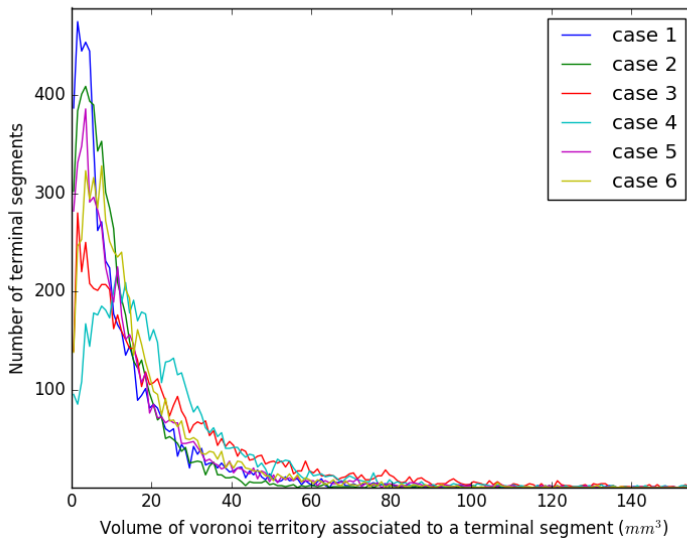


Figure 30 – Distribution of  $\Omega_i$ , volume associated to each terminal segment, obtained from a Laguerre Tessellation, for 6 patients.

We also observed the distribution of  $\Omega_i$  along the ventricle wall, which are quite homogeneous, as can be seen on figure 31. The standard deviation of volumes for terminal segments located on epicardium surface is pretty wide due to the initialization issues that generate single segment trees (particularly for case 1 and 5). These single segment trees have thus large diameters (close to the corresponding segmented vessel tip diameter), and conquer more territory given their associated speed. Toward the endocardium the territory volumes are slightly increasing, but always with comparable standard deviation.

Since we induced an increasing gradient on terminal segment distribution from epicardium to endocardium, we would expect to obtain smaller  $\Omega_i$  close to the endocardium. To investigate this unexpected distribution we analyze the distribution of terminal segments along the ventricle thickness, see figure 32.

The high peak on the epicardium surface corresponds to the surface growth stage: we generated 1000 terminal segments with location on potential domain  $\omega(\chi) = 1$ . Since we divide this number by the volume of the sub-layer, we can observe the difference of ventricle volume among the different patients: case 5 shows the smallest left ventricle while case 1 is the largest.

Following the end of this peak we can observe a general increase of terminal segments toward the endocardium, corresponding to the gradient imposed in the algorithm during stage 2 (growth in volume). However, in the algorithm we imposed a selection of new location 3 times greater in the endocardium than epicardium (see section 2.4.2.2), and we do not obtain such a factor in results (the factor is

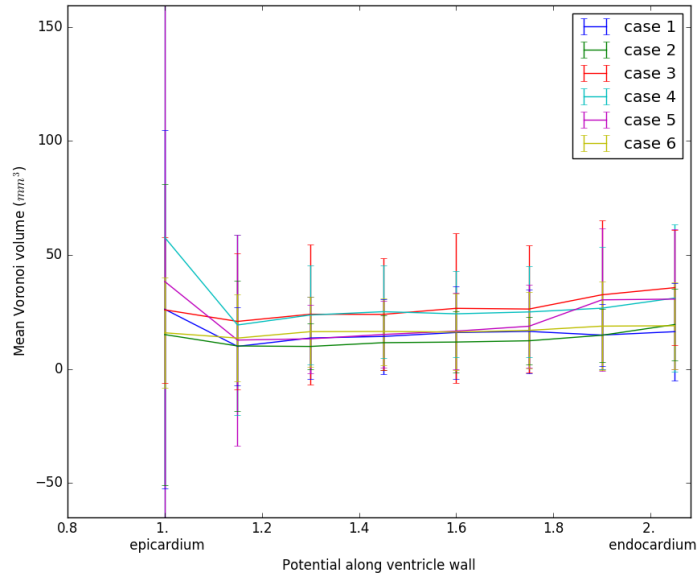


Figure 31 – Distribution of  $\Omega_i$ , e.g. volume associated to each terminal segment, along ventricle wall thickness, based on domain potential value, for 6 cases.

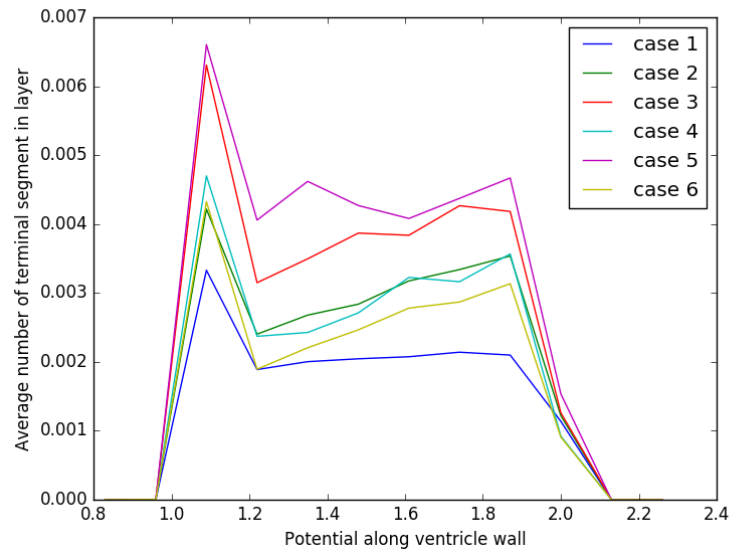


Figure 32 – Distribution of terminal segment ends along ventricle wall thickness, for 6 cases.

closer to 2 for most cases). This is definitely a consequence of imposing the distribution test before submitting to the connection test, so the connection test actually influences the final distribution. Since many segments lie on surface because of stage 1 growth, the probability of success close to them is higher than close to the endocardium (avoiding intersection between trees for instance).

The peak on the epicardium surface is unavoidable, but its proeminence is number of the fraction of vessel on the surface. These observations could instigate lowering number of segment during stage 1 for the next vasculature generated.

Finally we summed the  $\Omega_i$  volumes per main vessel, to compare with reference distribution of territory per label in left ventricle. We obtain similar range than animal and human studies, see table 3. To note: our dataset contains 1 left dominant case (so 16%), while Weaver's results [105] are obtain with a dataset containing 5% left dominant cases. The results of Reig [80] do not share information about dominance within the dataset, but we could assume it is representative of distribution in humans found by Fuster et al. [30], so about 20%.

Table 3 – Perfused volume associated to each main vessel

Result from	RCA (%)	LAD (%)	LCX (%)
Voronoi on 6 patients	28.2	41.0	30.3
Reig (90 human hearts)	22.5	43.5	32.2
Weaver (60 swine hearts)	25.5	49	25.5

### 3.4 SUMMARY OF THE RESULTS

We have analyzed the generated models in terms of satisfaction of the algorithm constraints, geometry of the network, and consequences on perfusion territories.

We first observed the repeatability of the algorithm for several generated networks on the same patient: total vascular volume, terminal segment diameter distribution, and perfusion territories distribution associated to terminal segments are equivalent despite various network geometries.

Then we measured the robustness of our algorithm to various patient anatomies with 6 different patients. The algorithm flow constraints are experimentally satisfied in majority for all patients. The generated networks are specific of the patient but show global homogeneity when compared to pig morphometry. The resulting perfusion territories are specific of the patients but match pattern distribution at regional scale.



## ALTERNATIVE METHOD OF VASCULAR MODEL GENERATION

---

### 4.1 ALGORITHM ALTERNATIVE

In the original [85] and 2006 paper [86], each tree root radius is calculated from current tree flow, pressure and reduced hydrodynamic resistance with

$$r_{\text{root}} = \left( R_{\text{sub,root}} \times \frac{q_{\text{Kterm}}}{p_{\text{perf}} - p_{\text{term}}} \right)^{\frac{1}{4}} \quad (20)$$

This method requires an estimation of inlet perfusion pressure  $p_{\text{perf}}$  and enforces a determined pressure at terminal segments  $p_{\text{term}}$ . We call this alternative method the “pressure-based (PB) algorithm”, to differentiate from the “radius based (RB)” algorithm for which we presented results in chapter 3.

### 4.2 COMPARING RB ALGORITHM RESULTS WITH PB RESULTS

With the RB method, the radius continuity is enforced at the junction between segmented and synthetic networks. However, since this algorithm does not ensure a specific pressure drop along the tree, terminal segments diameter are less constrained.

**ROOT RADII** With the PB method, the radius continuity is not enforced at the junction between segmented and synthetic networks: many synthetic tree roots generated by the PB algorithm do not perfectly match the diameter of their corresponding vessel tip, with a low correlation of 0.41. Compared to RB algorithm, the generated trees have significantly smaller root radii than with the PB algorithm: average values are  $0.26 \pm 0.01$  mm vs  $0.45 \pm 0.01$  mm.

**FLOW** Radius variability at tree roots does not originate from an incorrect flow distribution: nearly all the 283 trees reach their target flow (shown in figure 33), with a correlation coefficient of 0.96.

With the RB algorithm, generated segments globally have larger diameters than those produced with PB algorithm. Consequently geometrical constraints, such as non degenerative bifurcation, affect the PB algorithm trees less. They can attain their target flow more easily.

**TERMINAL SEGMENT DIAMETERS** In the PB algorithm the specified pressure drop along the tree constraints the terminal segment

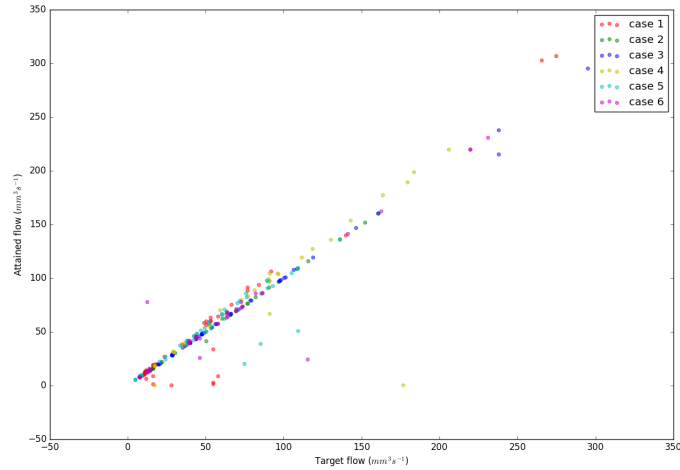


Figure 33 – Correlation between target and attained flow on 6 cases, with PB algorithm.

diameters more. Thus it is not surprising to observe a more compact distribution of terminal segments diameters averaging  $111 \pm 29 \mu\text{m}$  in figure 34. This average diameter is significantly lower than with the RB algorithm, which makes sense since the tree root radii are also smaller.

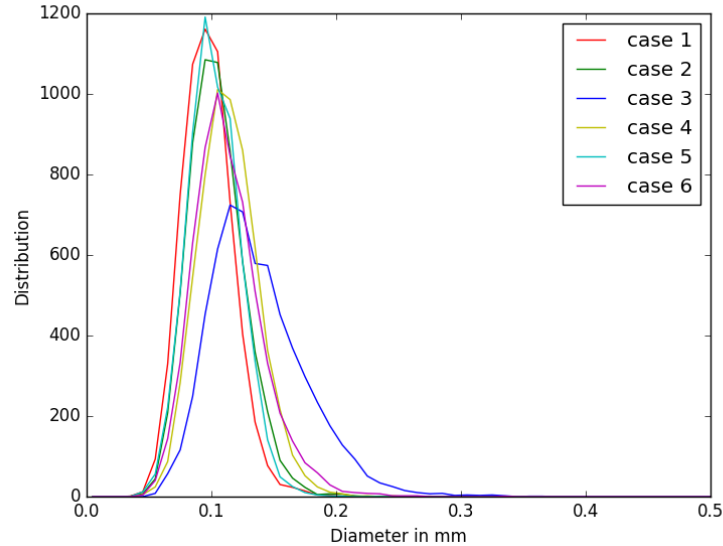


Figure 34 – Terminal segment diameters distribution for all 5 seeds, with PB algorithm.

All the other geometrical analyses based on Strahler ordering are similar to the RB method, see figures 35, 36, 37.

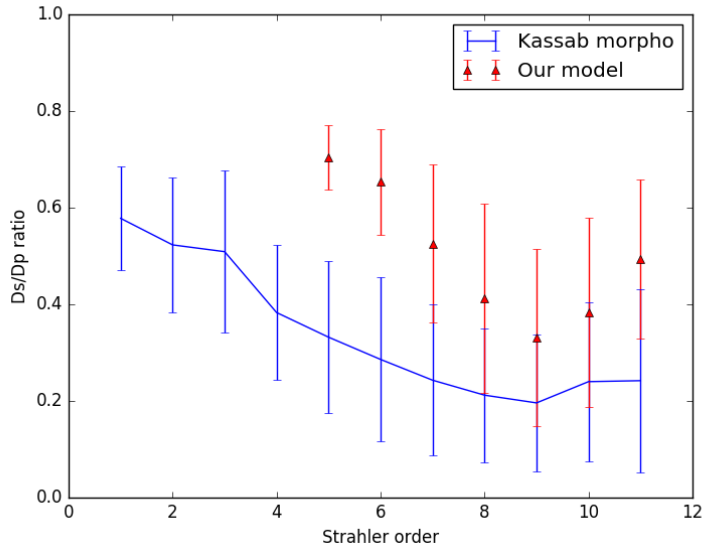


Figure 35 – Asymmetry study compared with Kassab morphometry: SCoP ratio with PB algorithm.

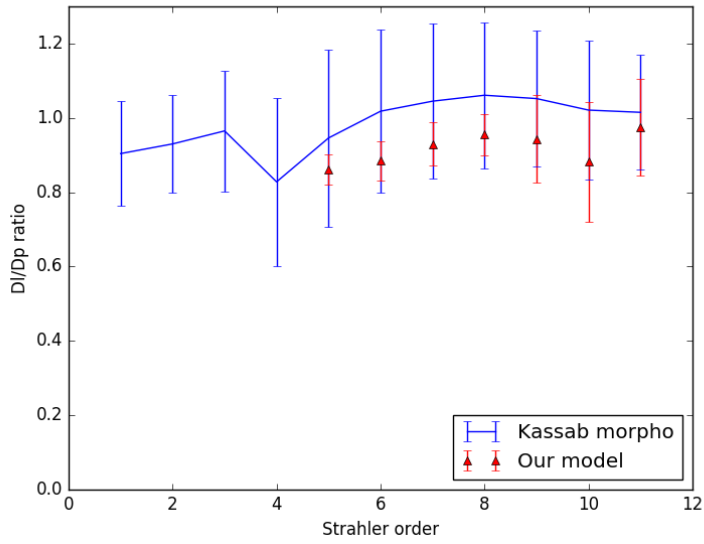


Figure 36 – Asymmetry study compared with Kassab morphometry: LCoP with PB algorithm.

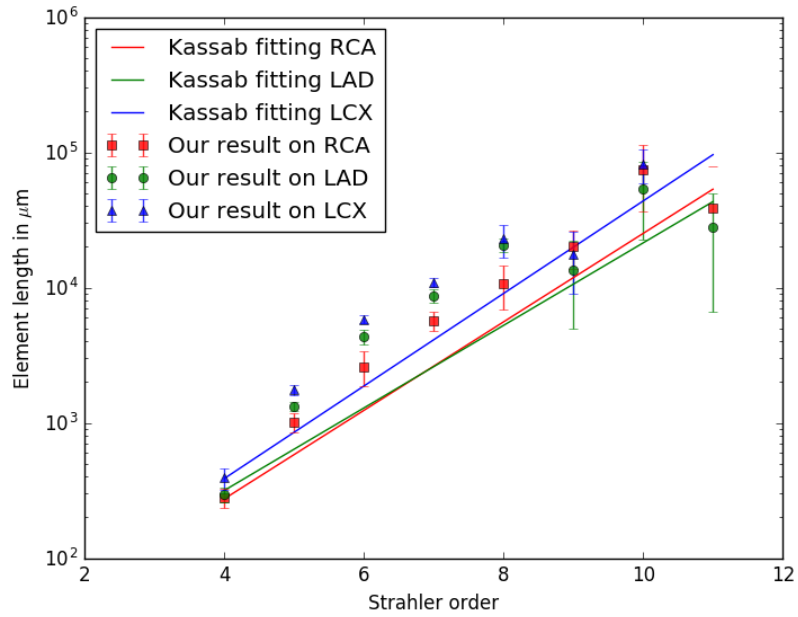


Figure 37 – Average element length per label in our model, with PB algorithm, compared with Kassab's.

Both algorithms satisfy literature morphometry. However, the PB algorithm generates smaller diameter networks, that do not enforce continuity with the segmented model. This algorithm is therefore unsatisfying. The continuity between synthetic and segmented models is crucial otherwise it would later involve artifacts in the functional assessment of the combined vasculature model.

The RB algorithm has a harder time attaining target flows, but enforces continuity between segmented and simulated networks. Consequently we rely on the RB method to generate vascular model for our project.

## DISCUSSION

---

We have proposed a patient-specific hybrid image-based and synthetic geometric model that extends coronary trees from large epicardial arteries to arterioles. With this method we generated 6000-terminal segment models for 6 different patients. We showed that the generated models globally respect the algorithm constraints, and their geometry satisfy literature morphometry. Their estimated regional perfusion territories also correlate with referenced distributions.

### 5.1 PERSPECTIVE OF IMPROVEMENTS

In future work, we should improve the algorithm initialization to always provide a first segment connection to the left ventricle, when this is physiologically possible. Also, we should provide more flexibility in the non-degenerative constraint to ensure that all trees can grow despite large diameter roots. Further improvements could include specific situations, for instance maintaining the exact segmented vessel direction for the first synthetic segment, or adapting tree growth more nicely to myocardial bridges. These changes would definitely improve final geometry, aesthetics and plausibility of the generated networks.

The generation algorithm assumes a constant power coefficient in Murray's law. In reality this coefficient varies on the position in the network. In particular, studies have shown that it increases as the diameter of the vessels decreases [39]. In future versions of the algorithm we could simulate the same trend using a stochastic distribution.

The impact of parameters such as source distribution, number of terminal segments, ratio between surface and inside ventricle segments, to find their optimal values remain to be studied. It could be relevant to make these parameters patient-specific, depending on the myocardial mass and segmented vessel characteristics.

The source distribution is patient specific, with a frequency of added branch based on the patient branching pattern. The relevance of this pattern is debatable for estimating the non segmented small diameter missed branch distribution. It would be interesting to compare with the distribution obtained via Kassab connectivity matrix. Also, deter-

mination of the right coronary vessel contributing to the left ventricle perfusion is empirical, and should be further assessed.

The number of terminal segments could be increased to provide a more complete vasculature, and potentially reach pre-capillary segments. More interesting, we could analyze how it relates to the terminal segment diameters in order to estimate a patient specific  $N_{\text{term}}$  that would enable to reach the same arteriole level for all patients.

The ratio of terminal segments generated between the two stages (surface over ventricle volume) could be questioned further, since the terminal segment density exhibits a mode located in the epicardium instead of endocardium. Meanwhile varying the ratio, the resulting perfusion territories should be analyzed. From visual observation the interpenetration between trees seems to be enforced in majority during extension on ventricle surface. This could be quantified by measuring interpenetration between convex hulls containing each tree. The stem-crown relationship relating territory volume to vessel diameter could also be of use to define the correct stage ratio.

Other aspects of the resulting vascular network could also be carried out. A recent study by Malkasian et al. [67] provides a minimum cost path technique to automatically assign territory per main vessel. This technique demonstrates high correlation with experimental territory measures. We could apply this technique on both the segmented models and the complete generated vasculature for comparison. If our model shows an interesting interpenetration between trees, from a visual assessment we can establish the borders of main vessel territories are not as clear as the one shown in experimental data of [67]. We should assess investigate how to better match this new reference.

Furthermore it would be of interest to analyze whether the generated network reproduce the layer dependent structure described by Van Horsen [40]. In this work, Van Horsen noted an increased arteriole density from epicardium to endocardium with a factor of 4, while we only applied a factor of 3. Given that the study [40] relies on high accuracy imaging acquisition we should also revise our gradient to better match this factor.

In addition, all these studies could be applied for simulations on the same patient with varying random seed, to further investigate repeatability of the algorithm.

We tested the CCO Forest with an alternative input: defining the tree pressure drop instead of its root diameter. This method does not ensure the diameter continuity between segmented and hybrid model thus it was not satisfying. The resulting differences could be further evaluated to better observe the impact of this alternative method.

We can also point out a limit of the model: the vascular network generation method assumes a dichotomous vascular tree. In reality, the vascular network can sometimes exhibit vascular closed loops,

named collateral vessels [98]. Such phenomena occurs particularly with chronic coronary artery disease as a biological response to improve circulation [112]. Seiler et al. provided proof of its relevant protective effect against mortality [69]. Our vascular model neglects collaterals, which do not satisfy energy minimization. However, collateral vessels growth does not always occur in patient with CAD, and reasons for this are not fully established, but seems to relate to disease speed or genetic factors [84]. Thus it seems more appropriate, as a start, to generate a vascular network model without collateral vessels. We could investigate later on how to estimate presence or absence of collaterals, and potentially simulate them.

Obviously, all these suggested additional studies would be of increased interest when provided ground-truth vascular model to compare with. Alternatively, to adjust all the above parameters, instead of considering the geometry, one could verify if the vasculature function is satisfactory.

The software implementation for this method is a prototype written in the Python language, thus the computation time could be reduced. At present, a 6000 terminal segment simulation can take several days. The first stage, surface growth, is the one taking the most time, due to strict spatial constraints.

## 5.2 LIMITS OF VALIDATION

First, the assessment of the method robustness could be improved by generating vascular networks for a higher number of patients. About this objective, the algorithm has been applied on an additional set of 8 low-diseased patients. The resulting networks show similar characteristics as the one obtained with the previous dataset. These results are presented in appendix 14.

A complete validation of the generated networks is difficult since we are not provided any ground-truth vasculature at this scale for our patient data. Thus we can only analyze the network geometry relatively to reference values. In addition, the morphometry statistics we compare with are extracted from animal anatomy. These two points explain why the validation of network geometry can be neither patient specific, nor fully endorsed by statistical analysis.

However the function of the generated networks constitute an additional validation assessment. Using multi-scale hemodynamic model, we can compute a functional analysis of the generated networks. Such models would enable full hemodynamic assessment in healthy and diseased patients, in both rest and stress conditions. Comparing with

reference values we could assess the functional validity of the generated networks, and potentially refine parameters of the vascular generation.

Furthermore, blood flow distribution inside the left ventricle tissue compartment could be estimated in rest and stress conditions. When perfusion is measured on the patient, by comparison we could finally assess whether the generated vasculature exhibits the patient-specific function. The additional 8 patient data-sets have been selected for this objective, with associated perfusion exams.

The second part of this manuscript describes the work aiming at building such a functional analysis of the generated vasculatures.

## Part II

### FUNCTIONAL ANALYSIS

In this part we present a functional analysis pipeline built to assess the hybrid vascular network generated in part I. First, in chapter 6 we introduce the context of blood flow simulation: cardiovascular function, and a review of blood flow modeling. In chapter 7 we present a method to compute fluid dynamics into the hybrid vascular model. In chapter 8 we analyze its results on 4 patients, and compute extrapolation analysis to provide comparison with ground-truth functional data. Finally in chapter 9 we discuss the potential improvements, limitations, and perspective of use of the functional analysis pipeline.



## CONTEXT

## 6.1 CARDIOVASCULAR FUNCTION

## 6.1.1 Cardiac cycle

blanco2013computational The cardiac cycle is composed of 2 phases, described in figure 38. During the diastole, the myocardium is re-

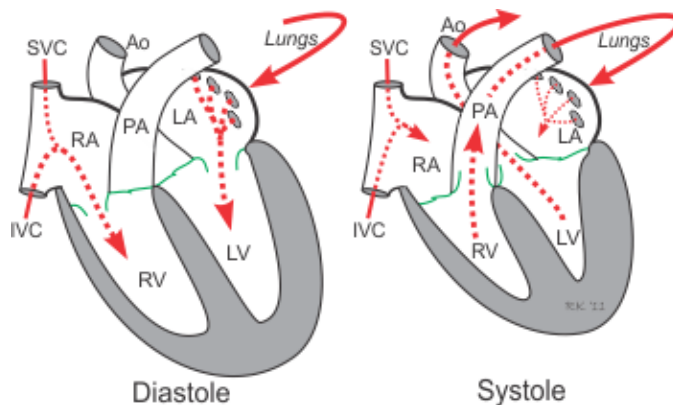


Figure 38 – Cardiac cycle phases: diastole and systole

laxed and atrioventricular valves are opened. On the right side, depleted oxygen blood arrives from the body via inferior and superior vena cava, it passively flows from the right atrium to the right ventricle. Simultaneously on the left side, the left atrium receives oxygenated blood from the lungs through the pulmonary veins. This blood passively flows to the left ventricle.

During the systole the myocardium contracts, and atrioventricular valves are closed, while pulmonary and aortic valves are open, which ejects blood out of the ventricles. From the right ventricle depleted oxygen blood is propelled into the pulmonary artery toward lungs, to be oxygenated. In parallel, oxygenated blood is ejected from the left ventricle through the aorta to be distributed to the whole body.

The frequency of the heart cycle, called heart rate, varies according to the body physical needs. The normal resting adult human heart rate is 60–100 beat per minute [4]. Physical activity, stress or specific drugs influence the heart rate, which is regulated via the central nervous system. These variations influence the total cardiac output, defined as the product of heart rate and the stroke volume (volume of blood ejected from the left ventricle).

### 6.1.2 *Coronary function*

Resting coronary blood flow is about 225 mL/min which results in 4–5% of the total cardiac output [35]. Only the first 0.1 mm layer of the endocardium is supplied by blood from the blood pool it is in contact with [35]. The rest of the heart needs its own nutrition. Therefore, coronary circulation is important for this function. Since the blood is supplied directly from the aorta, the blood is highly oxygenated.

During systole the heart muscle contraction constricts the coronary vessels, particularly the left ventricle intramuscular vessels. During diastole the cardiac muscle relaxation enables blood to flow through the capillaries with no obstruction, providing the heart with nutrition. Local arteriolar vasodilation, widening of the vessel, is the main controller of coronary blood flow. Whenever the heart activity is increased (induced by physical activity, stress or drug), the rate of coronary flow is also increased. This also applies to decreased activity, the blood flow is slowed down. It responds to the local need of nutrition for the heart. This is also known as the local muscle metabolism. To assess functional severity of Coronary Artery Disease maximal blood flow in vessels, called maximal hyperemia, is necessary: cardiologists rely on this metabolic regulation to induce maximal hyperemia by the use of a vasodilator.

### 6.1.3 *Cardiovascular complexity*

Many physiological phenomena happen within a single heart beat: an electrico-chemical signal induces myocardium muscle contraction, that propels blood of the ventricles through arteries to be distributed to the whole body for biochemical exchange via capillaries, and eventually returns to the cardiac pump via the venous network. This cyclic activity requires a multi-scale functioning loop from the microscopic scale (metabolism : molecular exchange) to the macroscopic scale (pump mechanics). In the whole vascular system, each scale exhibits specific vascular and fluid properties. In addition, when looking specifically at coronaries, because of the pump mechanism the interaction between vessels and myocardium compartments depends on cycle stage. Coronary properties, varying across space and time, are insufficient to explain the observed characteristics of myocardium perfusion.

#### 6.1.3.1 *Properties varying across space and time*

Along common arterial path, from aorta to capillaries, vascular properties adapt to specific role. Thanks to their elasticity, the largest arteries, close to the heart, exhibit a high wall distensibility (compliance) to dampen the high velocity pulsatile flow ( $1 \text{ m s}^{-1}$ ). They deliver blood to smaller arteries, which convey blood into the whole

body. When reaching smaller diameter vessels like arterioles, vessel resistance increases which enables delivering of continuous steady blood flow with low velocity (around  $0.01 \text{ cm s}^{-1}$ ) necessary for cellular exchange at the capillary level. This resistance to flow of arterioles is commonly referred as peripheral resistance. The combination of high compliance arteries and peripheral resistance, that enables to transform the pulsed flow into a continuous flow, is commonly described as the windkessel effect.

Blood properties also vary along vascular path. Blood is a concentrated suspension of blood cells and thus an anisotropic fluid. As described by Pries [79], it exhibits apparent viscosity variations, depending on strain rate. Under condition of laminar flow, the nature of viscosity dictates a flow profile where the velocity increases toward the center of the tube, see figure 39. When the radius decreases to

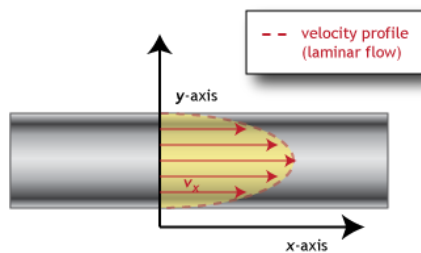


Figure 39 – Velocity profile in a vessel in laminar flow conditions

$\sim 100 \mu\text{m}$ , blood cells concentrate in the center of the tube because of the high velocity away from the walls. They have an increased velocity, which decreases the apparent blood viscosity. Later, when reaching smaller diameter vessels  $\sim 7 \mu\text{m}$  (capillaries), the blood cells have less space, need to align one after another: this decreases the velocity, which increases the apparent viscosity. The apparent viscosity is thus factor of both vessel diameter and hematocrit (blood cell concentration). To illustrate this principle, the apparent viscosity along vessel diameter for a varying hematocrit is presented in figure 40.

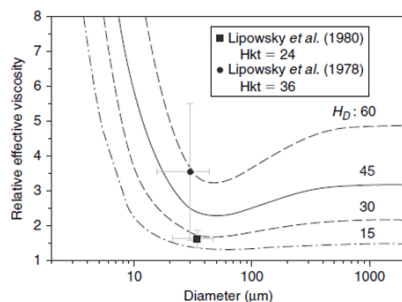


Figure 40 – From Pries [79] figure 1.12: Apparent viscosity in vivo derived from an analysis of blood flow, for varying hematocrit, in microvascular networks compared with experimental measurements.

Vascular and blood properties explain the resulting pressure along vessels, shown in figure 41. Normal human systolic pressure is 120 mmHg, while diastolic pressure is 80 mmHg.

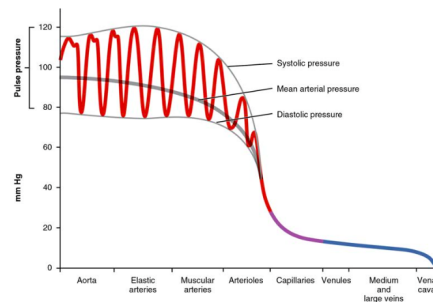


Figure 41 – Components of blood pressure throughout vessels, from [courses.lumenlearning.com](https://courses.lumenlearning.com)

In his work, Pries also shows that blood cells do not partition in proportion to flow at bifurcation, which is responsible for wide variations of microvascular hematocrit.

The above properties describing arterial multiscale variations can actually differ for the coronary vasculature, because of its location in the cardiac pump. Deeply described by Westerhof et al. [108], the interaction between muscle mechanics and coronaries has been identified as crucial in the heart cycle. This two way interaction, referred as cross-talk, varies in the different stages of cardiac cycle. Cardiac muscle affects coronary vasculature mostly during systole: the ventricle contraction impedes blood flow in coronary arteries. On the other hand coronary vasculature also affects cardiac muscle during both diastole and systole. During diastole, vessel filling increases myocardium wall stiffness, while during systole, vessel emptying facilitates cardiac contraction. The cross talk induces unusual functional variations in the microvasculature: the myocardium contraction flushes blood from the capillary bed into opposite directions, resulting in negative flow in arterioles, and high positive flow in veinules during systole [52]. Inversely, during diastole arteriole blood flows toward the capillary bed, and blood in veinules undergoes slightly retrograde flow.

Consequences of these vascular properties on the myocardium perfusion have not been all elucidated yet. Despite a globally homogeneous flow distribution, substantial regional flow heterogeneity occurs in myocardium tissue. This heterogeneity exhibits spatial self-similarity following a fractal pattern for near-neighbors regions. The cause of the blood flow fractal nature has so far not been clearly explained (even by fractal artery structure) but this system has been reproduced within generated vascular models, from statistical pig data [9] and from the CCO method [56].

The cardiovascular system, and in particular coronary arteries, exhibit properties varying across both time and space. Consequences on the function have not been all explained. Computational fluid dynamics is therefore complex to model in this system.

## 6.2 HEART MODELING: STATE OF THE ART

Fluid dynamics is a field of science which studies physical phenomena involving fluid flow. Computational Fluid Dynamics (CFD) is an engineering branch of fluid mechanics that uses numerical methods to solve and analyze the physical laws governing the flow of fluids under various conditions. Fluid Structure Interaction (FSI) can be crucial to produce physiologically plausible models. It couples CFD with structural mechanics to characterize interactions between a solid structure and the surrounding or internal fluid.

The numerical analysis methodology requires to define:

- the physical modeling equations, also called governing equations, that describe the physical fluid law,
- the geometry of the region of interest, called domain,
- the assumptions on the fluid and solid properties (physical parameters such as viscosity, elasticity, and density),
- the boundary conditions: mathematical relationships between the variables of the interest specified at the boundaries of the domain.

The complex set of modeling equations is solved in the geometrical domain, taking into account assumptions and boundary conditions. It results into a detailed characterization of pressure and flow fields inside the domain.

CFD has increasingly been applied to the cardiovascular system because of facilitating rapid, economical and low risk prototyping. Combined with cardiovascular imaging CFD can be applied as patient specific and multi-scale modeling to provide individual diagnostic, risk prediction and virtual treatment planning.

Various models have been proposed to describe cardiovascular physiology. The complexity of the problem is inversely related to the dimension and resolution of the studied domain.

### 6.2.1 Existing models

#### 6.2.1.1 Poiseuille and lumped model

Poiseuille law defines a pressure drop as the product of flow and resistance in a cylindrical segment, see equations 2 and 3 previously defined in section 2.1. By electric analogy, the correspondence from flow, viscosity and pressure respectively to current, resistance and voltage is established. Associated with pressure continuity and mass

conservation at bifurcations, all segments of vascular network can be connected in series or parallel. The resulting model, also referred as "first principles", has been used for blood flow analysis of several generated vasculatures derived from Kassab porcine morphometry [57], [58]. In particular, Mittal et al. [71] integrate Pries law into the Poiseuille model to compute blood flow analysis of the 2D complete coronary model reconstructed from statistical data [70], containing millions of vessels. Within this study they observe a power law relationship between radius and flow and estimate total equivalent resistance of the main vessels.

The Poiseuille model provides analysis in stationary flow conditions. A more sophisticated model, called lumped model or 0D model, also relying on electrical analogy, is used to simulate the whole heart cycle. Adding capacitance and inductance components, like in Westerhof work [107], such model enables to study pulsatile flow in the entire circulation.

However, since they do not rely on detailed geometry these models do not capture the whole complexity of cardiovascular function, in particular spatial flow distribution and wave propagation. The 0D models are also used to represent single compartment coupled to more complex models, or as boundary conditions (the non modeled extremities of the system).

#### 6.2.1.2 1D models

The Navier-Stokes governing equations describe the motion of viscous fluids relying on mass conservation and momentum. The 1D integration of Navier-Stokes model considers velocity of the fluid is only related to the axial component. This means the geometry of the vessel is considered as a tube with a varying radius along its length. The model can take into account energy loss at bifurcations of the network. It intrinsically reproduces wave propagation but it is not perfectly adapted for lesion study in complex geometry.

Matthys et al. showed the ability of the 1D formulation to capture the main features of pulse wave propagation in a 37 vessel model of the largest human body arteries [68]. Using 0D model for boundary condition, including energy loss at bifurcation, they describe good pressure and flow correlation with 70 experimental measures along the system. However, they did not succeed to remove some non-physiological oscillation at terminal branches, suggesting that wall visco-elasticity might play an important role in the experimental results.

Smith et al. applied a 1D CFD on the extended coronary canine vasculature [91]. In this work [92], they use the same geometrical model to stand for artery and veinous vasculature. A 0D model of the micro-circulation connect them. Like Matthys et al., they also model the pressure loss at bifurcations. In addition, they characterize

wall elasticity via a pressure-radius relationship. They obtain realistic flow rates (exhibiting fractal flow heterogeneity) and pressure distribution demonstrating functional plausibility of the generated vasculature. They intend to adapt the model to physio-pathology using Stettler work [93] to represent stenosed regions, relying on empirical models of viscous loss.

#### 6.2.1.3 3D models

The 3D Navier-Stoke modeling considers the full geometry of the domain. This model is more expensive to solve, but provides phenomena behavior with high precision. In particular, it captures wall shear stress, the tangential force exerted by flowing fluid corresponding to friction with vessel wall.

Vignon-Clementel et al. successfully apply it to simple bifurcation, simple tree, and multi-branched arterial trees [102]. They demonstrate the importance of boundary conditions as they represent vessels downstream of the modelled domain. They provide a method to define them implicitly at outlets by coupling with 0D or 1D models. With such framework, they can capture the impact of stenosis and provide patient-specific measures.

Kim et al. specifically adapted the 3D Navier-Stokes multidomain modeling above to the coronary function [62]. They couple the 3D CFD in aorta and epicardial coronaries, with a lumped model at vessel outlets. They consider vessel wall dynamics along the cardiac cycle to account for cross-talk interaction. This model reproduces realistic pressure and flow for rest and stress conditions, but also healthy or simulated diseased vessels.

To optimize computation time of 3D Navier-Stokes model, Heart-Flow suggests approaches combining reduced order models and machine learning [82].

Adapting to complex geometry, this model is useful to study diseased regions, and is intrinsically patient-specific. For large vessels, to consider pulsatility one can use FSI where the arterial walls are modeled with 1D or 3D, elastic or visco-elastic solid model.

#### 6.2.1.4 Porous model

The large number of vessels of vascular networks is a computational challenge for all previously described models. In addition the vasculature geometry is truncated at some microlevel, since the capillary network cannot be extracted, which induces boundary conditions sometimes difficult to determine. Another approach of vascular CFD uses a porous medium as geometrical domain. It is a continuous anisotropic material constituted of 2 phases: a solid phase, or matrix, which contains pores, and a fluid phase, that fills the pores. The porous medium is commonly described as a sponge, and is char-

acterized by several properties, for instance porosity (volume fraction of fluid) and permeability (ability to let fluid go through).

The fluid flow through a porous medium is governed by Darcy's law, a homogenization of Navier-Stokes equations. Resolution of the governing equations involves estimation of the domain properties relating to conductance of flow through tissue. Such a model is commonly used to represent micro-vasculature, or precisely capillary networks.

Huygues et al. proposed a viscoelastic porous model including stress fibers to represent the beating left ventricle [42]. Chapelle et al. [15] applied and detailed a similar model to simulate drainage and swelling of ventricle under large deformation. The specificity of this model is its compatibility with tissue incompressibility and thermodynamic principles. It exhibits several key phenomena of cardiac perfusion: main flows consistent with experimental measure, and perfusion heterogeneity. This model is therefore well suited for investigations of cross talk phenomena.

### 6.2.2 *Coupled perfusion and coronary models*

Methods aiming at a complete modeling of the cardiac physiology couple CFD in vessel and porous models.

Such methods are computed with detailed vessel and tissue domains. For instance Hyde et al. [43] worked with porcine and canine heart extracted from cryomicrotome, providing vessel down to arteriole level and ventricle segmentations. They couple a Poiseuille model in large arteries with a porous model for smaller vessels. This porous model contains several compartments, each of them describing a subset of embedded vessels based on radius range. For such multi-compartment model parameterisation can be difficult to obtain physiologically plausible results. Hyde et al. [44] provide several parameterisation methods.

A direct clinical application of this coupled model is the contrast agent simulation, achieved by Lee et al. [64]. They couple 1D coronary model with a poromechanical model representing the contracting myocardium. On top of this model they compute myocardial transport model for calculating contrast agent dynamics. Based on advection-reaction-diffusion equations, they simulate tracer agent kinetics that underlies image formation, and successfully identified a perfusion deficit region.

An alternative strategy proposed by D'Angelo et al. [20] couples 1D coronary model with a porous model containing 3D diffusion-reaction equations. This approach simulates blood through tissue by leaking from the vessel into a fractured porous medium. It was extended to biomechanical transport model in 3D vascular domain, and

applied for drug eluting stent in coronary artery [21].

A more detailed review of the state of the art is presented by Sinclair et al. [90].

### 6.3 OBJECTIVE

Our work subscribes in the perspective of perfusion simulations from X-Ray CT exam. As such, our goal is to develop the tools for functional analysis of the hybrid vascular network generated in Part 1. This pipeline aims at assessing the validity of the vascular network function against literature expectations, and also with regards to functional ground-truth data. In this objective we are provided by VU Medical Center of Amsterdam both X-ray CT and perfusion exam for a set of 8 low-diseased patients.

Using HeartFlow solution outputs on the X-ray CT, for each patient we generated a hybrid image based and synthetic geometric network, as described in part i, that provides vasculature geometry down to the arterioles.

To build a functional analysis providing comparison with ground-truth measures, we aim at establishing several instruments. First, we need to define a fluid dynamics model compatible with the hybrid network. Second, a set of tools must be developed to assess the resulting vascular function, and its extrapolated consequences into the myocardium compartment. The final step of this pipeline is to provide a patient-specific functional analysis, in the comparison with perfusion exams, from which acquisition is described in the following section.

#### 6.3.1 *Myocardium perfusion imaging data*

In our project, the provided perfusion images are computed with water-PET.

Positron emission tomography (PET), is an exam based on a radio-tracer to highlight metabolic activity in the body. The radio tracer used is modified water, in which the oxygen is  $^{15}\text{O}$ , a radio-isotope with only 7 neutrons instead of the normal 8. The radio tracer is thus called  $^{15}\text{O}$ -labeled water. The  $^{15}\text{O}$ -labeled water is an optimal tracer for flow quantitation as its uptake is linearly related to flow and a single compartment model is used for flow quantitation.

The exam consists of two steps: a first scan in rest condition, and a second scan in stress conditions. For each of these scans, the patient is injected a bolus of radio tracer. A total of 990 images are collected along a 6 minute scanning period, starting at the bolus injection. The PET sequence is immediately followed by a low dose X-ray CT. A

10 minute interval is observed between rest and stress exams, to allow for decay in radioactivity. Starting before, and during the stress exam, the patient is submitted to a continuous infusion of a common vasodilator, called adenosine, by intra veinous that induces maximal hyperemia. This simulates physical activity, corresponding to stress conditions. More details of this protocol are provided in Danad paper [22].

Absolute myocardial blood flow (MBF), in mL/ min /g of tissue, is calculated from the 990 captured images in rest and stress conditions. This process is achieved thanks to a in-house interactive software called cardiacVUer built by Harms et al. for VU Medical Center [36]. This tool can identify the myocardium, and calculate the absolute MBF values inside 17 standardized myocardium regions called AHA segments [14]. Extracted from kinetic analysis of the tracer in each voxel, the MBF is calculated for each segment. For this calculation the low dose CT, anatomical exam, is matched with the functional image to correct for emission attenuation depending on tissue thickness and composition. Finally, this tool generates a polarmap output: a 2 dimensional representation of the 17 segments, showing the averaged MBF values over the segment thickness, for rest, stress, and reserve, see example figure 42. The myocardial flow reserve correspond to the ratio of stress over rest.

The normal MBF values defined for water PET in this protocol are, cf [23]:

- at rest: around 1 mL/ min /g
- at stress: around 3.5 mL/ min /g, but can goes up to 5 in some healthy patients.

If a patient shows a MBF value at stress below the cutoff 2.3 mL/ min /g, it is defined as diseased. The MBF reserve value is also considered as a threshold for diagnosis: the cutoff value is 2.5. Because the radio tracer exhibits a high spatial resolution, local heterogeneity can be observed in a normal patient (such local details are not obviously seen with other tracers like rubidium).

This  $^{15}\text{O}$ -labeled water-PET exam provides precise quantitative and qualitative absolute MBF measures. In order to produce comparison with such functional data, we define a CFD model to compute on the hybrid vascular network, which is presented in the next chapter.

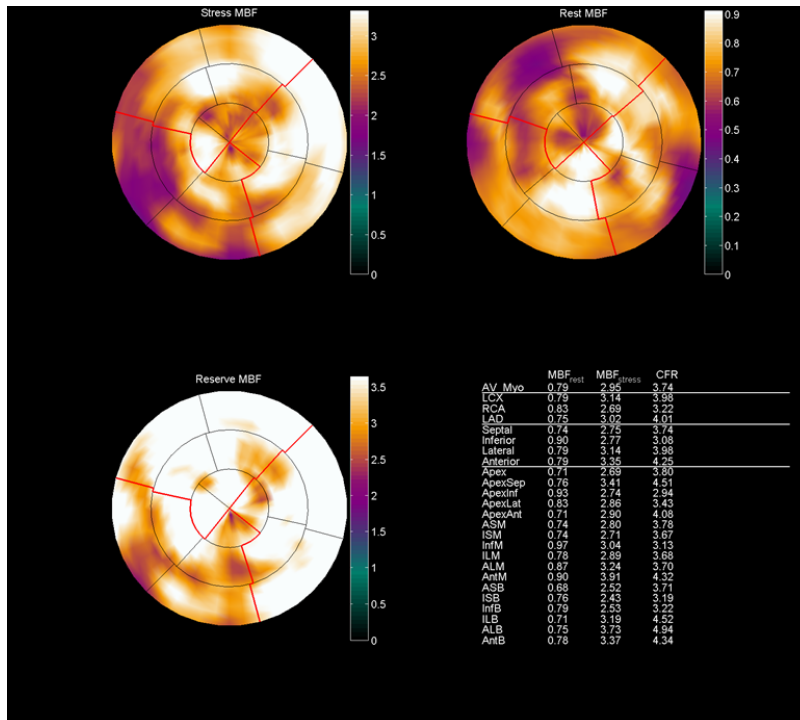


Figure 42 – Example of polarmap of low diseased patient: rest and stress MBF results in mL/min/g, Coronary Flow Reserve (CFR or reserve) corresponds to the ratio of stress MBF over rest MBF. The red lines on the polarmaps delineate segments statistically associated respectively to LAD (top), RCA (bottom left) and LCX (right) vessels. Image produced by Cardiac VUer, in-house software of VU Medical Center.



In this chapter we compute the solution to the 1D-Euler equations of blood flow in the hybrid geometrical model composed of the segmented vasculature and synthetic network. The 1D equations of blood flow can be derived in each vessel by cross sectional integration of the Navier-Stokes equations.

### 7.1 ASSUMPTIONS

To compute CFD in coronaries, we make several assumptions on the domain and fluid properties.

- The blood is modeled as an incompressible, homogeneous Newtonian fluid. This means that we ignore complex rheological properties, in particular Pries law defining varying viscosity. This is quite an important approximation considering that we work on a multi-scale vasculature. Such assumption is acceptable for large and small arteries [83], but is a significant simplification when reaching the arteriole level, in the terminal branches our vascular trees. This is a conscious decision to simplify the initial model, that can later on be improved with more realistic blood properties. Blood behaves as a non-Newtonian fluid at low shear rate. However the cut-off shear rate is about  $100 \text{ s}^{-1}$  [49], [6]: flow in large coronaries usually exhibit higher values. We would expect to see lower shear rates either in underperfused vessels or in aneurysm-like complex geometry.
- The blood is approximated as a fully developed flow under laminar conditions. This is relevant for the majority of the domain. Complex flow is only expected close to the ostium into the large arteries or around diseased regions.
- We assume steady state, i.e. independent of time. This assumption implies that only cycle-averaged quantities can be estimated. In contrast, absolute MBF measures from perfusion imaging correspond to averaged values over several heart cycles. However this strategy is effective for coronary functional analysis since Tu et al. demonstrate a good correlation between mean volumetric flow rate and FFR measures [99]. In addition, Morris et al. showed that steady state analysis is more robust and reliable than transient analysis [72]. We also note that an internal study achieved at HeartFlow demonstrated that flow values averaged over cycles are equivalent to those obtained in steady-state simulations in their segmented coronary models.

We focus on modeling resting and hyperemic conditions, necessary to provide perfusion analysis.

- We do not consider fluid-structure mechanical interaction: in our model, vascular walls are non elastic, we neglect ventricle contraction and cross talk. We seek overall effect over heart beat.

## 7.2 MODEL

The Navier-Stokes equations governing the isothermal flow of an incompressible fluid derives from conservation of motion quantity. They ensure mass conservation and momentum balance.

Mass conservation states that the variation of the mass of fluid with time is null. The momentum equation states that the sum of all forces (here acceleration, inertia, pressure, and viscous forces) is null, in other words, the momentum is balanced.

These equations are defined for a fluid of volumetric mass density  $\rho$ , of viscosity  $\mu$ , moving into the vessel with a longitudinal mean velocity  $v$ , within an Eulerian system. The 1D integration of Navier-Stokes equations, defined along the centerline axis of each vessel of coordinate  $z$ , can be written as:

$$\frac{\partial S}{\partial t} + \frac{\partial Q}{\partial z} = 0 \quad (21a)$$

$$\frac{\partial Q}{\partial t} + \frac{\partial}{\partial z} \left( \alpha \frac{Q^2}{S} \right) + \frac{S}{\rho} \frac{\partial P}{\partial z} + \lambda \frac{Q}{S} = 0 \quad (21b)$$

$S$  represents the cross sectional area of the vessel, and  $Q$  the flow rate related to velocity by  $Q = Sv$ , and  $P$  the pressure. In equation 21a, for mass conservation, because of steady flow, we do not consider  $S$  versus time, so the first term is neglected. Thus, the flow is not a function of the  $z$  axis.

In the momentum equation, 21b, the first term corresponds to the acceleration, which is neglected due to steady flow assumption. The second term represents inertia, and the third term refers to the pressure gradient along the vessel. Finally the fourth term expresses viscous losses, with  $\lambda$  representing the viscous resistance of the flow per unit of length of the vessel. This constant  $\lambda$  is derived from kinematic viscosity of blood by assuming here a parabolic velocity profile. The constant  $\alpha = 4/3$  is obtained by integrating the parabolic velocity profile over the cross sectional area [103].

At each bifurcation, conservation of mass and continuity of pressure provides a relationship between vessels, allowing to build a system of equations.

The equation system must be solved in the whole hybrid model:

- in the synthetic segments,  $S$  is known and constant along  $z$  of each vessel, so we can resolve directly with Poiseuille law. The inertia term disappears.
- in the segmented vessels,  $S$  is known and varies along  $z$ . The inertia term is taken into account.

### 7.2.1 Boundary conditions

At the inlet of each left and right coronary tree, we set the aortic pressure to  $P_{AO} = 93$  mmHg. This value can be derived from average systolic (120 mmHg) and diastolic pressure (80 mmHg), considering systole occurs during a third of heart cycle [10], and was also calculated from a 400 patient datasets by HeartFlow.

At each of the segment outlets, we set a boundary condition corresponding to the terminal segment flow. This boundary condition is estimated and updated differently in rest and stress conditions.

### 7.2.2 Algorithm for the 1D model

#### 7.2.2.1 Rest conditions

The total myocardium baseline flow  $Q_{rest}^{tot}$  is estimated from the myocardial mass  $m$ , following the relationship defined by Choi et al. [16]:

$$Q_{rest}^{tot} = \zeta \times m^\gamma \quad (22)$$

Currently  $\gamma$  is set to 0.75 [16]. Note that the coefficient  $\gamma$  can be tuned to better match experimental myocardial blood flow values. The coefficient  $\zeta = \frac{3291}{60}$  corresponds to a normalization factor. It was obtained to compute a normal distribution with a median myocardial blood flow rate value of 1.0 mL/min/g at baseline using more than 400 patients.

We initialize all terminal segment flows based on their diameter:

$$q_{rest}^{T,i} = \frac{(r^{T,i})^{2.7}}{\sum_{i=1}^{N_{term}} (r^{T,i})^{2.7}} Q_{rest}^{tot} \quad (23)$$

With these initialized flows we calculate the baseline resistance at each terminal segment:

$$R_{base}^{T,i} = \frac{P_{AO}}{q_{rest}^{T,i}} \quad (24)$$

From this we can estimate a minimum resistance expected at each terminal segment end to be:

$$R_{min}^{T,i} = \frac{1}{4} R_{base}^{T,i} \quad (25)$$

This minimum resistance is calculated once, and then values are fixed for the whole algorithm. This minimum resistance assumes a maximal radius dilation capacity of about 40% ( $\sqrt{2}$ ) as referenced in [110]. It relates to the resistance given by the Poiseuille formula equation 2. This radius dilation capacity is applied to synthetic trees to replicate dilation of arterioles.

Using the terminal segment flows as boundary condition for the first iteration, flow and pressure are simulated in the entire tree, by solving the 1D equations. With the resulting values for terminal segment pressures ( $P^{T,i}$ ), and the known terminal segment flows ( $q_{rest}^{T,i}$ ) we estimate the simulated terminal segment resistance  $R_{sim}^{T,i}$ :

$$R_{sim}^{T,i} = \frac{P^{T,i}}{q_{rest}^{T,i}} \quad (26)$$

If the simulated terminal segment resistance falls below the minimum resistance value  $R_{min}^{T,i}$ , we update both geometry and flow. We compute the radii dilation of the terminal segment and its upstream synthetic segments using the factor  $\left(\frac{R_{base}^{T,i}}{R_{min}^{T,i}}\right)^{0.25} = \sqrt{2}$ . And then we reduce the terminal segment flow, by multiplying it with the factor  $\frac{R_{sim}^{T,i}}{R_{min}^{T,i}}$ .

If the simulated terminal segment resistance is over or equal to  $R_{min}^{T,i}$ , then we update the geometry, but maintain the same flow. The radii dilation of the terminal segment and all its upstream synthetic segments is performed with the same factor  $\left(\frac{R_{base}^{T,i}}{R_{min}^{T,i}}\right)^{0.25} = \sqrt{2}$ .

Note that each terminal segment can have a different radius dilation factor as the resistance of the terminal segment will depend on the upstream pressure loss. Several iterations are necessary to obtain a stabilized flow in the system, determined when:

$$\max \left( \frac{R_{sim,n+1}^{T,i} - R_{sim,n}^{T,i}}{R_{sim,n+1}^{T,i}} \right) < 1\% \quad (27)$$

Also, note that for synthetic trees arising from vessel tips, the dilation propagation stops just before reaching the root segment. This ensure we maintain continuity between the segmented and synthetic networks. For synthetic trees arising along a vessel, the dilation propagation reaches the root segment.

#### 7.2.2.2 Stress conditions

The hyperemic state imitates invasive FFR measure conditions. For this exam, the patient is administrated intravenous adenosine, a vasodilator. Wilson et al. showed that under this condition, the total coronary resistance falls to a fourth of the resting value [110]. Thus, the total ideal hyperemic flow is defined as:

$$Q_{stress}^{tot} = 4Q_{rest}^{tot} \quad (28)$$

and all the synthetic segments are subject to a 40 % dilation regardless of the rest dilation, their radii are thus called  $r_d^{T,i}$ . Initial terminal segment flows are calculated with:

$$q_{\text{stress}}^{T,i} = \frac{(r_d^{T,i})^{2.7}}{\sum_{i=1}^{N_{\text{term}}} (r_d^{T,i})^{2.7}} Q_{\text{stress}}^{\text{tot}} \quad (29)$$

So that the minimal terminal segment resistances are estimated with the initial terminal segment flows as:

$$R_{\text{min},\text{stress}}^{T,i} = \frac{P_{\text{AO}}}{q_{\text{stress}}^{T,i}} \quad (30)$$

Since the whole system is already at maximal radius dilation capacity, all terminal segment resistances are fixed. The system is solved using  $q_{\text{stress}}^{T,i}$  as terminal segment outlet boundary conditions. With the resulting simulated pressures and flow, we compute the simulated resistance:

$$R_{\text{sim},\text{stress}}^{T,i} = \frac{p_{\text{sim},\text{stress}}^{T,i}}{q_{\text{sim},\text{stress}}^{T,i}} \quad (31)$$

Whatever the simulated resistance, the terminal segment flow is always multiplied by the factor  $\frac{R_{\text{sim},\text{stress}}^{T,i}}{R_{\text{min},\text{stress}}^{T,i}}$ . That way, if the simulated resistance falls below the minimum resistance, the flow is increased, otherwise it is decreased.

Simulation is then run again with the updated terminal flow values. Over iterations, the computed terminal resistance values converge to the minimum resistance values. The convergence criteria is:

$$\max \left( \left| \frac{p_{\text{stress}}^{T,i}/q_{\text{stress}}^{T,i} - R_{\text{min},\text{stress}}^{T,i}}{R_{\text{min},\text{stress}}^{T,i}} \right| \right) < 0.01 \quad (32)$$

### 7.2.2.3 Vessels non perfusing left ventricle

For the vessels non perfusing the left ventricle (mostly arising from RCA), we define terminal segment flow boundary condition based on the equation 23. However if the calculate terminal vessel flow is lower than the main vessel flow contribution to the left ventricle, we neglect the vessel non perfusing left ventricle by assigning a zero flow boundary condition.



The 1D coronary model is applied with both rest and hyperemic conditions on the hybrid vasculature of 7 patients, each containing 6000 terminal segments. It is computed with a C++ hand-written solver implemented by Hyun Jin Kim. The computation time for rest or stress conditions takes on average 10 hours.

We provide a set of tools to assess the resulting pressure and flows.

First, we achieve a study of the flow and pressure along the vessels to verify they continuously decrease down to arterioles, and satisfy literature ranges. We also verified the total tree resistance is much less than terminal segment resistance in stress conditions. Then, we perform an analysis of flow distribution at terminal segments, looking at their relative values, and their spatial distribution into the myocardium. This study provides assessment of the global homogeneity, and local fractal heterogeneity pattern. We also implement a comparison of this spatial flow distribution with the MBF measures of perfusion exams.

### 8.1 VESSEL FLOW

We compare the flow results with Kassab flow analysis achieved in vascular trees generated from porcine statistical data [58]. In this reference work, fluid dynamic is computed with a Poiseuille model on vascular models down to the pre-capillary vessel.

We assign the Diameter Defined Strahler order, similarly as in part I, section 3.3. We measure flow along Strahler order for both rest and stress conditions, see figure 43. In rest condition flow values follow similar logarithmic law as in Kassab analysis. In stress conditions the logarithmic law is maintained with a similar slope. Since the flow is increased in this condition, the intercept is higher.

### 8.2 VESSEL PRESSURE

We analyze pressure along element order, segment order and along vessel path, in both rest and stress conditions, for each patient or each main vessel.

#### 8.2.1 *Study per element*

In rest condition over the 7 patients the pressure drop between element order 11 and order 5 ranges between 4–13 mmHg, see figure

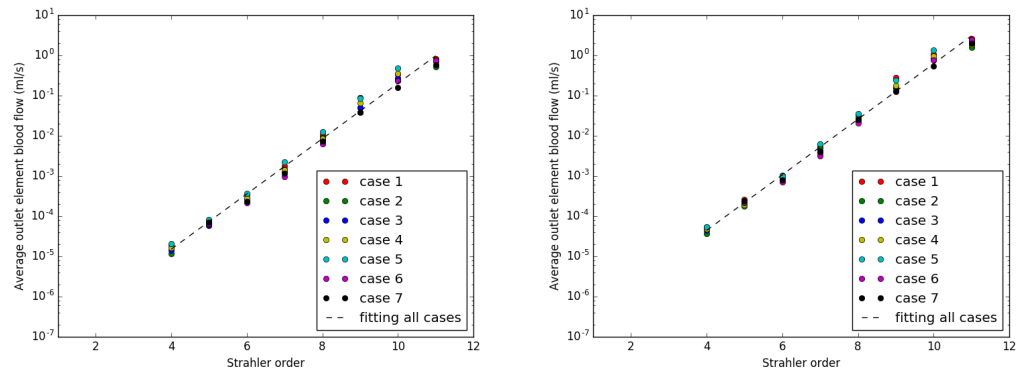


Figure 43 – Element average flow along Strahler order for 7 patients in rest (left) and stress (right) conditions.

44 which corresponds to the literature [58]. In stress conditions the pressure drop is increased of 2–3 times. Some cases, in particular 1, 3 or 4, show an average increasing pressure when reaching the lowest order, but this is actually a statistical artifact, explained later on.

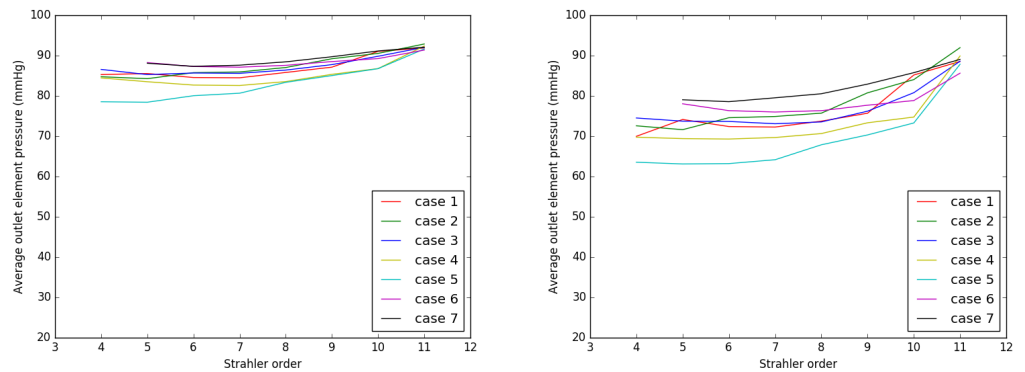


Figure 44 – Element average pressure along Strahler order for 7 patients in rest (left) and stress (right) conditions.

When classified by main vessel, pressure distributions are pretty similar along vessels, see figure 45.

The apparent low order pressure increase is more visible on the LAD vessel. We demonstrate that this effect is an artifact in the next sections.

### 8.2.2 Study along segment order

We observe that the element classification impacts on the pressure distribution. To investigate this we produce boxplots of pressures

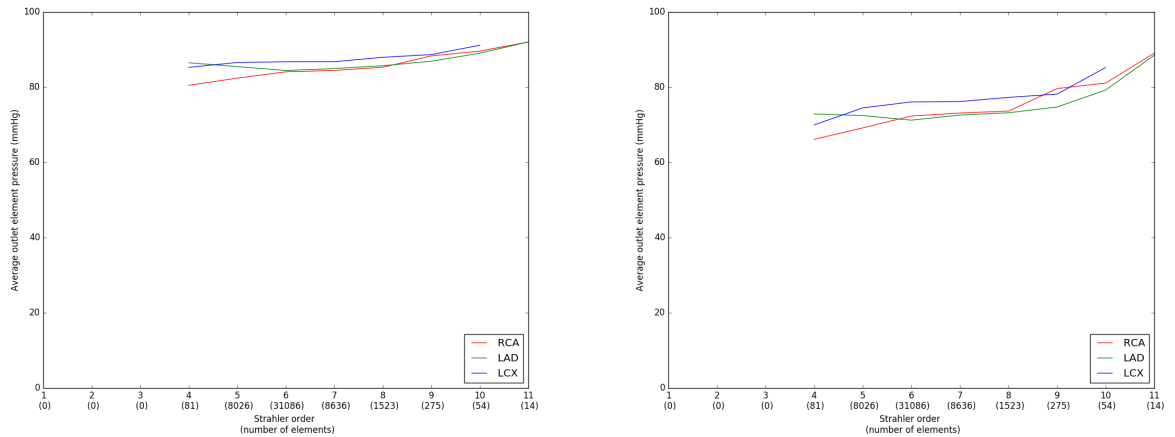


Figure 45 – Element average pressure along Strahler order for each main vessel over 7 patients in rest (left) and stress (right) conditions. The total number of elements in each Strahler order is indicated along the x axis.

along Strahler order for either element outlets or all segments outlets, see figures 46 and 47, respectively for rest and stress conditions.

Median pressures at element outlets between order 8 and 4 are alternatively increasing then decreasing. However, visualizing the results per segment shows continuously decreasing pressure values with decreasing Strahler order. This points out the element classification induces a bias in the pressure distributions. To confirm that the low order increasing pressure is an artifact, we also study pressure results along each vessel path.

### 8.2.3 Study along vessel path

We analyzed the pressure along all vessel paths for each of the cases. Apart from a slight pressure increase observed in the ostium regions, due to the diameter approximation within the bulbing region, we did not detect any pressure increase toward the terminal segments. For visualization purpose, we randomly picked 50 paths in LAD, LCX and RCA vessels of our 7 patients. In figure 48 we plot the average pressure along Strahler order for rest conditions. It shows terminal segments of order  $n$  with pressure values over average are arising from vessel of  $n + 2$  or  $n + 3$  order. This is in good agreement with the principle of connectivity matrix described by Kassab and explains the wide pressure ranges for each Strahler order. Note that for RCA paths, the ones ending at order 9 correspond to segmented

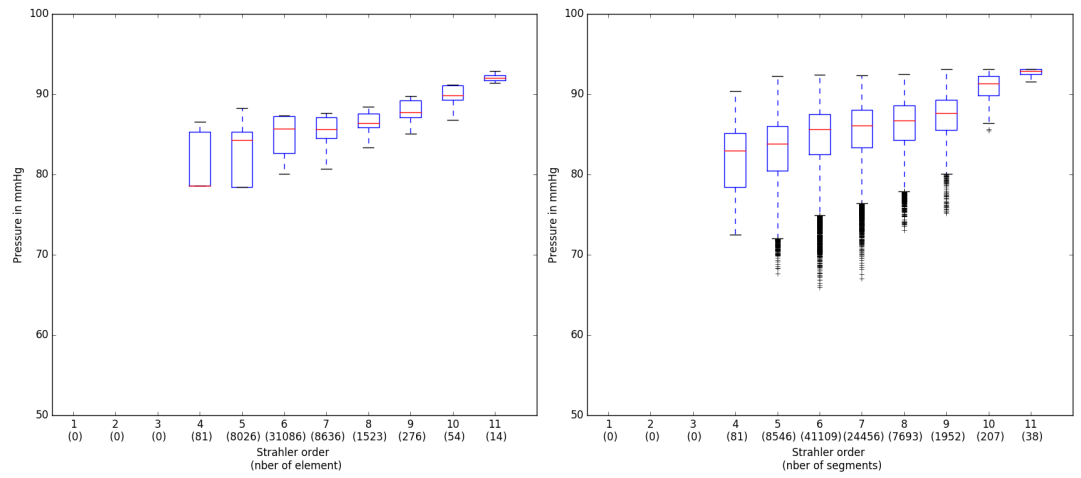


Figure 46 – Average pressure distribution (boxplot) along Strahler order for elements (left) and segments (right), over 7 patients in rest conditions.

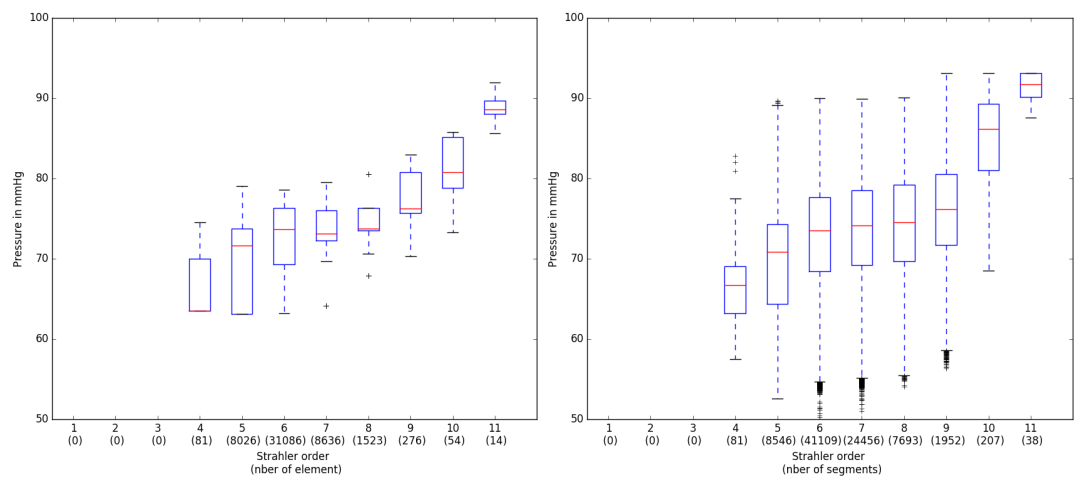


Figure 47 – Average pressure distribution (boxplot) along Strahler order for elements (left) and segments (right), over 7 patients in stress conditions.

vessels identified as perfusing the right ventricle, thus these vessels were not extended with synthetic segments.

The same observations apply for the stress conditions, see figure 49.

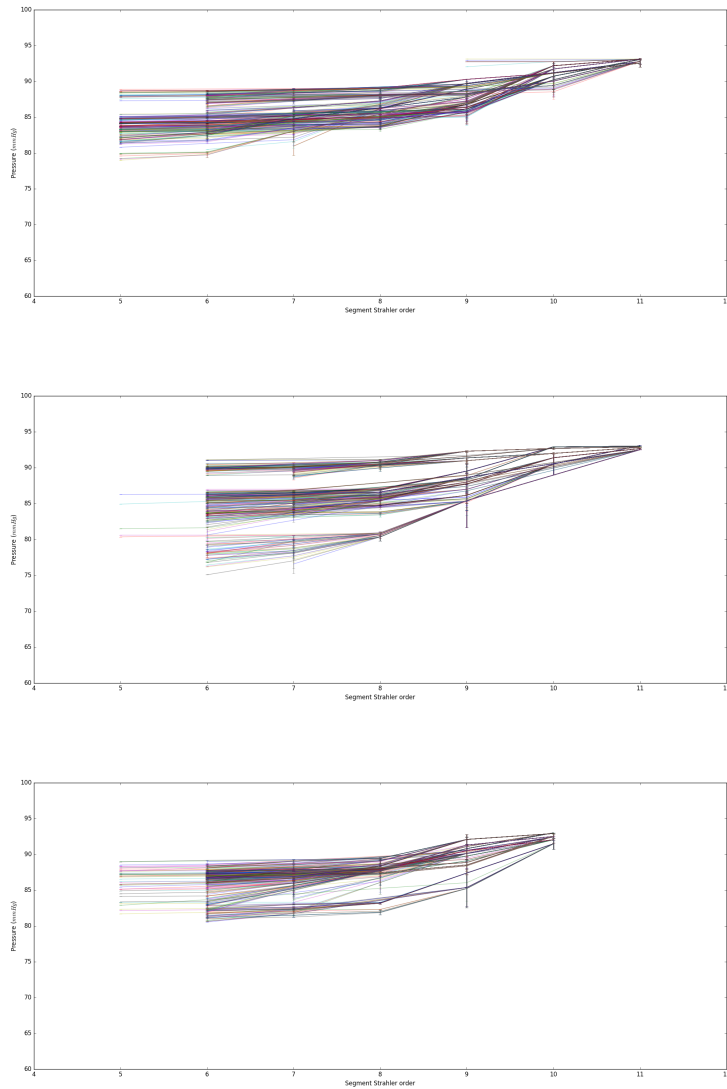


Figure 48 – Average pressure along 50 paths of a main vessel over 7 patients in rest conditions. Top: RCA, Mid: LAD, Bottom: LCX.

Ranges of pressure and flow obtained over the 7 patients match literature values.

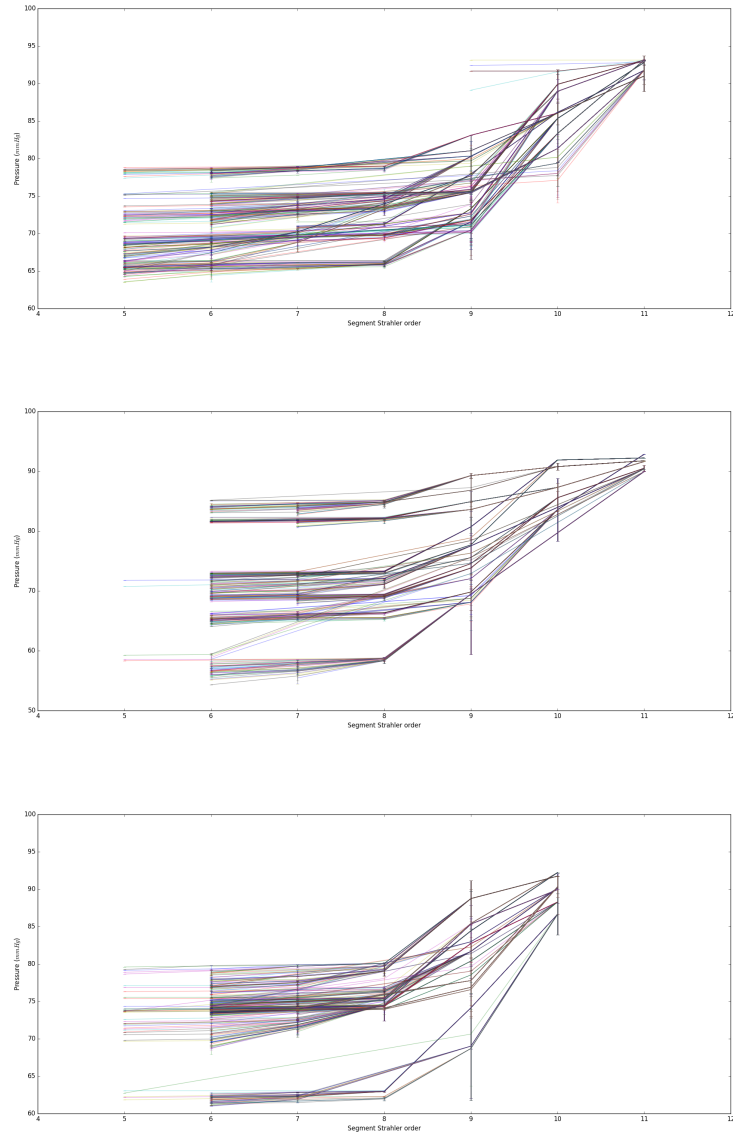


Figure 49 – Average pressure along 50 paths of a main vessel over 4 patients in stress conditions. Top: RCA, Mid: LAD, Bottom: LCX.

## 8.3 RESISTANCE

To verify resistance consistency, we calculated for each coronary tree  $j$  its resistance as:

$$R_{tree}^j = \frac{P_{ostium}^j - \min(P^{T,i})}{Q_{tot}^j} \quad (33)$$

with  $P^{T,i}$  the terminal segment pressures,  $P_{ostium}$  and  $Q_{tot}^j$  the pressure at ostium and total coronary tree flow. We calculate the maximal terminal segment resistance with:

$$R_{term}^{max} = \max\left(\frac{P^{T,i}}{q^{T,i}}\right) \quad (34)$$

Values for rest and stress conditions are reported respectively in the table 4 and 5. The coronary tree resistance is always much less than the maximal terminal segment resistance, which is expected and coherent with our assumption to neglect total tree resistance in the 1D coronary model. Also, the right coronary tree resistances are all higher than left coronary. This is in agreement with a much less parallelized network in the right coronary, since we only extended vessels perfusing the left ventricle. On the right coronary these correspond to just a few vessels close to the posterior wall. It is also partially induced by globally longer vessels on right coronary, because they wrap around the right ventricle before reaching the left ventricle.

Table 4 – Resistance values in left and right coronary for each case in rest conditions

in $\text{Pa mm}^{-3} \text{s}^{-1}$	Right coronary tree		Left coronary tree	
	$R_{tree}$	$R_{term}^{max}$	$R_{tree}$	$R_{term}^{max}$
case 1	4.88	$3.95 \times 10^5$	1.54	$1.76 \times 10^6$
case 2	12.07	$1.21 \times 10^6$	1.17	$3.82 \times 10^5$
case 3	9.00	$1.23 \times 10^6$	1.53	$1.64 \times 10^6$
case 4	7.96	$7.46 \times 10^5$	2.25	$3.04 \times 10^5$
case 5	16.60	$1.25 \times 10^6$	1.89	$7.53 \times 10^5$
case 6	3.26	$6.35 \times 10^5$	1.15	$2.90 \times 10^5$
case 7	2.67	$5.39 \times 10^5$	1.42	$3.30 \times 10^5$

Table 5 – Resistance values in left and right coronary for each case in stress conditions

in $\text{Pa mm}^{-3} \text{ s}^{-1}$	Right coronary tree		Left coronary tree	
	$R_{\text{tree}}$	$R_{\text{term}}^{\text{max}}$	$R_{\text{tree}}$	$R_{\text{term}}^{\text{max}}$
case 1	3.17	$1.03 \times 10^5$	0.96	$4.54 \times 10^5$
case 2	7.79	$3.32 \times 10^5$	0.85	$1.0 \times 10^5$
case 3	4.87	$3.28 \times 10^5$	1.04	$1.70 \times 10^5$
case 4	4.63	$2.09 \times 10^5$	1.47	$1.10 \times 10^5$
case 5	9.89	$3.72 \times 10^5$	1.19	$2.02 \times 10^5$
case 6	1.99	$1.69 \times 10^5$	1.0	$7.64 \times 10^4$
case 7	1.74	$1.43 \times 10^5$	0.93	$8.53 \times 10^4$

#### 8.4 SHEAR RATE

Based on the Poiseuille law (3), the shear rate of a vessel, with a radius  $r$  and flow  $q$ , can be calculated as:

$$\dot{\gamma} = \frac{4q}{\pi r^3} \quad (35)$$

We calculated shear rate for all segments of each of the cases in rest conditions. Nearly all segments obtain medium to high shear, with a value above  $100 \text{ s}^{-1}$ , cf figure 50. There are only 8 segments among all patients segments with low shear (between  $30$  and  $100 \text{ s}^{-1}$  value). These correspond to large diameter vessels of the segmented model. Since they are short and located in between close bifurcations, we assume their diameter measurement, based on a maximally inscribed sphere, might be overestimated, inducing the low shear rate calculation.

Given these shear rate results, the assumption of a Newtonian flow seems consistent for our 1D model.

#### 8.5 TERMINAL SEGMENT FLOWS

This analysis aims at assessing the relative and spatial distribution of terminal segment flows.

Some terminal segments exhibit very high flow, corresponding to synthetic trees that did not extend properly, inducing large terminal segment diameters. We neglect these outliers defined by flow values greater than mean plus two standard deviations. These outliers correspond on average to 0.8% of terminal segments over the 7 patients. The following analysis is inspired from two studies made respectively by Karch [56] and Beard [9] on single vascular trees. Karch analyzed the resulting terminal segment flows on several CCO simulations of

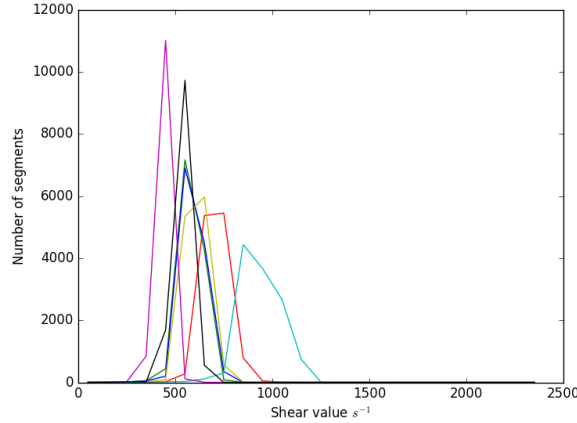


Figure 50 – Shear rate histogram for each case

16 000 terminal segments trees grown in cubic volumes. From statistical porcine data, Beard generated a representation of the LAD vessel with about  $5 \times 10^6$  terminal segments inside a cylindrical territory. He computed a blood flow analysis with a Poiseuille model including Pries law.

#### 8.5.1 *Relative distribution*

We study the distribution of the 6000 terminal segment flows in rest conditions. The distributions of relative flow ( $q^{T,i} / \sum q^{T,i}$ ) at terminal segments over the 7 patients are pretty similar. As in Karch analysis [56], the log log Probability Density Function (PDF) exhibits a parabolic shape, which corresponds to a log-Gaussian distribution. Since we have only 6000 terminal segments, our normalized expected terminal segment flows should be of  $1.66 \times 10^{-4}$ . Over the 7 patients, we observe an average mode of  $1.59 \times 10^{-4}$ , which is satisfactory, see figure 51.

#### 8.5.2 *Distribution in myocardium*

This study aims at assessing the spatial distribution of terminal segment flows. For this, we compute an estimation of relative regional flows at various resolutions.

Since the geometry of the left ventricle is complex, and its division could be subjective, we rely on randomness to objectively identify subvolumes. Picking randomly  $P$  points inside the myocardium, we compute a Voronoi tessellation using them as markers, thus identifying  $P$  subvolumes in the myocardium. The tessellation is calculated with a watershed algorithm [76]. For each subvolume we sum all ter-

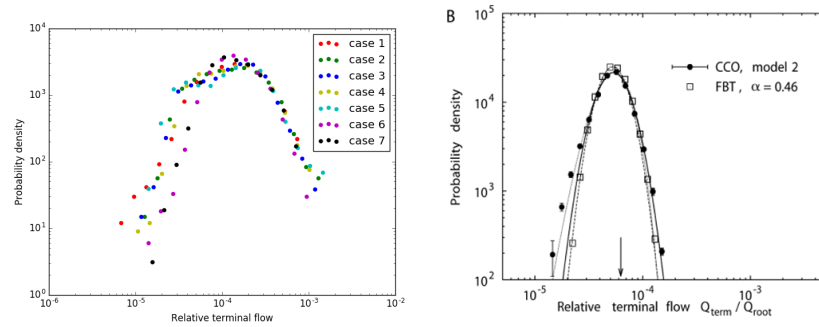


Figure 51 – Log log Probability Density Function of the relative terminal segment flow. Left: Our result. Right: figure 7B from Karch study.

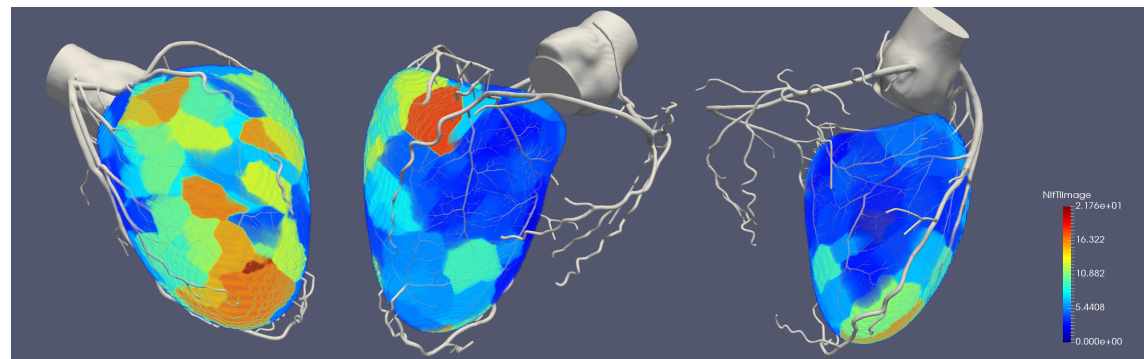


Figure 52 – Visualization of terminal segment flow distribution with Voronoi of 100 points on case 2. The high flow regions are concentrated around RCA and LAD main vessel paths.

terminal segment flows dumping into it, and normalize by the size of the subvolume in mL.

#### 8.5.2.1 Global homogeneity study

We analyze the flow distribution in the whole myocardium. Over all 7 patients, at lowest resolution ( $P = 100$ ) we observe maximal range of 3 to 5 times the mean flow value, while only 0.5 to 1.5 times of mean values are referenced in measures on dogs [24]. When visualizing the flow distribution in the myocardium, we observe high flow regions are concentrated close to the large coronaries, while low flow regions are mostly away from large vessels, see example of case 2 and 6 in figure 52 and 53. This suggests the synthetic networks fails to distribute the flow in the whole myocardium homogeneously.

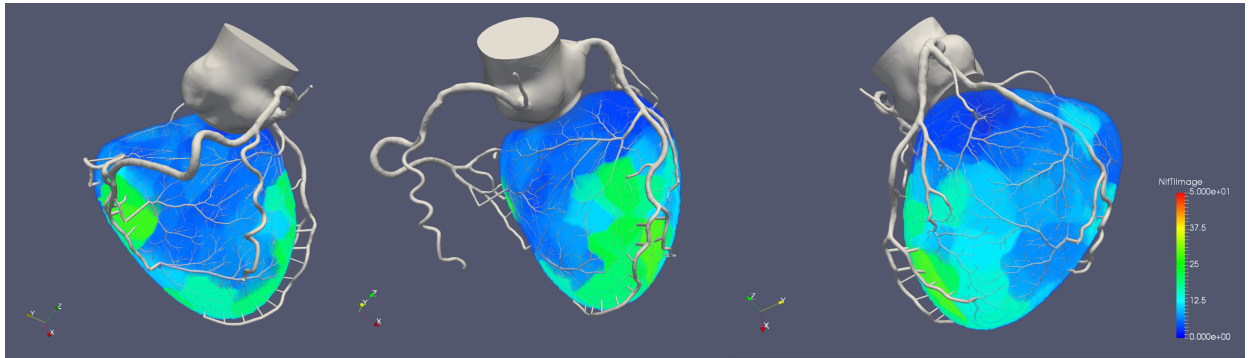


Figure 53 – Visualization of terminal segment flow distribution with Voronoi of 100 points on case 6. The high flow regions are concentrated around RCA and LAD main vessel paths.

#### 8.5.2.2 Local heterogeneity study

This study aims at identifying the fractal pattern of local flow distribution heterogeneity in the myocardium. In this goal we compute the probability density function of the relative regional flows at various spatial resolutions. The relative dispersions (RD) associated to each curve are expected to align in a log-log plot against subvolume size in mm. The slope of this line corresponds to the fractal coefficient. Reference measured values range between 1.21 and 1.37 among mammals. The study made by Beard et al. [9], on a  $1 \times 10^6$  segment representation of LAD built from statistical data showed a fractal coefficient of 1.235.

We plot the probability density function for each of the resolution, and calculate the relative dispersion (RD) associated to each curve, see figure 54.

Given that our vascular networks contain 6000 terminal segments, despite its non physiological meaning it is not surprising to obtain subvolumes with null flow when the resolution is over a  $1/6000$  of the myocardium volume. Whatever the resolution, the RD values are higher than literature values [9] by a factor of 10 (for smallest subvolumes) to 15 (for largest subvolumes). For comparison, Smith et al [92] obtained a factor of 4 to 6, when computing the same study on a simulated vascular network containing 6 Strahler order generations. Their result is imputed to the insufficient number of generations. Our RD values are significantly higher, which is consistent with the cumulation of small number of generations and the global heterogeneity observed in previous section.

The log-log plot of relative dispersion along the subvolume size is obtained for all patients, and presented in figure 55. Because of the global flow heterogeneity, in general they do not align.

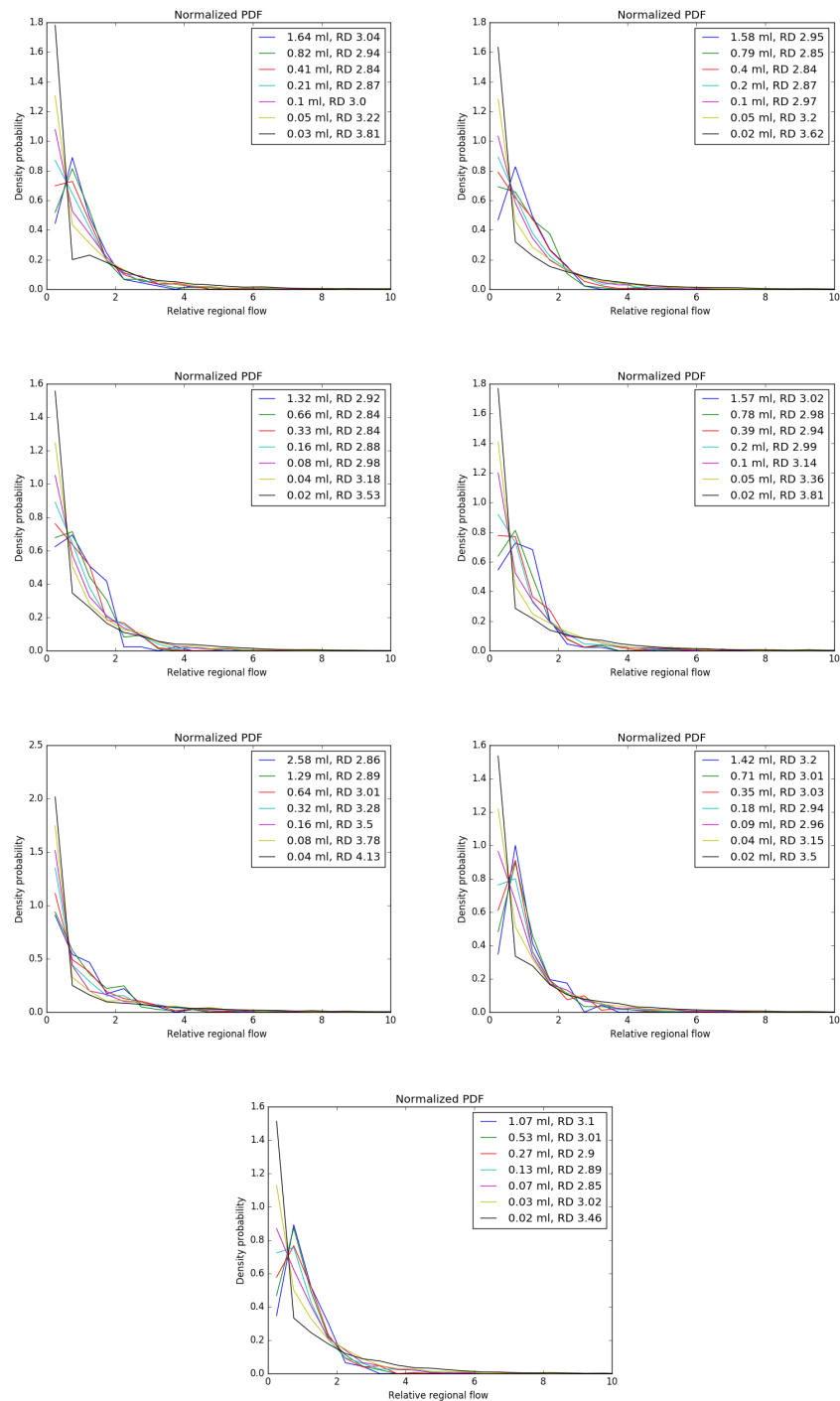


Figure 54 – Probability Density Functions of relative regional flow for each case (reading left to right, then top to bottom) at varying resolution. Mean volume and relative dispersion are calculated for each curve.

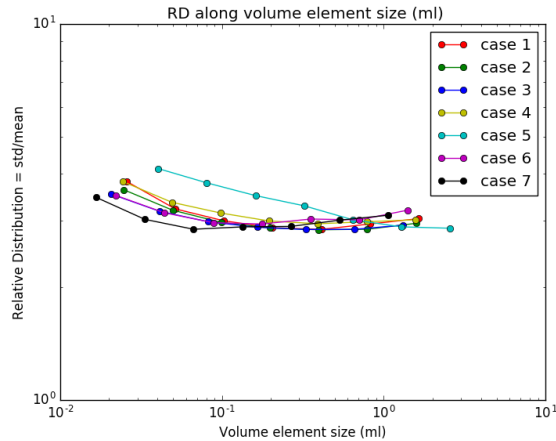


Figure 55 – Log-log plot of relative dispersion along subvolume.

One case makes an exception though: case 5, in which all relative dispersions are decreasing with volume element size, so that we can fit a line. The slope of RD versus log of element volume is  $1 - D = -0.09$ , or a fractal dimension  $D$  equal to 1.09. This coefficient is close to the value 1.12 obtained by Smith et al. [92]. However, since this case demonstrates flow values in a range of 5 times the mean value at lowest resolution, and relative dispersion corresponding to more than twice the values obtained by Smith et al., this result should be interpreted with caution. We noticed that among all cases this patient exhibits the highest myocardium surface combined with one of the lowest segmented coronary volumes. A larger territory with less vessels would provide lower constraints, which could explain a more homogeneous distribution of terminal segments. This interpretation needs to be further investigated.

### 8.5.3 Comparison with perfusion exams

The terminal segment flow distribution in the myocardium can be put in parallel with MBF values obtained from perfusion exams.

To work with a similar resolution as perfusion exams (voxel volume of 0.064 mL), we use the myocardium flow distribution image divided into 1600 Voronoi subvolumes, corresponding to an average of 0.07–0.1 mL per subvolume.

#### 8.5.3.1 Standardized parcellation of the myocardium

Comparison with perfusion exams requires a standardized myocardium parcellation according to the American Heart Association (AHA) nomenclature [75], see description in figure 56.

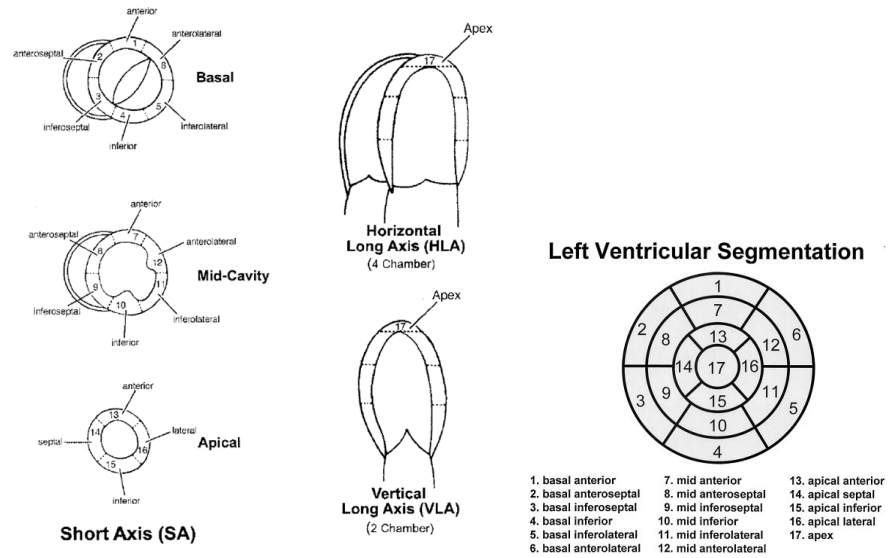


Figure 56 – Figures 3 and 4 of the AHA nomenclature [75]. Left: figure 3 describes the decomposition into numerical segments for each ring: basal, mid, apical and apex. Right: figure 4 shows the segment representation into a circumferential polar plot (called polarmap).

This process is achieved on a mask image of the myocardium. Each myocardium voxel is associated with cylindrical coordinates derived from 3 myocardium landmarks: the basal point, the apex and the heart-crux. The former corresponds to center of the atrio-ventricular valve. The latter corresponds to the highest intersection point of the right and left ventricle on the posterior wall. The apex is the tip of the left ventricle. With the basal point it defines the  $z$  axis. Based on these cylindrical coordinates, each myocardium voxel is assigned to one of the 17 AHA segments, following the nomenclature definition.

To assess the division along the  $z$  axis, we measured the volume of each 3 rings over all cases. The mean volumes, normalized by the sum of the 3 volumes, are respectively of  $36.0 \pm 0.2$ ,  $36.0 \pm 0.2$  and  $28.0 \pm 0.3\%$  for basal, mid and apical rings. This satisfies reference values (respectively 35, 35, and 30%), and demonstrate a good robustness.

The identification of the 17 segments has been qualitatively assessed by visual analysis. The location of the basal point, does not seem perfectly satisfactory for the coordinate system since its is not exactly in the center of the cavity. A more appropriate point could correspond to the barycenter of the basal ring. Due to lack of time, we did not press further the assessment of the parcellation.

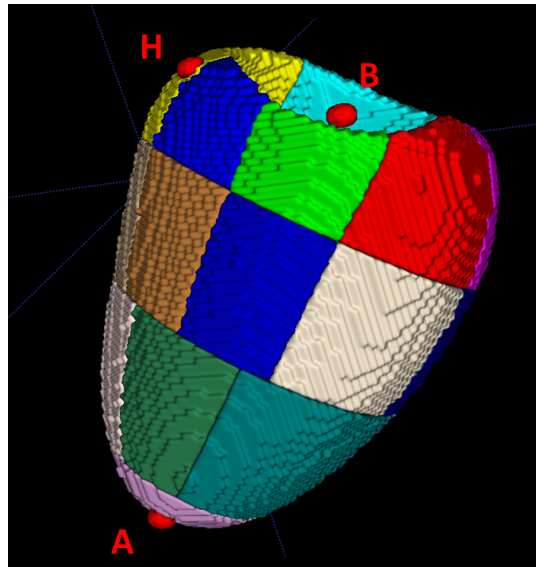


Figure 57 – 3D illustration of the myocardium AHA parcellation. The red ellipsoids correspond to the 3 landmarks defining the cylindrical coordinate system: apex (A), basal point (B), heart-crux (H).

#### 8.5.3.2 *Flow distribution comparison, with polarmap visualization*

We compute the average terminal vessel flow in each of the 17 AHA segments, and normalize them by the whole myocardium mean flow value. The resulting distribution of terminal flow per AHA segment is produced in the same fashion as the perfusion exam : a 2D projection in a polarmap, see exemple in figures 58 and 59. Note that in figure 59, showing results for case 3, we find again the line connecting high flow regions along LAD and RCA in particular in the mid and apical rings. Also, we can observe a technical difference in AHA parcellation computation between the cardiacVUer software and our method. Within cardiacVUer experts interactively define one landmark for each ring. Since this landmark indicates the reference of rotation, it induces the slight angular difference between rings, that does not occur within our system.

Comparison with the MBF segment values does not show significant correlation, with a  $R^2$  coefficient below 0.24 over all patients for rest and stress. Note that the highest correlation is obtained with the case 5, which is twice as high as the other cases. Considering the global heterogeneity of flow observed in previous section, this result was expected. However, this study was still conducted in order to construct the pipeline all the way to the comparison with functional measures. With such a functional analysis, we will be able to further improve vascular network generation to better match patient-specific myocardium flow distribution.

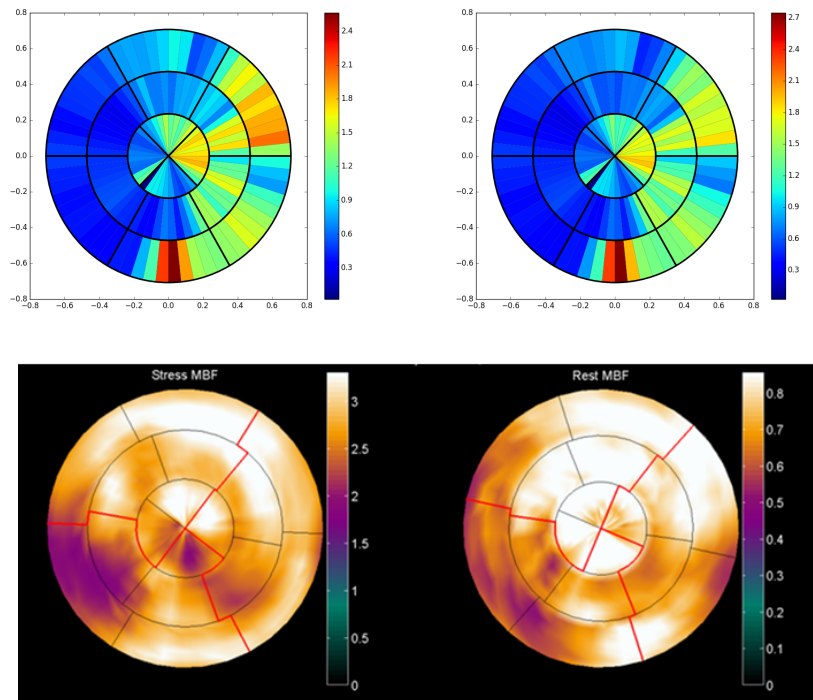


Figure 58 – Polarmap comparison between terminal segment flow distribution and MBF values from water-PET for case 2. Top: our result in stress (left), and rest (right). Bottom: water PET results.

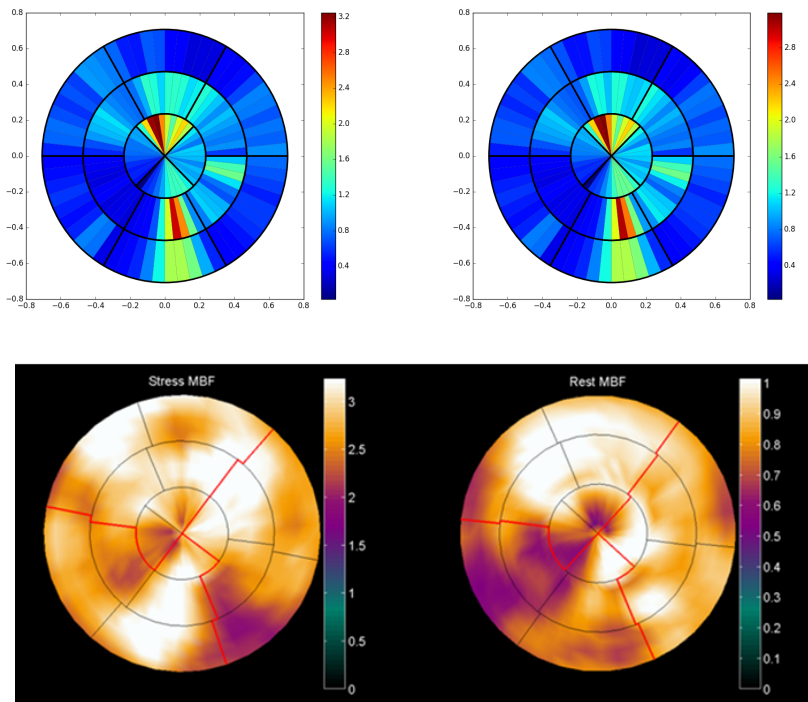


Figure 59 – Polarmap comparison between terminal segment flow distribution and MBF values from water-PET for case 3. Top: our result in stress (left), and rest (right). Bottom: water PET results.



## DISCUSSION

---

We produced a complete pipeline for the assessment of the hybrid vascular network function, leading to a comparison with ground-truth data.

First, we defined a 1D coronary model to compute fluid dynamics in the hybrid coronary networks for both rest and hyperemic conditions.

Then, we developed a set of tools for the functional analysis of the resulting flows and pressures. These enabled us to assess pressure, flow and resistance along the vessels and to estimate flow distribution inside the myocardium. To provide analysis against experimental measures, we computed the 17 AHA segments myocardium parcellation, and estimated correlation with the MBF values of the perfusion exams.

The results of this pipeline on 7 patients points out good agreement with the literature of flows and pressures along the vessels, and network resistance. In particular terminal segments exhibit the expected average flow values at vessel outlets. Also the vast majority of our segments exhibit mid to high shear rates and so, our assumption of a Newtonian fluid is verified. However our distribution of flow into the myocardium exhibits a non physiological global heterogeneity, preventing local flow patterns identification. As a consequence, the distribution does not correlate well with functional ground truth.

### 9.1 IMPROVEMENT AND VALIDATION OF THE PIPELINE TOOLS

Several steps of the pipeline can be reviewed.

The 1D coronary model should be assessed on more vascular networks to demonstrate its robustness. Due to time constraints, we have applied it only on 7 patients. Investigation of recent functional in vivo coronary studies should help provide more statistical data to compare with. Also, alternative strategies for the 1D model can be compared within this pipeline. For instance, a method relying on the terminal segment associated volume territories from the Voronoi tessellation has been concurrently developed. With this method terminal segment flow is distributed according to these volumes, and help estimating minimal resistances. Its results still need to be investigated and assessed against the current method to identify interests and drawbacks. In addition, an assumption made in the 1D coronary model is a constant dilation along synthetic segment path. It could

be interesting to assess instead the impact of a gradient factor along the vascular path.

Our functional extrapolation can be improved. The distribution of flow from the terminal segments to the whole myocardium could be assessed by associating a more physiologically representative model. With this goal in mind, we are currently working on coupling a porous model to the vascular CFD. This work in progress is presented in appendix 15. With this porous model we would obtain quantitative results in similar units as the absolute MBF values of ground-truth data. This would benefit the comparison by providing also simulated MBF reserve, ratio of absolute MBF in stress and rest conditions. The MBF reserve is an additional quantitative result taken into account for diagnosis with MPI, and is thus an important feature.

The AHA 17 segment parcellation of the myocardium has been only partially assessed, and despite detailed nomenclature we cannot ensure it perfectly corresponds to the current parcellation achieved in perfusion exams. We will submit it to a qualitative assessment by experts at the VU Medical Center. A quantitative assessment by comparison with parcellation achieved by these expert's hands or their semi-automatic software *cardiacVUer* would represent a significant effort but would lead to an optimal validation. Alternatively observing functional similarity would help demonstrate parcellation equivalence.

We should take advantage of the high spatial resolution of water PET to compute a more detailed qualitative analysis. In this objective the polarmap representation should be produced with a higher resolution. The AHA segments are currently subdivided according to the angular coordinate. One could consider subdividing them again along the z-axis, or co-register the average result image on the corresponding wedge. Such a qualitative comparison will be of particular interest when identifying perfusion defect regions. In addition, when the porous model provides simulated MBF values, we will use the same colormap as in perfusion exam to facilitate visual comparison. In order to propose a better comparison, it would be preferable to obtain the perfusion result in the 3D myocardium. Unfortunately the *Cardiac VUer* software application does not provide this output as an option. Obtaining this would require modification to the VU Medical Center in-house software package to add this functionality.

## 9.2 VALIDATION OF THE PERSONALIZED COMPUTATIONAL MODEL EXTRAPOLATION

Analyses resulting from the proposed pipeline demonstrate that the vascular network geometry satisfies fluid dynamics laws but does not achieve the function of distributing homogeneous flow into the myocardium. Many avenues exist to improve on this result, and can

be assessed by using the proposed pipeline, relying on the comparison with functional ground truth data.

First, the functional analysis should help improving vascular network generation. The aim is to obtain homogeneous terminal segment flow distribution into the myocardium. As we mentioned in Part 1, section 5.1, several parameters related to vascular growth can be fine-tuned: number of trees generated, ratio between surface and inner ventricle segments, and number of terminal segments. Thanks to our proposed work we can now assess their influence on the function of the network, and identify the set of parameters that induce improvements. In addition, we will be able to evaluate the functional differences between varying vascular networks generated for the same patient, which could provide additional insights for algorithm improvement. And also, to improve spatial distribution we could consider refining the Forest CCO algorithm itself using recent outcomes, with suggestions detailed in the conclusion.

The coronary model parameters could also be adapted to match experimental values. In particular, we will be able to assess the calculation of patient total baseline flow in regard of its average MBF value, and potentially refine the coefficients used in the model. The relationship between rest and stress total flows can also be assessed with the perfusion exams comparison. It would be interesting to verify if we obtain the intra-veinous adenosine effect observed by Wilson[110].

Finally, we have been working only with low diseased patients. This personalized computational model extrapolation will only be fully validated when demonstrating functional correlation in physiopathology context. To achieve this, we may rely first on simulated pathology, then on high diseased patient data. The later case would provide ground-truth from perfusion exams, and therefore provide a stronger validation. However we should carefully select the patient data. Working at first with single acute disease data, would avoid potential interference induced by multi-vessel disease. Such selection process is currently ongoing with our clinical partner from VU Medical Center.



## CONCLUSION



## CONCLUSION

---

### ACHIEVEMENTS

In our work we have produced a framework connecting functional analysis in large coronaries to blood flow distribution inside the myocardium, that enables comparison with ground truth data.

To achieve this we have proposed a patient-specific vascular network generation method, CCOForest, that extends segmented coronaries with smaller synthetic vessels down to the arterioles. We have expanded a tree generation method based on the satisfaction of functional principles, CCO, to account for multiple, competing vascular trees in a patient-specific context. The algorithm simulates angiogenesis under vascular volume minimization with flow-related and geometrical constraints, adapting the simultaneous tree growths to patient priors. To obtain a plausible coronary organization the vascular growth is decomposed into 2 stages: the first is carried out on the myocardium surface, and the second inside the whole volume. This method has been applied on 14 patient datasets producing 6000 terminal segments network each. It demonstrates good repeatability and robustness overall. Morphometry of the vessel shows good correlation with reference values extracted from porcine vasculatures.

To assess the generated hybrid vascular model we have proposed a functional analysis pipeline. We have built a 1D coronary model to compute blood flow simulation, in both rest and hyperemic conditions. We have analyzed resulting blood transport along the vessels, and distribution of terminal segment flows inside the myocardium. Finally we have produced the parcellation of the myocardium and projection of myocardium flow distribution into a polarmap, that enables comparison with functional ground-truth data. This pipeline was assessed on 7 patient vasculatures. And it has allowed us to identify weaknesses and perspectives of improvements for all the stages of our proposed framework.

The software application of this work was achieved with the help of several collaborators, specific software contributions are detailed in appendix [16](#).

### FRAMEWORK : INDEPENDENT REFINEMENTS

Within this framework, each step can be refined, independently of the functional validation against ground-truth.

Several aspects of the vascular network generation algorithm can be improved. The initialization should be more robust to always provide

first segments connecting on the myocardium surface. Growth constraints, such as non-degenerative bifurcation, could be also reviewed to better ensure the target extension of each vascular tree. It would be interesting to study further the organization of the generated network. For instance we could analyze bifurcation angle distributions, and in particular the perforation angle, at which vessels penetrate the myocardium. Also, we could investigate if the generated network exhibit organization patterns such as the ones identified by Van Horsen across myocardium layers [40]. In addition, even if the vascular generation cannot be fully assessed by anatomical comparison with human data, we could nonetheless relate it to anatomical ground-truth on animal. Work is currently on-going to generate vascular network for a porcine dataset. The latter is provided with anatomical ground-truth extracted from cryomicrotome images [32]. Also, we generated vasculatures based on resting flow conditions. It could be of interest to produce a vascular network with hyperemic flow conditions. We could measure the consequences on both the geometry and the function of the network.

In the functional analysis pipeline we have identified potential improvements independent from comparison with ground-truth data. The estimation of blood flow distribution within the myocardium would be more accurately represented by a porous model coupled to the 1D coronary model. This refinement is in progress, and is described in appendix 15. Our microvasculature did not model orientation of the smallest arterioles and capillaries along the myofiber direction, contrary to what has been described in the literature [59], [45]. We could integrate this anatomical information in the porous model by defining the domain as an anisotropic material with oriented fibers. The scalar permeability  $\kappa$  would be then replaced by a tensor [15]. The tensor field is difficult to estimate in-vivo, only recent studies propose techniques with MRI diffusion tensor imaging on animals [77], [28]. The permeability tensor could be nonetheless initiated with a generic model adjusted to the patient ventricle geometry, which would also avoid additional exam for the patient.

Anatomical correspondence of the AHA parcellation between the two different modalities is difficult to assess accurately. We pointed differences in parcellation techniques, and refinement to be achieved with our method. Qualitative or quantitative analysis with experts could help validating the parcellation process. Working upstream, with co-registration of the 2 perfusion images could also be investigated, which would enable wider correlation measures, independent of the parcellation. Also, the projection into a 2D polar map should be computed with a higher resolution in order to provide more detailed qualitative comparison with ground-truth data.

We evaluated both network generation and functional analysis with a limited number of data. Due to time constraints we have assessed

vascular network morphometry for a total of 14 patients, but the functional analysis was only applied on 7 patients. Robustness of both anatomy generation and vascular function could be confronted with more patient data.

The computation time of each step could potentially be optimized. However it would seem relevant to first identify adjustments leading to correlation with functional ground-truth data.

#### VALIDATION USING THE FRAMEWORK

Reaching comparison with ground-truth data is a major achievement, that provides a patient-specific functional assessment. In order to validate the obtain correlation with ground-truth data, we can now iterate to refine each step of the framework, from vascular generation to functional analysis.

The vascular network generation can now be adjusted with regards to functional analysis. Many parameters were empirically determined and their impact can now be assessed. Identification of vessels perfusing the left ventricle, distribution of new vascular trees, number of terminal segments, ratio between segments on surface and inside the myocardium have to be studied. Note that these parameters could also be compared with potential anatomical ground-truth data, even though such opportunities are rare for human data.

In order to aim at a better homogeneity of terminal segment distribution, we propose a refinement of the algorithm based on recent outcomes. According to a study by Malkasian [67], main vessel territories can be identified with minimum-cost path assignment technique. Dividing the left ventricle into per main-vessel sub-territories would provide more compact regions to grow vascular trees in, with our CCO Forest algorithm. Thus homogeneous terminal segment distributions would potentially be easier to produce. In addition this strategy can help parallelize the generation task, which could improve computation time.

The comparison with functional ground-truth data should help adjust the internal parameters of the 1D coronary and porous models, such as total baseline flow, to better match experimental values. Also, alternative strategies for the 1D model can now be compared within the same framework. Our fluid dynamic model is computed with assumptions simplifying the physiological reality. We could use the framework to assess their influence, and possibly adapt the model to integrate the relevant ones. Constant viscosity is an example of assumption that could be reviewed with integration of Pries law for small diameter vessels [79]. A non-Newtonian model could also be tested to ensure consistency with our assumptions.

To build the bridge between vascular anatomy and myocardium flow distribution we have focused on low diseased patient. This panel should be enlarged with more pathological cases. Validation could be extended with single acute disease, and then possibly multiple-vessel disease. First, we could assess the generic impact of simulated lesions. For instance we could identify the causal relationship between varying simulated stenosis severity and perfusion defect regions. Then, assessment with ground-truth data should be used to validate our functional model at patient-specific scale. We will look for correlation between simulated results and ground-truth data. When provided with a severe diseased patient data, we could also concurrently assess the effect of simulated stenting on the perfusion deficit region. Note that considering diseased vessel regions might require revision of the flow simulation to better represent complex flow behaviors.

Finally our framework does not clearly integrate yet the modeling of microvascular disease. But is microvascular disease actually independent of macrovascular disease? In clinical practice, microvascular disease is commonly expected as a consequence of macro-lesions in the upstream vessels. Nonetheless, cardiovascular complexity can sometimes provide unexpected results: for example, perfusion defect not correlated with identified stenosis. One could potentially associate such results to microvascular disease manifestation independent of macro-lesions. However, we should keep in mind that other macrovascular disease are still under assessment, and their influence on perfusion still investigated. Diffuse disease is less obviously identified but certainly impacts blood transport. In addition, recent outcomes suggest unsatisfying vascular volume relative to myocardial mass (found in hypertrophic cardiomyopathy) are related with globally lower  $FFR_{ct}$  values [88]. This ratio might have an influence on the perfusion, and thus could be an additional parameter to consider in our modeling.

#### PERSPECTIVES

The current framework comes within the viewpoint of simulating myocardium perfusion from X-Ray CT data. Defining the bridge from coronary vascular anatomy to myocardium perfusion at patient specific scale leads to many perspectives.

Validation of the generated vascular network itself would provide refinement of blood flow modeling in large coronaries by incorporating more realistic boundary conditions. Also, the functional connection between vascular and myocardium compartments would foster a more global consideration of the system, enabling to solve inverse problems. Identification of the territories perfused by the diseased vessel could ameliorate both prognostic and treatment planning.

In the context of computational model, our project has not been relying on a recent, trendy and powerful one, that imitates the neural network function: deep learning. Since such model requires a high amount of data, its use is limited in our project. In fact, the current framework could lead to the production of data to feed these models. Deep learning could help to produce faster solutions for parts of the framework. It would be interesting to study the possibility of learning complex vessel network structures for automated generations, following for example the Generative Adversarial Network type of methodologies. However these methods should be handled with care, since functional capacity could be difficult to integrate in the model.

Once validated, an alternative way of reducing the framework computation time could be to approximate the effect of the generated synthetic vasculature directly via the porous model. This could rely on coupling a porous model featuring leaking fractures at the segmented vessel location, such as the one described by D'Angelo et al. [20]. Parameterization of this technique could be challenging since we would only use vessels at the surface of the myocardium. Blood transport would probably need to be modeled differently at the surface and inside the myocardial tissue. In addition, flow might require to be differently modeled between the outlets and along the vessels. The current framework would likely help in the optimization of plausible parameters.

Our work has focused on the left ventricle perfusion, since functional ground truth data was limited to this compartment. However one could consider extending the framework to include the right ventricle, and even the atria chambers to complete the cardiac chamber anatomy. This would avoid the complex and partial identification of vessel perfusing the left ventricle. In exchange, it would bring the challenge of working with more diverse blood flow demand. Since contraction is less important in the right ventricle, the myocardial oxygen uptake and perfusion is reduced compared to left ventricle [19].

In a similar trend, the venous system could also be modeled, to obtain a more complete flow loop. However, venous anatomy is difficult to segment from our X-Ray CT modality, since the contrast agent is more diffused when reaching this compartment. An approach proposed by Smith [92] approximates the venous tree as a mirror of a 6 Strahler generations arterial tree. When modeling transient flow with wall elasticity in both venous and arterial trees, they achieve a finer model of the flow rates and pressure distribution. Time dependent simulation is computationally expensive, compared to steady flow. However such transient study enables to verify that tracer wash

out kinetics satisfies literature. This is an extra validation to compare with specific  $^{15}\text{O}$  water-PET results.

Also, extending the modeling with estimation of collateral vessels could help investigate pathology evolution. Since it is possible to stimulate collaterals development [84], collateral growth simulation could potentially help identify a less invasive treatment planning alternative.

Incorporating then cardiac mechanics with cross-talk interactions, and furthermore, electric and hormonal regulation system, would lead closer to an ambitious complete virtual physiological model of the whole organ.

Finally, similar approach establishing microvasculature anatomy to estimate tissue perfusion could be applied to other organs, in order to investigate additional physiological systems and dysfunctions. These many perspectives of personalized computational models are inspiring by both their complex challenges, and their benefits to patient care.

THESIS CONTENT - APPENDICES

---



Part III

APPENDIX





# Constrained Constructive Optimization implementation

## Reproducing Rudolph Karch paper

CLARA JAQUET  
Paris-Est University  
December 20, 2018

### Abstract

This report aims to explain the CCO algorithm implementation in 2D, and its 3D extension. This algorithm has been detailed by Schreiner in 2D [3] and Karch in 3D [1]. Because the implementation principle is spread between several articles, we propose to summarize hereafter the whole implementation. Along the way, we provide our own interpretation of some finer details of the method, that leave room for variants.

The CCO algorithm combines computational fluid dynamics laws, network geometry and topology optimization to mimic vascular network growth.

*Keywords:* constrained constructive optimization, implementation

## Contents

<b>1</b>	<b>Global tree optimization</b>	<b>2</b>
1.1	Assumptions and boundary conditions . . . . .	2
1.2	Initialization step . . . . .	4
1.3	Loop to add new segment . . . . .	5
1.3.1	Constrained new location $n_{loc}$ . . . . .	6
1.3.2	Test connection . . . . .	6
1.3.3	Propagate new bifurcation impact on the whole tree . . . . .	7
1.3.4	Measure target function . . . . .	8
1.3.5	Select best connection between neighbors . . . . .	8
1.4	Example of results and comparison . . . . .	8
<b>2</b>	<b>Local optimization: single bifurcation scale</b>	<b>11</b>
<b>Appendix A</b>	<b>Equation (25), from Kamiya &amp; Togawa 1972 equation (6)</b>	<b>16</b>

## Introduction

Constrained Constructive Optimization (CCO) consists of growing a tree governed by minimizing a target function.

In Karch's method the tree is constrained into a growing convex perfusion volume, and the target function minimizes the total tree volume. Segments are added one by one and subjected to both local optimization (single bifurcation scale) and global optimization (tree scale). The local optimization is based on Kamiya's work [2], whereas the global tree optimization has been implemented first by Schreiner in 2D [3].

## 1 Global tree optimization

Initialization of the method requires as input some physiological parameters, the number of terminal segments to reach, and a randomized starting point.

The CCO algorithm is introduced with the organigram in figure 1.

Each loop of the algorithm determines a new segment to be added onto the tree. Figure 2 provides an example of the result of the first three loops. The perfusion territory is slightly increased before each new added segment, to simulate tissue growth concomitant with vascular growth. A random location is picked under some constraints (geometrical and physiological), to use it as a candidate for segment extremity. Its connection is tested with neighbor segments, producing a bifurcation under topological, structural and functional constraints. Due to mechanical laws, each connection also induces a specific adjustment of all existing segment diameters. The optimal connection is then selected among all connections as the one minimizing a target function (the minimal volume of the total tree).

### 1.1 Assumptions and boundary conditions

The vascular tree grows under specific assumptions and boundary conditions.

The perfused volume is supposed convex and homogeneously filled. The terminal segments correspond to pre-arteriole level, feeding a non modeled micro-vasculature. The blood is an incompressible, homogeneous Newtonian fluid, studied in a steady state and in laminar flow conditions.

The resistance and the pressure drop of a segment  $j$  are defined by:

$$R_j = \frac{8\mu l_j}{\pi r_j^4} \text{ with } \mu \text{ the viscosity} \quad (1)$$

$$\Delta P_j = R_j Q_j \quad (2)$$

The total resistance of the tree is calculated recursively by tree decomposition, considering parallel and serial arrangements.

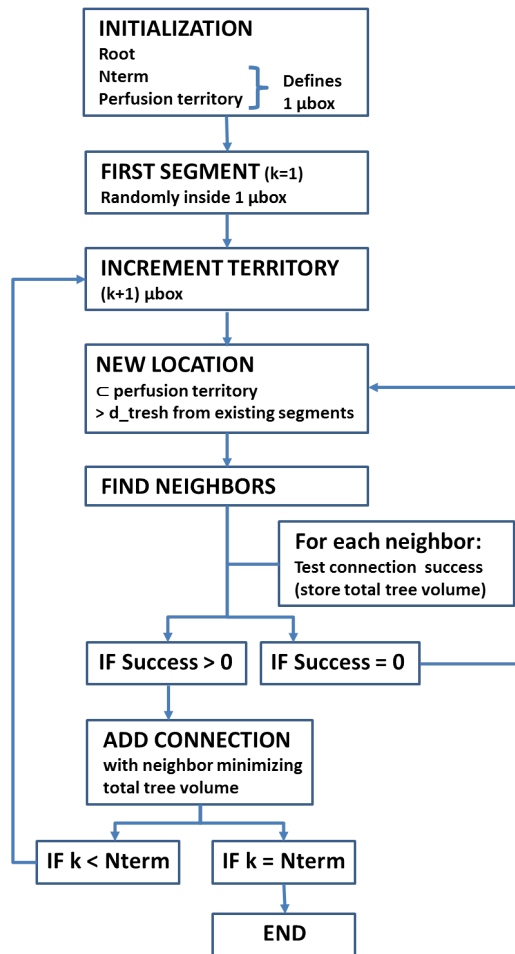


Figure 1: Algorithm of CCO.  $d\_tresh$  is a distance threshold calculated at each iteration. A microbox corresponds to an average area per terminal segment.

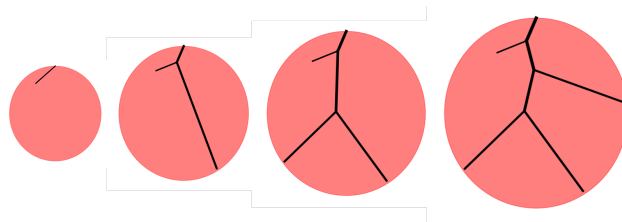


Figure 2: CCO example : output images of the first three loops.

Parameter	Meaning	Value
$V_{perf}$	perfusion volume	100 cm <sup>3</sup>
$P_{perf}$	perfusion pressure	100 mmHg
$P_{term}$	terminal pressure	60 mmHg
$Q_{perf}$	perfusion flow	500 mL/ min
$Q_{term}$	terminal flow	0.125 mL/ min
$N_{term}$	number of terminals	4000
$\mu$	viscosity of blood	3.6 cp
$\gamma$	Murray bifurcation exponent	3

Table 1: Global model parameters

The physiological parameters are set following table 1:

The pressures at distal end of terminal segments,  $P_{term}$ , are equal and correspond to the inflow pressure to the micro-circulation.

The terminal flows  $Q_{term,j}$  are equal, and delivered into the micro-circulation against  $P_{term}$ . Because of flow conservation, the  $Q_{term,j}$  sum corresponds to the perfusion flow at the root  $Q_{perf}$ .

The laminar flow resistance of the whole tree induces a given total  $Q_{perf}$  across the overall pressure drop  $\Delta P$ .

The produced tree is binary and its total number of segments is calculated from:

$$N_{tot} = 2N_{term} - 1 \quad (3)$$

This tree is subjected to Murray's law, with a power coefficient equal to 3.

## 1.2 Initialization step

Inputs:

- convex perfusion surface ( $A_{perf}$ ) or volume ( $V_{perf}$ ) definition: position and shape. In our case we work within simple shapes: circular or spherical shape.
- number of terminal segments,  $N_{term}$
- location of the root (in our case on the border of the perfusion territory)
- a random location inside the perfusion territory for the end of the first segment

From these inputs we estimate the average perfusion territory of each terminal segment when reaching the goal  $N_{term}$ , named "micro-circulatory black-box" [3]. We calculate  $r_{supp}$ , the average radius of the black-boxes:

$$\pi r_{supp}^2 = A_{perf} / N_{term} \quad (4)$$

Before adding a segment, the perfusion territory area is incremented of one micro-circulatory black-box. So, calling  $k_{term}$  the number of terminal segments at the current step of the algorithm, we obtain after the inflation the perfusion territory area  $A_k$ :

$$A_k = (k_{term} + 1)\pi r_{supp}^2 \quad (5)$$

The segments are stretched correspondingly to this inflation. First their new lengths are calculated, then each segment radius is rescaled in order to adapt the new tree resistance. Note that, as Schreiner does, we do not recalculate segment positions after tree stretching but compute a conversion to the  $k_{world}$  via a scaling factor relating to  $r_{supp}$ , thus  $A_k$ . Considering the radius of the final territory  $r_f$

$$r_f = \sqrt{\frac{A_{perf}}{\pi}} \quad (6)$$

And considering the radius of territory of current step  $r_k$ :

$$r_k = \sqrt{\frac{A_k}{\pi}} \quad (7)$$

We define the length factor  $lf$  as the ratio :

$$lf = \frac{r_k}{r_f} \quad (8)$$

This ratio can actually be simplified to:

$$lf = \sqrt{\frac{k_{term} + 1}{n_{term}}} \quad (9)$$

Respectively in 3 dimension we obtain a length factor:

$$lf = \sqrt[3]{\frac{k_{term} + 1}{n_{term}}} \quad (10)$$

The tree is adjusted to the inflated world before starting the loop to add a new segment.

In a similar fashion, knowing the flow at terminal segments  $Q_{term}$ , we will increase the perfusion flow with each during the loop to add a new segment, calculating as:

$$Q_{pk} = k_{term}Q_{term} \quad (11)$$

### 1.3 Loop to add new segment

We are provided a new location,  $n_{loc}$ , and want to find its optimal connection to the existing tree. For this purpose we select the  $N_{con}$  closest existing segments to this location, test their optimal connection to the new location, and store the total tree volume resulting of it. Then, as a global optimization process, we select the neighbor connection best minimizing the total tree volume.

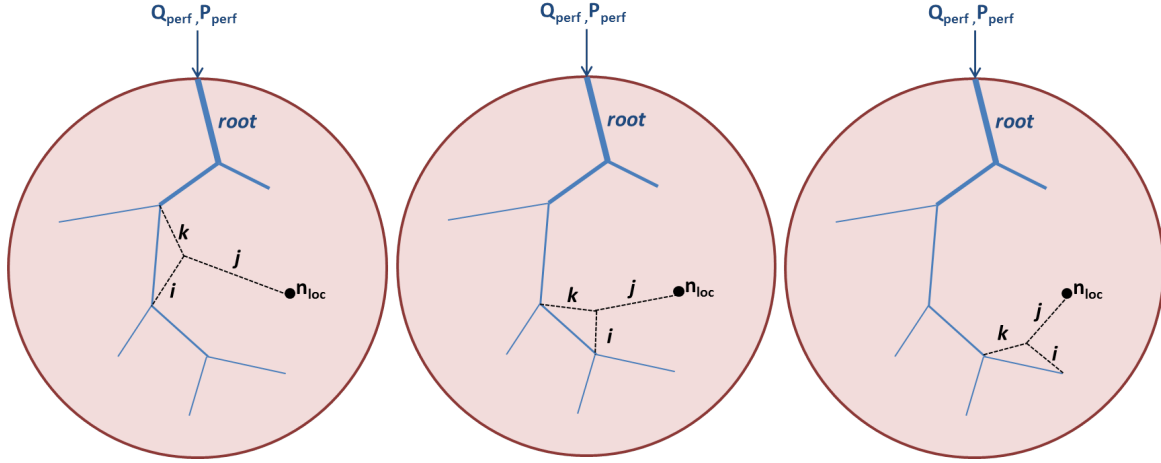


Figure 3: To add a new segment: test connection with neighbors of the new location  $n_{loc}$

### 1.3.1 Constrained new location $n_{loc}$

A random position is picked, that has to fulfill two constraints: belonging to the perfusion territory and respecting a distance criterion. This criterion is defined based on the final and current size of the tree. In 2D, it is given by the following equation:

$$d_{thresh} = (\pi r_{supp}^2 / k_{term})^{\frac{1}{2}} \quad (12)$$

with  $r_{supp}$  calculated from equation (4).

In 3D this criterion is defined as:

$$d_{thresh} = (\frac{4}{3} \pi r_{supp}^3 / k_{term})^{\frac{1}{3}} \quad (13)$$

with

$$\frac{4}{3} \pi r_{supp}^3 = V_{perf} / N_{term} \quad (14)$$

This distance criterion is updated after each new segment is added, so that it decreases during tree growth. If no location is found (after  $max\_trial = 1000$ ) that respects this distance to existing segments within the perfusion territory, then the distance criterion is multiplied by 0.9 and the process repeated until a new position is found that fulfills both constraints.

### 1.3.2 Test connection

The connection test corresponds to a single bifurcation optimization while taking into account its impact on the whole tree.

Kamiya proposes a single bifurcation optimization by an iterative procedure [2], which is fully detailed in section 2. At each of Kamiya's iteration, we are provided a bifurcation point location and radii of the concerned segments.

1. We control that the resulting segments are not degenerate, which means all three segments of the new bifurcations respect the following constraint between length and radius:  $2r_i \leq l_i$ . If they do degenerate we consider this bifurcation non plausible, skip it, and go to testing another neighbor segment.
2. We assess and apply the consequence of this connection on the whole tree before measuring the total tree volume. This process is detailed in sections 1.3.3 and 1.3.4.
3. We calculate the total tree volume gradient (relative to the previous result of Kamiya iteration). Along Kamiya's iterations, the total tree volume is expected to converge to a local minimum. The convergence is determined with a tolerance empirically fixed (in our case  $tolerance = 0.01$ ).

If the convergence is reached, we apply an additional checks: we control that none of the three resulting segments overlap any other existing tree segment. The bifurcation location, segments radii, and total tree volume at convergence are stored to be later compared with other connections.

If the convergence has not been reached yet, we set the current radii and point location as a new starting point for Kamiya's optimization search.

### 1.3.3 Propagate new bifurcation impact on the whole tree

By adding a new terminal segment, generating a new bifurcation, we perturb the distribution of segmental flows. In order to reestablish the correct terminal flows, the hydrodynamic resistance of the tree must be adjusted. As the lengths of the segments as well as the terminal and perfusion pressures are fixed, this can only be accomplished by proper rescaling of the segment's radii.

If we define the reduced hydrodynamic resistance  $R^*$  as  $R_i^* = R_i r_i^4$  we can calculate the reduced hydrodynamic resistance of a segment including its left and right subtrees by recursively traversing the subtrees:

$$R_{sub,j}^* = \frac{8\mu}{\pi} l_j + \left( \frac{(r_{left,j}/r_j)^4}{R_{left,j}^*} + \frac{(r_{right,j}/r_j)^4}{R_{right,j}^*} \right)^{-1} \quad (15)$$

Considering the equations (2) and (1), we can calculate the radius ratio of two children segments from resistance and flow:

$$\frac{r_i}{r_j} = \left( \frac{Q_i R_{sub,i}^*}{Q_j R_{sub,j}^*} \right)^{\frac{1}{4}} \quad (16)$$

with  $Q_i$  and  $Q_j$  the respective flow of sibling segments  $i$  and  $j$ .

Instead of storing the absolute radius for each segment, we consider the ratio between parent and its children:  $\beta_k^i = r_i/r_k$  and  $\beta_k^j = r_j/r_k$  with  $i$  and  $j$  the children,  $k$  the parent segment. Since the tree respects Murray's law, these ratios can actually be calculated directly from the ratio between children segments (see appendix A for details):

$$\beta_k^i = \left( 1 + \left( \frac{r_i}{r_j} \right)^{-\gamma} \right)^{-\frac{1}{\gamma}} \quad \text{and} \quad \beta_k^j = \left( 1 + \left( \frac{r_i}{r_j} \right)^{\gamma} \right)^{-\frac{1}{\gamma}} \quad (17)$$

Calculating the reduced resistance for each children with (15), and knowing the flow, we obtain the children radius ratio from (16), which is used to calculate the  $\beta$  values, stored with the parent segment properties. The subtrees distal to the new bifurcation remain constant and unaffected by the addition of the new branch, whereas upstream bifurcations are updated following this exact same process. By this method, called "balancing of bifurcation ratios", radius rescaling is propagated up the tree.

### 1.3.4 Measure target function

Calculate the root radius from

$$r_{root} = \left( R_{sub,root}^* \frac{Q_{pk}}{P_{perf} - P_{term}} \right)^{\frac{1}{4}} \quad (18)$$

Then for each segment we obtain the radius from:

$$r_i = r_{root} \prod_{k=i}^{root} \beta_k \quad (19)$$

So we can calculate the total tree volume. This is the target function that we seek to minimize:

$$T_i = l_i^\mu r_i^\lambda \quad (20)$$

### 1.3.5 Select best connection between neighbors

We store the target function result in the Connection Evaluation Table (CET), for each of the tested neighbor connection. The connection yielding the lowest total tree volume is considered as the optimal one and added to the tree, updating flows and resistances.

If the CET does not contain at least two plausible connections among the  $N_{con} = 20$  neighbors tested, then we extend the search to the  $N_{max} = 40$  neighbor segments. If at least two plausible connections still do not come out of this process, we reject the tested location  $n_{loc}$  and start again the main loop to add a new segment with a new random location. By plausible connection we mean the local optimization converges, with no degenerate segment and no crossing of any other tree segment.

## 1.4 Example of results and comparison

When comparing image results of our simulated 4000  $N_{term}$  tree, figure 4, with Schreiner's results [3], see figure 5, it seems we do not obtain the same radii.

Actually, this visual difference might be due to their visualization tool resolution, that could be limited. Such assumption seems coherent when comparing the measured radii on 250  $N_{term}$  tree along bifurcation levels, cf figure 6.

Schreiner computed these 10 tree models with a Murray coefficient  $\gamma = 2.55$ . In figure 6 right, we provide the same study with different gamma values. Our curve for  $\gamma = 2.55$  is pretty similar to Schreiner result, except that the slope is slightly steeper at the beginning. Also, our mean diameter tends to 0.5mm when reaching the 35th bifurcation level.

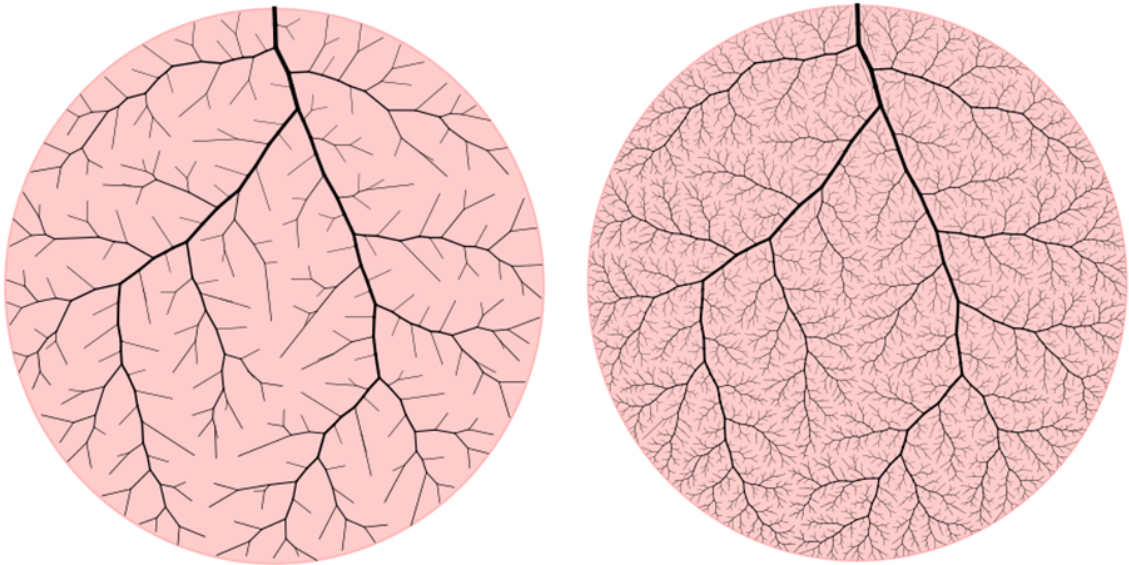


Figure 4: Output of CCO in 2D with different  $N_{Term}$ . (left) A  $250N_{term}$  tree generated in 9 min. Note: The terminal pressure is adapted to the number of terminal segments,  $P_{term}=63$  mmHg. (right) A  $4000N_{term}$  tree generated in 33 hours.

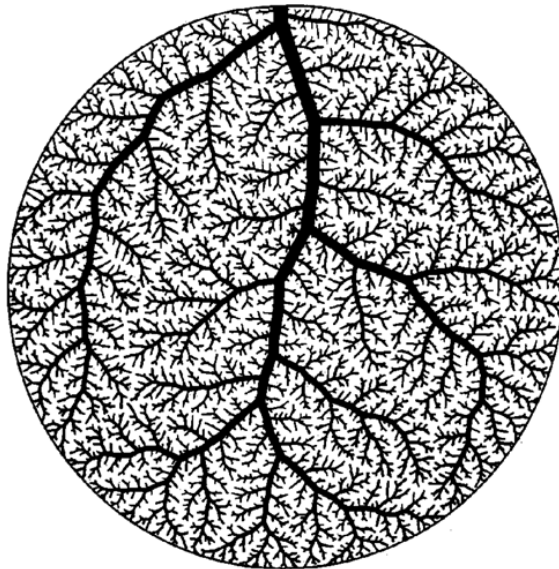


Figure 5: Fig 3 from Schreiner [3] :  $4000N_{term}$  tree.

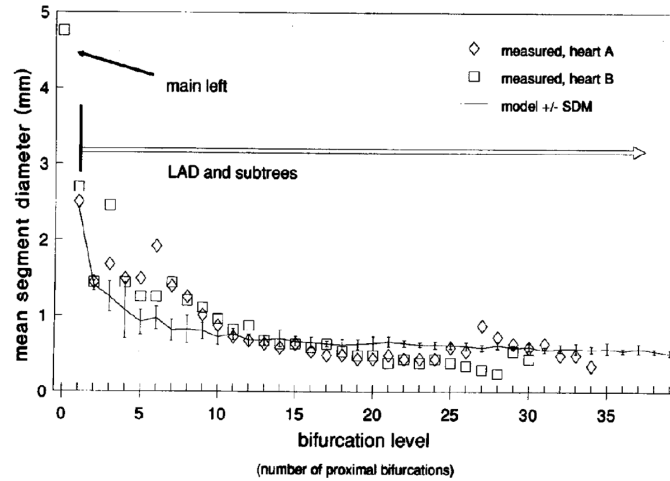


Fig. 4. Morphometric comparison between model and the left coronary artery trees of two humans. Vertical axis: averaged segment diameter. Horizontal axis: bifurcation level (= number of proximal bifurcations). Measurements from corrosion casts (1) of the left coronary circulation of two human hearts (symbols  $\diamond$  and  $\square$ ). Model simulations with 250 terminal branches (499 in total) refer to the LAD (or LCX) bed only and hence start at level 1 (polygon curve). Vertical bars represent standard deviations of means obtained from 10 model replicates with identical parameters (Table I), using different pseudo-random numbers, however. Computation time about 15 min per run.

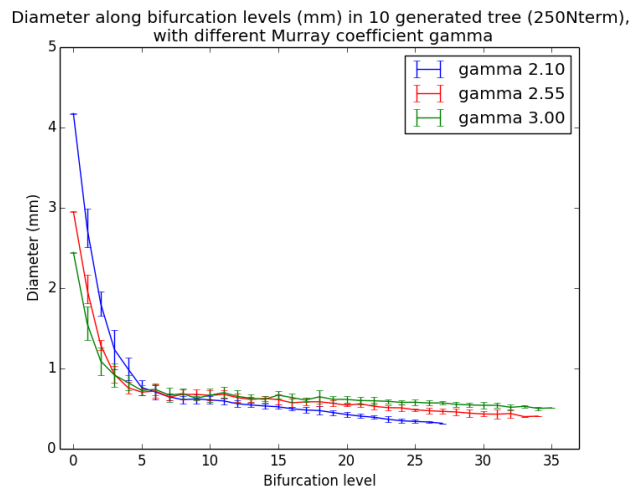


Figure 6: Radius study along bifurcation levels: mean and standard deviation at each bifurcation level on 10 simulated trees. Top: result from Schreiner [3], including simulated model and measured radii on anatomical data, computed with  $\gamma = 2.55$ . Bottom: our result comparing  $\gamma$  values: 2.1, 2.55 and 3.0.

If we compare our 2D CCO radii distribution with Karch results (computed in 3D), in figure 7 we have similar mean variations, in particular the slope steepness along the first bifurcation levels.

The algorithm we implemented might not be exactly the same as Karch and Schreiner, due to internal parameters that were not detailed in their work, such as:

- *d\_tresh* adaptation: we decrease *d\_tresh* of 10% after 1000 unsuccessful iterations to get a new location inside perfusion territory far enough from existing segments. There are no precision, neither in Schreiner nor Karch work about this boundary.
- convergence boundary: we consider reaching convergence when total tree volume gradient between iterations is below  $0.01 \text{ mm}^3$ , and should be reached before 100 Kamiya's iterations.

Nonetheless, by comparing results, visually and quantitatively (radii study), we can assume we produced a similar CCO implementation.

## 2 Local optimization: single bifurcation scale

Kamiya proposes a numerical solution to determine minimum volume bifurcation under restriction of physiological parameters, determinant pressure and flow, and locations of origin and terminals.

This method assumes the flow to be laminar and vessels are composed of straight ducts. In 2D the vessels are lying on a plane, whereas they are contained in a volume for the 3D implementation.

Note: Karch found that the optimum positions of the bifurcations in their 3D model trees were always found to lie in the plane defined by the endpoints of the respective three neighboring segments, which is consistent with the literature [4].

### Process: iterative nested loops

Defining a starting position as the convex average of origin and terminal locations, weighted by respective flows.

$$(x, y) = \left( \frac{f_0 x_0 + f_1 x_1 + f_2 x_2}{2f_0}, \frac{f_0 y_0 + f_1 y_1 + f_2 y_2}{2f_0} \right) \quad (21)$$

Calculate each segment length.

$$l_i^2 = (x - x_i)^2 + (y - y_i)^2 \quad (22)$$

Numerically calculate the new radii  $r_0, r_1, r_2$ . They are expected to satisfy both Hagen-Poiseuille's law and volume minimization.

When location of origin and two terminals segments, their pressure, and their flows are given, according to Hagen - Poiseuille's law:

$$\Delta P_1 = P_1 - P_0 = \kappa \left( \frac{f_0 l_0}{r_0^4} + \frac{f_1 l_1}{r_1^4} \right), \quad (23)$$

$$\Delta P_2 = P_2 - P_0 = \kappa \left( \frac{f_0 l_0}{r_0^4} + \frac{f_2 l_2}{r_2^4} \right) \quad (24)$$

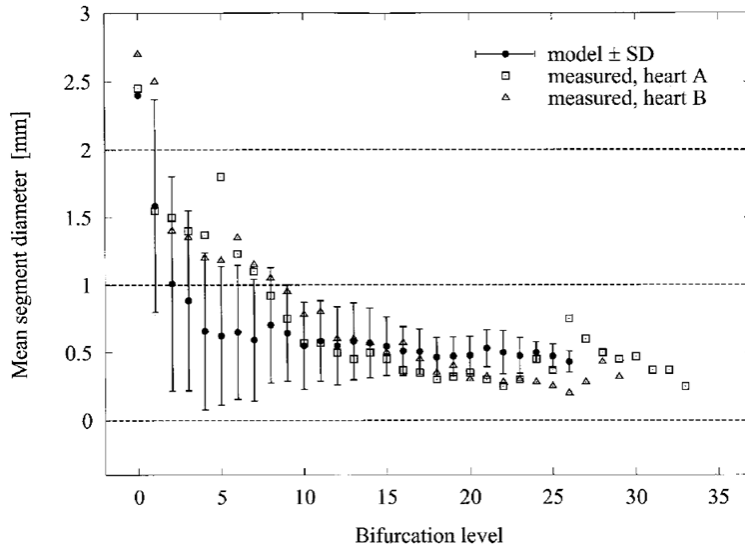


Fig. 6. Averaged segment diameters at respective bifurcation levels. Solid circles indicate the mean diameters of all vessel segments at a certain bifurcation level (defined as the number of proximal bifurcations). These data points were calculated from a CCO model tree with 250 terminal segments (499 segments in total) and with  $p_{term}$  set to 72 mm Hg. The remaining simulation parameters were identical to those used for Fig. 5 (cf. Table 1). Vertical bars represent standard deviations (S.D.) from the mean diameter values. Open squares and triangles denote measurements from corrosion casts of the coronary networks of two human hearts [39].

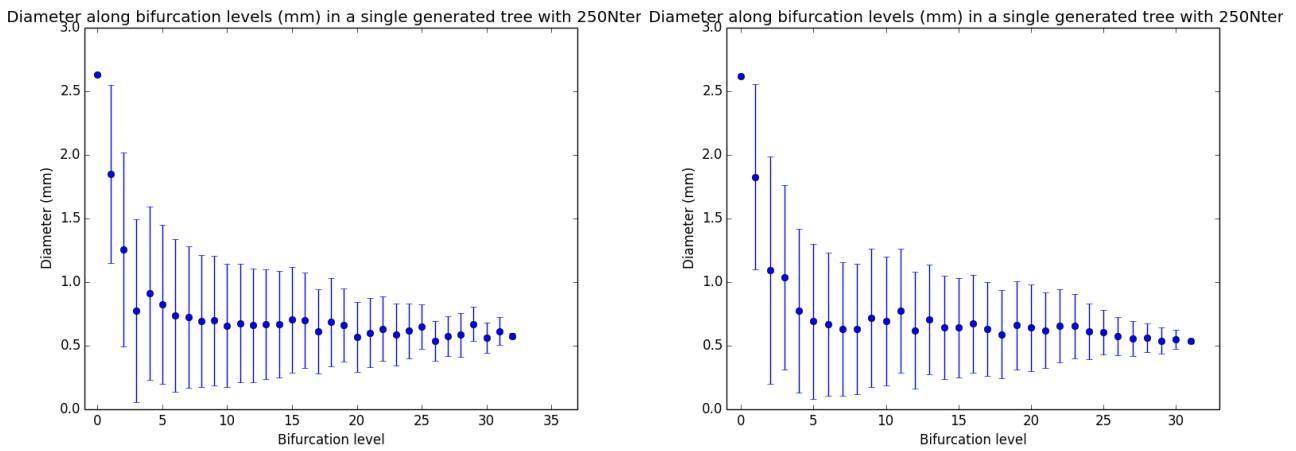


Figure 7: Radius study along bifurcation levels: mean and standard deviation at each bifurcation level on 1 single simulated 250Nterm tree. Top: result from Karch on 3D CCO [1], including simulated model and measured radii on anatomical data, computed with  $\gamma = 3.0$ . Bottom: our result computed on two trees from 2D CCO, with same  $\gamma$  value.

Differentiating the tree volume with  $x$ ,  $y$  and  $r_0$  and equating them to zero, Kamiya obtains:

$$\frac{r_0^6}{f_0} = \frac{r_1^6}{f_1} + \frac{r_2^6}{f_2} \quad (25)$$

and

$$x = \frac{x_0 r_0^2 / l_0 + x_1 r_1^2 / l_1 + x_2 r_2^2 / l_2}{r_0^2 / l_0 + r_1^2 / l_1 + r_2^2 / l_2}, y = \frac{y_0 r_0^2 / l_0 + y_1 r_1^2 / l_1 + y_2 r_2^2 / l_2}{r_0^2 / l_0 + r_1^2 / l_1 + r_2^2 / l_2} \quad (26)$$

The details to get these equations is provided in appendix B.

Using  $R = r^2$  in (25), we can express  $R_0$  as:

$$R_0^3 = f_0 \left( \frac{R_1^3}{f_1} + \frac{R_2^3}{f_2} \right) \quad (27)$$

Substituting this inside (24), one obtains the non linear system:

$$\begin{cases} \frac{\Delta P_1}{\kappa} R_1^2 \left( f_0 \left( \frac{R_1^3}{f_1} + \frac{R_2^3}{f_2} \right) \right)^{\frac{2}{3}} - f_0 l_0 R_1^2 - f_1 l_1 \left( f_0 \left( \frac{R_1^3}{f_1} + \frac{R_2^3}{f_2} \right) \right)^{\frac{2}{3}} = 0 \\ \frac{\Delta P_2}{\kappa} R_2^2 \left( f_0 \left( \frac{R_1^3}{f_1} + \frac{R_2^3}{f_2} \right) \right)^{\frac{2}{3}} - f_0 l_0 R_2^2 - f_2 l_2 \left( f_0 \left( \frac{R_1^3}{f_1} + \frac{R_2^3}{f_2} \right) \right)^{\frac{2}{3}} = 0 \end{cases} \quad (28)$$

We are looking for the root satisfying these equations using a non linear solver. If the solution converges, we get the new radii, that are needed to calculate the new position of the branching point in (26). This locations is a new input for the loop to iterate again (calculating length (22), then new radii (28), new location (26) and so on). If this iterative loop converges and the bifurcation total volume decreases, the equation system is solved and provides optimal radii and position for the bifurcation.

Note: in CCO the pressure is not determined all along vessels (only at the root and terminal segments). In order to adapt to our situation, we use an estimated radius to calculate the pressure drops using (24). At the first iteration the estimated radii are all equal to the segment's radius on which is connected the branch:  $r_0 = r_1 = r_2 = r_{ori}$ . Then, we will use the previously calculated radii to update the pressure drops at each iteration.

## Example of results

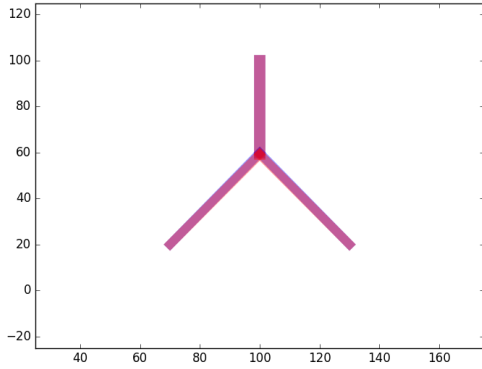
We give examples of results on different type of bifurcations. For these examples we used a tolerance of 0.01 and maximum number of iteration of 100.

In the figure 8 (a), for symetric flows and child locations: the optimal bifurcation point corresponds to the convex average.

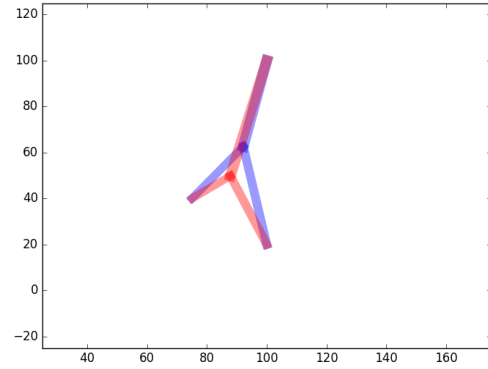
The figure 8 (b) illustrates well a Steiner solution to optimal network [5]: it is more advantageous to transport flows together by delaying bifurcation. In fluid mechanics context, this subadditivity follows from Poiseuille's law, according to which the resistance of a tube increases when it gets thinner.

The figure 8 (c) shows influence of blood demand on the bifurcation geometry: because flow is more important on the right child, the radius is bigger and the bifurcation is dragged toward this child. Also, we note that the bifurcation is less delayed than for symmetrical flows.

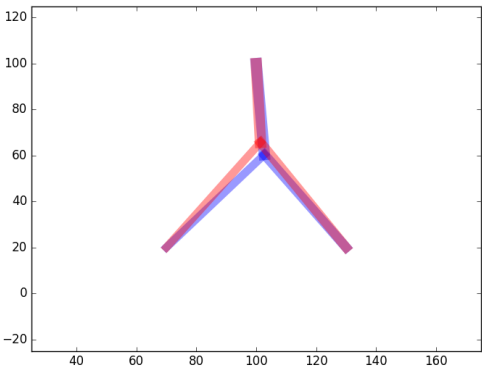
The figure 8 (d) shows the influence of both destination and demand.



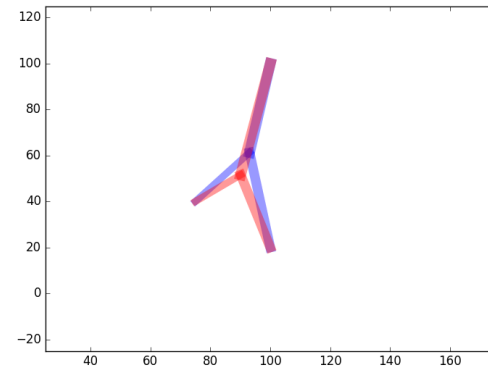
(a)  $Q_l = Q_r = \frac{1}{2}Q_p$



(b) Random child locations and  $Q_l = Q_r = \frac{1}{2}Q_p$



(c)  $Q_l = \frac{1}{4}Q_p$  and  $Q_r = \frac{3}{4}Q_p$



(d) Random child locations and  $Q_l = \frac{1}{4}Q_p$ ,  $Q_r = \frac{3}{4}Q_p$

Figure 8: In blue the starting bifurcation (convex average position), in red the final bifurcation after Kamiya's algorithm reached convergence (tolerance = 0.01). Convergence was reached at 15th, 24th, 31st and 21st iteration respectively in (a),(b),(c),(d).  $Q_p$  is the flow in parent branch,  $Q_l$  and  $Q_r$  are flows in left and right children.

### Karch implementation

Karch added lower and upper bounds to Kamiya's algorithm that ensures: (1) the bifurcation position within the perfusion volume; (2) the non degeneracy of the bifurcation (by constraining segment length over segment diameter).

## Conclusion

We implemented this CCO method with the same  $N_{con}$  and  $N_{max}$  as Karch (respectively 20 and 40). The 2D procedure is a good start for debugging, visualizing the results and should be easily convertible into 3D CCO.

We improved computation time by parallelizing the connection test of neighbor segments.

# Appendices

## A Equation (25), from Kamiya & Togawa 1972 equation (6)

Kamiya uses Murray definition at equation (7) from Physiological principle of minimum work [6] that he calls the simplest requirement for efficiency in the circulation:

$$f = kr^3$$

with  $k$  being a constant, so that the flow of blood past any section shall everywhere bear the same relation to the cube of the radius of the vessel at that point. Using it as:

$$r_i^3 = \frac{r_i^6 k}{f_i}$$

and combining it this with Murray's law,

$$r_0^\gamma = r_1^\gamma + r_2^\gamma \text{ with } \gamma = 3$$

where  $r_0$  is the parent radius,  $r_1$  and  $r_2$  are the children radii, one obtains:

$$\frac{kr_0^6}{f_0} = \frac{kr_1^6}{f_1} + \frac{kr_2^6}{f_2}$$

that can be simplified into equation (25).

## B Equation (26), from Kamiya & Togawa 1972 equation (7)

We have

$$V = \pi(r_0^2 l_0 + r_1^2 l_1 + r_2^2 l_2)$$

and

$$l_0^2 = (x - x_0)^2 + (y - y_0)^2$$

$$l_1^2 = (x - x_1)^2 + (y - y_1)^2$$

$$l_2^2 = (x - x_2)^2 + (y - y_2)^2$$

We rewrite (B)

$$V = \pi(r_0^2 \sqrt{(x - x_0)^2 + (y - y_0)^2} + r_1^2 \sqrt{(x - x_1)^2 + (y - y_1)^2} + r_2^2 \sqrt{(x - x_2)^2 + (y - y_2)^2})$$

We derive each term with respect to  $x$ .

$$\frac{\partial}{\partial x} \sqrt{(x - x_0)^2 + (y - y_0)^2} = \frac{x - x_0}{\sqrt{(x - x_0)^2 + (y - y_0)^2}} = \frac{x - x_0}{l_0},$$

same for the  $x_1$  and  $x_2$  term, so we have

$$\frac{\partial V}{\partial x} = \pi \left[ \frac{r_0^2(x - x_0)}{l_0} + \frac{r_1^2(x - x_1)}{l_1} + \frac{r_2^2(x - x_2)}{l_2} \right] = 0$$

Discarding the  $\pi$  factor and separating the terms,

$$\begin{aligned} x \frac{r_0^2}{l_0} + x \frac{r_1^2}{l_1} + x \frac{r_2^2}{l_2} &= x_0 \frac{r_0^2}{l_0} + x_1 \frac{r_1^2}{l_1} + x_2 \frac{r_2^2}{l_2} \\ x \left( \frac{r_0^2}{l_0} + \frac{r_1^2}{l_1} + \frac{r_2^2}{l_2} \right) &= x_0 \frac{r_0^2}{l_0} + x_1 \frac{r_1^2}{l_1} + x_2 \frac{r_2^2}{l_2} \end{aligned}$$

and thus

$$x = \frac{x_0 \frac{r_0^2}{l_0} + x_1 \frac{r_1^2}{l_1} + x_2 \frac{r_2^2}{l_2}}{\frac{r_0^2}{l_0} + \frac{r_1^2}{l_1} + \frac{r_2^2}{l_2}}$$

This is one half of Eq.(7) in Kamiya & Togawa. The other half is obtained by substituting  $x$  with  $y$  everywhere. This is formally correct but not 100% satisfying since the  $l_i$  depend on  $x$  and  $y$ .

## References

1. Rudolf Karch, Friederike Neumann, Martin Neumann, and Wolfgang Schreiner. A three-dimensional model for arterial tree representation, generated by constrained constructive optimization. *Computers in biology and medicine*, 29(1):19–38, 1999.
2. Akira Kamiya and Tatsuo Togawa. Optimal branching structure of the vascular tree. *The Bulletin of mathematical biophysics*, 34(4):431–438, 1972.
3. Wolfgang Schreiner and Peter Franz Buxbaum. Computer-optimization of vascular trees. *Biomedical Engineering, IEEE Transactions on*, 40(5):482–491, 1993.
4. M Zamir and H Chee. Branching characteristics of human coronary arteries. *Canadian journal of physiology and pharmacology*, 64(6):661–668, 1986.
5. Marc Bernot, Vicent Caselles, and Jean-Michel Morel. *Optimal transportation networks: models and theory*, volume 1955. Springer Science & Business Media, 2009.
6. Cecil D Murray. The physiological principle of minimum work i. the vascular system and the cost of blood volume. *Proceedings of the National Academy of Sciences*, 12(3):207–214, 1926.

## CONVERGENCE PROCESS

---

### CONTEXT

Inner growth cannot handle speed growth process due to 3D. Nevertheless we want to grow trees that converge to their prescribed flow  $q_{\text{presc}}^i$ , and reach the forest total flow  $Q_{\text{presc}}$  for a N tree forest.

$$Q_{\text{presc}} = \sum_N q_{\text{presc}}^i \quad (36)$$

This is not trivial since geometrical constraints prevent some of the  $F_N$  trees to deploy as much as required or even to get any new connection. We build a method that can compensate such issues and distribute  $Q_{\text{presc}}$  close to the prescribed tree values.

### ALGORITHM

The only action we can have on a tree during inner growth is to deactivate it. The deactivation excludes the tree from any new connection test. We cannot reactivate the tree after that, otherwise it will lead to chaos in forest growth. Then the question is when shall we deactivate the tree, knowing that not all of them can reach their prescribed flow? To answer this, we observe the forest growth at a tree scale every 500 iterations.

We call b all trees which did not have new connections within this period, they are considered as "blocked" trees.

We call d all trees that are deactivated at the current step. To be noted, the deactivated trees have not reached exactly their prescribed flow, but a bigger value called final flow  $q_f^i$ . We can deduce  $\Delta q^i$  which correspond to non available flow:

$$\Delta q^i = q_f^i - q_{\text{presc}}^i \quad (37)$$

Observing the blocked and deactivated trees we calculate the amount of flow that is "lost", e.g. won't be assigned if trees stay blocked, and should be redistributed on the rest of the forest:

$$Q_{\text{lost}} = \sum_{i \in b} (q_{\text{presc}}^i - q_k^i) - \sum_{i \in d} \Delta q_f^i \quad (38)$$

We apply a rule after each new connection k inside the forest:

We distribute the available flow  $Q_{\text{lost}}$  among all active and not blocked trees, proportionally to their relative prescribed flow. The value of  $p^i$  is calculated such as:

$$p^i = \alpha^i Q_{\text{lost}} \quad (39)$$

---

**if** tree is active and not blocked  $q_k^i \geq q_{\text{presc}}^i + p^i$  **then**  
 deactivate tree i  
**end if**

---

with

$$\alpha^i = \frac{q_{\text{presc}}^i}{Q_{\text{presc}} - \sum_{i \in d} q_{\text{presc}}^i - \sum_b q_{\text{presc}}^i} \quad (40)$$

Because we only apply the rule for activated non blocked trees we can verify that

$$\sum \alpha^i = 1 \quad (41)$$

Knowing that the number of trees that are activated and not blocked is  $F_{\text{an}}$ :

$$F_{\text{an}} = F_N - F_d - F_b \quad (42)$$

And consequently:

$$\sum_{i \in \text{an}} q_{\text{presc}}^i = \sum_{i \in N} q_{\text{presc}}^i - \sum_{i \in d} q_{\text{presc}}^i - \sum_{i \in b} q_{\text{presc}}^i \quad (43)$$

For the trees that are activated but blocked, we apply the simple rule:

---

**if** tree is active and blocked  $q_k^i \geq q_{\text{presc}}^i$  **then**  
 deactivate tree i  
**end if**

---

Final note: getting closer to the last iteration, we might find a negative  $Q_{\text{lost}}$  value. Since we do not want to take risk to deactivate all trees before reaching the last iteration, we set  $Q_{\text{lost}}$  to zero in this situation.

## MORPHOMETRY STUDY ON EPICARDIAL NETWORKS

---

We computed a morphometrical study of 1287 epicardial networks provided by HeartFlow, cf appendix [13](#). We observed significantly longer element in human than in pig (data from [\[59\]](#)), see the figure below [60](#) extracted from the morphometry study.

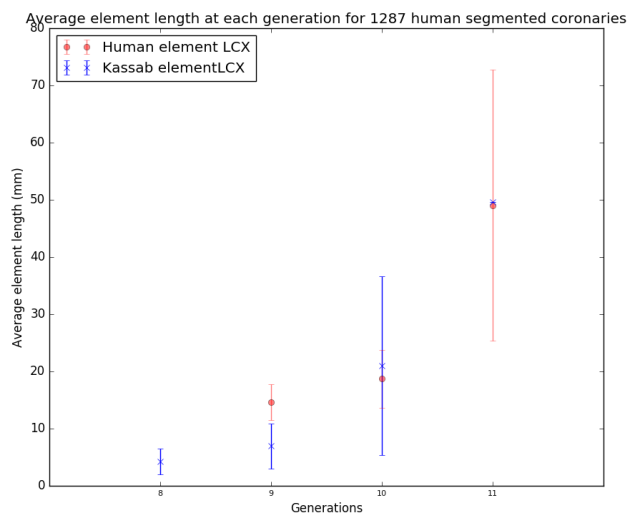
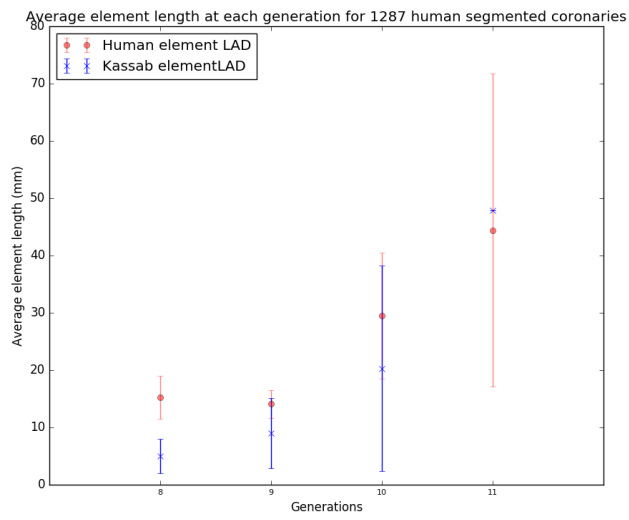
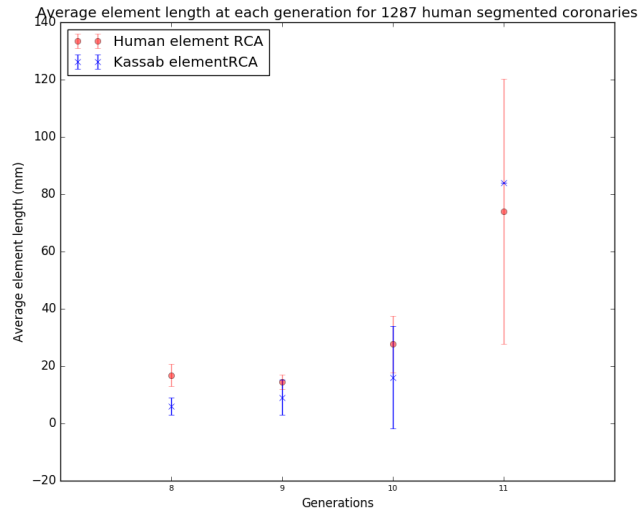


Figure 60 – Element length study per label on 1287 epicardial networks.

## MORPHOMETRY STUDY OF EPICARDIAL CORONARIES

---

# Report

## Epicardial coronary morphometry study

CLARA JAQUET  
*ESIEE, HeartFlow*  
December 20, 2018

### Introduction

In the last few years HeartFlow has securely stored a large database of patient cardiac CT. We are interested in studying the segmented coronaries processed in the 1.4 workstation version. This processing provides aorta and vessel segmentation from ostium down to 0.5 mm diameter, but also a segmentation of left ventricle and its estimated mass.

We wonder if epicardial coronaries contains any specific pattern that could either help improve the segmentation process (detect missing branch) or the patient diagnostic (provide physio-pathological information). To this end we conduct a morphometry study of the patient epicardial coronary network.

### State of the art: coronary anatomy

Coronary anatomy has been mainly studied on animals (pigs [1], [2], [3], [4], [5] and dogs [6]). Because of ethical constraints few studies on human have been conducted ([7], [8], [9]), and always on small amount of post mortem data. The HeartFlow database is significant in size. We want to qualify and quantify the coronary network. What is the structure and function of the segmented vessels? To analyze it we need to classify the coronaries. Several methods have been used so far:

### Anatomical classification

Methods to assign each segment a generation, between ostium and capillary vessels:

- Weibel's method was applied on bronchial tree [10]. The trunk is assigned order 0, then it is extended as  $2^n$  branches of generation  $n$ .
- Strahler's system originally comes from geographical studies ([11], [12]): it has been used then for bronchial tree, pulmonary arteries and veins by Horsfield [13].
  - The first method defined corresponds to the reverse of Weibel's, which means the order is assigned starting from the leaves.

- In the second Strahler method, a constraint is added. If generation 3 meets generation 2, parent vessel remains generation 3 (instead of 4), so method handles asymmetry. Van Bavel used it to study area expansion ratio and bifurcation asymmetry of porcine coronaries. The observed distribution was used to simulate a synthetic tree, which show a constant bifurcation ratio, diameter ratio and length ratio from generation 2 to 8.
- A third method is called Diameter Defined Strahler Order (DD Strahler), and was created by Kassab [1]. It reproduces Strahler's system, but uses radii intervals to determine the generation. It defines 11 radius ranges, from generation 1, corresponding to pre-capillaries (about 10  $\mu\text{m}$ ) to generation 11, corresponding to largest epicardial coronaries (around 3 mm in diameter).

## Functional classification

Vascular networks have also been studied from a functional aspect.

- Murray explained the design of a vascular tree based on the principles of minimum work with a relationship between parent and daughters diameters at bifurcations [14]. This law was then generalized by Zhou among subtree and their feeding segment [15].
- The bifurcation diameters' distribution was also studied by Van Bavel [5] on cast data (diameter range 10 to 500  $\mu\text{m}$ ) to explain flow heterogeneity.
- Using a measure of the branching rate on cast data, Zamir classified coronaries according to their function : conveying vs delivering vessels [7].

The functional approach obviously tends to a more global scale, to the point of considering the relationship with the myocardium. For instance, the stem-crown structure defined by Zhou is shown by Van Horssen [16] to adapt to the layers of myocardium : endomyocardial territories have larger stem segment diameter compared with epicardial and mid-cardial territories. The crown distribution is also specific to the tissue layer because perfusion territories increase in size and decrease in number from epi to endocardium. Before this, many studies were conducted to relate myocardium mass [17], [18], [19] or volume [20], [21] to coronary diameter, length, or volume.

We studied anatomical and functional aspects of the coronary network.

## Method and results

### Implemented method

We want to quantify the network organization from an anatomical aspect. Because the segmentation is limited to epicardial coronaries over 0.5 mm diameter, we cannot use a method based on upstream assignment from capillary scale. Kassab's method provides diameter ranges that we can directly use to assign a generation to each vessel. Even though these scales come from pig measurements, human

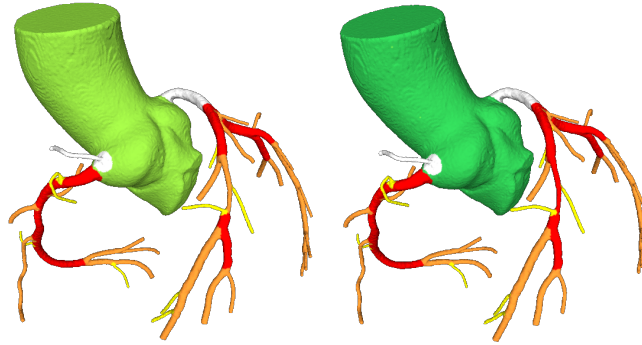


Figure 1: Generation assignment on coronary tree: order 11 (red vessels), 10 (orange vessels), 9 (yellow vessels). Left: assignment based on the DD Strahler system. Right: after detection of the diseased segment on LAD .

coronary diameters are expected closely conform to it.

We implement the automatic generation assignment defined by Kassab's diameter ranges and specific of to label (LCX, LAD, RCA). For each segment we calculate its median radius, using the maximally inscribed sphere value from the model statistics. According to this median radius and Kassab's morphometry table, we assign a generation number, see figure 1. The DD Strahler generation assignment enables us to obtain information regarding the network organization.

When recording each generation characteristics, we use two different definitions of an element.

The first one follows Kassab's morphometry method, with an element defined as a serie of segment belonging to the same generation. We will call this definition Kassab Element (KE). In the second method, an element is defined by one stem and multiple ends connected segments of same generation, which enables us to assemble segments of same diameter into a crown shape. This is supposed to preserve the functional unit of the network. We will call this definition Multiple End Element (MEE).

Because we work on potentially diseased vessels, we want to minimize the impact of pathology on our measures (either during the generation assignment, or in the studies). We used several methods to prevent the influence of pathology:

- Assuming that a segment of generation 11 (the largest) cannot arise from any smaller generation (10,9,...), we ensure the generation decrease at each bifurcation. We apply this for all generations. This induce corrections such as in figure 1.
- We detect diseased segments (stenosis, calcification, stent stored in artifacts properties) so we do not consider them in average diameter measurements.
- We exclude from all studies the main vessels (LAD/LCX/RCA) containing occlusions.

## Results of the two methods

The number of segment per element, and connectivity values are collected for generations 11 to 8, for each label on 1286 datasets (data A), which represent 56483 segments. The calculated average values are stored in the `ConnectivitySummary.json` files, and the connectivity matrix in a `ConnectivityMatrix.txt` files, provided for both methods in the zip archive. Looking first at the average number of segments per element (SE), we notice the porcine network contains a higher SE than the human one, see figure 2.

It also appears that we detect a generation 11 on the human LCX, whereas there is none on pigs. And, on the contrary, we do not detect any generation 8 on LCX, whereas Kassab does.

It is important to remember that Kassab epicardial studies, either from cast or CT measurement, were made on a small dataset (respectively 1 and 7 hearts). With our data, we are able to get more insights about coronary diversity, which seems wide, see figure 3.

As expected, the MEE definition shows element with a higher number of segment than the KE definition, at least for the biggest generations (11 and 10).

It is not surprising to find smaller connectivity values on humans for whom the SE value is smaller. That is the case for both KE and MEE definitions, see figure 4. The first one shows average values not too different from the pig's connectivity. And again, there is still a significant diversity among these see figure 5, presenting connectivity distribution for the 11th generation.

We can also notice that with MEE definition, the connectivity of the generation  $i$  with generation  $i$  corresponds to the number of segment per element minus one. The MEE definition has the advantage of including the size of the element into the connectivity matrix.

When looking at all these SE values and connectivity coefficients, and noticing such a diverse distribution, we wonder if there is a coherence among the generations or labels.

Tracking SE along generations for each case shows quite an heterogeneity, see figure 6. This could be induced by the global morphology of the patient, and we shall discuss this later in the biometric study.

Tracking cases based on their first connectivity coefficient (connectivity of generation 11th with 11th), we observe a relative homogeneity along generations: coronary trees with highly connected 11th generation will maintain it on the downstream generations (10th and 9th). This relationship is clearly seen with the MEE definition, see figure 8. It is difficult to show at generation 11 with the KE definition, because most of the first coefficients are equal to zero (so all quartile values are zero which does not allow us to differentiate subgroups). However the homogeneity clearly appears for the 10th generation, see figure 7. Note, the figures for each generation and each label are provided in the zip archive.

Tracking cases based on SE of a reference label to get their SE for another label, a relative homogeneity also appears, see figure 9.

Despite obvious coronary diversity among patients (as evidenced by SE analysis), the SE analysis shows an internal tree homogeneity between main arteries (labels). Our connectivity study proves an internal homogeneity of the tree within generations. We could assume these homogeneity properties

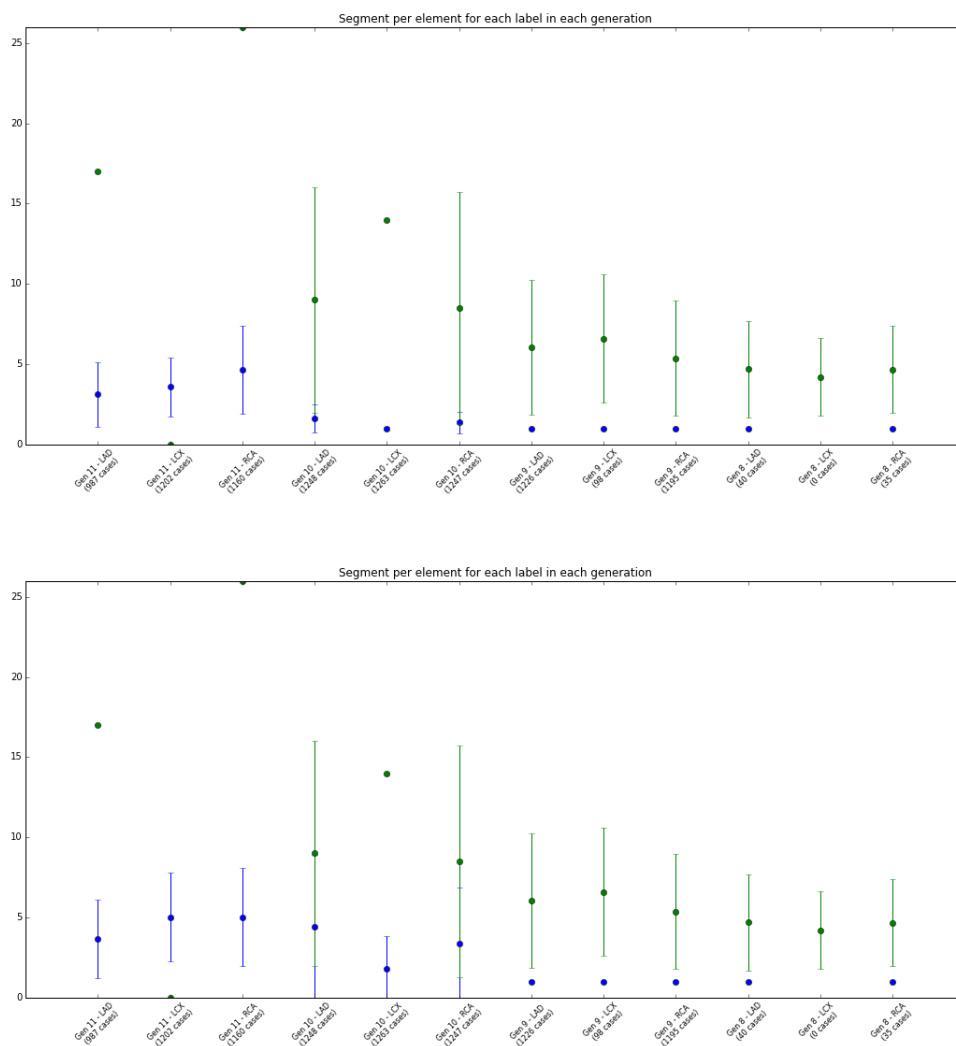


Figure 2: Average segments per element for each label at generations 11 to 8. In blue: measures on human coronary, in green Kassab's measures on pig coronaries. Top : KE definition, Bottom : MEE definition.

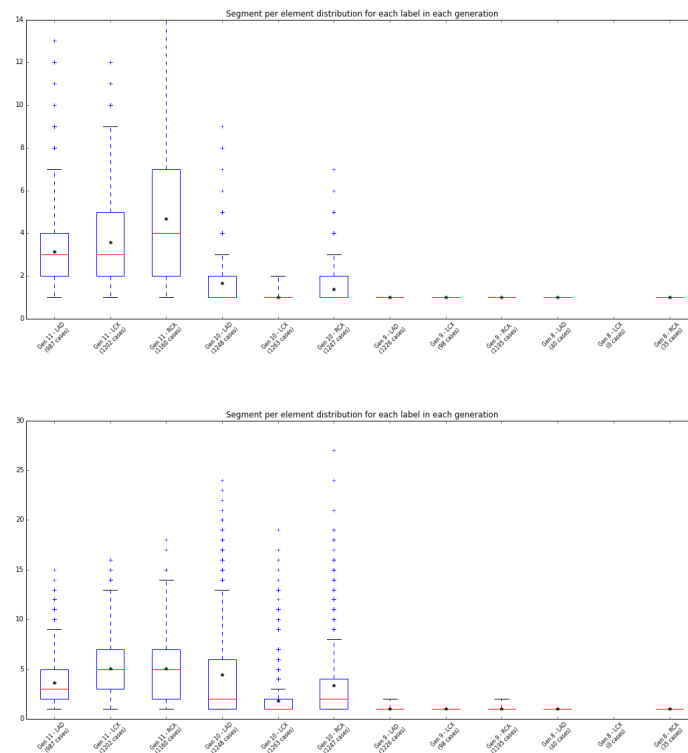


Figure 3: Boxplot representing SE distribution for generation 11 to 8 at each label. Top: KE definition, Bottom: MEE definition

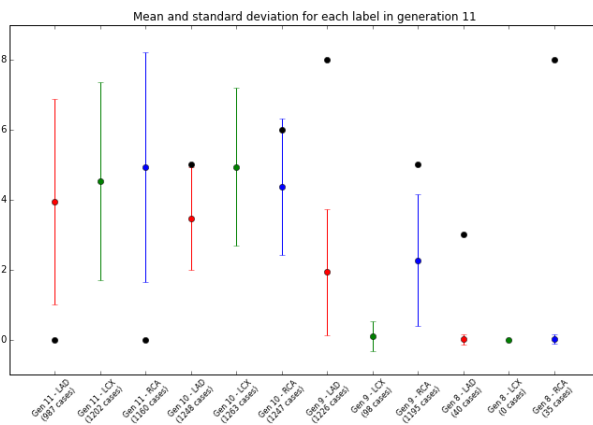
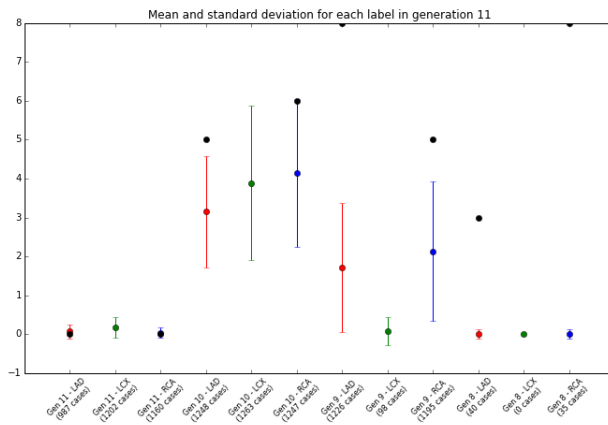
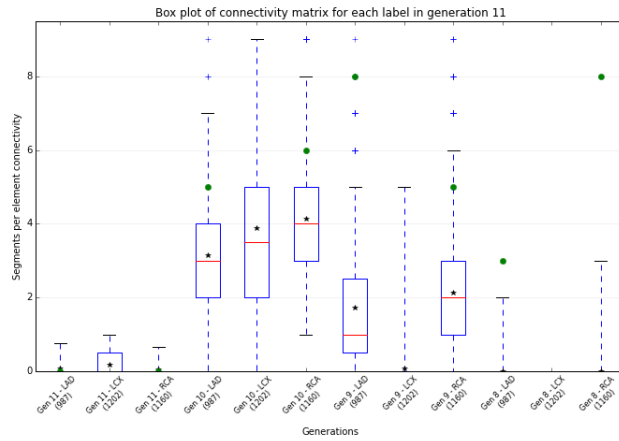
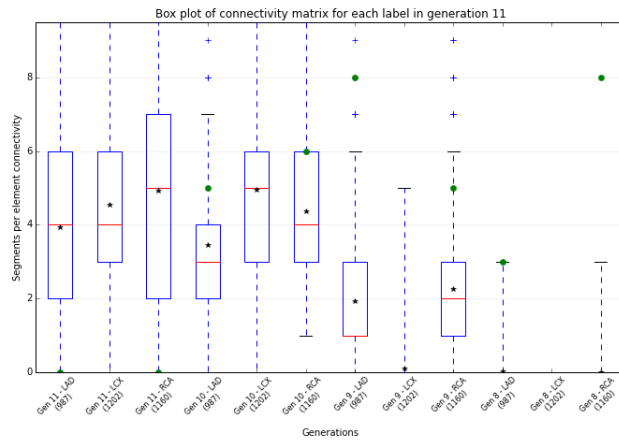


Figure 4: Average connectivity at generation 11 for each label. Top: KE definition, Bottom: MEE definition



○ Kassab's average value  
 \* Average value on human data



○ Kassab's average value  
 \* Average value on human data

Figure 5: Boxplot representing connectivity distribution for generation 11 for each label. Top: KE definition, Bottom: MEE definition

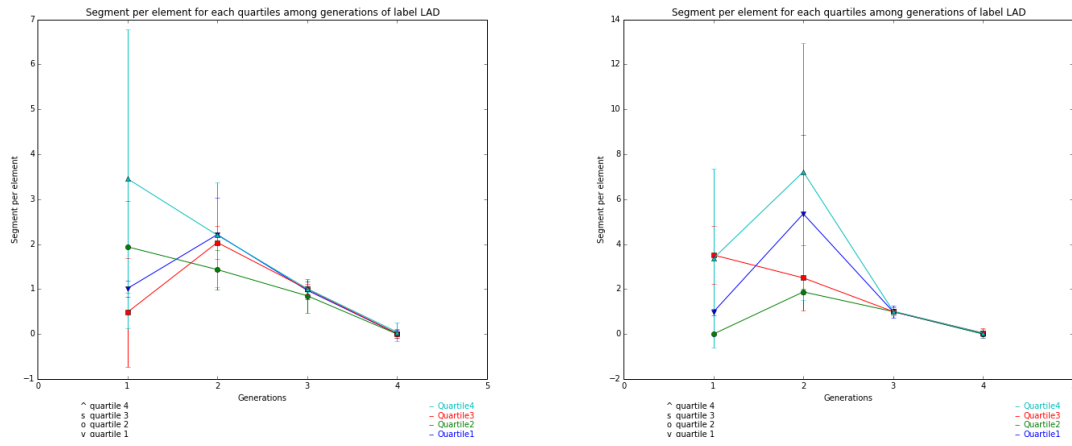


Figure 6: Tracking SE values of LAD based on generation 11, classified into quartiles. Left: KE definition, Right: MEE definition

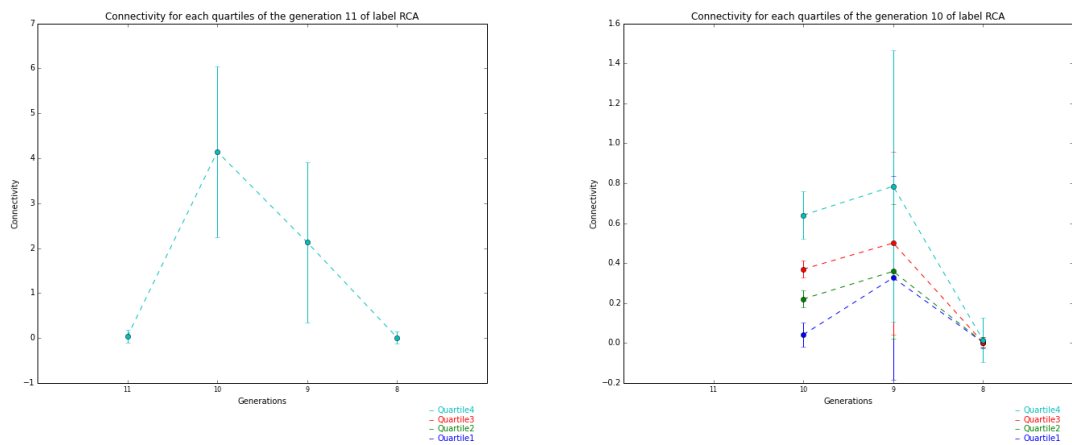


Figure 7: KE connectivity tracked for each case depending on the first connectivity coefficient of the generation, classified by quartiles.

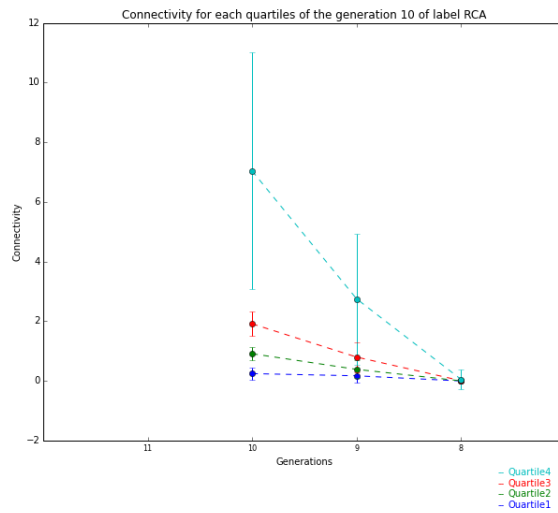
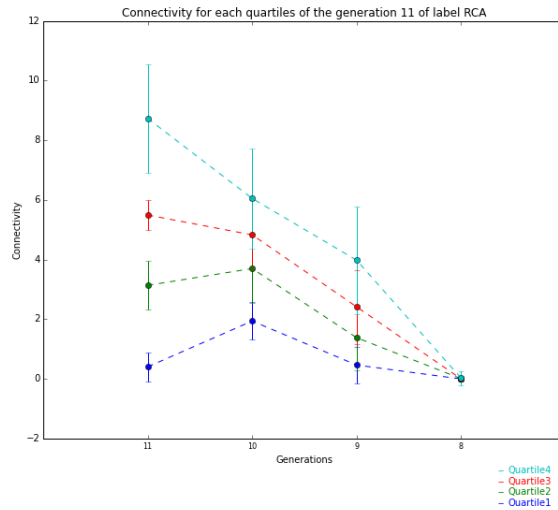


Figure 8: MEE connectivity tracked for each case depending on the first connectivity coefficient of the generation, classified by quartiles.

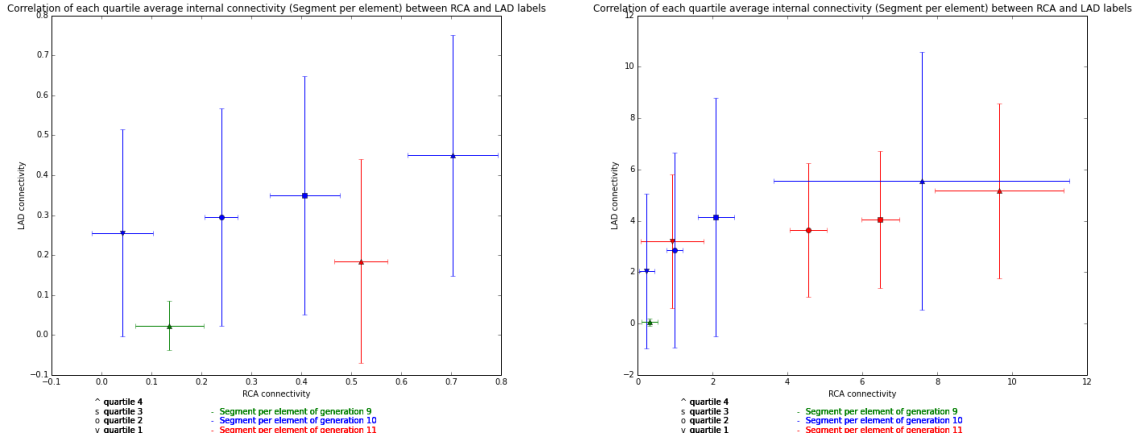


Figure 9: Connectivity tracked along cases based on reference label SE (horizontal axis). Top: KE definition, bottom: MEE definition

comes from optimal network design.

## Sub-studies

### Segment length

We measured the average segment length at each generation. Comparing with Kassab's results, see figure 10, we observe that the vessel length is specific to the species, but pretty homogeneous among generations. The human vessels are about three times as long as pigs. This is strongly related to the heart shape [22], which is more elongated for bipeds such as human because of gravity effect. Consequently the coronaries need to spread around a bigger surface, with longer segments.

### Murray's law

Murray's law is a formula relating the radii of daughter branches to parent branch, built on the hypothesis that the vascular system flow is achieved with the least possible biological work.

The two energy terms that contribute to the cost of maintaining blood flow in any section of any vessel are  $Pf$ , that overcomes the viscous drag, and  $Pm$ , that maintains blood volume (metabolic requirements for blood and vessel wall tissue). Both these terms are related to the radius in opposite way, and the sum of them is to be minimized. With the flow noted  $f$ , radius noted  $r$ , and  $k$  depending on both  $Pm$  and  $Pf$ , the equation is minimized by

$$f = kr^3 \quad (1)$$

If flow, viscosity and metabolism are constant along the vascular system then the sum of cubic radii

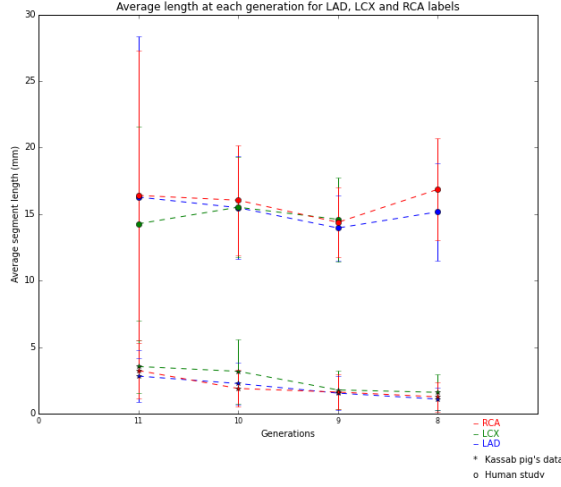


Figure 10: Average segment length for each label at each generation: comparison between pig (Kassab) and human (our data) results.

should be constant, and Murray establishes the relationship:

$$r_0^\gamma = r_1^\gamma + r_2^\gamma \text{ with } \gamma = 3 \quad (2)$$

This law is constructed for optimal situation, and in reality the gamma observed in coronaries varies between 2 and 3 [5], [15], [23].

We collected measurements on 929 datasets. For each parent and its children the intersection contour area is measured along the 2.5 mm closest to the centerline bifurcation point, but outside the bifurcation field defined by the model statistics.

We studied a total of 12892 bifurcations. For each of them we calculate the gap to Murray's law,  $\epsilon$ , defined as:

$$\epsilon^\gamma = r_0^\gamma - r_1^\gamma + r_2^\gamma \quad (3)$$

We test gamma values in the range 0.5-3.5, and plot the number of bifurcations along the measured  $\epsilon$  see figure 11.

When decreasing the gamma value, the error epsilon shifts from high to small values, but the cumulated error among all bifurcation (measured by the weighted area) find a local minimum around  $\gamma=1.5$ . Because this value is far from those of the literature (between 2 and 3), we visualized the relationship between parent radius and  $\epsilon$  values, see figure 12. Murray's law doesn't hold along the whole radius range. It seems to hold better for small radii, under 0.8mm. For this reason, we conducted the same study on these small parent radius bifurcations, a total of 1294 segments. The minimal  $\epsilon$  is found with a  $\gamma = 1.9$ , see figure 13, which matches the literature slightly better.

Taking a more distant look at the bifurcations to visualize their diversity, we clearly observe bifurcation asymmetry, see figures 14. This one is quantified by the asymmetry factor defined as :

$$AF = r_1/r_2 \text{ with } r_1 < r_2 \quad (4)$$

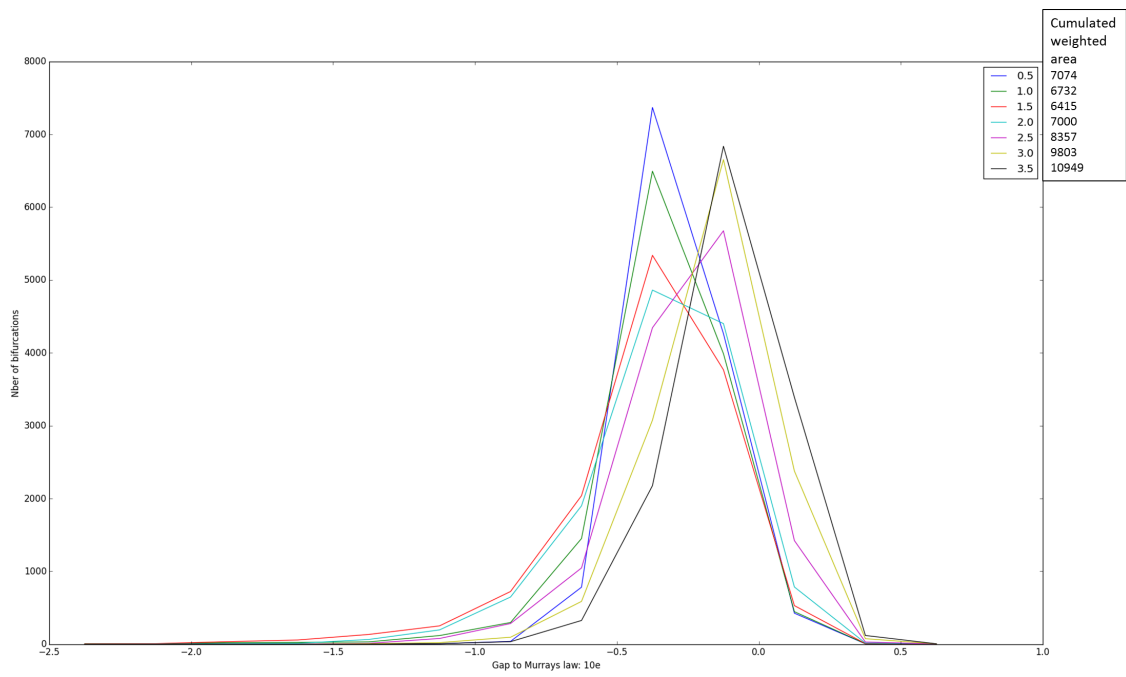


Figure 11:  $\epsilon$  distribution for  $\gamma$  value from 0.5 to 3.5

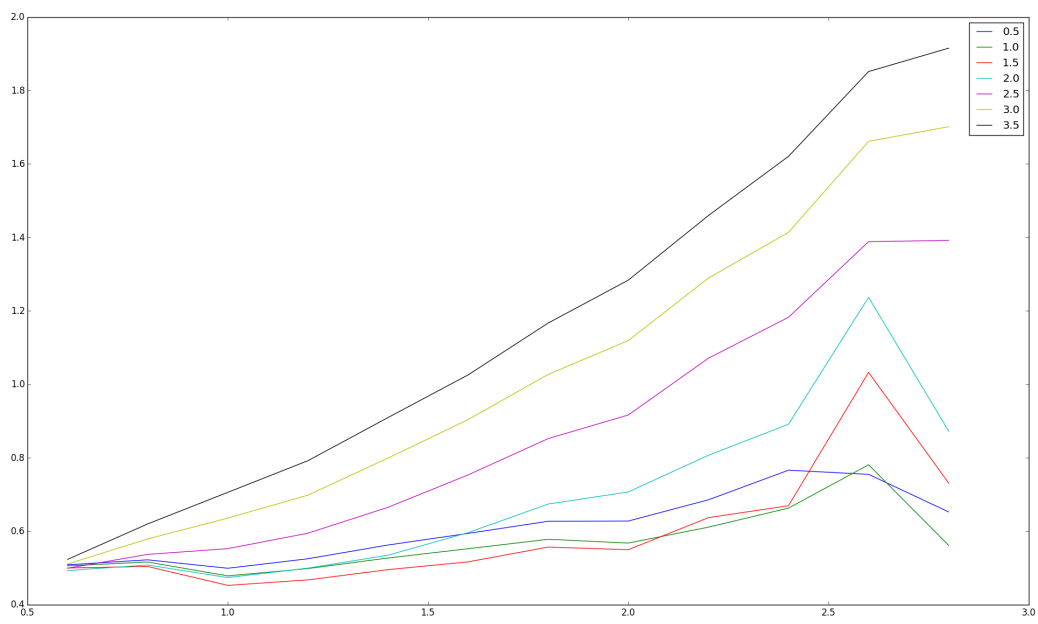


Figure 12: Cumulated  $\varepsilon$  depending on parent radius diameter for  $\gamma$  value from 0.5 to 3.5

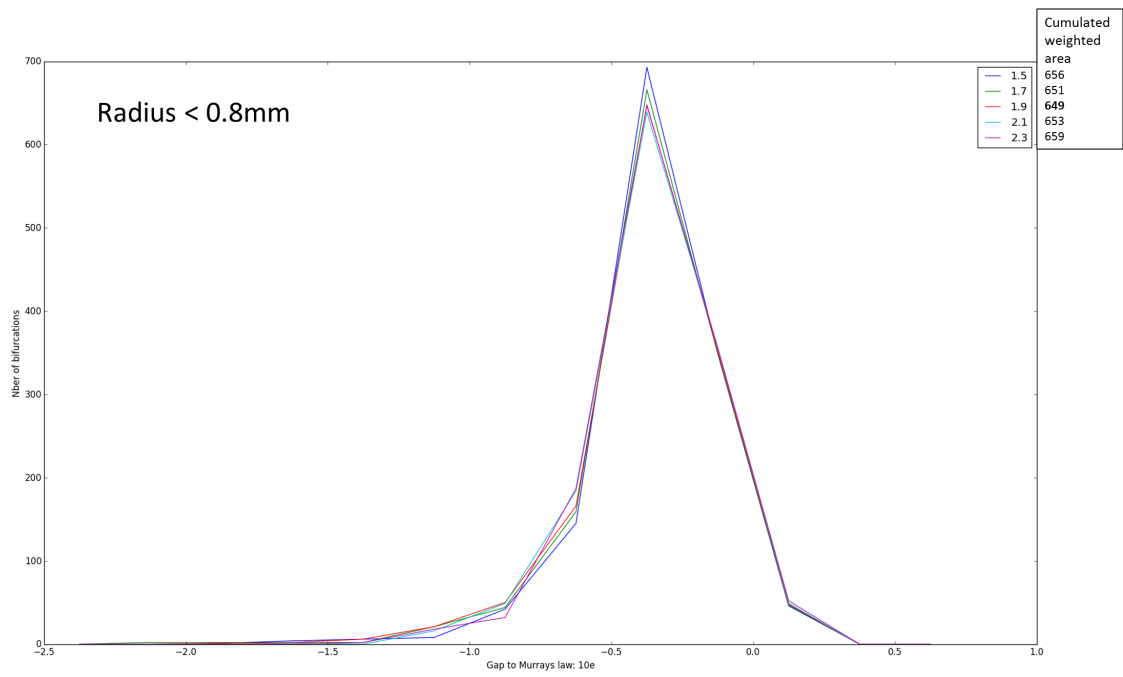


Figure 13:  $\epsilon$  distribution for bifurcations with parent radius under 0.8mm with  $\gamma$  value from 1.5 to 2.3

the ratio of the smaller child radius over the larger child radius. We also analyzed the expansion ratio:

$$ER = (r_1^2 + r_2^2) / r_0^2 \quad (5)$$

Both asymmetry factor and expansion ratio tends to increase with smaller radii, which is expected in the literature.

Also, we noticed a pretty good correlation between the squared parent radius and the sum of squared daughter radii, see figure 15.

Studying the data closer, we noticed 40% of the bifurcations are actually excluded from the study because we do not get 5 area measurements (5 centerline points with 0.5 mm sampling) for each child and parent of the bifurcation. This happens when one of the segment mostly or entirely belongs to a bifurcation field. In this case there may be fewer than 5 measurements, and we do not use this bifurcation in the study.

In addition, we noticed that a significant amount of bifurcations (26.6%) have a parent radius smaller than one of the children radii, see top of figure 16. It is even more concentrated in small parent bifurcations (under 0.8 mm radius): 39%. Visualizing coronary meshes, we observe this is either due to stenosis, natural gap (which does exist, as pointed by Kassab [1],[24], and Kaimovitz [25] ) or measurement errors (low quality segmentation, depends itself on image quality and analyst precision), see bottom of figure 16.

Consequently we decided to exclude bifurcations showing parent smaller than a child, and apply robust statistics on the remaining ones.

We applied a non linear least square minimization using Python and applying various formula to estimate the error relative to Murray's law. The results are presented in figure 17.

It seems the Murray's coefficient obtained for small vessels is more coherent than for large ones. However it is still lower than expected. These results could be due to measurement errors, disease, or we consider vessels that are still too large or bifurcates too asymmetrically to respect Murray's law. Several authors reached this last conclusion: Sherman [26], Lubashevsky [27], and, more recently, Wijngaard [28].

Nonetheless we made sure the first method we implemented (measuring the cumulated  $\epsilon$  error) would actually work to detect the correct gamma if it does exist, by testing it on synthetic data (created as following Murray's law and with random noise added). Even though the synthetic data is only degraded with a simple noised, this allowed us to confirm that our method can discover the correct gamma value (which is not mathematically trivial), see figure 18.

Also, we attempted to find a law that could fit the large vessel data only. Showed in figure 19 we found a correlation coefficient and coefficient of determination of 0.9 and 0.8 for the equation:

$$r_0^2 = r_1^2 + r_2^2 \quad (6)$$

We can observe a pretty good alignment of the line defined by Orthogonal Distance Regression in figure 19.

We cannot decisively conclude on this study: if it is not clear whether Murray's law should or not apply on large asymmetrical vessels, we are also unsure of the measurements accuracy, that can be altered by disease and image quality.

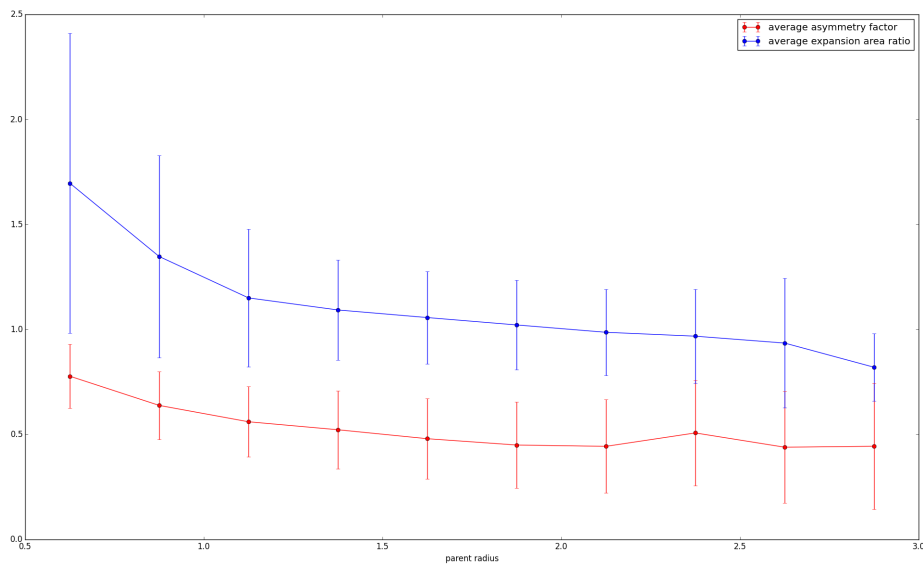
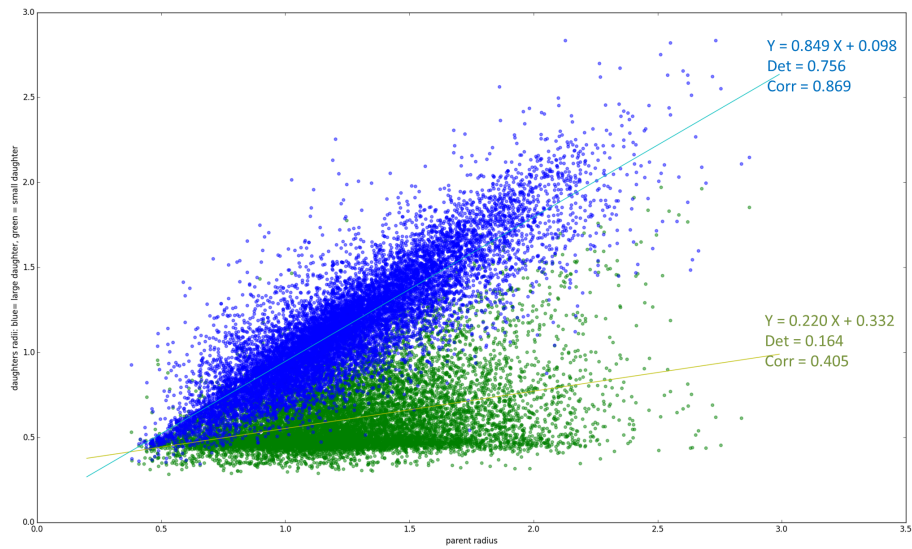


Figure 14: Asymmetry study. Top: children radii along parent radius (in blue: the bigger the child vessel, in green the smaller one.) Bottom: Average asymmetry factor (red) and expansion ratio (blue) along parent radius

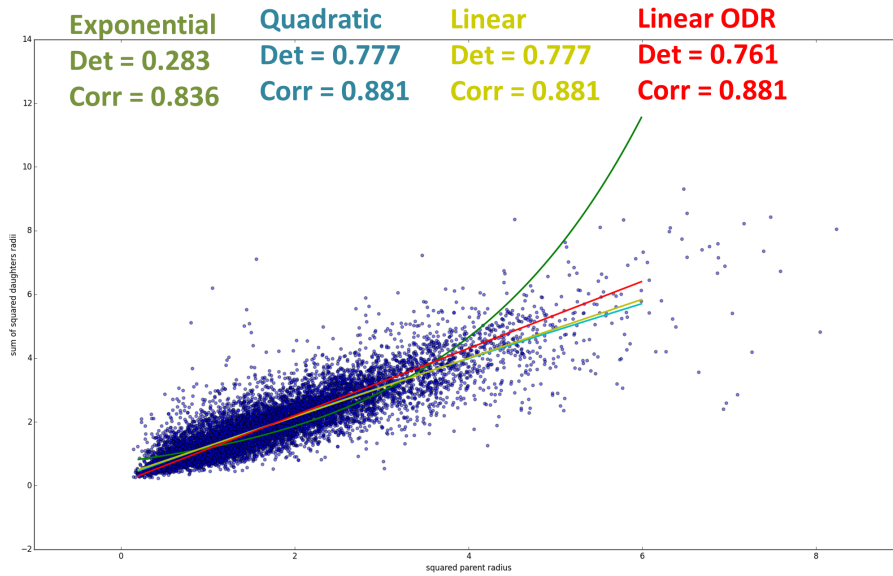


Figure 15: Squared parent radius along squared daughter radii fitted with different regressions. Det = coefficient of determination, Corr = coefficient of correlation, ODR = Orthogonal Distance Regression.

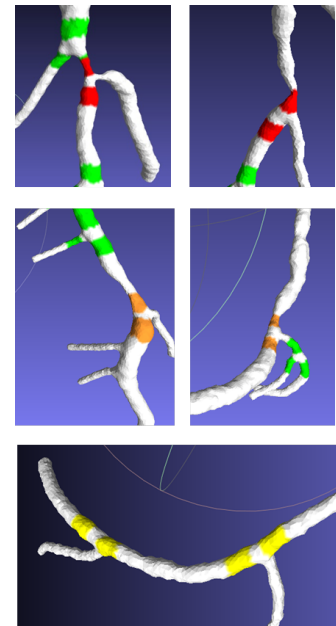
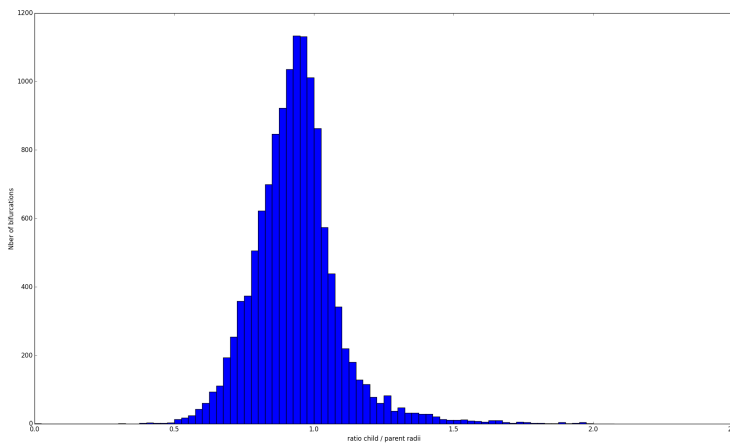


Figure 16: Larger child radius over parent's one. Left: histogram of all bifurcations. Right: visualization of some examples,  $rc$  = larger child radius,  $rp$  = parent radius (red:  $rc > 2 * rp$ , orange:  $rc > 1.5 * rp$ , yellow:  $rc > rp$ , green:  $rc < rp$ ).

Minimized function on 8673 datasets (vessels > 0.8mm diameter)	Gamma found	Chi squared	Reduced chi	Minimized function on 787 datasets (vessels < 0.8mm diameter)	Gamma found	Chi squared	Reduced chi
$\epsilon = ((r_1^\gamma + r_2^\gamma - r_0^\gamma)^2)^{(1/\gamma)}$	1.062	0.128	1.4e-05	$\epsilon = ((r_1^\gamma + r_2^\gamma - r_0^\gamma)^2)^{(1/\gamma)}$	2.073	4.4e-05	0.035
$\epsilon = 1 - \exp( r_1^\gamma + r_2^\gamma - r_0^\gamma ^{(1/\gamma)} / k)$	1.511	2.6e-05	3.0e-09	$\epsilon = 1 - \exp( r_1^\gamma + r_2^\gamma - r_0^\gamma ^{(1/\gamma)} / k)$	1.990	2.0e-04	0.256e-07

Figure 17: Results of non linear least square minimization. Left: on large vessels. Right: on small vessels. r0 is parent radius, r1 and r2 daughter radii, k the number of bifurcations studied

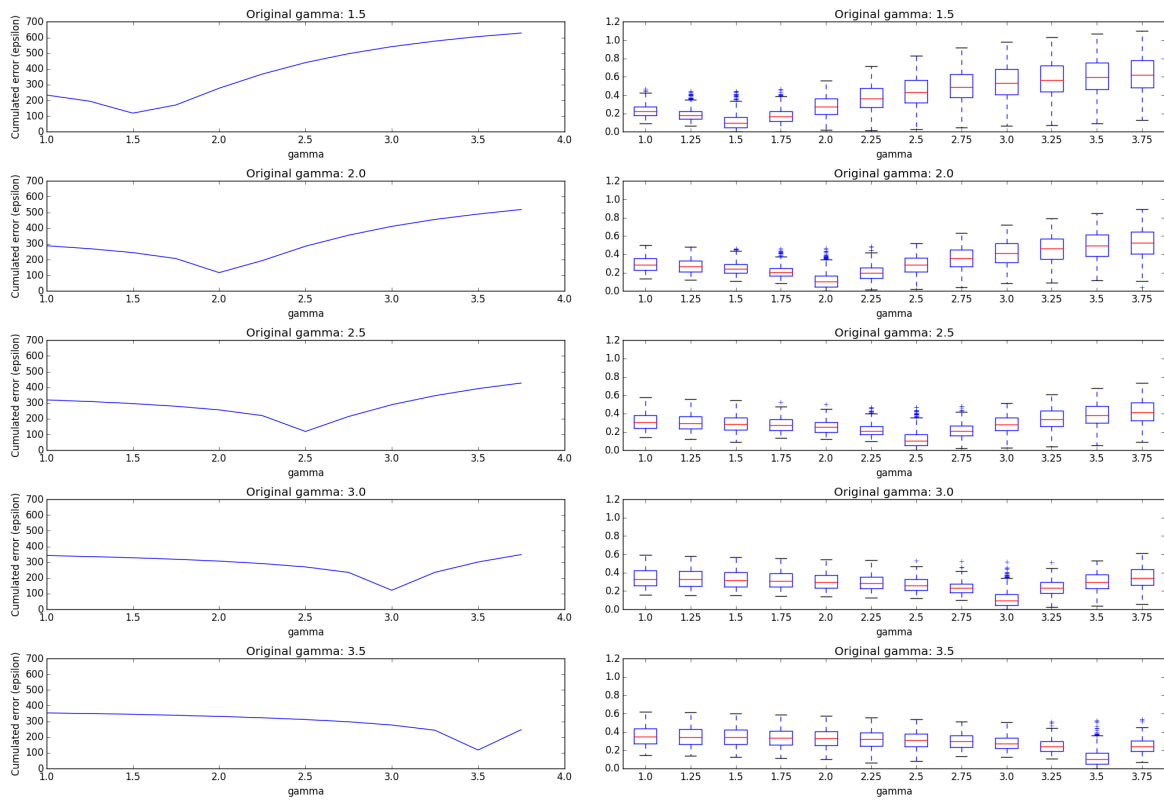


Figure 18: Cumulated error for synthetic data and their original distribution

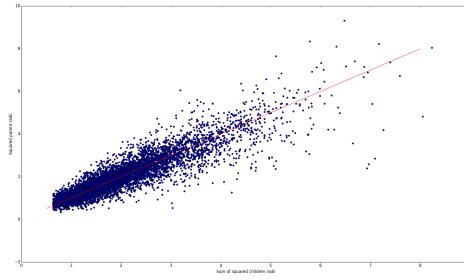


Figure 19: Orthogonal Distance Regression finds the line of equation  $0.907x + 0.18$

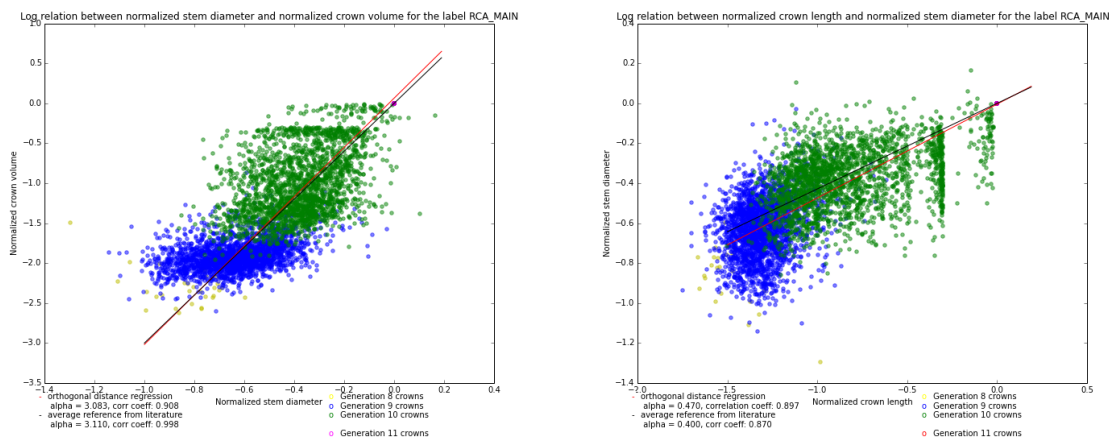


Figure 20: Stem crown relationship for data B

### Crown stem relationship

The crown stem relationship comes from a generalization of Murray’s law [15]. We collected the values for diameter, length and volume relationships.

This requires us to measure for the most proximal stem: the stem diameter, the cumulated length and volumes of all downstream vessels, noted  $D_r$ ,  $V_r$ , and  $L_r$ . Then for the stem of each element in the entire tree we take the same measurements and normalize them by  $D_r$ ,  $V_r$  and  $L_r$ . If there are more than one element per generation we calculate the average ratio. This relationship was studied on a larger dataset (2436 cases, data B). The volumes and diameters were calculated based on the Maximally Inscribed Sphere (MIS) method from the model statistics. We find coefficient of the power law similar to Zhou and Huo studies performed on pigs, see figures 20.

We actually also collected the stem crown ratios on the dataset A, but the measurements were made using the intersection contour area estimation from the model statistics, which is supposed to be less reliable at bifurcations. The obtained results seem to be closer to the literature values, see figure 21.

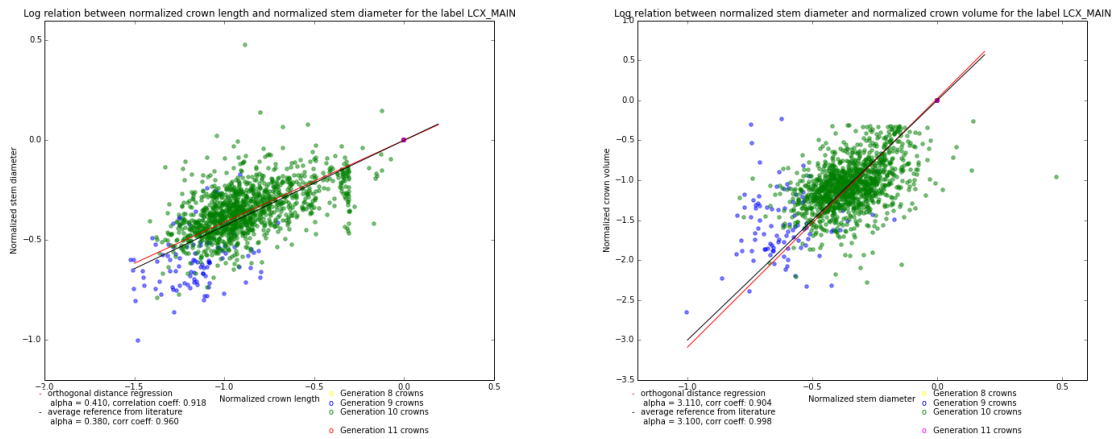


Figure 21: Stem crown relationship for data A

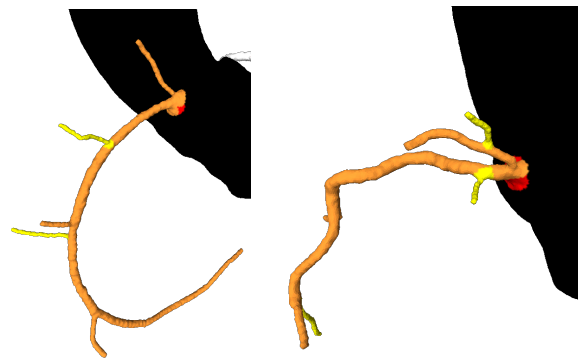


Figure 22: Examples of data showing ratios close to 0.5 for generation 10. Left: length ratio = 0.497, volume ratio = 0.482. Right: length ratio = 0.489, volume ratio = 0.440

This could mean that the manual measurement error is similar to the error on the intersection contour.

In both datasets, but mostly in B, it seems there are some typical length and volume ratios for generation 10 (in green). The lines we distinguish in the cloud of points are more distinct for the RCA vessel so we choose to find the source of the artifact on this label. The cases corresponding to the main vertical direction on normalized crown length show ratios values between 0.479 and 0.525 (-0.32 and -0.28 in log10 scale), there are 149 cases of these. The cases corresponding to the main horizontal direction on normalized crown volume show ratios values between 0.399 and 0.501 (-0.4 and -0.3 in log10 scale), there are 183 of these. Ninety percent of this specific length ratio cases also show the specific volume ratio, the correspondence is coherent because vessel length is used to calculate vessel volume. Visualizing these data we notice they all present along the main vessel, a small branch arising close to the ostium, so that there are two elements of generation 10 in the coronary tree, see figure 22.



Figure 23: Examples of data showing ratios close to 1 for generation 10. Left: volume ratio = 1. Right: volume ratio = 1

For each tree, the ratio is calculated as the average value of all crowns of the same generation ( $C_i^j$ ), and then normalized by the most proximal crown value ( $C_0$ ).

$$SC_i = (\sum_j (C_i^j) / j) / C_0 \quad (7)$$

So if there are two elements of generation  $i$ :  $j = 2$ ,  $C_i^0 \ll C_0$ , and  $C_i^1 \sim C_0$ , then  $SC_i \sim 0.5$ .

When carrying out the same study for the vertical and horizontal lines closed to the zero value on log10 scale (so a ratio equal to 1), it appears that the ratios are equal to 1 for generation 10 when there is no generation 11 on the RCA. The ratios are also closed to 1 when the generation 11 is a really short segment, see figure 22 right.

The stem crown relationship is easier to put in evidence than Murray's law in our data because the measure are made at a less local scale, which is more reliable in terms of accuracy.

### Connectivity related to patient biometrics

We focused on the LAD connectivity because this label is assumed to be less impacted by the coronary dominance diversity (whereas LCX and RCA are directly influenced).

We want to test several hypothesis:

1. Are extreme connectivity values related to a biometric pattern? (e.g. we expect young women with low BMI to show high connectivity)
2. Can we predict the average coronary connectivity for one label from these biometrics information? (a model for each gender using BMI and age)
3. Some patients have a globally thin vessel morphology (detected by absence of generation 11, using the DD Strahler ordering system), do these patient follow a bio-metric pattern ?

We screened the `Information.xml` files of 2469 cases using the `CollectBioMetrics.py` code. In cardiovascular pathology, 3 biometrics are important to identify and diagnose patient risk: age, Body Mass Index (BMI) and gender. We will start studying these metrics. Among all cases, 1405 files are

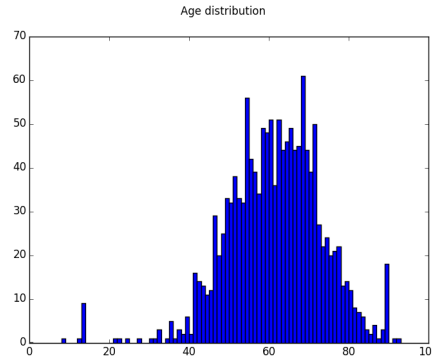


Figure 24: Age distribution of 1405 patients.

Generation	11	10	9
11	$C_{00}$	$C_{01}$	$C_{02}$
10	0	$C_{11}$	$C_{12}$
9	0	0	$C_{22}$

Figure 25: Connectivity matrix provides us with 5 coefficients.

provided with these 3 pieces of data, 473 women and 932 men. Taking a look at the age panel, see figure 24, we observe a near Gaussian distribution, excepting for two peaks: one under 20 years old and one at 90 years old. It appears there is no underage patient so the first peak is a consequence of typos, whereas the second is induced by an age limit in some scanner machines. We will make sure to get rid of these data in the following study. The median age of the population is 61 years old. The connectivity is provided for each patient with at least 5 coefficient linking generation 11 to 9, see figure 25 . We tested two approaches to use and analyze this information with biometrics parameters. We tested them on the men's data.

### First approach : Principal Component Analysis (PCA)

To reduce the number of dimensions we apply PCA on the whole dataset containing connectivity coefficient and BMI or age. When doing so, we notice the sum of the variance of the first two eigen-vectors show that most of the information is present on the first axis:

- PCA on age and connectivity:  $\sum \text{Variance}(2 \text{ eigen-vectors}) > 95\%$
- PCA on BMI and connectivity:  $\sum \text{Variance}(2 \text{ eigen-vectors}) > 84\%$
- PCA on age, BMI and connectivity:  $\sum \text{Variance}(3 \text{ eigen-vectors}) > 87\%$

The resulting scatter plot shows neither clusters, nor correlation between parameters, see figure 26.

## Second approach: linear embedding

Here we assume that the information contained in the connectivity coefficient follows can be reduced to a sub-manifold, i.e. a subspace of lower dimension, also called embedding.

Testing different embedding, we ended using the Modified Locally Linear Embedding (MLLE) provided by the scikit-learn python module (sklearn). Locally Linear Embedding (LLE) seeks a lower-dimensional projection of the data which preserves distances within local neighborhoods. It can be thought of as a series of local Principal Component Analyses which are globally compared to find the best non-linear embedding. MLLE addresses the regularization problem by using multiple weight vectors in each neighborhood.

Seeking such an embedding research on the 5 connectivity coefficients, we obtain figure 27.

The sklearn package does not provide the transform that is applied to obtain the two vectors, but we analyzed the results looking at the coefficient values and observing the coronary tree. It appears the coefficients C00, C01, C02 increase while C11, C12 decrease along the first vector (horizontal axis). The second vector (the vertical axis) seems to be an indicator of the homogeneity of matrix coefficient.

This is coherent with the coronary tree we looked at in figure 28: toward the negative x values, the number of generation 10 segments (in orange) is high, and is very connected to generation 9. Also, the number of segment of generation 11 is very small into this direction. We observe the opposite when going toward positive x values: generation 11 is more present, shows more connections with generation 10 and 9. Nineteen coronary meshes were studied to make these observation, and are stored in the `ConnectivityMeshes` folder in the zip.

We noticed the artifacts inducing alignments of points on the figure 27 is due to discretization: connectivity for the generation 11 is an integer, so cases with the same coefficient C00 end up all aligned.

No correlation or cluster were found between BMI and connectivity, or age and connectivity, or the three parameters at once, see figure 29. It seems difficult to build any predictive model with this information (answer to hypothesis 2).

We wondered if this representation of the tree structure would not be actually directly related to the patient global morphology. Because the generation assignment is based on the segment diameter it could influence the analysis that way. To check this we try to relate connectivity with two other pieces of information: patient height (from xml) and left ventricle mass (calculated from its volume and provided in the zhf).

We do not find any correlation between left ventricle mass and connectivity, neither in 1D, 2D, nor 3D, see figure 30.

We do not find any correlation between patient height and connectivity, neither in 1D, 2D, nor 3D, see figure 31.

We considered studying the relationship with the three other cardiac chambers: right ventricle, left and right atria. These are simulated starting from their respective blood pool segmentations. The

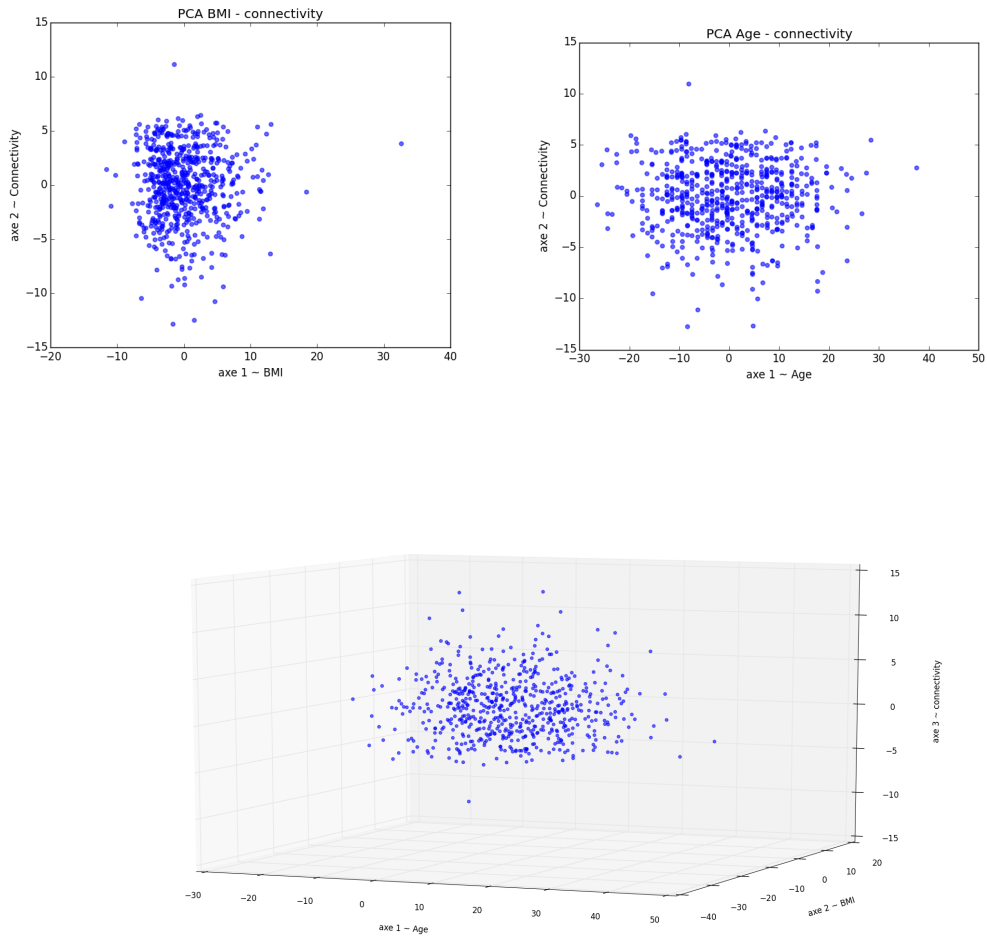


Figure 26: PCA applied to reduce data dimensions. Top left: BMI and connectivity, Top right: age and connectivity, Bottom: Age, BMI and connectivity.

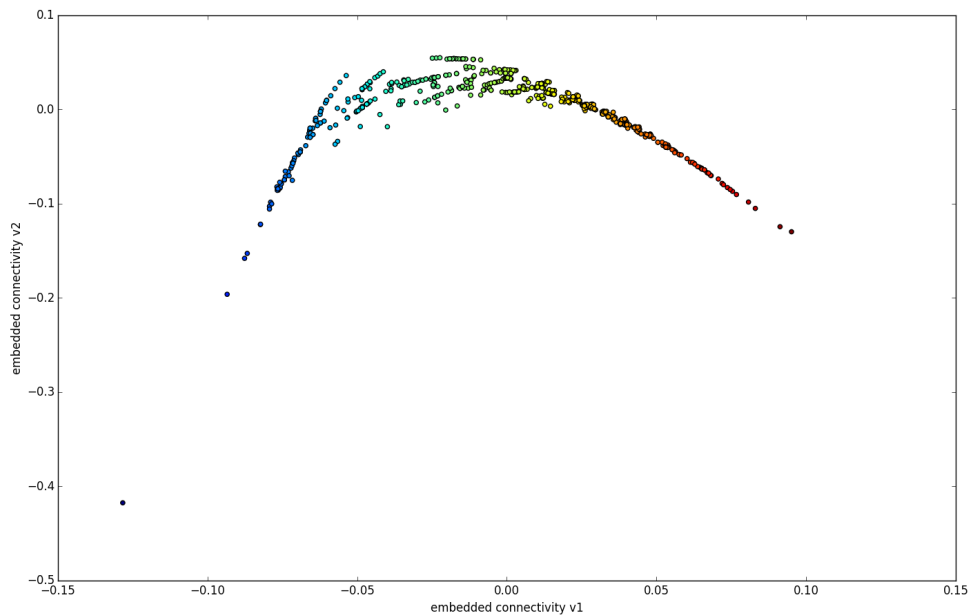


Figure 27: Plot of the 2D MLL Embedding. The colormap is set on the horizontal axis value

dilation of the blood pool surface until it reaches a wall thickness defined in the literature provides an estimation of each chamber segmentation. However this process is based only on the inner surface (blood pool), and because hypertrophy or hypotrophy can be induced from either inner or outer myocardium surface, this process is not robust to detect hyper or hypotrophy of the myocardium. Consequently we did not conduct this additional study.

Conclusion on the BMI-age-connectivity study: it seems there is no correlation between these data. It is important to note that the median patient age is 61 years old. In the elderly (defined as over 65 years old), the BMI is difficult to interpret because of the muscle and height loss induced by ageing [29]. Another metrics, waist circumference (WC), is more reliable for characterizing overweight in the elderly, however we are not provided with this measure for any patient. We recommend to integrate the WC measure in the acquisition protocol using the scout image, but medical protocol changes are difficult to obtain. We looked at the relationship between age and BMI to make sure we did not miss any correlation, see figure 32. We noticed some BMI outlier values due to unit conversions, that we excluded from the previous and next studies.

We were expecting to observe tree pruning due to ageing, or unhealthy behavior. If vascular pruning is studied on micro-vascular tree [30], it would be surprising to see it on such large vessels as epicardial coronary. It is also complicated to prove this connectivity change because we do not have patient follow up images.

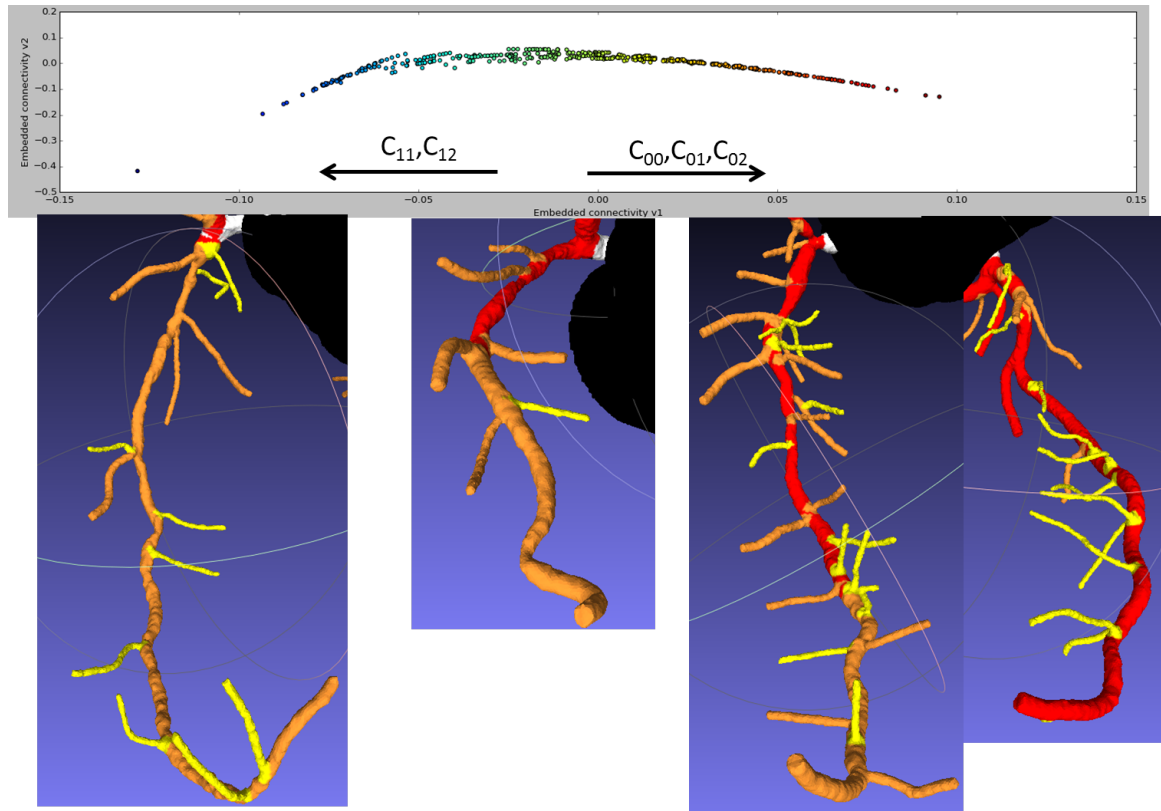


Figure 28: Plot of the 2D MLL Embedding and coronary tree colored according to their generation (red: generation 11, orange: generation 10, yellow: generation 9).

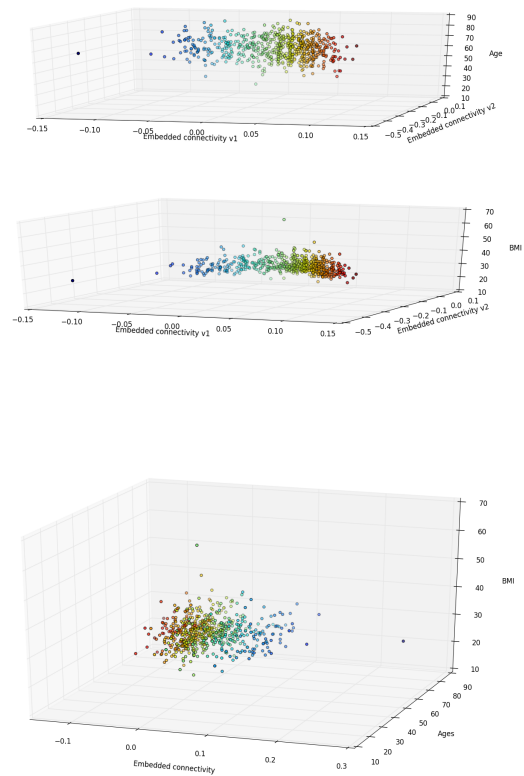


Figure 29: Embedded connectivity, BMI and Age. Top: the connectivity is embedded in 2 vectors and projected with Age (top) and BMI (bottom). Bottom: The connectivity is embedded in only 1 dimension to project it with both BMI and age. Colormap is set on the first connectivity vector value.

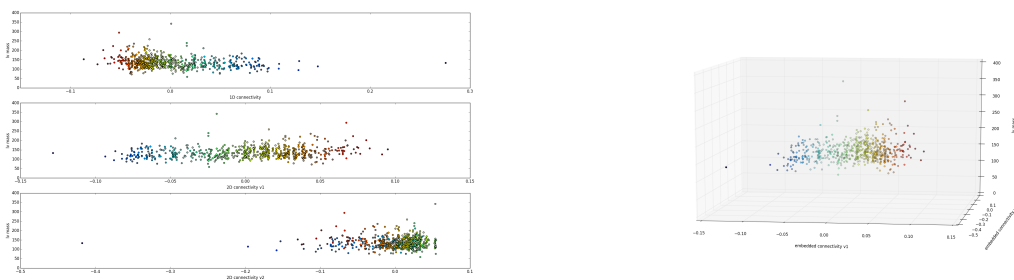


Figure 30: Embedded connectivity and left ventricle mass relationship. Left: Looking for correlation between LV mass, 1D connectivity embedding, and each of the 2 vectors of the 2D connectivity embedding. Right: Looking for a 3D correlation between LV mass and 2D embedded connectivity

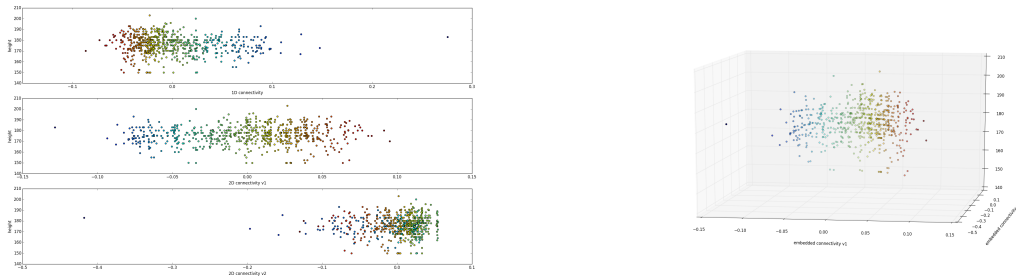


Figure 31: Embedded connectivity and patient height relationship. Left: Looking for correlation between height, 1D connectivity embedding, and each of the 2 vectors of the 2D connectivity embedding. Right: Looking for a 3D correlation between height and 2D embedded connectivity

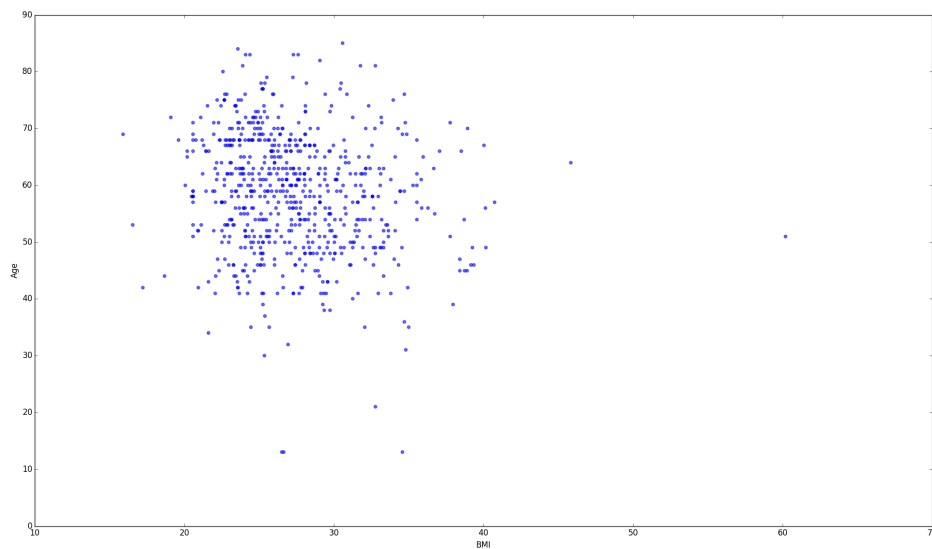


Figure 32: Age and BMI of all patient. It appears the outlier BMI is due to unit confusion.

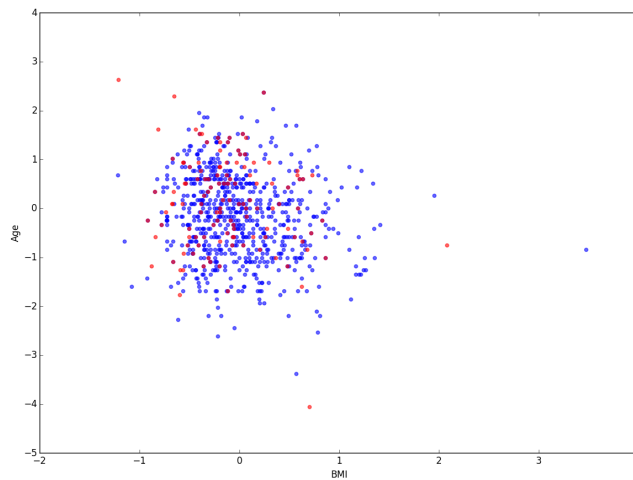


Figure 33: Global morphology comparison related to age and BMI. In red: small morphology patients (no generation 11), in blue: normal morphology patients.

### Checking small morphometry: answer to hypothesis 3

We also looked at the global morphology of patient: if there is no generation 11 found in the coronary tree, we consider the patient to feature a small morphology. We find 125 patients of this type, and look at their BMI in comparison of other patients, see figure 33. No clusters appear. Among these patients, 56 are women and 69 are men. Knowing that the original panel contains about twice as many men as women, these numbers show that there are proportionally more women than men with small morphology. This is expected because of natural mensuration difference.

### Other biometrics

Because all previously used biometrics did not correlate with connectivity, we tested some additional ones. We considered blood pressure information that are provided in the Xml. If we find the correlation between diastolic and systolic pressure, there is none with 1D embedded connectivity. We also looked specifically for hyper and hypotension relationship with connectivity, age and BMI, see figure 34. Showing in red and blue hypertensive and hypotensive (defined by National Institute of Health), and in blue normal tension patients. On 649 men provided with BMI, age, blood pressure values and connectivity, 210 are hypertensive, 20 hypotensive. Note : we found 9 patients that simultaneously correspond to both hypertensive and hypotensive definitions, this is probably due to typos in the data.

We are provided some cases with additional information such as smoking and diabete, but they don't have BMI, age, gender all at once, for a total of 1648 patients.

Among these 1648, 72 are mentioned as smokers, the others are not provided with the information.

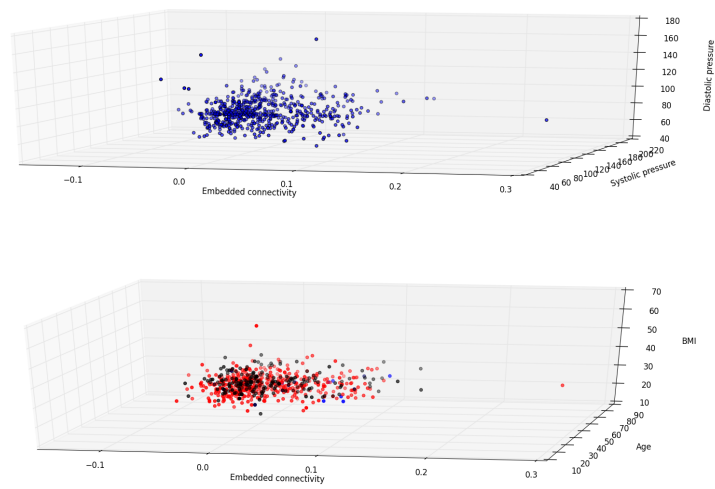


Figure 34: Blood pressure relationship with connectivity, BMI and age. Top: Relationship between embedded connectivity, systolic and diastolic pressure. Down: Relationship between BMI, age and connectivity for hypertensive patients (red), hypotensive patients (blue) and normal blood pressure patient (black).

On the left of figure 35, we cannot see any specific distribution of the smoker population. Among these 1648, 34 are mentioned as having diabete, the others are not provided with the information. On the right of figure 35, we cannot see any specific distribution of the diabete population either.

In conclusion of the biometric study, it seems difficult for us to produce a predictive model related to the patient profile.

## Conclusion

### Limitations of the data

The measure of the connectivity is impacted by many parameters: image quality, patient disease, expert reproducibility, and so on. The connectivity definition itself is based on diameter models, that are influenced by the natural patient morphology. Consequently the measures are directly representative of patient coronary diversity. It is however difficult at this point to provide another anatomical method that would classify each vessel in order to analyze the whole vascular network. We are also limited by the scale we look at: we are only provided with the epicardial coronaries over 0.5 mm in diameter, whereas the network subdivides all the way down to 10  $\mu\text{m}$ .

The biometric data provided show us that we work on a restricted panel of sick and old patients. The information stored are not all relevant (BMI), nor fully reliable (typos, unit limit or conversions), and not always provided for all patients (for instance smoking, diabete). Also, we do not have follow up images of the patient, nor final diagnosis.

For the next studies it will be important to classify patients to identify the panel we have. It will be interesting to classify the degree of disease but also the type: functional or strictly anatomical, du to plaques or calcification, involving hypertension or hypertrophy etc..

## References

1. Ghassan S Kassab, Carmela A Rider, Nina J Tang, and Yuan-Cheng Fung. Morphometry of pig coronary arterial trees. *American Journal of Physiology-Heart and Circulatory Physiology*, 265(1):H350–H365, 1993.
2. Morris E Weaver, GEORGE A PANTELY, J David Bristow, and HERBERT D LADLEY. A quantitative study of the anatomy and distribution of coronary arteries in swine in comparison with other animals and man. *Cardiovascular research*, 20(12):907–917, 1986.
3. Thomas Wischgoll, Jenny S Choy, and Ghassan S Kassab. Extraction of morphometry and branching angles of porcine coronary arterial tree from ct images. *American Journal of Physiology-Heart and Circulatory Physiology*, 297(5):H1949–H1955, 2009.
4. Ghassan S Kassab, Edith Pallencaoe, Amy Schatz, and Yuan-Cheng B Fung. Longitudinal position matrix of the pig coronary vasculature and its hemodynamic implications. *American Journal of Physiology-Heart and Circulatory Physiology*, 273(6):H2832–H2842, 1997.

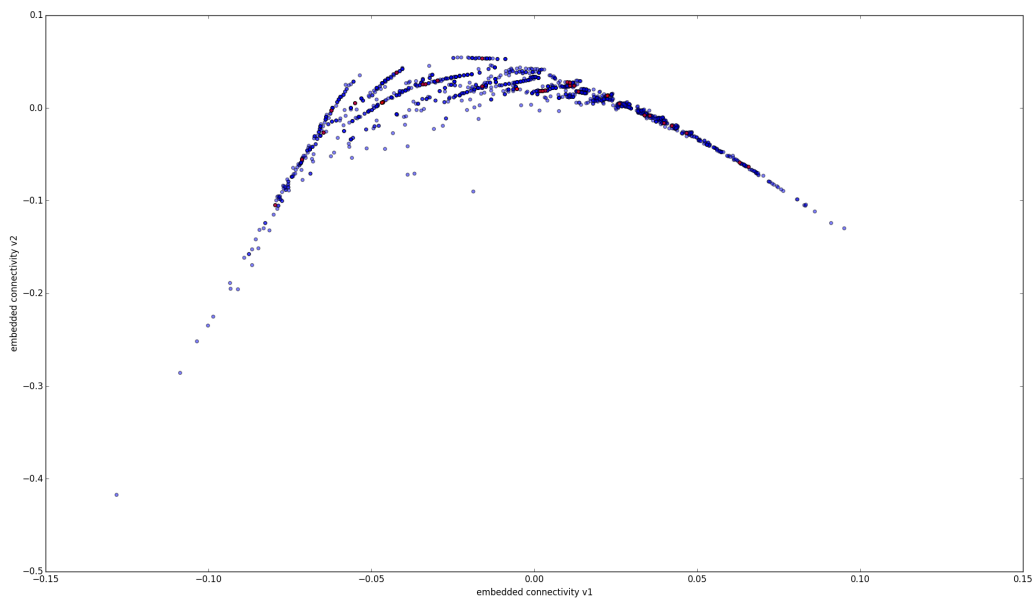
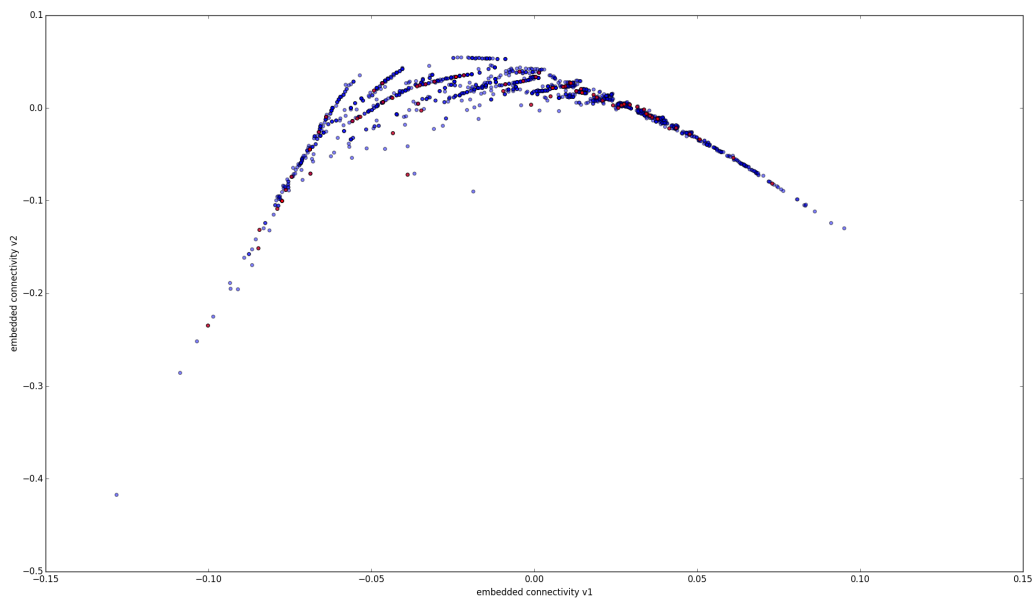


Figure 35: Embedded connectivity studied for different populations: smokers and diabetes. Left: blue dots represent patient without smoking information, red: patient known as smoker. Right: red dots are patients with known diabete, blue: patient without information about diabete

5. E VanBavel and JA Spaan. Branching patterns in the porcine coronary arterial tree. estimation of flow heterogeneity. *Circulation research*, 71(5):1200–1212, 1992.
6. Akira Tanaka, Hidezo Mori, Etsuro Tanaka, Minhaz Uddin Mohammed, Yutaka Tanaka, Takafumi Sekka, Kuniyoshi Ito, Yoshiro Shinozaki, Kazuyuki Hyodo, Masami Ando, et al. Branching patterns of intramural coronary vessels determined by microangiography using synchrotron radiation. *American Journal of Physiology-Heart and Circulatory Physiology*, 276(6):H2262–H2267, 1999.
7. M Zamir. Distributing and delivering vessels of the human heart. *The Journal of general physiology*, 91(5):725–735, 1988.
8. Wing-Huang Leung, Michael L Stadius, and Edwin L Alderman. Determinants of normal coronary artery dimensions in humans. *Circulation*, 84(6):2294–2306, 1991.
9. JT Dodge, B Greg Brown, Edward L Bolson, and Harold T Dodge. Lumen diameter of normal human coronary arteries. influence of age, sex, anatomic variation, and left ventricular hypertrophy or dilation. *Circulation*, 86(1):232–246, 1992.
10. ER Weibel. Morphometry of the human lung: the state of the art after two decades. *Bulletin europeen de physiopathologie respiratoire*, 15(5):999–1013, 1978.
11. Arthur N Strahler. Hypsometric (area-altitude) analysis of erosional topography. *Geological Society of America Bulletin*, 63(11):1117–1142, 1952.
12. Robert E Horton. Erosional development of streams and their drainage basins; hydrophysical approach to quantitative morphology. *Geological society of America bulletin*, 56(3):275–370, 1945.
13. K Horsfield. Pulmonary airways and blood vessels considered as confluent trees. *The lung: scientific foundations*, 2nd ed. Philadelphia: Lippencott-Raven Publishers, pages 1073–1079, 1997.
14. Cecil D Murray. The physiological principle of minimum work i. the vascular system and the cost of blood volume. *Proceedings of the National Academy of Sciences*, 12(3):207–214, 1926.
15. Yifang Zhou, Ghassan S Kassab, and Sabee Molloy. On the design of the coronary arterial tree: a generalization of murray's law. *Physics in medicine and biology*, 44(12):2929, 1999.
16. Pepijn van Horsen, Jeroen PHM van den Wijngaard, MJ Brandt, Imo E Hofer, Jos AE Spaan, and Maria Siebes. Perfusion territories subtended by penetrating coronary arteries increase in size and decrease in number toward the subendocardium. *American Journal of Physiology-Heart and Circulatory Physiology*, 306(4):H496–H504, 2014.
17. Jenny Susana Choy and Ghassan S Kassab. Scaling of myocardial mass to flow and morphometry of coronary arteries. *Journal of Applied Physiology*, 104(5):1281–1286, 2008.
18. BS Lewis and MS Gotsman. Relation between coronary artery size and left ventricular wall mass. *British heart journal*, 35(11):1150, 1973.
19. CH Seiler, RL Kirkeeide, and KL Gould. Basic structure-function relations of the epicardial coronary vascular tree. basis of quantitative coronary arteriography for diffuse coronary artery disease. *Circulation*, 85(6):1987–2003, 1992.

20. Y Koiwa, RC Bahn, and Erik L Ritman. Regional myocardial volume perfused by the coronary artery branch: estimation in vivo. *Circulation*, 74(1):157–163, 1986.
21. YH Liu, RC Bahn, and Erik L Ritman. Myocardial volume perfused by coronary artery branches: A three-dimensional x-ray computed tomographic evaluation in pigs. *Investigative radiology*, 27(4):302–307, 1992.
22. Simon J Crick, Mary N Sheppard, SIEW YEN HO, Lior Gebstein, and Robert H Anderson. Anatomy of the pig heart: comparisons with normal human cardiac structure. *Journal of anatomy*, 193(1):105–119, 1998.
23. Ghassan S Kassab. Scaling laws of vascular trees: of form and function. *American Journal of Physiology-Heart and Circulatory Physiology*, 290(2):H894–H903, 2006.
24. N Mittal, Y Zhou, S Ung, C Linares, S Molloy, and GS Kassab. A computer reconstruction of the entire coronary arterial tree based on detailed morphometric data. *Annals of biomedical engineering*, 33(8):1015–1026, 2005.
25. Benjamin Kaimovitz, Yoram Lanir, and Ghassan S Kassab. Large-scale 3-d geometric reconstruction of the porcine coronary arterial vasculature based on detailed anatomical data. *Annals of biomedical engineering*, 33(11):1517–1535, 2005.
26. Thomas F Sherman. On connecting large vessels to small. the meaning of murray's law. *The Journal of general physiology*, 78(4):431–453, 1981.
27. IA Lubashevsky and VV Gafiychuk. Analysis of the optimality principles responsible for vascular network architectonics. *arXiv preprint adap-org/9909003*, 1999.
28. Jeroen PHM van den Wijngaard, Janina CV Schwarz, Pepijn van Horssen, Monique GJT van Lier, Johannes GG Dobbe, Jos AE Spaan, and Maria Siebes. 3d imaging of vascular networks for biophysical modeling of perfusion distribution within the heart. *Journal of biomechanics*, 46(2):229–239, 2013.
29. TS Han, Abdelouahid Tajar, and MEJ Lean. Obesity and weight management in the elderly. *British medical bulletin*, page ldr002, 2011.
30. Martin Rodriguez-Porcel, Xiang-Yang Zhu, Alejandro R Chade, Beatriz Amores-Arriaga, Noel M Caplice, Erik L Ritman, Amir Lerman, and Lilach O Lerman. Functional and structural remodeling of the myocardial microvasculature in early experimental hypertension. *American Journal of Physiology-Heart and Circulatory Physiology*, 290(3):H978–H984, 2006.

## VASCULAR MODEL RESULTS ON ADDITIONAL DATASET

---

We selected 8 low diseased cases, based on their  $\text{FFR}_{\text{CT}}$  and perfusion results. We applied the vascular model generation method on all of them. The number of generated trees was respectively 100, 72, 57, 60, 51, 65, 35, 49.

Visualization of the results are presented in figure 61 and 62.

We note that for the case 6 the algorithm ended before reaching the 6000 terminal segments. The growth ended after reaching 687 segments on left ventricle surface. The patient specific constraints prevented from finding new connected segments, so that the algorithm finally stopped.

We investigated the reason of this difficulty. Compared to other cases, we observe a specific distribution of the rejected connections for the case 6, see figure 63. Looking at the geometrical aspects of the case 6, we noted that, the myocardium surface and epicardial coronary volume are pretty small relative to the other patients, shown in figure 64. This point suggests constraints to generate 1000 terminal segments on surface of the left ventricle are too high for this small territory. This encourage algorithm parameters to be adapted to patient-specific geometry, and possibly to reduce the number of terminal segment on left ventricle surface. Meanwhile, we should test another random seed on the case 6, to assess if randomness can overcomes this constraints issue.

The morphometry study of the 7 fully generated networks, against porcine statistical data, is presented below.

### *Diameter Defined Strahler ordering*

As in part I, section 3.3, we classify the vessels according to Kassab's ordering. As for the previous set of data, all segments range between order 4 and 9, while vessels range between order 9 and 11. The segment average diameter along order correlated with the Kassab measures, see figure 65. Also, for all labels, the coefficient determination  $R^2$  values relative to Kassab's fits are all above 0.99. This classification is then used to study other morphometric parameters.

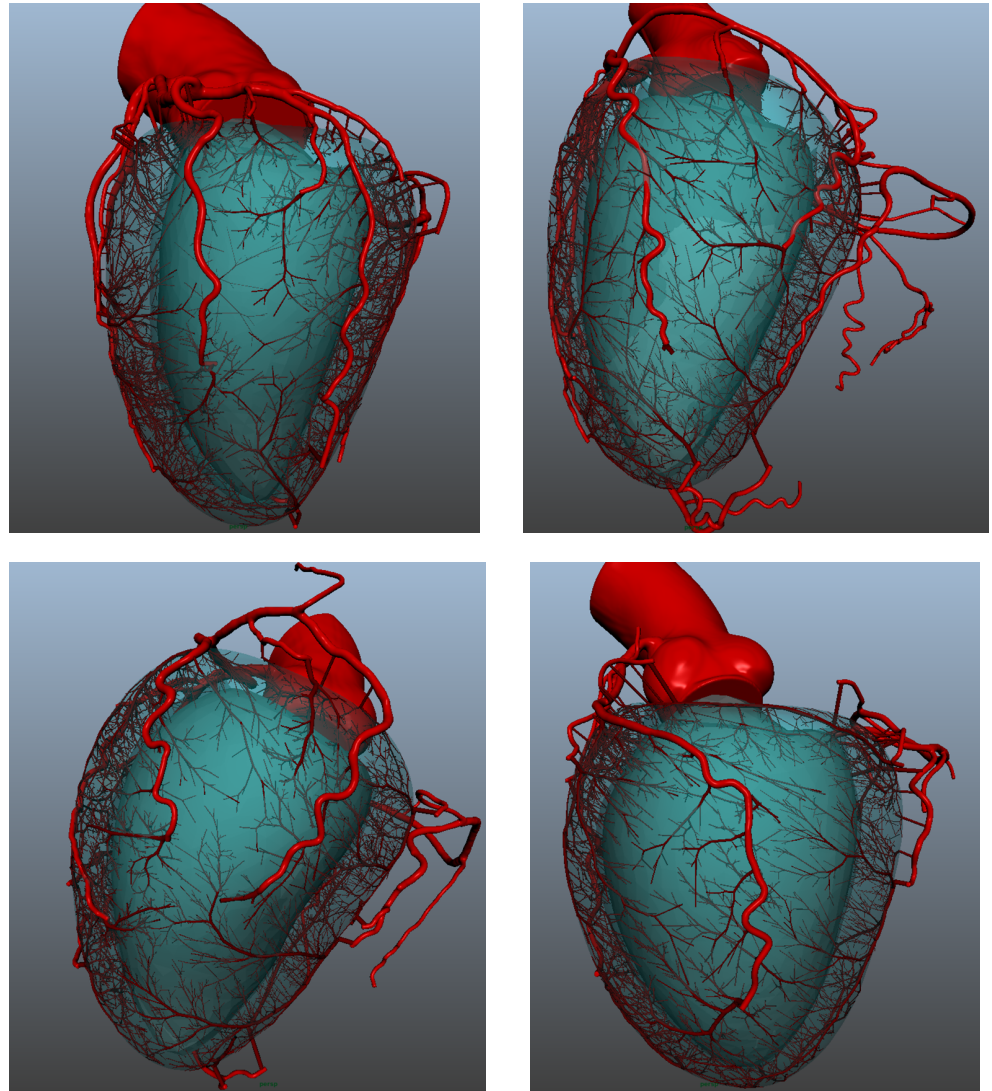


Figure 61 – Results on 8 patients (case 1 to 4): 6000 terminal segment networks. Rendering achieved with *Renderman* in *Maya Autodesk*.

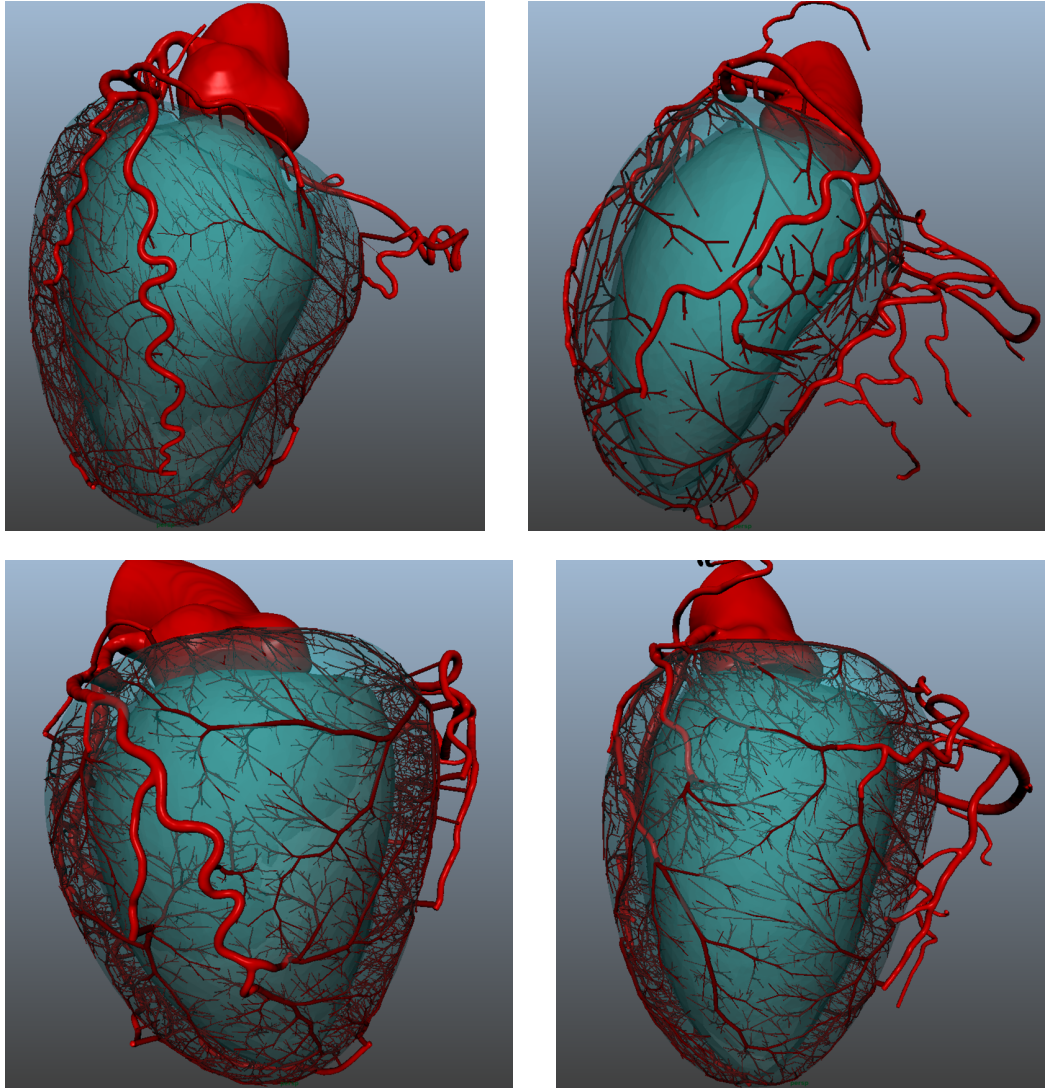
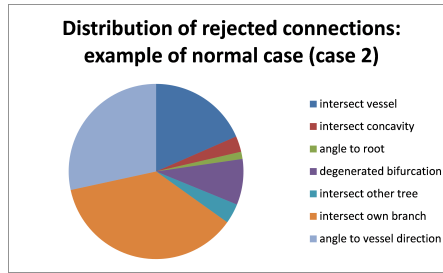


Figure 62 – Results on 8 patients (case 5 to 8): 6000 terminal segment networks. Rendering achieved with *Renderman* in *Maya Autodesk*.



**Distribution of rejected connections:  
case 6 (stop before end)**

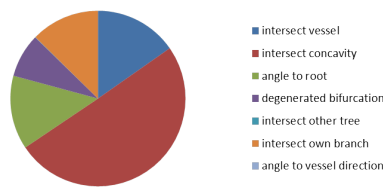


Figure 63 – Distribution of rejected connection test: example of standard case (top), and case 6

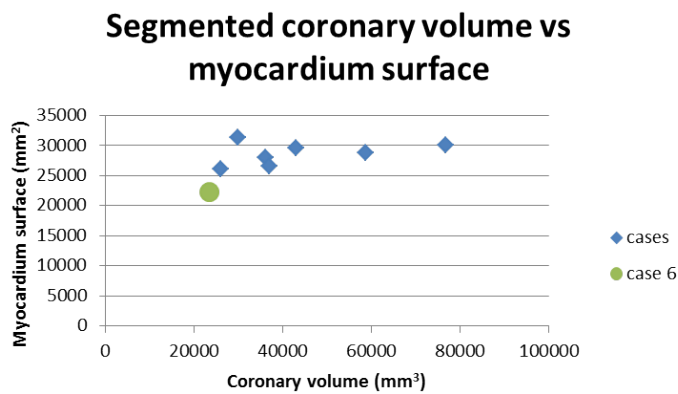


Figure 64 – Segmented coronary volume versus myocardium surface

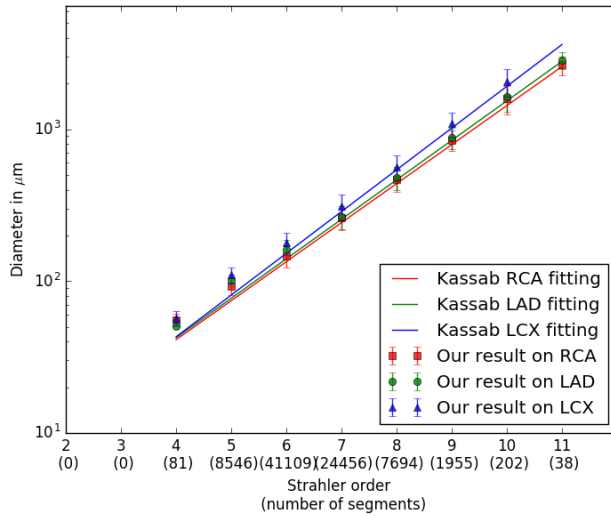


Figure 65 – Measures along Strahler order for each label on 7 patients: Average segment diameter compared with Kassab’s fit.

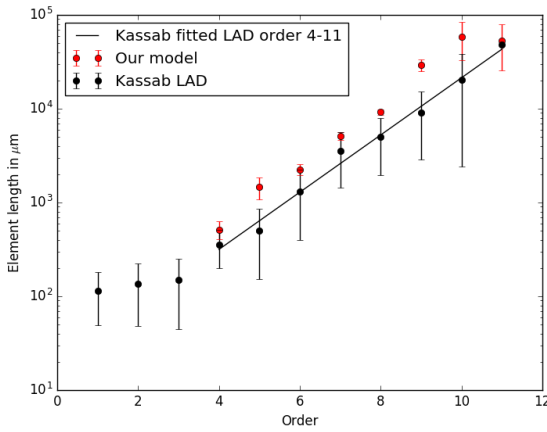


Figure 66 – Measures along Strahler order for each label on 7 patients: Average element length compared with Kassab’s fit.

*Element length*

We plot element length against Kassab fitted models in figure 66. As for the previous set of data, apart from the order 11, elements are equal or significantly longer in our model, which is coherent for human data.

*Bifurcation asymmetry*

As for the previous set of data, bifurcation asymmetry follows similar trend as online supplement of Kaimovitz [51], see figure 67. Our generated networks are globally more symmetrical; continuity is ensured between segmented and simulated networks.

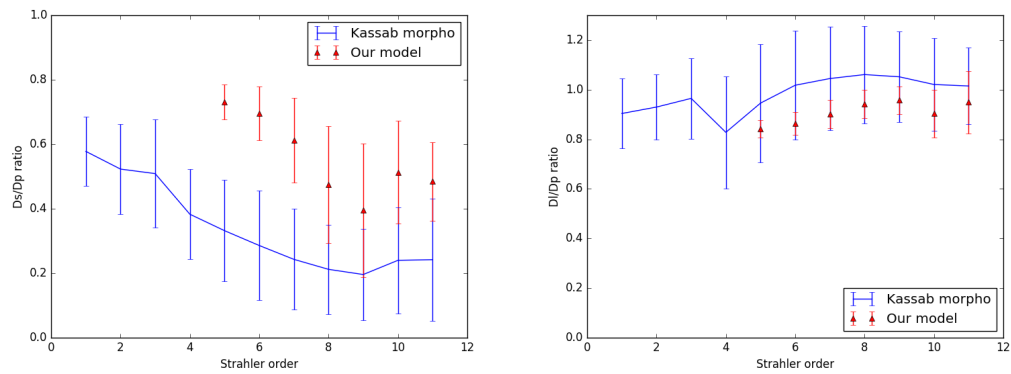


Figure 67 – Asymmetry study on 7 patients compared with Kassab morphometry. Top: SCoP segment radius ratio. Bottom: LCoP segment radius ratio.

### *Tree flows*

Most of the 432 trees reach their target flow, with a correlation coefficient of 0.82, see figure 68.

Out of the 432 trees, 113 had difficulty growing, for similar reasons as detailed in Part 1, section 3.3. When we remove these outlier trees, the correlation coefficient between target and attain flow improves to 0.96 again.

### *Terminal segment diameter*

We observe a unimodal terminal segment diameter distributions for all but the case 3 and 5, see figure 69. The average value is  $153 \pm 53 \mu\text{m}$ .

The non unimodal distributions of cases 3 and 5 are due to difficulties of tree growths. These two cases exhibit the lowest flow correlation coefficient (0.76 and 0.71). Trees that did not reach their target flow lack subdivision branching, maintaining terminal segment diameters relatively larger than trees that have reached their target.

### *Perfusion territories*

As in part I, chapter 3 we also estimated terminal segment associated perfusion territory with a Voronoi Tessellation. Statistics are presented in table 6, and visualization of the distribution is plotted in figure 70.

Finally, average distribution of territories per main vessel is also compared to the literature in table 7. They are also close to referenced values, even if showing a higher RCA territory and lower LAD territory.

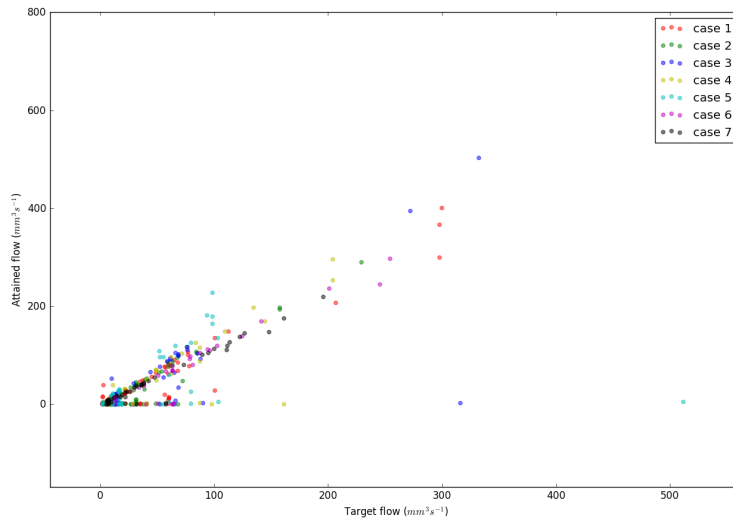


Figure 68 – Correlation between target and attained flow on 7 cases

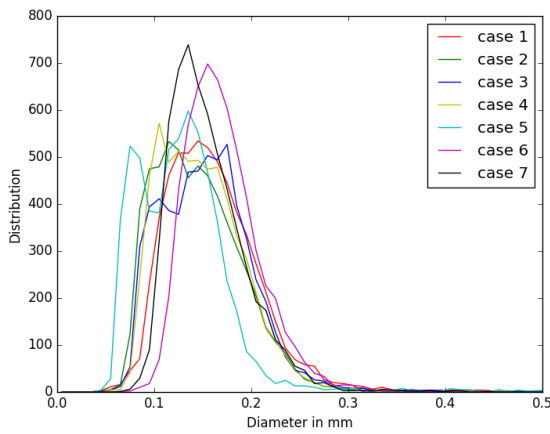


Figure 69 – Terminal segment diameter distribution for 7 cases.

Table 6 – Voronoi distribution

Volumes in mm <sup>3</sup>	$M_{box}$	Mean $\Omega_i$	Std $\Omega_i$	$\Omega^{MF}$
Case 1	23.5	22.7	30.8	5.
Case 2	18.5	17.3	44.4	5.
Case 3	17.2	16.5	51.7	3.
Case 4	14.8	14.2	32.5	3.
Case 5	17.7	16.8	64.6	4.
Case 6	16.9	16.2	29.	1.
Case 7	13.6	12.9	26.4	4.

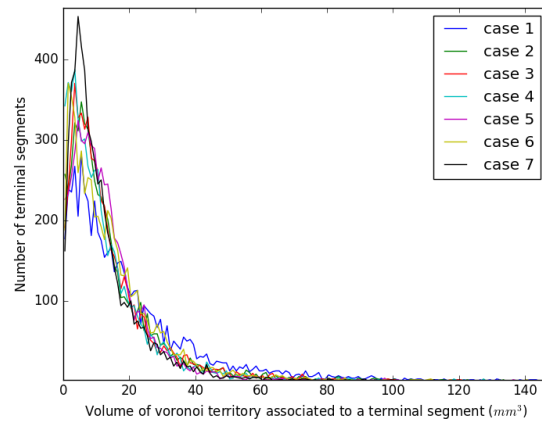


Figure 70 – Distribution of  $\Omega_i$ , volume associated to terminal segments for 7 cases.

Table 7 – Perfused volume associated to each main vessel

Result from	RCA (%)	LAD (%)	LCX (%)
Voronoi on 5 patients	31.0	39.3	29.3
Reig (90 human hearts)	22.5	43.5	32.2
Weaver (60 swine hearts)	25.5	49	25.5

This part of the project has been implemented by Lazaros Papanolis under the supervision of Irene Vignon-Clementel and I.

To extend functional analysis into the myocardium with the help of a computational model, here we consider the myocardium as a porous medium. It is a continuous material constituted of 2 phases: a solid phase, or matrix, which contains pores, and a fluid phase, that fills the pores.

Among the different parameters describing the porous media, the most important ones are porosity  $\Phi$  and permeability  $\kappa$ . Porosity is defined as the volume fraction of fluid:

$$\Phi = \frac{\text{pore volume}}{\text{domain volume}} \quad (44)$$

It proportionally connects the fluid velocity  $v$  and the perfusion velocity (or Darcy velocity)  $w$ :

$$w = \Phi v \quad (45)$$

The permeability,  $\kappa$ , is the ability to let fluid go through, corresponding to a conductance factor.

The porous model is constructed considering the same assumptions as for the 1D coronary model, see part II section 7.1.

To assess implementation of the porous model and its coupling with the 1D coronary model of chapter 7, we initiate this work on simulated data with simple geometry. We define the porous model with the partial differential equation solver FreeFem++, verify it, and then compute a coupling with the 1D coronary model.

### 15.1 POROUS MODEL EQUATIONS

Because blood is considered incompressible and newtonian fluid, it is governed by Darcy's law in porous media. Darcy's law, a homogenization of Navier-Stokes, is described by a constitutive equation and combined with the fluid mass conservation equation:

$$w + \kappa \nabla P = 0 \quad (46a)$$

$$\nabla \cdot w = \beta_{\text{source}} (P_{\text{source}} - P) - \beta_{\text{sink}} (P - P_{\text{sink}}) \quad (46b)$$

with  $\nabla P$  the pressure gradient,  $\beta$  a coefficient describing the flow conductance into and out of the tissue, and  $P$  the capillary bed pressure.

In the constitutive equation, 46a, since fluids flow from higher pressure to lower pressure, it follows the pressure drop direction.

In the fluid mass conservation equation, 46b,  $\beta_{\text{source}}$  represents the inlet through which the blood enters the myocardium with a pressure  $P_{\text{source}}$ , while  $\beta_{\text{sink}}$  represents the outlet through which blood exits the myocardium with a pressure  $P_{\text{sink}}$ . In terms of physiological meaning, sources and sinks correspond respectively to arteriole outlets and venous drainage.

The system is solved for the unknowns Darcy velocity and capillary bed pressure, with pre-estimated parameters.

### Verification test

A verification is designed into a cube geometry to verify the implementation of the porous model is correct.

For this purpose, we set boundary conditions on the 6 surfaces of the cube as followed:

- Dirichlet boundary conditions
  - On the face positioned at  $x = 0$ , named  $\Gamma_{\text{in}}$ , we applied a constant pressure in arbitrary unit:  $P_{\Gamma_{\text{in}}} = 0$ .
  - On the opposite face named  $\Gamma_{\text{out}}$ , we applied a constant pressure  $P_{\Gamma_{\text{out}}} = 1000$ .
- On the four other faces we impose a Neumann boundary condition called "no flux", which induces that the normal velocity of our fluid on those surfaces is zero. Thus our fluid cannot pass through those surfaces, they are considered as hermetic walls.

We obtained the exact same value between simulated results and analytical solution see figure 71. The visualization of the result is provided in figure 72.

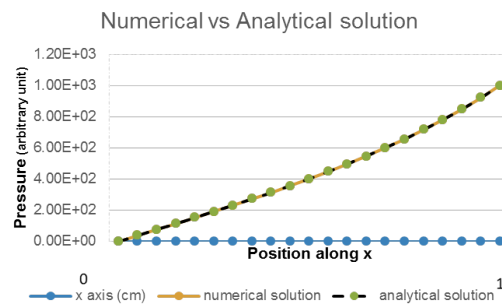


Figure 71 – Verification test.

The porous model implementation is thus verified.

Note that in our coupling conditions, we will have to set the entering flow through source terms corresponding to the vessel outlets.

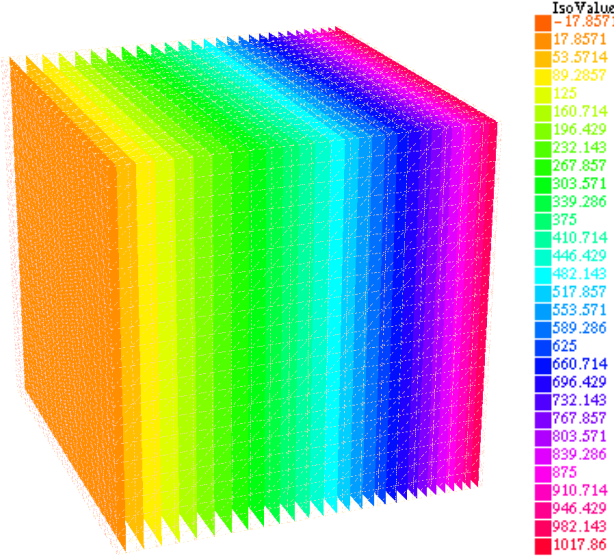


Figure 72 – Visual result of verification test.

Also, the exiting flow will be represented by distributed sinks, it will not be a boundary condition anymore.

## 15.2 COUPLING

We aim at coupling the 1D coronary model of chapter 7 with the porous model of the section 15.1, in both rest and hyperemic conditions. The process involves an initialization at the step  $k = 0$ , followed by iterations coupling the two models.

The initialization is specific of the condition. It defines the dilation of synthetic segments radii, and porous model parameters, which will all be maintained constant along the iterations.

In the coupling iterations, the resulting pressure of the coronary model at terminal segment ends  $P_k^{T,i}$  is used as input for the porous model. The latter calculates flow values at terminal segments, that are used as new inputs for the coronary model,  $q_{k+1}^{T,i}$ . The convergence is established considering the terminal segment flow values between iteration  $k$  and iteration  $k + 1$ .

$$\frac{|q_k^{T,i} - q_{k+1}^{T,i}|}{q_k^{T,i}} < 1\% \text{ for all } i \quad (47)$$

The figure 73 illustrates the coupling loop.

### 15.2.1 Initialization

Initialization is made specifically for rest and hyperemic conditions at iteration  $k = 0$ . It involves a first computation of the coronary 1D model, and the estimation of parameters for the porous model.

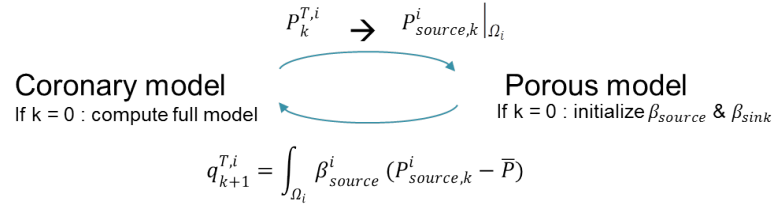


Figure 73 – Illustration of the coupling loop.

#### 15.2.1.1 Coronary model initialization

The initialization of the coronary model corresponds to the algorithm described in part II, chapter 7 section 7.2.2.1. The model is run until convergence specifically for rest or stress condition. It defines synthetic segment dilation in the tree, which will be maintained along iterations, and the first measure of pressure and flow at terminal segments. These two values are used to estimate parameters of the porous model.

#### 15.2.1.2 Estimation of the parameters for the porous model

To initialize the porous model, we need to estimate the parameters  $\kappa$ ,  $\beta_{source}$  and  $\beta_{sink}$ .

The permeability  $\kappa$  is estimated to  $0.002 \text{ mm Pa}^{-2} \text{ s}^{-1}$  from the literature [15].

For each terminal segment end, we estimate  $\beta_{source}$  relative to the terminal segment perfusion territory  $\Omega_i$  and the terminal segment flow  $q^{T,i}$ . This perfusion territory is estimated from a weighted Voronoi tessellation (Laguerre Tessellation, see part I, section 3.2, paragraph *Perfusion territories*).

To get a sense of how to estimate  $\beta_{source}$ , we should consider the physical meaning of the porous model equations. When considering only the source term, if we integrate the perfusion velocity for each terminal segment end  $i$ :

$$\int_{\Omega_i} \nabla \cdot \mathbf{w} = \int_{\Omega_i} \beta_{source} (P_{source} - P) d\Omega \quad (48)$$

$$\int_{\partial\Omega_i} \mathbf{w} \cdot \mathbf{n} \approx \beta_{source} (P_{source} - \bar{P}) \Omega_i \quad (49)$$

The relation defined in equation 49 is exactly equal when  $P_{source}$  and  $\beta_{source}$  are constant over each  $\Omega_i$ .

The value  $P_{source}$  is known, it corresponds to the pressure at the terminal segment end. The pressure drop corresponds to the pressure difference between the terminal segment  $i$  and the local region of the porous compartment around this terminal segment (the volume  $\Omega_i$ ).

Considering the left term of equation 49 corresponds to the local flow  $q^{T,i}$ , we can thus estimate  $\beta_{\text{source}}$  as dimensionally similar to:

$$\beta_{\text{source}}^i \sim \frac{1}{R^{T,i}\Omega_i} \quad (50)$$

Using the pressure and flow at terminal segment provided by the coronary model, we estimate each  $\beta_{\text{source}}$  value with:

$$\beta_{\text{source}}^i = \frac{q^{T,i}}{(P_{\text{source}}^i - \bar{P})\Omega_i} \quad (51)$$

For this we use the average capillary pressure  $\bar{P} = 15$  mmHg as an estimation of  $P$  [15].

The sinks are considered homogeneously distributed in the volume (not explicitly generated), thus we have to determine one single value  $\beta_{\text{sink}}$ . In order to estimate  $\beta_{\text{sink}}$ , we should consider the system behaviour when integrating over the whole myocardium  $\Omega_{\text{myo}}$ , which should be null, since there is as much flow entering as much flow exiting:

$$\int_{\Omega_{\text{myo}}} \nabla \cdot \mathbf{w} = 0 \quad (52)$$

Thus

$$\int_{\Omega_{\text{myo}}} \beta_{\text{source}} (P_{\text{source}} - P) = \int_{\Omega_{\text{myo}}} \beta_{\text{sink}} (P - P_{\text{sink}}) \quad (53)$$

Considering  $P_{\text{sink}}$  null, and estimating  $\beta_{\text{source}}$  and  $P_{\text{source}}$  as the mean value of all  $\beta_{\text{source}}^i$  and  $P_{\text{source}}^i$  respectively, we can now estimate the  $\beta_{\text{sink}}$  value for the whole myocardium.

### 15.2.2 Iterations

For the iteration with  $k > 0$ , the coronary model is simplified into a single solver step. The flows  $q^{T,i}$  provided by the porous model are used as a boundary condition at the terminal segment ends. The aortic boundary condition is maintained the same as in 7.2.2.1. The solver provides pressure and flow along the vessels. Only the terminal segment end pressures are provided as input for the porous model. The porous model is solved with the parameters defined during initialization.

### 15.2.3 Test results on simplified geometry

In this section, we work with simplified domain geometries: a single bifurcation represents the vascular network, and the shell of a half

ellipsoid stands for the left ventricle, see figure 74 (a). The two terminal segments of the bifurcation, labeled 19 and 30, end on the top of the ventricle, on two opposite sides. They are assigned equivalent perfusion territories  $\Omega_i$ , see figure 74 (b).

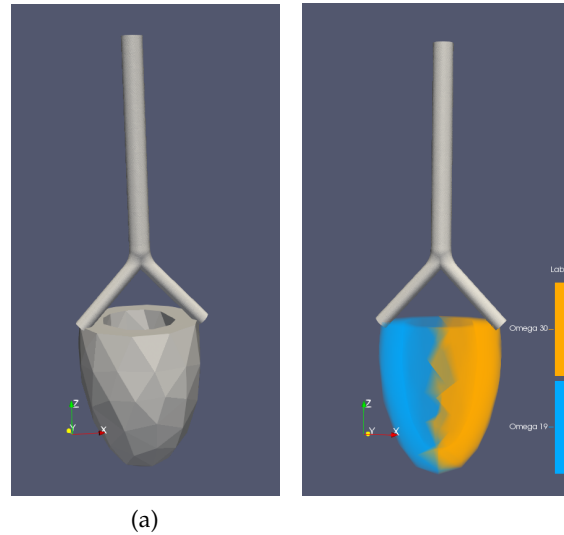


Figure 74 – Visualization of (a) the simulated coronary and myocardium domains, and (b) the  $\Omega_i$  territory associated to each terminal segment.

We study different cases in regards to

- the condition: either rest or stress
- the diameter of the terminal vessels: either equal or unequal
- the parameterisation of the beta coefficients: either calculated, as described in section 15.2.1.2, or independent.

The varying studies are summarized in the table 8.

	Rest	Stress	Rest with independent $\beta$
Equal diameter	case 1	case 2	case 5
Unequal diameter	case 3	case 4	case 6

Table 8 – Definition of the 6 cases studied.

The variable of interests are :

- the source term pressures, provided by the 1D coronary model at each iteration,
- the flow per terminal vessel, noted  $CFD_{flow}$ , also output by the 1D coronary model at each iteration,
- the flow per source term, noted  $Myo_{flow}$ , provided by the porous model at each iteration.

Below we detail parameters and results for cases 1, 3, and 6. Then we summarize results of all cases in the next section.

### 15.2.3.1 Results for case 1

The case 1 corresponds to an equal diameter bifurcation in rest condition. The table 75 summarizes the initial parameters.

Figure 75 – Initial parameters for case 1

Parameter	Value	Units	Description	
$K$	0.002	$\text{mm}^2 \text{Pa}^{-1} \text{s}^{-1}$	Permeability div. by blood viscosity	
$P_{\text{sink}}$	0	Pa	Venous tree pressure	
$\beta_{\text{sink}}$	$10.9844 \times 10^{-5}$	$\text{Pa}^{-1} \text{s}^{-1}$	Venous tree beta	
$\bar{P}$	1999.84	Pa	Average capillary tree pressure	
	<b>tv 19</b>	<b>tv 30</b>		
$P_{\text{source},k=0}^i$	12 374.4655	12 373.4995	Pa	Source pressure for term. vessel i
$\beta_{\text{source}}^i$	$2.0718 \times 10^{-5}$	$2.1632 \times 10^{-5}$	$\text{Pa}^{-1} \text{s}^{-1}$	Beta of term. vessel i
$q_{k=0}^{T,i}$	27.0567	27.7974	$\text{mm}^3 \text{s}^{-1}$	Flow rate of term. vessel i
$R_{k=0}^{T,i}$	457.3523	445.1306	$\text{Pa mm}^{-3} \text{s}$	Resistance of term. vessel i
$V_{\text{perf}}^i$	126.5640	123.1915	$\text{mm}^3$	Perfusion volume of term. vessel i

The figures 76 and 77(a) show respectively flow and pressure evolution at terminal segment outlets along iterations. Pressures have converged to their final values at iteration 2. Flow values are exactly equal at  $k = 3$ . The figure 77(b) provides visualization of the iso-pressure in the porous model at the 9th iteration, so reached convergence. The minimum and maximum pressure values obtained in myocardium are respectively 1982.44 and 2016.87 Pa, equivalent to 14.87 and 15.13 mmHg.

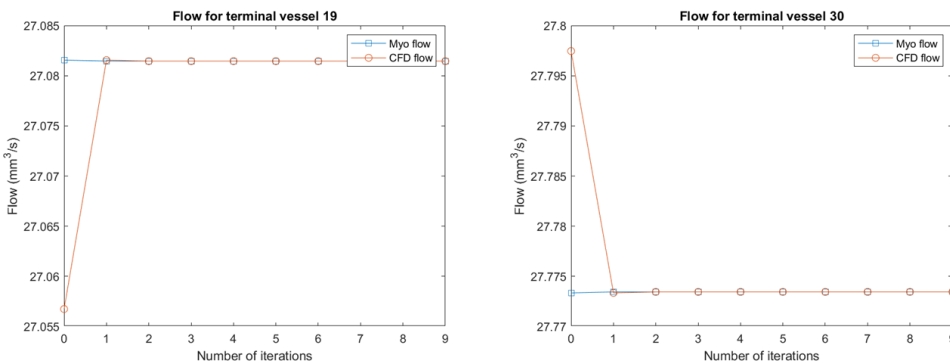


Figure 76 – Flow results along iterations at terminal segments 15 and 30 in case 1.

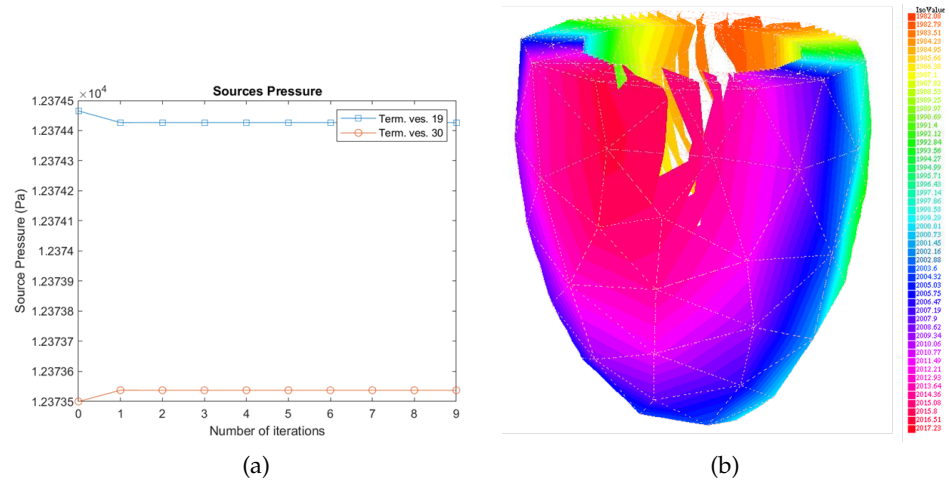


Figure 77 – Pressure results in case 1. (a) Pressure along iterations at terminal segments 15 and 30 in case 1. (b) Visualization of pressure iso values in porous model at iteration 9

### 15.2.3.2 Results for case 3

The case 3 corresponds to an unequal diameter bifurcation in rest condition. However the associated territory to each terminal segment  $\Omega_i$  are still equivalent, as in case 1. The table 78 summarizes the initial parameters.

Figure 78 – Initial parameters for case 3

Parameter	Value	Units	Description	
K	0.002	$\text{mm}^2 \text{Pa}^{-1} \text{s}^{-1}$	Permeability div. by blood viscosity	
$P_{\text{sink}}$	0	Pa	Venous tree pressure	
$\beta_{\text{sink}}$	$10.1821 \times 10^{-4}$	$\text{Pa}^{-1} \text{s}^{-1}$	Venous tree beta	
$\bar{P}$	1999.84	Pa	Average capillary tree pressure	
	<b>tv 19</b>	<b>tv 30</b>		
$P_{\text{source},k=0}^i$	12 353.1806	12 394.3465	Pa	Source pressure for term. vessel i
$\beta_{\text{source}}^i$	$3.1116 \times 10^{-5}$	$1.1107 \times 10^{-5}$	$\text{Pa}^{-1} \text{s}^{-1}$	Beta of term. vessel i
$q_{k=0}^{T,i}$	40.5528	14.3013	$\text{mm}^3 \text{s}^{-1}$	Flow rate of term. vessel i
$R_{k=0}^{T,i}$	304.619	862.2408	$\text{Pa mm}^{-3} \text{s}$	Resistance of term. vessel i
$V_{\text{perf}}^i$	126.5640	123.1915	$\text{mm}^3$	Perfusion volume of term. vessel i

The figures 79 and 80(a) show respectively flow and pressure evolution at terminal segment outlets along iterations. The simulation requires one more iteration than in case 1 to converge, which can be expected since the bifurcation is unbalanced. The pressures con-

verged to their final values at the third iteration, and flow values are exactly equal at the next one. The figure 80(b) provides visualization of the iso pressure in the porous model at the 9th iteration, so reached convergence. The pressure values obtained in myocardium show a larger range than in case 1: minimum and maximum are respectively 1605.75 and 2360.15 Pa, corresponding to 12.04 and 17.70 mmHg.

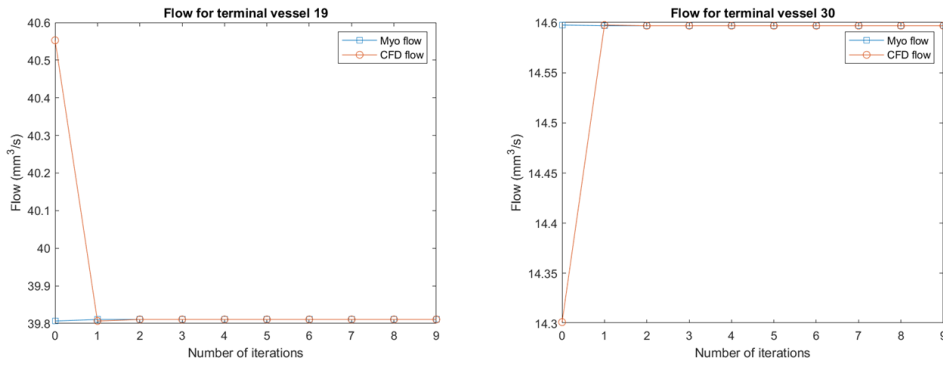


Figure 79 – Flow results along iterations at terminal segments 19 and 30 in case 3.

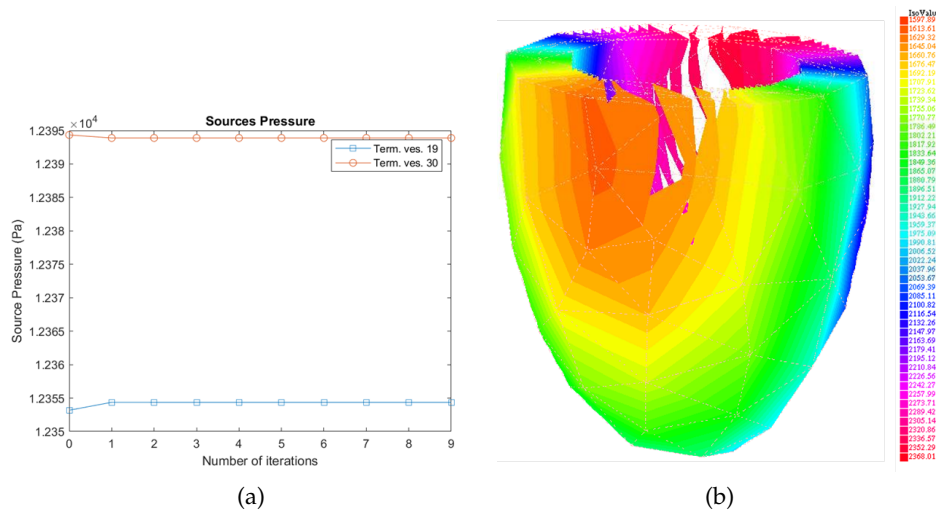


Figure 80 – Pressure results in case 3. (a): along iterations at terminal segments 15 and 19. (b): Visualization of pressure iso values in porous model at iteration 9.

### 15.2.3.3 Results for case 6

The cases 6 challenges the porous model properties by imposing equal  $\beta_{source}$  values for an unequal diameter bifurcation, in rest condition. With this parameterization we expect convergence to be achieved with equal flow values at terminal vessels.

Figure 81 – Initial parameters for case 6

Parameter	Value		Units	Description
K	0.002		$\text{mm}^2 \text{Pa}^{-1} \text{s}^{-1}$	Permeability div. by blood viscosity
$P_{\text{sink}}$	0		Pa	Venous tree pressure
$\beta_{\text{sink}}$	$10.8935 \times 10^{-5}$		$\text{Pa}^{-1} \text{s}^{-1}$	Venous tree beta
$\bar{P}$	1999.84		Pa	Average capillary tree pressure
	<b>tv 19</b>	<b>tv 30</b>		
$P_{\text{source},k=0}^i$	12 353.1806	12 394.3465	Pa	Source pressure for term. vessel i
$\beta_{\text{source},\text{independent}}^i$	$2.1 \times 10^{-5}$	$2.1 \times 10^{-5}$	$\text{Pa}^{-1} \text{s}^{-1}$	Beta of term. vessel i
$q_{k=0}^{T,i}$	40.5528	14.3013	$\text{mm}^3 \text{s}^{-1}$	Flow rate of term. vessel i
$R_{k=0}^{T,i}$	304.619	862.2408	$\text{Pa mm}^{-3} \text{s}$	Resistance of term. vessel i
$V_{\text{perf}}^i$	126.5640	123.1915	$\text{mm}^3$	Perfusion volume of term. vessel i

The table 81 summarizes the initial parameters.

The figures 82 and 83(a) show respectively flow and pressure evolution at terminal segment ends along iterations. Pressure and flow convergence are reached at same iteration as in case 3. As expected, converged terminal flow values are equal despite the unbalanced diameter bifurcation. Also, the terminal segment end pressures converge toward close values, respectively 12 373.89 and 12 374.76 Pa for vessel 19 and 30. The resulting pressure field in the myocardium is nearly constant: only a  $4 \times 10^{-2}$  Pa drop, see figure 80(b). These results show the homogenization impact of the porous model on the whole simulation.

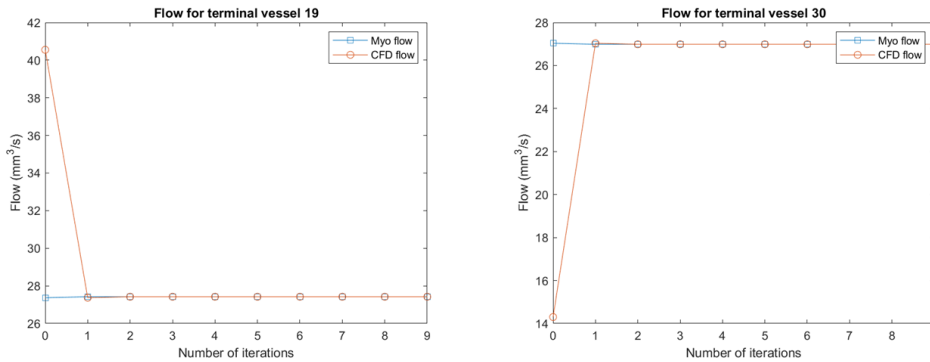


Figure 82 – Flow results along iterations at terminal segments 19 and 30 in case 6.

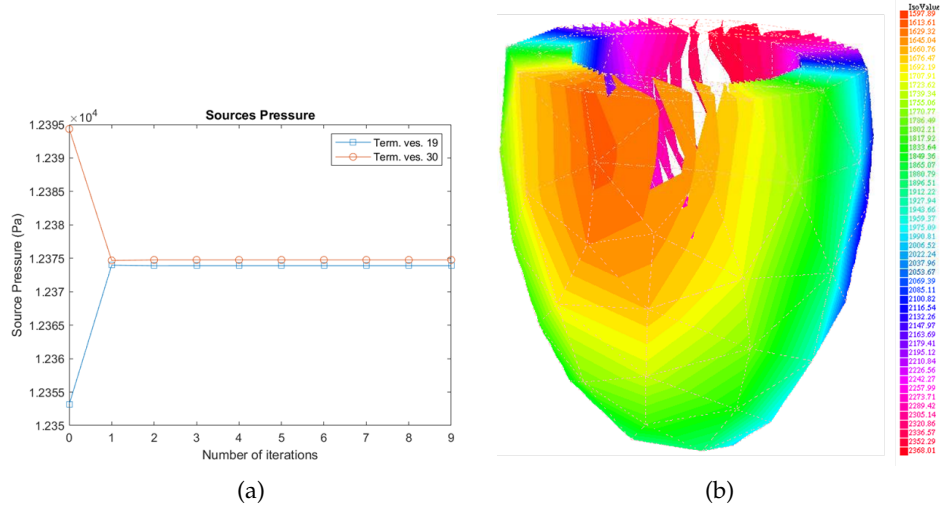


Figure 83 – Pressure results in case 6. (a): along iterations at terminal segments 19 and 30. (b): Visualization of pressure iso values in porous model at iteration 9.

#### 15.2.3.4 Summary of results on simulated data

All case results are summarized in table 84. The coupling results show communication between the two models, and convergence within 2 – 3 iterations for all cases.

Results obtained in stress conditions exhibit both higher terminal segment flows, and higher pressure drop in the myocardium, which is coherent.

Case 5 and 6 highlight the impact of porous model  $\beta_{source}$  parameterization on the coupling. Unequal values induce differentiation of terminal segment flow and higher pressure drop inside the myocardium. Equal value on whole myocardium is responsible for homogenization of terminal segment flow and myocardium pressure drop decrease.

#### 15.2.4 Preliminary result on patient data

We obtained a preliminary result on patient data. This result corresponds to a 1 way coupling, meaning at the end of the step  $k = 0$ . It was computed in rest condition for two different definition of the  $\beta_{source}$  parameters.

In the case (i) we calculate the  $\beta_{source}$  as described in 15.2.1.2, we obtain minimum and maximum pressure value inside the myocardium respectively of 10.16 and 23.07 mmHg, see figure 85. In the case (ii), we use a single  $\beta_{source}$  for the whole myocardium, of value  $3 \times 10^{-6} \text{ Pa}^{-1} \text{ s}^{-1}$ . We obtain a smaller pressure drop inside the my-

	Rest	Stress	Rest with independent $\beta$
Equal diameter	case 1	case 2	case 5: unequal $\beta_{source}^i$ (~case 3 values)
$q^{T,19}$ ( $\text{mm}^3 \text{s}^{-1}$ )	27.08	106.90	39.81
$q^{T,30}$ ( $\text{mm}^3 \text{s}^{-1}$ )	27.77	109.40	14.60
$\Delta P_{myo}$ (Pa)	34.43	61.57	754.40
Unequal diameter	case 3	case 4	case 6: equal $\beta_{source}^i$ (~case 1 values)
$q^{T,19}$ ( $\text{mm}^3 \text{s}^{-1}$ )	39.81	153.07	27.42
$q^{T,30}$ ( $\text{mm}^3 \text{s}^{-1}$ )	14.60	59.60	26.99
$\Delta P_{myo}$ (Pa)	754.40	1336.72	0.06

Figure 84 – Definition of the 6 cases studied.

ocardium, with minimum and maximum pressure value respectively of 14.69 and 15.49 mmHg, see figure 86.

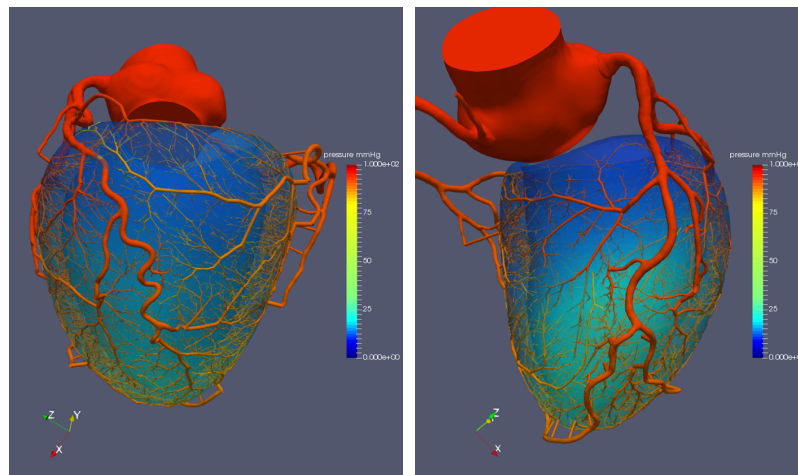


Figure 85 – Pressure results of the 1 way coupling on case (i) for 1 patient

Technical issues need to be resolved, and these results will be submitted to further investigations. We are also working on implementation of the last step of the loop.

#### 15.2.5 Future work

The final objective is to assess this coupling on patient data: with the 6000 terminal segment generated network, and our left ventricle segmentation. It will be interesting to compare with the flow distribution obtained in chapter 8. We expect the coupling to induce homogenization of the flow distribution.

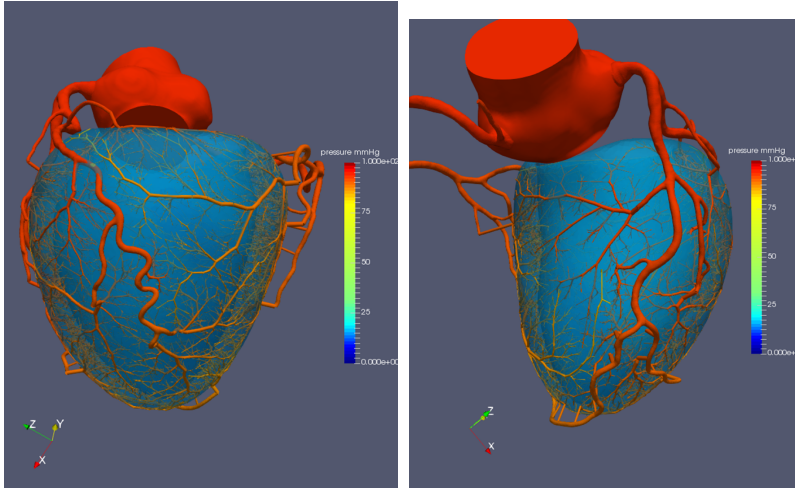


Figure 86 – Pressure results of the 1 way coupling on case (ii) for 1 patient

Parameterization of both coronary and porous model can be studied in regard of the ground-truth data. In particular  $\beta_{SOURCE}$  can be estimated locally, globally, or interpolated via the distance to the source term.

Also, the coupling could be assessed on vascular network of various size (number of terminal segments), to identify the adequate size that enables to reach flow homogenization. In order to confirm the parameterization of the coupled modelization, we will also need to assess it on patient data with acute disease.



CONTRIBUTIONS

---

This appendix summarizes individual software contributions to the project.

## 16.1 PERSONAL CONTRIBUTIONS

- Automated generation of input images necessary for CCO Forest algorithm, starting from left ventricle, left atrium and whole heart segmentation, cf Part 1 figures 17 and 18.
- CCO Forest algorithm, cf chapter 2.
- Conversion tool for visualization of synthetic vascular network geometry in *Maya Autodesk* with *RenderMan*. This tool generates a polygonal network in object file format (obj), that is then smoothed with fast subdivision, see figure 87.
- Studies of vascular network morphometry, comparing with Kassab porcine data, cf chapter 3.
- Studies of flow, pressure, resistance along vessels, and myocardium flow distribution resulting from CFD, cf chapter 8.
- Design of AHA parcellation tool and verification against nomenclature, cf section 8.5.3.1.
- Polarmap projection and per segment measure comparison with experimental data, 8.5.3.2.
- To assess porous model results within patient data, two tools have been achieved. One uses *gmsk* and *mmg* softwares to convert the left ventricle surface mesh to a volume mesh, with possibility of refinement, see figure 88. Another one transfers MBF values from the mesh (value per tetrahedron) to an image (value per voxel). This latter format is the input one for the functional analysis within the myocardium (AHA parcellation and polarmap projection). This second tool is illustrated on simulated data in figure 89.

## 16.2 CONTRIBUTIONS OF COLLABORATORS

- Identification of segmented vessel perfusing left ventricle and distribution of synthetic trees along segmented vessels: Hyun Jin Kim (HeartFlow).
- 1D coronary model for rest and stress conditions: Hyun Jin Kim (HeartFlow).
- AHA parcellation tool implementation: Karl Hahn (HeartFlow).

- Porous model in FreeFem++ and coupling with 1D coronary model, for both simulated and patient data: Lazaros Papamanolis (CentralSupélec) under supervision of Irene Vignon-Clementel (INRIA) and I.

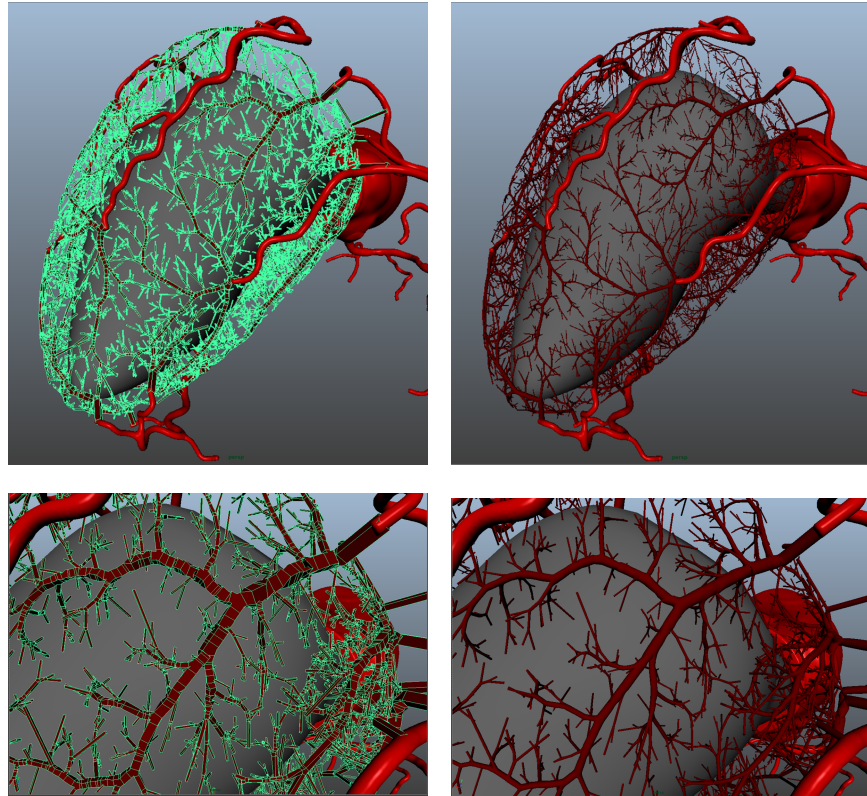


Figure 87 – Visualization of the polygonal network from obj format (left), and its smoothed version (right)

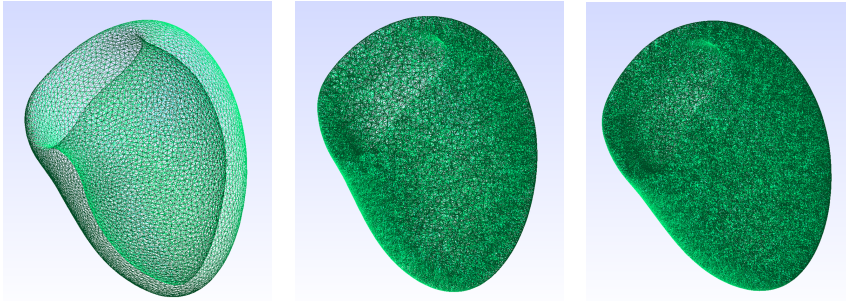


Figure 88 – Conversion from surface mesh (left), to a 57453 tetrahedral mesh (mid), and 122941 tetrahedral mesh (right).

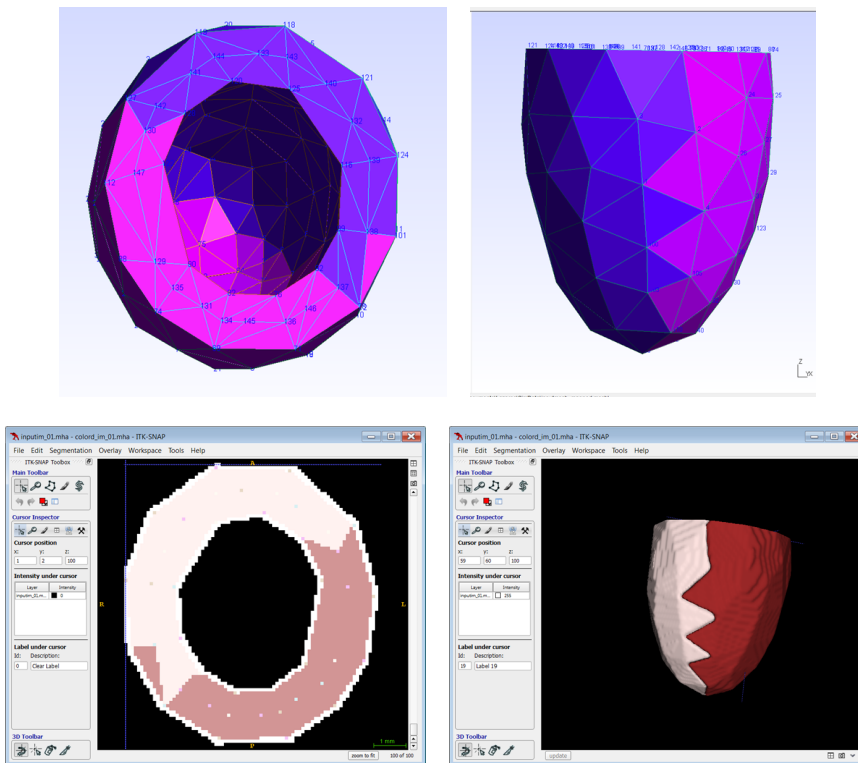


Figure 89 – Bi-labeled mesh (top) transfer to an image format visualized with itk snap (bottom). In the image the multi-color points correspond to vertices locations. There is a loss of information at borders of the object during the transfer (white voxels).



## BIBLIOGRAPHY

---

- [1] .
- [2] Suhny Abbara, Philipp Blanke, Christopher D Maroules, Michael Cheezum, Andrew D Choi, B Kelly Han, Mohamed Marwan, Chris Naoum, Bjarne L Norgaard, Ronen Rubinshtein, et al. « SCCT guidelines for the performance and acquisition of coronary computed tomographic angiography: A report of the society of Cardiovascular Computed Tomography Guidelines Committee: Endorsed by the North American Society for Cardiovascular Imaging (NASCI). » In: *Journal of cardiovascular computed tomography* 10.6 (2016), pp. 435–449.
- [3] Stephan Achenbach, Werner Moshage, Dieter Ropers, Jörg Nossen, and Werner G Daniel. « Value of electron-beam computed tomography for the noninvasive detection of high-grade coronary-artery stenoses and occlusions. » In: *New England Journal of Medicine* 339.27 (1998), pp. 1964–1971.
- [4] American Heart Association. *All About Heart Rate*. 2018. URL: <https://www.heart.org/en/health-topics/high-blood-pressure/the-facts-about-high-blood-pressure/all-about-heart-rate-pulse> (visited on 10/04/2018).
- [5] Nicholas Ayache. « Medical Imaging Informatics: Towards a Personalized Computational Patient. » In: *Yearbook of medical informatics* Suppl 1 (2016), S8.
- [6] Oguz K Baskurt and Herbert J Meiselman. « Blood rheology and hemodynamics. » In: *Seminars in thrombosis and hemostasis*. Vol. 29. 05. Copyright© 2003 by Thieme Medical Publishers, Inc., 333 Seventh Avenue, New ... 2003, pp. 435–450.
- [7] James B Bassingthwaighte, Richard B King, and Stephen A Roger. « Fractal nature of regional myocardial blood flow heterogeneity. » In: *Circulation Research* 65.3 (1989), pp. 578–590.
- [8] Michael G Bateman, Jason L Quill, Alexander J Hill, and Paul A Iaizzo. « Detailed Anatomical and Functional Features of the Cardiac Valves. » In: *Handbook of Cardiac Anatomy, Physiology, and Devices*. Springer, 2015, pp. 115–135.
- [9] Daniel A Beard and James B Bassingthwaighte. « The fractal nature of myocardial blood flow emerges from a whole-organ model of arterial network. » In: *Journal of vascular research* 37.4 (2000), pp. 282–296.
- [10] Robert M Berne and Matthew N Levy. *Cardiovascular physiology*. Mosby, 1967.

- [11] PJ Blanco, RA B de Queiroz, and RA Feijóo. « A computational approach to generate concurrent arterial networks in vascular territories. » In: *International journal for numerical methods in biomedical engineering* 29.5 (2013), pp. 601–614.
- [12] DD Buss, DM Hyde, and MY Stovall. « Application of stereology to coronary microcirculation. » In: *Basic research in cardiology* 76.4 (1981), pp. 411–415.
- [13] Rodrigo J Cerci, Armin Arbab-Zadeh, Richard T George, Julie M Miller, Andrea L Vavere, Vishal Mehra, Kihei Yoneyama, John Texter, Courtney Foster, Wei Guo, et al. « Aligning coronary anatomy and myocardial perfusion territories: an algorithm for the CORE320 multicenter study. » In: *Circulation: Cardiovascular Imaging* 5.5 (2012), pp. 587–595.
- [14] Manuel D Cerqueira, Neil J Weissman, Vasken Dilsizian, Alice K Jacobs, Sanjiv Kaul, Warren K Laskey, Dudley J Pennell, John A Rumberger, Thomas Ryan, and Mario S Verani. « Standardized myocardial segmentation and nomenclature for tomographic imaging of the heart: a statement for healthcare professionals from the Cardiac Imaging Committee of the Council on Clinical Cardiology of the American Heart Association. » In: *Journal of the American Society of Echocardiography* 15.5 (2002), pp. 463–467.
- [15] Dominique Chapelle, J-F Gerbeau, J Sainte-Marie, and IE Vignon-Clementel. « A poroelastic model valid in large strains with applications to perfusion in cardiac modeling. » In: *Computational Mechanics* 46.1 (2010), pp. 91–101.
- [16] Jenny Susana Choy and Ghassan S Kassab. « Scaling of myocardial mass to flow and morphometry of coronary arteries. » In: *Journal of Applied Physiology* 104.5 (2008), pp. 1281–1286.
- [17] Timothy F Cootes, Christopher J Taylor, David H Cooper, and Jim Graham. « Active shape models-their training and application. » In: *Computer vision and image understanding* 61.1 (1995), pp. 38–59.
- [18] Simon J Crick, Mary N Sheppard, Siew Yen Ho, Lior Gebstein, and Robert H Anderson. « Anatomy of the pig heart: comparisons with normal human cardiac structure. » In: *Journal of anatomy* 193.1 (1998), pp. 105–119.
- [19] George J Crystal and Paul S Pagel. « Right Ventricular Perfusion Physiology and Clinical Implications. » In: *Anesthesiology: The Journal of the American Society of Anesthesiologists* 128.1 (2018), pp. 202–218.

- [20] Carlo D'ANGELO and Alfio Quarteroni. « On the coupling of 1d and 3d diffusion-reaction equations: application to tissue perfusion problems. » In: *Mathematical Models and Methods in Applied Sciences* 18.08 (2008), pp. 1481–1504.
- [21] Carlo D'Angelo and Paolo Zunino. « Robust numerical approximation of coupled Stokes' and Darcy's flows applied to vascular hemodynamics and biochemical transport. » In: *ESAIM: Mathematical Modelling and Numerical Analysis* 45.3 (2011), pp. 447–476.
- [22] Ibrahim Danad, Pieter G Raijmakers, Hendrik J Harms, Martijn W Heymans, Niels van Royen, Mark Lubberink, Ronald Boellaard, Albert C van Rossum, Adriaan A Lammertsma, and Paul Knaapen. « Impact of anatomical and functional severity of coronary atherosclerotic plaques on the transmural perfusion gradient: a [<sup>15</sup>O] H<sub>2</sub>O PET study. » In: *European heart journal* 35.31 (2014), pp. 2094–2105.
- [23] Ibrahim Danad, Valteri Uusitalo, Tanja Kero, Antti Saraste, Pieter G Raijmakers, Adriaan A Lammertsma, Martijn W Heymans, Sami A Kajander, Mikko Pietilä, Stefan James, et al. « Quantitative assessment of myocardial perfusion in the detection of significant coronary artery disease: cutoff values and diagnostic accuracy of quantitative [<sup>15</sup>O] H<sub>2</sub>O PET imaging. » In: *Journal of the American College of Cardiology* 64.14 (2014), pp. 1464–1475.
- [24] Ulrich KM Decking. « Spatial heterogeneity in the heart: recent insights and open questions. » In: *Physiology* 17.6 (2002), pp. 246–250.
- [25] JT Dodge, B Greg Brown, Edward L Bolson, and Harold T Dodge. « Lumen diameter of normal human coronary arteries. Influence of age, sex, anatomic variation, and left ventricular hypertrophy or dilation. » In: *Circulation* 86.1 (1992), pp. 232–246.
- [26] Leon Menezes Ernest Lo Ryo Torii. « Use of PET-based boundary conditions in coronary artery blood flow computations to estimate clinically important hemodynamic indicators. » In: *World Conference of Biomechanics* (2018).
- [27] Tracy L Faber, Cesar A Santana, Ernest V Garcia, Jaume Candell-Riera, Russell D Folks, John W Peifer, Andrew Hopper, Santiago Aguade, Joan Angel, and J Larry Klein. « Three-dimensional fusion of coronary arteries with myocardial perfusion distributions: clinical validation. » In: *Journal of Nuclear Medicine* 45.5 (2004), pp. 745–753.

- [28] Pedro F Ferreira, Sonia Nielles-Vallespin, Andrew D Scott, Ranil de Silva, Philip J Kilner, Daniel B Ennis, Daniel A Auger, Jonathan D Suever, Xiaodong Zhong, Bruce S Spottiswoode, et al. « Evaluation of the impact of strain correction on the orientation of cardiac diffusion tensors with in vivo and ex vivo porcine hearts. » In: *Magnetic resonance in medicine* 79.4 (2018), pp. 2205–2215.
- [29] Stephan D Fihn, James C Blankenship, Karen P Alexander, John A Bittl, John G Byrne, Barbara J Fletcher, Gregg C Fonarow, Richard A Lange, Glenn N Levine, Thomas M Maddox, et al. « 2014 ACC/AHA/AATS/PCNA/SCAI/STS focused update of the guideline for the diagnosis and management of patients with stable ischemic heart disease: a report of the American College of Cardiology/American Heart Association Task Force on Practice Guidelines, and the American Association for Thoracic Surgery, Preventive Cardiovascular Nurses Association, Society for Cardiovascular Angiography and Interventions, and Society of Thoracic Surgeons. » In: *Journal of the American College of Cardiology* 64.18 (2014), pp. 1929–1949.
- [30] Valentin Fuster et al. *Hurst's the heart*. Vol. 1. McGraw-Hill, Medical Pub. Division, 2004.
- [31] Manfred Georg, Tobias Preusser, and Horst K Hahn. « Global Constructive Optimization of Vascular Systems. » In: ().
- [32] Ayush Goyal, Jack Lee, Pablo Lamata, Jeroen van den Wijngaard, Pepijn van Horssen, Jos Spaan, Maria Siebes, Vicente Grau, and Nic P Smith. « Model-based vasculature extraction from optical fluorescence cryomicrotome images. » In: *IEEE transactions on medical imaging* 32.1 (2013), pp. 56–72.
- [33] Leo Grady. « Random walks for image segmentation. » In: *IEEE transactions on pattern analysis and machine intelligence* 28.11 (2006), pp. 1768–1783.
- [34] Leo Grady, Michiel Schaap, Charles A Taylor, and Clara Jaquet. *Systems and methods for predicting perfusion deficits from physiological, anatomical, and patient characteristics*. US Patent App. 15/088,733. 2016.
- [35] AC Guyton and JE Hall. « Textbook of Medical Physiology, 11thEdn. » In: *Elsiever Saunders* (2006), pp. 788–817.
- [36] Hendrik J Harms, Paul Knaapen, Stefan de Haan, Rick Halbmeijer, Adriaan A Lammertsma, and Mark Lubberink. « Automatic generation of absolute myocardial blood flow images using  $[^{15}\text{O}]\text{H}_2\text{O}$  and a clinical PET/CT scanner. » In: *European journal of nuclear medicine and molecular imaging* 38.5 (2011), pp. 930–939.

- [37] Stefan Heinzer, Thomas Krucker, Marco Stampanoni, Rafael Abela, Eric P Meyer, Alexandra Schuler, Philipp Schneider, and Ralph Müller. « Hierarchical microimaging for multiscale analysis of large vascular networks. » In: *Neuroimage* 32.2 (2006), pp. 626–636.
- [38] K Horsfield. « Pulmonary airways and blood vessels considered as confluent trees. » In: *The lung: scientific foundations, 2nd ed.* Philadelphia: Lippencott-Raven Publishers (1997), pp. 1073–1079.
- [39] P van Horssen, MGJTB van Lier, JPHM van den Wijngaard, E VanBavel, IE Hoefler, JAE Spaan, and M Siebes. « Influence of segmented vessel size due to limited imaging resolution on coronary hyperemic flow prediction from arterial crown volume. » In: *American Journal of Physiology-Heart and Circulatory Physiology* 310.7 (2016), H839–H846.
- [40] Pepijn van Horssen, Jeroen PHM van den Wijngaard, MJ Brandt, Imo E Hoefler, Jos AE Spaan, and Maria Siebes. « Perfusion territories subtended by penetrating coronary arteries increase in size and decrease in number toward the subendocardium. » In: *American Journal of Physiology-Heart and Circulatory Physiology* 306.4 (2014), H496–H504.
- [41] Robert E Horton. « Erosional development of streams and their drainage basins; hydrophysical approach to quantitative morphology. » In: *Geological society of America bulletin* 56.3 (1945), pp. 275–370.
- [42] Jacques M Huyghe, THEO Arts, Dick H Van Campen, and ROBERT S Reneman. « Porous medium finite element model of the beating left ventricle. » In: *American Journal of Physiology-Heart and Circulatory Physiology* 262.4 (1992), H1256–H1267.
- [43] Eoin R Hyde, Christian Michler, Jack Lee, Andrew N Cookson, Radek Chabiniok, David A Nordsletten, and Nicolas P Smith. « Parameterisation of multi-scale continuum perfusion models from discrete vascular networks. » In: *Medical & biological engineering & computing* 51.5 (2013), pp. 557–570.
- [44] Eoin R Hyde, Andrew N Cookson, Jack Lee, Christian Michler, Ayush Goyal, Taha Sochi, Radomir Chabiniok, Matthew Sinclair, David A Nordsletten, Jos Spaan, et al. « Multi-scale parameterisation of a myocardial perfusion model using whole-organ arterial networks. » In: *Annals of biomedical engineering* 42.4 (2014), pp. 797–811.
- [45] Tohru Izumi, Masaru Yamazoe, and Akira Shibata. « Three-dimensional characteristics of the intramyocardial microvasculature of hypertrophied human hearts. » In: *Journal of molecular and cellular cardiology* 16.5 (1984), pp. 449–457.

- [46] Clara Jaquet, Michiel Schaap, Ying Bai, Leo Grady, and Charles A Taylor. *Systems and methods for determining and visualizing a functional relationship between a vascular network and perfused tissue*. US Patent App. 15/088,512. 2016.
- [47] Clara Jaquet, Laurent Najman, Hugues Talbot, Leo J Grady, Michiel Schaap, Buzzy Spain, Hyun Jin Kim, Irene Vignon-Clementel, and Charles A Taylor. « Generation of patient-specific cardiac vascular networks: a hybrid image-based and synthetic geometric model. » In: *IEEE Transactions on Biomedical Engineering* (2018).
- [48] Clara Jaquet, Laurent Najman, Hugues Talbot, Leo Grady, Hyung Jin Kim, Irene Vignon-Clementel, and Charles J Taylor. « Hybrid image-based and synthetic geometric models for patient-specific simulation of coronary blood flow from the large arteries to the myocardium. » In: *World Conference of Biomechanics* (2018).
- [49] Barbara M Johnston, Peter R Johnston, Stuart Corney, and David Kilpatrick. « Non-Newtonian blood flow in human right coronary arteries: steady state simulations. » In: *Journal of biomechanics* 37.5 (2004), pp. 709–720.
- [50] Benjamin Kaimovitz, Yoram Lanir, and Ghassan S Kassab. « Large-scale 3-D geometric reconstruction of the porcine coronary arterial vasculature based on detailed anatomical data. » In: *Annals of biomedical engineering* 33.11 (2005), pp. 1517–1535.
- [51] Benjamin Kaimovitz, Yunlong Huo, Yoram Lanir, and Ghassan S Kassab. « Diameter asymmetry of porcine coronary arterial trees: structural and functional implications. » In: *American Journal of Physiology-Heart and Circulatory Physiology* 294.2 (2008), H714–H723.
- [52] Fumihiko Kajiya and Masami Goto. « Integrative physiology of coronary microcirculation. » In: *The Japanese journal of physiology* 49.3 (1999), pp. 229–241.
- [53] Akira Kamiya and Tatsuo Togawa. « Optimal branching structure of the vascular tree. » In: *The Bulletin of mathematical biophysics* 34.4 (1972), pp. 431–438.
- [54] Rudolf Karch, Friederike Neumann, Martin Neumann, and Wolfgang Schreiner. « A three-dimensional model for arterial tree representation, generated by constrained constructive optimization. » In: *Computers in biology and medicine* 29.1 (1999), pp. 19–38.
- [55] Rudolf Karch, Friederike Neumann, Martin Neumann, and Wolfgang Schreiner. « Staged growth of optimized arterial model trees. » In: *Annals of biomedical engineering* 28.5 (2000), pp. 495–511.

- [56] Rudolf Karch, Friederike Neumann, Bruno K Podesser, Martin Neumann, Paul Szawłowski, and Wolfgang Schreiner. « Fractal properties of perfusion heterogeneity in optimized arterial trees: a model study. » In: *The Journal of general physiology* 122.3 (2003), pp. 307–322.
- [57] Ghassan S Kassab. « Scaling laws of vascular trees: of form and function. » In: *American Journal of Physiology-Heart and Circulatory Physiology* 290.2 (2006), H894–H903.
- [58] Ghassan S Kassab, Jeff Berkley, and Yuan-Cheng B Fung. « Analysis of pig’s coronary arterial blood flow with detailed anatomical data. » In: *Annals of biomedical engineering* 25.1 (1997), pp. 204–217.
- [59] Ghassan S Kassab, Carmela A Rider, Nina J Tang, and Yuan-Cheng Fung. « Morphometry of pig coronary arterial trees. » In: *American Journal of Physiology-Heart and Circulatory Physiology* 265.1 (1993), H350–H365.
- [60] Ghassan S Kassab, Edith Pallencaoe, Amy Schatz, and Yuan-Cheng B Fung. « Longitudinal position matrix of the pig coronary vasculature and its hemodynamic implications. » In: *American Journal of Physiology-Heart and Circulatory Physiology* 273.6 (1997), H2832–H2842.
- [61] Jonathan Keelan, Emma ML Chung, and James P Hague. « Simulated annealing approach to vascular structure with application to the coronary arteries. » In: *Open Science* 3.2 (2016), p. 150431.
- [62] HJ Kim, IE Vignon-Clementel, JS Coogan, CA Figueroa, KE Jansen, and CA Taylor. « Patient-specific modeling of blood flow and pressure in human coronary arteries. » In: *Annals of biomedical engineering* 38.10 (2010), pp. 3195–3209.
- [63] Marek Kretowski, Yan Rolland, Johanne Bézy-Wendling, and J-L Coatrieux. « Physiologically based modeling of 3-D vascular networks and CT scan angiography. » In: *IEEE transactions on medical imaging* 22.2 (2003), pp. 248–257.
- [64] Jack Lee, Andrew Cookson, Radomir Chabiniok, Simone Rivolo, Eoin Hyde, Matthew Sinclair, Christian Michler, Taha Sochi, and Nicolas Smith. « Multiscale modelling of cardiac perfusion. » In: *Modeling the heart and the circulatory system*. Springer, 2015, pp. 51–96.
- [65] Wing-Huang Leung, Michael L Stadius, and Edwin L Alderman. « Determinants of normal coronary artery dimensions in humans. » In: *Circulation* 84.6 (1991), pp. 2294–2306.
- [66] Ihor A Lubashevsky and Vasil V. Gafiychuk. « Analysis of the optimality principles responsible for vascular network architectonics. » In: *arXiv preprint adap-org/9909003* (1999).

- [67] Shant Malkasian, Logan Hubbard, Brian Dertli, Jungnam Kwon, and Sabee Molloi. « Quantification of vessel-specific coronary perfusion territories using minimum-cost path assignment and computed tomography angiography: Validation in a swine model. » In: *Journal of Cardiovascular Computed Tomography* (2018).
- [68] Koen S Matthys, Jordi Alastruey, Joaquim Peiró, Ashraf W Khir, Patrick Segers, Pascal R Verdonck, Kim H Parker, and Spencer J Sherwin. « Pulse wave propagation in a model human arterial network: assessment of 1-D numerical simulations against in vitro measurements. » In: *Journal of biomechanics* 40.15 (2007), pp. 3476–3486.
- [69] Pascal Meier, Harry Hemingway, Alexandra J Lansky, Guido Knapp, Bertram Pitt, and Christian Seiler. « The impact of the coronary collateral circulation on mortality: a meta-analysis. » In: *European heart journal* 33.5 (2011), pp. 614–621.
- [70] N Mittal, Y Zhou, S Ung, C Linares, S Molloi, and GS Kassab. « A computer reconstruction of the entire coronary arterial tree based on detailed morphometric data. » In: *Annals of biomedical engineering* 33.8 (2005), pp. 1015–1026.
- [71] N Mittal, Y Zhou, C Linares, S Ung, B Kaimovitz, S Molloi, and GS Kassab. « Analysis of blood flow in the entire coronary arterial tree. » In: *American journal of physiology-Heart and circulatory physiology* 289.1 (2005), H439–H446.
- [72] Paul D Morris, Daniel Alejandro Silva Soto, Jeroen FA Feher, Dan Rafiroiu, Angela Lungu, Susheel Varma, Patricia V Lawford, D Rodney Hose, and Julian P Gunn. « Fast virtual fractional flow reserve based upon steady-state computational fluid dynamics analysis: results from the VIRTU-Fast study. » In: *JACC: Basic to Translational Science* 2.4 (2017), pp. 434–446.
- [73] Manish Motwani, Mahsaw Motlagh, Anuj Gupta, Daniel S Berman, and Piotr J Slomka. « Reasons and implications of agreements and disagreements between coronary flow reserve, fractional flow reserve, and myocardial perfusion imaging. » In: *Journal of Nuclear Cardiology* 25.1 (2018), pp. 104–119.
- [74] Cecil D Murray. « The physiological principle of minimum work: I. The vascular system and the cost of blood volume. » In: *Proceedings of the National Academy of Sciences* 12.3 (1926), pp. 207–214.
- [75] American Heart Association Writing Group on Myocardial Segmentation et al. « Standardized myocardial segmentation and nomenclature for tomographic imaging of the heart: a statement for healthcare professionals from the Cardiac Imaging Committee of the Council on Clinical Cardiology of the

- American Heart Association. » In: *Circulation* 105.4 (2002), pp. 539–542.
- [76] Peer Neubert and Peter Protzel. « Compact watershed and pre-emptive slic: On improving trade-offs of superpixel segmentation algorithms. » In: *Pattern Recognition (ICPR), 2014 22nd International Conference on*. IEEE. 2014, pp. 996–1001.
- [77] Sonia Nielles-Vallespin, Zohya Khalique, Pedro F Ferreira, Rani de Silva, Andrew D Scott, Philip Kilner, Laura-Ann McGill, Archontis Giannakidis, Peter D Gatehouse, Daniel Ennis, et al. « Assessment of myocardial microstructural dynamics by in vivo diffusion tensor cardiac magnetic resonance. » In: *Journal of the American College of Cardiology* 69.6 (2017), pp. 661–676.
- [78] Nico HJ Pijls, Bernard de Bruyne, Kathinka Peels, Pepijn H van der Voort, Hans JRM Bonnier, Jozef Bartunek, and Jacques J Koolen. « Measurement of fractional flow reserve to assess the functional severity of coronary-artery stenoses. » In: *New England Journal of Medicine* 334.26 (1996), pp. 1703–1708.
- [79] Axel R Pries and Timothy W Secomb. « Blood flow in microvascular networks. » In: *Microcirculation*. Elsevier, 2008, pp. 3–36.
- [80] J Reig, A Jornet, and M Petit. « Coronary arterial territories of the left ventricle: extension and exclusivity. » In: *Surgical and Radiologic Anatomy* 16.3 (1994), pp. 281–285.
- [81] Simone Rivolo, Lucas Hadjilucas, Matthew Sinclair, Pepijn van Horsen, Jeroen van den Wijngaard, Roman Wesolowski, Amedeo Chiribiri, Maria Siebes, Nicolas P Smith, and Jack Lee. « Impact of coronary bifurcation morphology on wave propagation. » In: *American Journal of Physiology-Heart and Circulatory Physiology* 311.4 (2016), H855–H870.
- [82] Sethuraman Sankaran, Leo Grady, and Charles A Taylor. « Fast computation of hemodynamic sensitivity to lumen segmentation uncertainty. » In: *IEEE transactions on medical imaging* 34.12 (2015), pp. 2562–2571.
- [83] Sethuraman Sankaran, Hyun Jin Kim, Gilwoo Choi, and Charles A Taylor. « Uncertainty quantification in coronary blood flow simulations: impact of geometry, boundary conditions and blood viscosity. » In: *Journal of biomechanics* 49.12 (2016), pp. 2540–2547.
- [84] W Schaper. *Collateral vessels reduce mortality*. 2011.
- [85] Wolfgang Schreiner and Peter Franz Buxbaum. « Computer-optimization of vascular trees. » In: *Biomedical Engineering, IEEE Transactions on* 40.5 (1993), pp. 482–491.

- [86] Wolfgang Schreiner, Rudolf Karch, Martin Neumann, Friederike Neumann, Paul Szawlowski, and Susanne Roedler. « Optimized arterial trees supplying hollow organs. » In: *Medical engineering & physics* 28.5 (2006), pp. 416–429.
- [87] Christian Seiler, Richard L Kirkeeide, and K Lance Gould. « Basic structure-function relations of the epicardial coronary vascular tree. Basis of quantitative coronary arteriography for diffuse coronary artery disease. » In: *Circulation* 85.6 (1992), pp. 1987–2003.
- [88] Stephanie L Sellers, Tim A Fonte, Rominder Grover, John Mooney, Jonathan Weir-McCall, Karen PL Lau, Anesh Chavda, Charis McNabney, Amir Ahmadi, Philipp Blanke, et al. « Hypertrophic Cardiomyopathy (HCM): New insights into Coronary artery remodelling and ischemia from FFRCT. » In: *Journal of cardiovascular computed tomography* (2018).
- [89] Jean Serra. *Image analysis and mathematical morphology, v.1*. English revised version. London: Academic Press, 1982. URL: <http://cds.cern.ch/record/235415>.
- [90] Matthew D Sinclair, Jack Lee, Andrew N Cookson, Simone Rivolo, Eoin R Hyde, and Nicolas P Smith. « Measurement and modeling of coronary blood flow. » In: *Wiley Interdisciplinary Reviews: Systems Biology and Medicine* 7.6 (2015), pp. 335–356.
- [91] NP Smith, AJ Pullan, and PJ Hunter. « Generation of an anatomically based geometric coronary model. » In: *Annals of biomedical engineering* 28.1 (2000), pp. 14–25.
- [92] NP Smith, AJ Pullan, and Peter J Hunter. « An anatomically based model of transient coronary blood flow in the heart. » In: *SIAM Journal on Applied mathematics* 62.3 (2002), pp. 990–1018.
- [93] JC Stettler, P Niederer, and M Anliker. « Theoretical analysis of arterial hemodynamics including the influence of bifurcations. » In: *Annals of biomedical engineering* 9.2 (1981), pp. 145–164.
- [94] Arthur N Strahler. « Hypsometric (area-altitude) analysis of erosional topography. » In: *Geological Society of America Bulletin* 63.11 (1952), pp. 1117–1142.
- [95] Akira Tanaka, Hidezo Mori, Etsuro Tanaka, Minhaz Uddin Mohammed, Yutaka Tanaka, Takafumi Sekka, Kuniyoshi Ito, Yoshiro Shinozaki, Kazuyuki Hyodo, Masami Ando, et al. « Branching patterns of intramural coronary vessels determined by microangiography using synchrotron radiation. » In: *American Journal of Physiology-Heart and Circulatory Physiology* 276.6 (1999), H2262–H2267.

- [96] M Howatson Tawhai, AJ Pullan, and PJ Hunter. « Generation of an anatomically based three-dimensional model of the conducting airways. » In: *Annals of biomedical engineering* 28.7 (2000), pp. 793–802.
- [97] CA Taylor, Timothy A Fonte, and James K Min. « CFD applied to cardiac CT for noninvasive quantification of FFR. » In: *J. Am. Coll. Cardiology* (2013).
- [98] Tobias Traupe, Steffen Gloekler, Stefano F de Marchi, Gerald S Werner, and Christian Seiler. « Assessment of the human coronary collateral circulation. » In: *Circulation* 122.12 (2010), pp. 1210–1220.
- [99] Shengxian Tu, Emanuele Barbato, Zsolt Köszegi, Junqing Yang, Zhonghua Sun, Niels R Holm, Balázs Tar, Yingguang Li, Dan Rusinaru, William Wijns, et al. « Fractional flow reserve calculation from 3-dimensional quantitative coronary angiography and TIMI frame count: a fast computer model to quantify the functional significance of moderately obstructed coronary arteries. » In: *JACC: Cardiovascular Interventions* 7.7 (2014), pp. 768–777.
- [100] P Van Horsen, JPHM van den Wijngaard, MJ Brandt, IE Hofer, JAE Spaan, and M Siebes. « Perfusion territories subtended by penetrating coronary arteries increase in size and decrease in number toward the subendocardium. » In: *American Journal of Physiology-Heart and Circulatory Physiology* 306.4 (2013), H496–H504.
- [101] E VanBavel and JA Spaan. « Branching patterns in the porcine coronary arterial tree. Estimation of flow heterogeneity. » In: *Circulation research* 71.5 (1992), pp. 1200–1212.
- [102] Irene E Vignon-Clementel, C Alberto Figueroa, Kenneth E Jansen, and Charles A Taylor. « Outflow boundary conditions for three-dimensional finite element modeling of blood flow and pressure in arteries. » In: *Computer methods in applied mechanics and engineering* 195.29-32 (2006), pp. 3776–3796.
- [103] Irene E Vignon and Charles A Taylor. « Outflow boundary conditions for one-dimensional finite element modeling of blood flow and pressure waves in arteries. » In: *Wave Motion* 39.4 (2004), pp. 361–374.
- [104] Alfonso H Waller, Ron Blankstein, Raymond Y Kwong, and Marcelo F Di Carli. « Myocardial blood flow quantification for evaluation of coronary artery disease by positron emission tomography, cardiac magnetic resonance imaging, and computed tomography. » In: *Current cardiology reports* 16.5 (2014), p. 483.

- [105] Morris E Weaver, GEORGE A PANTELY, J David Bristow, and HERBERT D LADLEY. « A quantitative study of the anatomy and distribution of coronary arteries in swine in comparison with other animals and man. » In: *Cardiovascular research* 20.12 (1986), pp. 907–917.
- [106] WebMD. *Picture of the Heart*. 2014. URL: <https://www.webmd.com/heart/picture-of-the-heart> (visited on 12/05/2018).
- [107] Nico Westerhof, Jan-Willem Lankhaar, and Berend E Westerhof. « The arterial windkessel. » In: *Medical & biological engineering & computing* 47.2 (2009), pp. 131–141.
- [108] Nico Westerhof, Christa Boer, Regis R Lamberts, and Pieter Sipkema. « Cross-talk between cardiac muscle and coronary vasculature. » In: *Physiological Reviews* 86.4 (2006), pp. 1263–1308.
- [109] Jeroen PHM van den Wijngaard, Janina CV Schwarz, Pepijn van Horssen, Monique GJTB van Lier, Johannes GG Dobbe, Jos AE Spaan, and Maria Siebes. « 3D Imaging of vascular networks for biophysical modeling of perfusion distribution within the heart. » In: *Journal of biomechanics* 46.2 (2013), pp. 229–239.
- [110] Robert F Wilson, Keith Wyche, Betsy V Christensen, Steven Zimmer, and David D Laxson. « Effects of adenosine on human coronary arterial circulation. » In: *Circulation* 82.5 (1990), pp. 1595–1606.
- [111] Thomas Wischgoll, Jenny S Choy, and Ghassan S Kassab. « Extraction of morphometry and branching angles of porcine coronary arterial tree from CT images. » In: *American Journal of Physiology-Heart and Circulatory Physiology* 297.5 (2009), H1949–H1955.
- [112] Kerstin Wustmann, Stephan Zbinden, Stephan Windecker, Bernhard Meier, and Christian Seiler. « Is there functional collateral flow during vascular occlusion in angiographically normal coronary arteries? » In: *Circulation* 107.17 (2003), pp. 2213–2220.
- [113] M Zamir. « Distributing and delivering vessels of the human heart. » In: *The Journal of general physiology* 91.5 (1988), pp. 725–735.
- [114] Yifang Zhou, Ghassan S Kassab, and Sabee Molloi. « On the design of the coronary arterial tree: a generalization of Murray’s law. » In: *Physics in Medicine & Biology* 44.12 (1999), p. 2929.